



INSA

N°d'ordre NNT : xxx

THESE de DOCTORAT DE L'INSA LYON, membre de l'Université de Lyon

Ecole Doctorale N° 162
Ecole Doctorale Mécanique, Energétique, Génie civil, Acoustique
(MEGA)

Spécialité/ discipline de doctorat :
Mécanique

Soutenue publiquement le jj/mm/aaaa, par :

Marjolaine Gonon-Caux

**A new approach of lubricant behavior in
highly loaded contact**

Devant le jury composé de :

Nom, prénom grade/qualité établissement/entreprise **Président.e (à préciser après la soutenance)**

MOLIMARD, Jérôme	Professeur, Ecole des Mines de Saint-Etienne	Rapporteur
PALOMBO, Francesca	Professeure, Université d'Exeter	Rapporteure
DWYER-JOYCE, Robert	Professeur, Université de Sheffield	Examineur
PHILIPPON, David	Maître de Conférences, INSA de Lyon	Examineur
MARTINIE, Laetitia	Maître de Conférences, INSA de Lyon	Co-directrice de thèse
MARGUERITAT, Jérémie	Chargé de Recherche, UCBL1	Invité

Département FEDORA – INSA Lyon - Ecoles Doctorales

SIGLE	ECOLE DOCTORALE	NOM ET COORDONNEES DU RESPONSABLE
ED 206 CHIMIE	CHIMIE DE LYON https://www.edchimie-lyon.fr Sec. : Renée EL MELHEM Bât. Blaise PASCAL, 3e étage secretariat@edchimie-lyon.fr	M. Stéphane DANIELE C2P2-CPE LYON-UMR 5265 Bâtiment F308, BP 2077 43 Boulevard du 11 novembre 1918 69616 Villeurbanne directeur@edchimie-lyon.fr
ED 341 E2M2	ÉVOLUTION, ÉCOSYSTÈME, MICROBIOLOGIE, MODÉLISATION http://e2m2.universite-lyon.fr Sec. : Bénédicte LANZA Bât. Atrium, UCB Lyon 1 Tél : 04.72.44.83.62 secretariat.e2m2@univ-lyon1.fr	Mme Sandrine CHARLES Université Claude Bernard Lyon 1 UFR Biosciences Bâtiment Mendel 43, boulevard du 11 Novembre 1918 69622 Villeurbanne CEDEX e2m2.codir@listes.univ-lyon1.fr
ED 205 EDISS	INTERDISCIPLINAIRE SCIENCES-SANTÉ http://ediss.universite-lyon.fr Sec. : Bénédicte LANZA Bât. Atrium, UCB Lyon 1 Tél : 04.72.44.83.62 secretariat.ediss@univ-lyon1.fr	Mme Sylvie RICARD-BLUM Laboratoire ICBMS - UMR 5246 CNRS - Université Lyon 1 Bâtiment Raulin - 2ème étage Nord 43 Boulevard du 11 novembre 1918 69622 Villeurbanne Cedex Tél : +33(0)4 72 44 82 32 sylvie.ricard-blum@univ-lyon1.fr
ED 34 EDML	MATÉRIAUX DE LYON http://ed34.universite-lyon.fr Sec. : Yann DE ORDENANA Tél : 04.72.18.62.44 yann.de-ordenana@ec-lyon.fr	M. Stéphane BENAYOUN Ecole Centrale de Lyon Laboratoire LTDS 36 avenue Guy de Collongue 69134 Ecully CEDEX Tél : 04.72.18.64.37 stephane.benayoun@ec-lyon.fr
ED 160 EEA	ÉLECTRONIQUE, ÉLECTROTECHNIQUE, AUTOMATIQUE https://edeea.universite-lyon.fr Sec. : Philomène TRECCOURT Bâtiment Direction INSA Lyon Tél : 04.72.43.71.70 secretariat.edeea@insa-lyon.fr	M. Philippe DELACHARTRE INSA LYON Laboratoire CREATIS Bâtiment Blaise Pascal, 7 avenue Jean Capelle 69621 Villeurbanne CEDEX Tél : 04.72.43.88.63 philippe.delachartre@insa-lyon.fr
ED 512 INFOMATHS	INFORMATIQUE ET MATHÉMATIQUES http://edinfomaths.universite-lyon.fr Sec. : Renée EL MELHEM Bât. Blaise PASCAL, 3e étage Tél : 04.72.43.80.46 infomaths@univ-lyon1.fr	M. Hamamache KHEDDOUCI Université Claude Bernard Lyon 1 Bât. Nautibus 43, Boulevard du 11 novembre 1918 69 622 Villeurbanne Cedex France Tél : 04.72.44.83.69 direction.infomaths@listes.univ-lyon1.fr
ED 162 MEGA	MÉCANIQUE, ÉNERGÉTIQUE, GÉNIE CIVIL, ACOUSTIQUE http://edmega.universite-lyon.fr Sec. : Philomène TRECCOURT Tél : 04.72.43.71.70 Bâtiment Direction INSA Lyon mega@insa-lyon.fr	M. Etienne PARIZET INSA Lyon Laboratoire LVA Bâtiment St. Exupéry 25 bis av. Jean Capelle 69621 Villeurbanne CEDEX etienne.parizet@insa-lyon.fr
ED 483 ScSo	ScSo¹ https://edsciencesociales.universite-lyon.fr Sec. : Mélina FAVETON Tél : 04.78.69.77.79 melina.faveton@univ-lyon2.fr	M. Bruno MILLY (INSA : J.Y. TOUSSAINT) Univ. Lyon 2 Campus Berges du Rhône 18, quai Claude Bernard 69365 LYON CEDEX 07 Bureau BEL 319 bruno.milly@univ-lyon2.fr

¹ ScSo : Histoire, Géographie, Aménagement, Urbanisme, Archéologie, Science politique, Sociologie, Anthropologie

Une nouvelle approche du comportement du lubrifiant dans un contact fortement chargé

Résumé : Cette recherche doctorale porte sur le comportement des lubrifiants dans les contacts lubrifiés fortement chargés (pression > 1 GPa), ou contacts EHD (élastohydrodynamiques), un aspect vital de l'ingénierie et de l'industrie. Sous une charge aussi élevée, le coefficient de frottement (= force tangentielle/charge normale) mesuré dans ces contacts peut présenter un régime de plateau à des vitesses de glissement moyennes ou élevées des surfaces solides. Cela signifie que la contrainte de cisaillement moyenne macroscopique devient indépendante de la vitesse de cisaillement, associée dans la littérature à la contrainte de cisaillement limite du lubrifiant (LSS). Cependant, les mécanismes physiques qui régissent le frottement restent aujourd'hui en cours de recherche. Les travaux antérieurs suggèrent que le plateau de frottement pourrait résulter soit du glissement du lubrifiant à l'interface de la paroi, soit de la formation de bandes de cisaillement dans le film de lubrifiant ou bien encore de la transition vitreuse du lubrifiant. Des simulations récentes de dynamique moléculaire ont révélé des profils de vitesse du lubrifiant homogènes et linéaires sur toute l'épaisseur du film de lubrifiant, même dans le régime de plateau de frottement, sans glissement au niveau des parois. Cela implique que le plateau de frottement devrait résulter d'une propriété intrinsèque du lubrifiant, rappelant le scénario de la transition vitreuse du lubrifiant.

La présente étude porte sur trois fluides modèles : le squalane, le benzoate de benzyle et le glycérol. Ces fluides ont été caractérisés dans une cellule à enclume de diamant à haute pression et un rhéomètre. Deux installations de spectroscopie de diffusion de la lumière Brillouin ont été utilisées : TFP-1 (ILM, Villeurbanne) et le spectromètre VIPA installé pendant la thèse à l'INSA de Lyon à Villeurbanne. Les résultats obtenus avec le nouvel appareil VIPA ont été comparés à ceux du TFP-1 et à ceux de la littérature. Les résultats des expériences à haute pression ont été comparés aux mesures de friction effectuées précédemment sur le squalane et le benzoate de benzyle. L'étude montre une corrélation entre la transition vitreuse de ces fluides et l'apparition du plateau de frottement dans les contacts EHD.

Cette recherche fait progresser notre compréhension du frottement dans les contacts lubrifiés fortement sollicités et souligne l'importance de prendre en compte la dynamique locale lors de l'étude de fluides complexes dans des conditions extrêmes. Ces connaissances pourraient permettre d'améliorer le développement des lubrifiants et de relever les défis liés au frottement dans les domaines de l'ingénierie et de l'industrie.

Mots clés : Contrainte limite de cisaillement, contacts lubrifiés fortement chargés, cellule à enclume de diamants, transition vitreuse, mesure in situ.

A new approach of lubricant behavior in highly loaded contact

Abstract: This doctoral research focuses on lubricants behavior in highly loaded lubricated contacts (pressure > 1 GPa), or EHD (elastohydrodynamic) contacts, a vital aspect of engineering and industry. Under such high load, the friction coefficient (= tangential force/normal load) measured in these contacts may display a plateau regime at medium to high sliding velocities of the solid surfaces. It means that the macroscopic average shear stress becomes shear rate independent, associated in the literature to the lubricant Limiting Shear Stress (LSS). Yet, the physical mechanisms governing friction remain poorly understood. Previous work provided by the literature suggested that the friction plateau could result from either the lubricant sliding at the wall interface, shear bands forming in the lubricant film, or the lubricant glass transition. Recent molecular dynamic simulations revealed homogeneous and linear lubricant velocity profiles across the lubricant film thickness, even in the friction plateau regime, with no sliding at the walls. This implies that the friction plateau should result from an intrinsic property of the lubricant, reminiscent of the lubricant glass transition scenario.

The present study investigates three model fluids: squalane, benzyl benzoate, and glycerol. Those fluids have been characterized in a high-pressure diamond anvil cell and a rheometer, both combined to two Brillouin light scattering spectroscopy set-ups: TFP-1 (ILM, Villeurbanne) and VIPA spectrometer installed during the PhD at INSA de Lyon, Villeurbanne. The results obtained from the new VIPA rig have been compared to those from TFP-1 and the literature. The results from high-pressure experiments have been compared to friction measurements previously conducted on squalane and benzyl benzoate. The study shows a correlation between the glass transition of these fluids and the onset of the friction plateau in EHD contacts.

This research advances our understanding on friction in highly loaded lubricated contacts and highlights the importance of considering local dynamics when studying complex fluids under extreme conditions. These insights have the potential to improve lubricant development and to address friction-related challenges in engineering and industry.

Keywords: Shear stress, highly loaded lubricated contacts, diamond anvil cell, glass transition, in situ measurement.

Preface

Table of content

PREFACE	7
NOMENCLATURE	13
RÉSUMÉ ÉTENDU	19
0.1. INTRODUCTION ET OBJECTIFS CONTEXTE ET ETAT DE L'ART DE LA FRICTION LUBRIFICATION	19
0.2. UTILISATION DE LA SPECTROSCOPIE BRILLOUIN POUR LA DETECTION DE LA TRANSITION VITREUSE	22
0.3. METHODE EXPERIMENTAL EMPLOYES	24
0.4. VALIDATION DU BANC EXPERIMENTAL	28
0.5 RESULTAT HAUTE PRESSION ET COMPARAISON AUX ETUDE DE FROTTEMENTS	31
0.6 LIMITATIONS ET PERSPECTIVES	37
GENERAL INTRODUCTION	39
1. GENERAL BACKGROUND ABOUT FRICTION IN LUBRICANT FILMS	43
1.1 ENVIRONMENTAL AND ECONOMICAL MOTIVATIONS	45
1.2 BASICS OF LUBRICATION	48
1.2.1 REGIME OF LUBRICATION.....	48
1.2.2 A BRIEF OVERVIEW OF A LUBRICATED CONTACT COMPLEXITY	50
1.2.3 TYPICAL FRICTION CURVE.....	51
1.3 FRICTION UNDER HIGH PRESSURE AND SHEAR STRESS	54
1.3.1 ORIGIN(S) OF FRICTION PLATEAU	54
1.3.2 GLASS TRANSITION AND RELAXATION TIME	59
1.4 BRILLOUIN LIGHT SCATTERING	63
1.4.1 CHARACTERIZATION OF THE GLASS TRANSITION	63
1.4.2 BRILLOUIN LIGHT SPECTROSCOPY CHARACTERIZATION OF LUBRICANTS	67
1.5 OUTLINES OF THE WORK	70
2. INTRODUCTION TO BRILLOUIN SPECTROSCOPY	73
2.1 HISTORY AND APPLICATIONS OF BRILLOUIN LIGHT SCATTERING SPECTROSCOPY	75
2.2 VIBRATIONAL SPECTROSCOPY	77
2.1.1 ELECTROMAGNETIC (EM) WAVES	77

2.1.2.	INTRODUCTION TO VIBRATIONS AND PHONONS.....	79
2.1.3.	INELASTIC LIGHT SPECTROSCOPY.....	81
2.2.	BRILLOUIN SCATTERING SPECTROSCOPY	83
2.2.1.	PHOTONS AND PHONONS INTERACTION, THE SCATTERING PROCESS AND GEOMETRY ...	83
2.2.2	BRILLOUIN SPECTRA	86
2.2.3	SCATTERING GEOMETRY.....	88
2.2.4	LIGHT POLARIZATION ON THE BRILLOUIN SPECTRA.....	89
2.3	FROM VISCOELASTIC PROPERTIES OF MATTER TO THE INELASTIC BRILLOUIN SPECTRUM	90
2.3.1	SIMPLE MODEL WITHOUT DAMPING.....	90
2.3.2	LINEARIZED HYDRODYNAMIC EQUATIONS WITH DAMPING.....	92
2.3.3	THE GENERALIZED HYDRODYNAMIC EQUATION FOR SIMPLE FLUIDS	92
2.3.4	THE GENERALIZED HYDRODYNAMIC EQUATION FOR VISCOELASTIC FLUIDS	93
2.4	DENSITY EQUATION FOR DIFFERENT REGIMES.....	94
2.4.1	RELAXED REGIME $\omega t_{rel} \ll 1$ BY DAMPING HARMONIC OSCILLATOR MODEL (DHO).....	96
2.4.2	FOR $\omega t_{rel} \sim 1$ DEBYE AND COLE DAVIDSON MODEL NEAR THE GLASS TRANSITION	97
2.4.3.	FOR $\omega t_{rel} \gg 1$ THE VOIGT MODEL.....	98
2.5.	LOCAL SPECTRUM ANALYSIS	98
2.6.	CONCLUSION	100
3.	<u>EXPERIMENTAL METHOD</u>	<u>101</u>
3.1.	SAMPLE DESCRIPTION	103
3.1.1.	FLUIDS AND RHEOLOGICAL MODEL DESCRIPTION	103
3.1.2.	DENSITY MODEL	105
3.2.	BRILLOUIN SET-UP	107
3.2.1.	FABRY-PÉROT BRILLOUIN SPECTROMETER	108
3.2.2.	VIPA SPECTROMETER.....	110
3.3.	MICROSCOPES.....	113
3.3.1.	ILM SET-UP	113
3.3.2.	LAMCOS SET-UP.....	114
3.4	HIGH-PRESSURE CELLS	118
3.4.1	HIGH-PRESSURE CELLS DESIGN	118
3.4.2	DETERMINATION OF THE PRESSURE INSIDE THE DAC	120
3.5.	TRIBOMETER SET-UP.....	123
3.6	CONCLUSION	126
4.	<u>FITTING, SOFTWARE, AND SETUP VALIDATION.....</u>	<u>127</u>
4.1.	INSTRUMENTAL FACTOR.....	129
4.1.1.	DECONVOLUTION	129
4.1.2.	NUMERICAL BROADENING	129

4.2.	VALIDATION OF THE PRESSURE EXTRACTION PROCESS	130
4.2.1.	EXPERIMENTAL SET-UP	130
4.2.2.	RUBY STANDARD DEVIATION	131
4.2.3.	BRILLOUIN STANDARD DEVIATION	133
4.3.	DATA PROCESSING: FITTING PROCEDURE	134
4.3.1.	SOFTWARE AND FITTING PROCEDURE.....	134
4.3.2.	SINGLE VERSUS MULTI-FIT LORENTZ PROCEDURE ON ORIGINPRO.....	138
4.3.3.	FITTING PROCEDURE: SINGLE LORENTZ VERSUS DHO FOR EACH SOFTWARE.....	141
4.3.4.	DIFFERENCE BETWEEN SINGLE LORENTZ GHOST AND MULTI-LORENTZ ORIGINPRO	144
4.4.	ASYMMETRY OF THE SPECTRA.....	146
4.4.1.	ASYMMETRY ON THE GLYCEROL SAMPLE AT LOW PRESSURE.....	146
4.4.2.	ASYMMETRY BETWEEN STOKES AND ANTI-STOKES OF THE INELASTIC PEAKS UNDER PRESSURE FOR BOTH SOFTWARES	147
4.4.3.	ASYMMETRY BETWEEN STOKES AND ANTI-STOKES INSIDE THE DAC UNDER PRESSURE FOR BOTH SOFTWARES	151
4.5.	VALIDATION OF THE PROCEDURE AND SET-UP	153
4.5.1.	COMPARISON BETWEEN VIPA AND FABRY-PÉROT MEASUREMENTS	153
4.5.2.	COMPARISON WITH LITERATURE: FLUID REFERENCE UNDER PRESSURE	154
4.6.	CONCLUSION	156
5	<u>HIGH-PRESSURE EXPERIMENTAL RESULTS AND COMPARISON TO FRICTION MEASUREMENTS</u>	<u>159</u>
5.1	DETERMINATION OF THE TRANSITION PRESSURE IN A HIGH-PRESSURE CELL BY BRILLOUIN SPECTROSCOPY	161
5.1.1	OPERATING CONDITIONS	161
5.1.2	PRESSURE DEPENDENCE	162
5.2.	LIQUID BEHAVIOR UNDER PRESSURE COMPARED TO THE GLASS TRANSITION	166
5.2.1.	GLASS TRANSITION PRESSURE DETERMINATION.....	166
5.2.2.	EVOLUTION OF BRILLOUIN PARAMETER IN FUNCTION OF THE GLASS TRANSITION PRESSURE.....	177
5.3.	EVALUATION OF MECHANICAL PARAMETERS.....	183
5.4	CORRELATION WITH FRICTION MEASUREMENTS.....	191
5.6.	RESULTS CONCLUSION.....	195
6.	<u>GENERAL CONCLUSION</u>	<u>197</u>
6.1	CONCLUSION	198
6.2	LIMITATION OF THIS WORK	199
6.3	PERSPECTIVES.....	200
	<u>BIBLIOGRAPHY.....</u>	<u>203</u>

<u>APPENDIX</u>	<u>217</u>
<u>A. APPENDIX: THEORETICAL BACKGROUND.....</u>	<u>218</u>
A.1: ACOUSTIC WAVE IN A TWO ATOMS CRYSTALLINE STRUCTURE	218
A.2 RELATIONSHIP BETWEEN THE DIELECTRIC FLUCTUATION PROVOKED BY THE DENSITY FLUCTUATION AND INTENSITY OF THE SCATTERED LIGHT.....	219
A.3 TWO RELAXATION PROCESSES: EXAMPLE OF POLYBUTADIENE	221
<u>B. APPENDIX: DETERMINATION OF THE LASER SPOT SIZE USING CLEAVED SILICON SAMPLE AND BRILLOUIN SPECTROSCOPY.....</u>	<u>223</u>
<u>C. APPENDIX: MICROSCOPE DESIGN</u>	<u>226</u>
C.1: DESCRIPTION OF B AND C UNITS	226
C.2. ANGLE CALCULATION	228
C.3 POLARIZATION EFFECT ON INTERFACES	230
<u>D. APPENDIX: BRILLOUIN SPECTRA ANALYSIS.....</u>	<u>231</u>
D.1 : SPECTRA ASYMMETRY.....	231
D.2 ZOOM ON FIGURES FROM CHAPTER 5	232
D.3 COMPLEX MODULUS CALCULATION	234
<u>E. APPENDIX: RHEOLOGY AND BRILLOUIN SPECTROSCOPY</u>	<u>236</u>
E.1 RHEOMETER	236
E.2 INFLUENCE OF SHEAR RATE ON THE BLS SPECTRA	239
<u>F. APPENDIX: PERSPECTIVES ON THE WORK</u>	<u>244</u>

Nomenclature

a	Distance between atomic layers	[Å]
a_H	Hertzian radius of contact	[mm]
a_v	Fitting parameter of the Tait equation of state	[K ⁻¹]
A_{is}	Intensity factor of the incident light	[count]
A_{rea}	Surface plane	[mm ²]
A_1, C_1	Modified WLF constants	[-]
$A_2, B_2,$	Modified WLF constants	[GPa ⁻¹]
C_2, T_g0	Modified WLF constants with glass transition	
	Temperature	[°C]
C	Spring constant	[Nm ⁻¹]
C_f	Friction coefficient	[-]
C_p	Specific heat capacity	[J. (kg. K) ⁻¹]
c_∞ or V_∞	Sound velocity (solid-like state)	[m. s ⁻¹]
c	Light velocity	[m. s ⁻¹]
D	Fitting parameter VFT model	[-]
D	Kinematic viscosity	[m ² s ⁻¹]
$\overrightarrow{dir_i}$	Incoming light polarization vectors	
$\overrightarrow{dir_s}$	Scattered light polarization vectors	
E	Young's modulus	[GPa]
\vec{E}	Electric field	[V. m ⁻¹]
\vec{E}_0	Constant amplitude of the electric field	[V. m ⁻¹]
E'	Reduced Young modulus of the contact $\frac{2}{E'} = \frac{1-\nu_1^2}{E_1} + \frac{1-\nu_2^2}{E_2}$	[GPa]
E_{eq}	Reduced Young's modulus	[GPa]
E_S	Scattered electromagnetic field	[V. m ⁻¹]
f	Frequency	[GHz]
f_b	Brillouin frequency shift	[GHz]
f_{phonon}	Phonon frequency	[GHz]
F	Spectrometer Finess	[-]
F_{atom}	Force displacement of an atom	[N]
$F(P)$	Variation of the thermal expansion coefficient with pressure	[GPa]
F_X	Friction force Sliding force	[N]
F_Z	Normal load	[N]
$I_{is}(\vec{q}, \omega)$	Scattered light power (intensity)	[?]
$I_{IRF_0}, I_{IRF_{LaMCoS}}$	Instrumental function	[GHz]
G	Shear modulus	[GPa]
G_{HD}	Hamrock & Dowson adimensional parameter $G = \alpha_p E'$	[-]
G_∞	Limiting elastic shear modulus	[GPa]
G_{eq}	Equivalent shear modulus	[GPa]
G_1	Shear modulus of the ball	[GPa]
G_2	Shear modulus of the disc	[GPa]
H_0	Gap between two plates in the rheometer	[µm]
h_c	Central film thickness	[nm]
h_m	Minimum film thickness	[nm]
\hbar	Reduce Planck constant	[kg. m ² . s ⁻¹]
$I(\omega)$	Intensity of scattered light spectrum	[count]

I_0	Area of the peak	
$I_{Lorentz}$	Intensity of the inelastic peak with Lorentz fit	[count]
I_{DHO}	Intensity of the inelastic peak with DHO fit	[count]
k	Wavenumber	$[m^{-1}]$
k_b	Boltzmann constant	$[m^2 kg s^{-2} K^{-1}]$
\vec{k}_i	Wavevectors incident light	$[m^{-1}]$
\vec{k}_s	Wavevectors scattered light	$[m^{-1}]$
K	Isothermal bulk modulus	[Pa]
K_0	Isothermal bulk modulus at $p = 0$	[Pa]
K_0'	Pressure rate of change of isothermal bulk modulus at $p = 0$	[-]
K_∞	K_0 at infinite temperature	[Pa]
\dot{K}_0	Rate of change of K_0 with reciprocal temperature	[Pa.K]
K_{00}	K_0 at zero absolute temperature	[Pa]
L	Mirror spacing	[nm.rad]
L_1	Cavity of the first FP	[nm]
L_2	Cavity length of the second FP	[nm]
M_1, M_2	Atomic mass in the diatomic chain	[kg]
M_w	Molecular weight	$[kg. mol^{-1}]$
M	Adiabatic elastic modulus (longitudinal)	[Pa]
$M^*(\omega)$	Generalised modulus	[Pa]
M_0	Relaxed modulus	[Pa]
M_∞	Unrelaxed modulus	[Pa]
M'	Storage Modulus	[Pa]
M''	Loss modulus	[Pa]
M_{Moes}, L_{Moes}	Moes dimensionless parameter	[-]
n	Refractive index	[-]
P	Pressure	[GPa]
\bar{P}	Mean contact pressure = $2/3 P_H$	[MPa]
P_g	Glass transition pressure	[GPa]
P_H	Hertzian contact pressure	[GPa]
P_p	Pressure of plateau regime	[GPa]
P_t	Pressure from transition liquid to the glassy state	[GPa]
P_{atm}	Atmospheric pressure	[MPa]
\vec{q}	Wavevector of the hypersonic wave	$[m^{-1}]$
R_{FP}	Reflectivity in the FP	[- or %]
R_0, R_1, R_2	Reflectivity in the VIPA interfaces	[- or %]
R	Disc radius	[mm]
r	Radius in the rheometer for brillouin measurements	[mm]
\vec{r}	Position vector in cartesian coordinates	[-]
R_{eq}	Equivalent radius	[mm]
r_s	Solid ratio	[-]
r_f	Fluid ratio	[- or %]
t_c	Characteristic time	[s]
T_{FP}	Transmittance in the FP	[- or %]
T_R	Reference temperature	[°C]
S	Contact surface	$[mm^2]$
$S(q, \omega)$	Dynamic structure factor	[-]
$S(q)$	Static structure factor	[-]

t_{rel}	Relaxation time	[s]
T	Temperature	[°C or K]
T_g	Glass transition temperature	[°C]
T_{in}	Inlet temperature	[°C]
T_R	Reference temperature	[°C]
T_0	Ambient temperature	[°C]
U	Speed parameter	[-]
U_{ball}	Ball velocity	[m. s ⁻¹]
U_{disc}	Ball velocity	[m. s ⁻¹]
U_e	Entrainment velocity	[m. s ⁻¹]
ΔU	Sliding velocity	[m. s ⁻¹]
$\Delta\lambda$	Distance between two transmitted peak	[nm]
ΔC_f	friction coefficient uncertainty	[-]
V	Acoustic sound velocity	[m. s ⁻¹]
V_{Tait}	Volume in Tait model	[m ³]
V^*	Activation volume	[m ³]
V_0	Longitudinal sound velocity in the unrelaxed limit	[m. s ⁻¹]
V_∞	Longitudinal sound velocity in the relaxed limit	[m. s ⁻¹]
V_L	Longitudinal acoustic sound velocity	[m. s ⁻¹]
V_T	Transversale acoustic sound velocity	[m. s ⁻¹]
V_0	Total volume at atmospheric pressure	[m ³]
W	Load	[N]
W_1	The load parameter	[N]
α	Polarisability at ambient conditions	[cm ³]
α_p	Piezo-viscosity coefficient	[Pa ⁻¹]
α^*	Reciprocal asymptotic isoviscous pressure	[GPa ⁻¹]
β	Limiting shear stress temperature coefficient	[MPa.°C]
β_{Debye}	Debye stretching parameter	[-]
β_K	Fitting parameter of the Tait equation of state	[K ⁻¹]
β	Thermal coefficient [Experimental condition]	[K]
Γ	FWHM inelastic peak	[GHz]
Γ_0	FWHM DHO model	[GHz]
Γ_b	Full Width at Half Maximum (FWHM) Brillouin of the inelastic light of the Brillouin spectra	[GHz]
Γ_{IRF}	FWHM of the instrumental response function	[GHz]
γ	Limiting shear stress pressure coefficient	[-]
$\dot{\gamma}$	Shear rate	[s ⁻¹]
$\dot{\gamma}_c$	Critical shear stress	[s ⁻¹]
ϵ_0	Permittivity	[F. m ⁻¹]
ϵ	Dielectric constant	[-]
$\delta\epsilon$	Dielectric fluctuation function	[-]
η_0	Viscosity of the lubricant at atmospheric pressure	[Pa.s]
η/μ	Viscosity of the lubricant for a given pressure	[Pa.s]
$\bar{\eta}$	Mean effective viscosity	[Pa.s]
η_{eff}	Effective viscosity of the lubricant	[Pa.s]
η_L	Longitudinal viscosity	[Pa.s]
η_s	Shear viscosity	[Pa.s]
η_b	Bulk viscosity	[Pa.s]
η_0	Low-frequency longitudinal viscosity	[Pa.s]
η_∞	High-frequency longitudinal viscosity	[Pa.s]

θ	Angle between the incident and scattered light	[rad]
θ_i	Incident angle of incoming laser beam	[rad]
θ_s	Scattered angle of the laser beam	[rad]
θ_{FP}	Transmitted angle in the TFP-1	[rad]
θ_λ	Transmitted angle in VIPA	[rad]
λ	Laser wavelength in a medium	[nm]
λ_0	Wavelength in vacuum	[nm]
Λ	Phonon wavelength	[nm]
$\Lambda_T, \Lambda_1, \Lambda_2, \Lambda_P$	Dimensionless parameters	[-]
μ_0	Permeability	[N.A ⁻²]
μ_g	Viscosity of the lubricant at glassy state	[Pa.s]
μ_{VFT}	Limiting low-shear viscosity by VFT	[Pa.s]
μ_{WLF}	Viscosity by WLF model	[Pa.s]
μ_0	Lubricant dynamic viscosity	[Pa.s]
μ_∞	Viscosity extrapolated to infinite temperature	[Pa.s]
ν	Poisson's coefficient	[-]
ν_{eq}	Equivalent Poisson's coefficient	[-]
ν_1	Poisson's coefficient of the ball	[-]
ν_2	Poisson's coefficient of the disc	[-]
ν_0	Frequency of the incident radiation	[GHz]
$\bar{\nu}$	Wave number	[cm ⁻¹]
ρ	Density	[kg.m ⁻³]
ρ_M	Average mass density	[kg.m ⁻³]
$\rho_q(t)$	Density fluctuations	[kg.m ⁻³]
ρ_r	Reference density in Tait model	[kg.m ⁻³]
ρ_0	Density of the lubricant at the inlet at T_0	[kg.m ⁻³]
$\sigma_{specimen}^{RMS}$	RMS roughness of a specimen	[nm]
τ	Shear stress	[Pa]
τ_0	Reference shear stress	[Pa]
τ_{0FP}	maximum transmittance	[-]
$\bar{\tau}$	Mean shear stress	[MPa]
τ_L	Limiting shear stress	[MPa]
$\bar{\tau}_L$	Mean limiting shear stress	[MPa]
τ_{L0}	Limiting shear stress extrapolated at ambient pressure	[MPa]
Ω	Angular frequency of the phonon	[-]
Ω_{rheo}	Angular velocity of the rotating plates	[rad.s ⁻¹]
ω	Angular frequencies in vacuum	[rad.s ⁻¹]
ω_i	Angular frequencies incident light	[rad.s ⁻¹]
ω_s	Angular frequencies scattered light	[rad.s ⁻¹]
ω_x		
Σ	Combined roughness of the specimen surfaces	[nm]
ϕ	Phase of the electromagnetic field	
ϕ_T	Film thickness thermal reduction coefficient according to Cheng	[-]
λ_0	Wavelength in vacuum	[nm]
$\chi(\omega)$	Susceptibility	[-]
ξ	Energy exchange	[eV]
SRR	Slide-to-roll ratio	[%]

Abbreviations

EHD	Elastohydrodynamic
EHL	Elastohydrodynamic Lubrication
EJ	ExaJoules
BLS	Brillouin Light Scattering
VIPA	Virtually Image Phase Arrays
TFP	Tandem Fabry-Pérot
DAC	Diamond anvil cell
SD	Standard Deviation
FWHM	Full width at half maximum
LSS	Limiting shear stress
LA	Longitudinal Acoustic wave
LO	Longitudinal optical wave
TA	Transversal Acoustic wave
TO	Transversale optical wave
<i>SRR</i>	Slide-to-roll ratio
SRR_{LSS}	Slide-to-roll ratio at LSS onset
GLY	GLYcerol
SQ	SQualane
BB	Benzyl Benzoate
DHO	Damping harmonic oscillator
TEM	Transverse Electro-Magnetic
WC	Tungsten Carbide
WLF	Williams–Landel–Ferry model

0.1. Introduction et objectifs Contexte et état de l'art de la friction lubrification

Cette thèse vise à explorer le potentiel de réduction des pertes d'énergie dans les systèmes mécaniques par la réduction des frottements et la prévention de l'usure, en mettant l'accent sur le domaine de la tribologie. La tribologie est l'étude du frottement, de l'usure et de la lubrification dans les contacts mécaniques. Plusieurs rapports récents, dont l'étude Holmberg et Erdemir, soulignent l'importance de la tribologie et indiquent les technologies clés à explorer pour réduire les pertes d'énergie [1–3].

Typiquement, dans ces contacts représentés schématiquement en Figure 0.1, le lubrifiant traverse le contact sur une fraction de millimètre ($\sim 100 - 300 \mu\text{m}$) en un temps très court ($< 10^{-4} \text{ s}$). Du fait de la géométrie non conforme des contacts, cela entraîne une augmentation soudaine de la pression, atteignant jusqu'à plusieurs GPa au centre du contact. L'épaisseur centrale du film qui en résulte, conditionnée par la viscosité du lubrifiant, varie de quelques dizaines de nanomètres à quelques micromètres.

La combinaison complexe de la pression, de la température et du taux de cisaillement dans un contact a un fort impact sur la réponse du lubrifiant. Il est donc essentiel de connaître le comportement rhéologique des lubrifiants industriels pour comprendre comment ils se comportent dans des conditions extrêmes. Leur caractérisation rhéologique fournit ainsi des informations précieuses sur leur viscosité, leur comportement rhéofluidifiant et leur réponse aux changements de pression et de température. Elle permet in fine de prédire le frottement pour des taux de glissement (ou identifiée dans la littérature comme slide to roll ratio $\text{SRR} = \text{ratio de la vitesse de glissement et de la vitesse moyenne dans le contact}$) faibles à modérés. Ces plages de glissement correspondent aux régimes linéaire et rhéofluidifiant des courbes de frottement, notés régimes I et II sur la Figure 0.2. Cependant, à des pressions de contact élevées, le coefficient de frottement peut présenter un comportement de type plateau, devenant indépendant de la vitesse de glissement. Ce régime plateau a été mis en évidence pour la première fois par Smith en 1959 [4] et a été largement étudié depuis lors [5]. Il a été souvent associé à la LSS (limiting shear stress), qui est définie comme la contrainte de cisaillement ultime que le lubrifiant peut supporter, mesurée dans un volume de fluide. Mais la complexité des conditions opératoires d'un contact rend difficile la corrélation directe entre LSS et plateau de frottement.

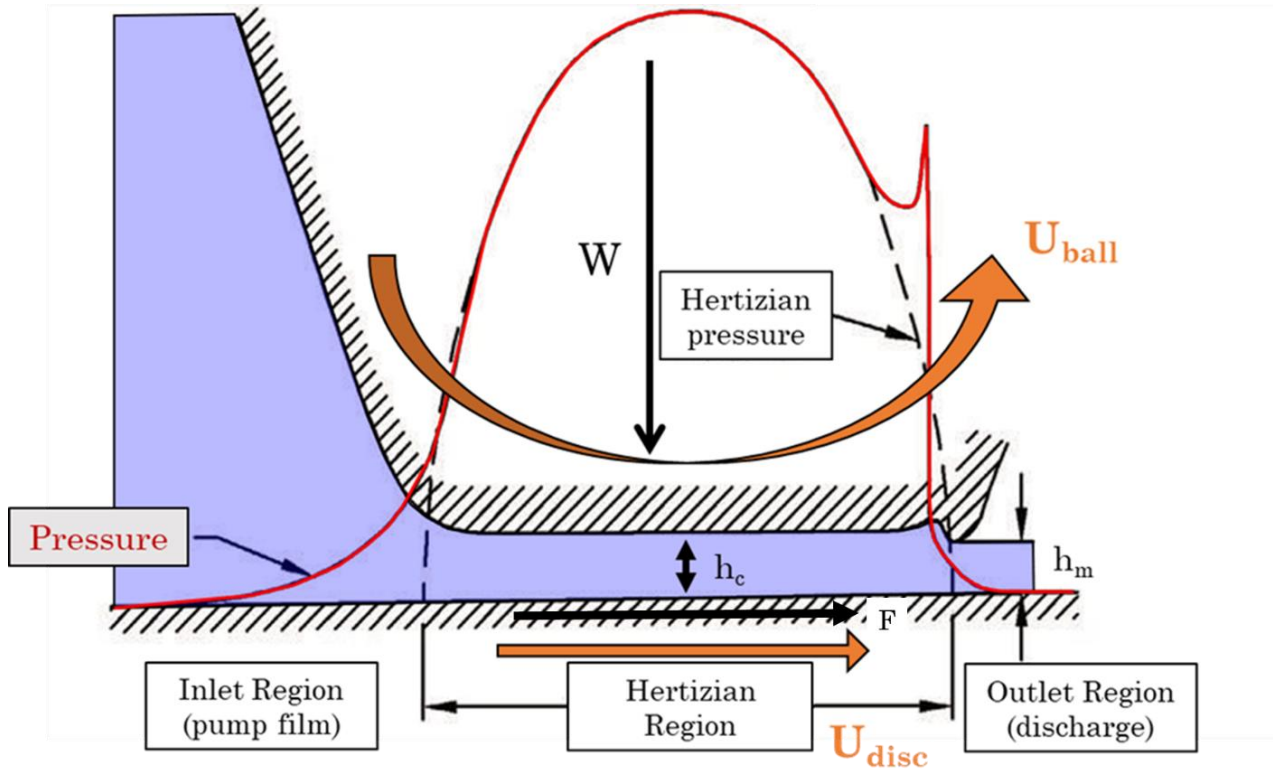


Figure 0.1 :Vue schématique du contact ElastoHydroDynamique (EHD), inspirée de la référence [6]. Les principales caractéristiques expérimentales sont explicitées. h_c et h_m représentent l'épaisseur centrale et l'épaisseur minimale du film. La pression est représentée par la ligne rouge pleine et la ligne pointillée par la pression Hertizienne. Cette charge est représentée par W la force normale. La flèche orange représente l'orientation rotationnelle des surfaces solides avec les vitesses U_{ball} et U_{disc} de la balle et du disque respectivement.

Aujourd'hui encore, l'origine de ce plateau est mal comprise et ne fait pas consensus. De ce fait, aucun modèle prédictif n'est proposé dans la littérature. Il est pourtant essentiel de comprendre et de contrôler le plateau de frottement pour minimiser les pertes d'énergie et améliorer l'efficacité des systèmes mécaniques.

Une des hypothèses avancées dans la littérature est la vitrification du lubrifiant sous forte pression. L'état vitreux fait référence à un état hors équilibre d'un matériau dans lequel il présente des propriétés mécaniques similaires à celles d'un solide pendant la durée d'observation de l'expérience [7]. La transition vitreuse d'un matériau, transition entre un état liquide et un état vitreux, peut être déclenchée par une baisse de la température ou une augmentation de la pression. Et en effet dans les contacts EHD, les fortes pressions peuvent dépasser la pression de transition vitreuse des lubrifiants. En franchissant cette pression, le temps mis par une molécule pour revenir à un état d'équilibre après une sollicitation est appelé le temps de relaxation du lubrifiant devient significativement plus long que celui du même lubrifiant à l'état liquide qui est typiquement de l'ordre de la nanoseconde, atteignant typiquement jusqu'à 100 secondes [8,9].

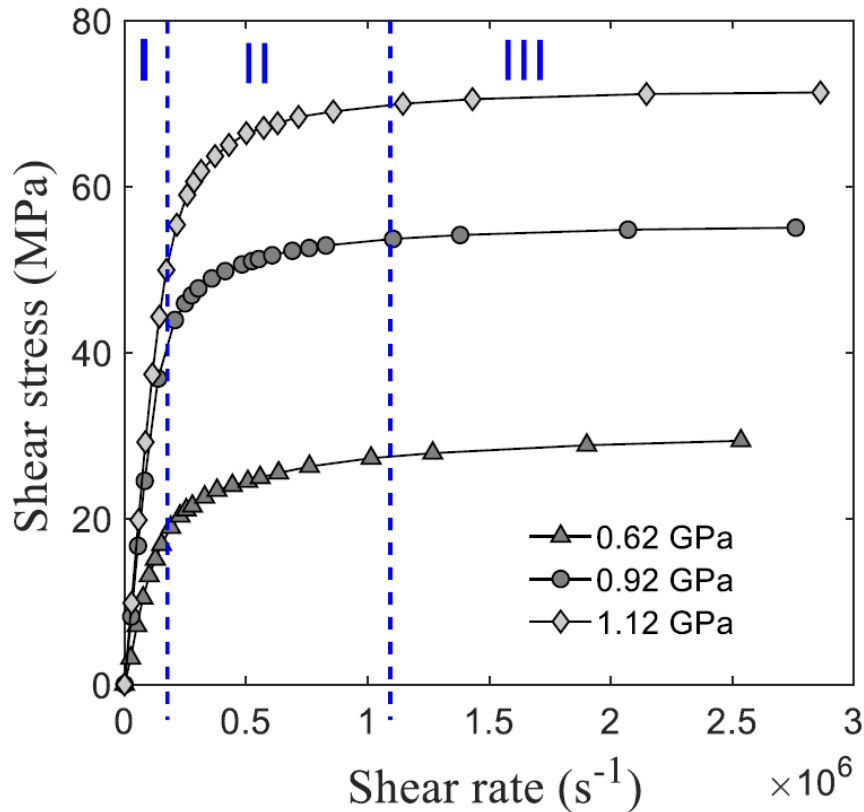


Figure 0.2 : Courbes de contrainte de cisaillement en fonction du taux de cisaillement pour le benzoate de benzyle à différentes pressions de contact, à partir de mesures de friction effectuées selon le protocole décrit dans la référence [10].

Cette hypothèse, largement partagée dans la littérature, n'a jamais été démontrée du fait de la difficulté de réaliser des mesures directement dans un contact. Dans ce travail, la spectroscopie Brillouin est apparue comme la technique idéale pour mener des expériences "in situ" dans les contacts mécaniques lubrifiés. Connue pour sa nature non invasive et non destructive (avec un contrôle minutieux de la puissance du laser), elle a déjà été utilisée dans de nombreuses études pour mesurer la température de transition vitreuse à pression atmosphérique [11–18]. Cependant, seules quelques études de spectroscopie Brillouin se sont intéressées à l'influence de la pression sur la transition vitreuse [19–21].

Des chercheurs comme Ng et al. [22] et Kim et al. [23] ont réussi à identifier la transition vitreuse du polyéthylène à l'aide de la spectroscopie Brillouin, en utilisant la discontinuité de la pente dans le décalage de fréquence et la largeur maximale à mi-hauteur (FWHM) en fonction de la température comme montré à la Figure 0.3.

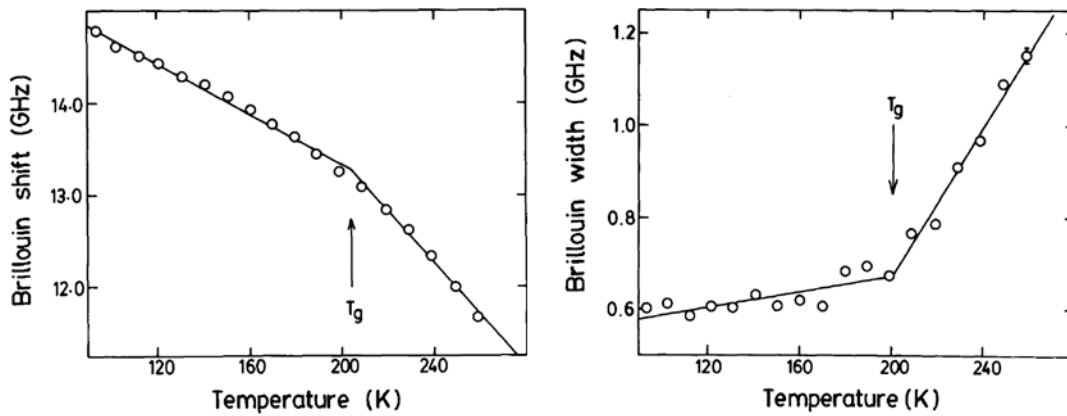


Figure 0.3 : Déplacement du pic inélastique Brillouin (à gauche) et largeur à mi-hauteur (à droite) du polyéthylène en fonction de la température [22]. Les lignes correspondent à l'ajustement par les moindres carrés. T_g est la température de transition vitreuse.

En outre, la spectroscopie Brillouin a déjà été utilisée pour mesurer la vitesse du son dans des lubrifiants dans des conditions de température et de pression variables [11,13,17,18,24,25].

Ces données ont facilité la dérivation de propriétés importantes du fluide, notamment la densité du lubrifiant [19], l'indice de réfraction [26], le module de cisaillement [27,28] et le temps de relaxation [29,30]. En caractérisant les pics de Brillouin (décalage de fréquence et largeur) [21], les chercheurs ont déterminé la vitesse du son [11,17,24,25,29,31,32] des lubrifiants sondés en fonction de la température et/ou de la pression.

En conclusion, cette thèse de doctorat étudie le phénomène de plateau de frottement dans les contacts élasto-hydrodynamiques et explore le rôle de la transition vitreuse dans le comportement du lubrifiant. En comprenant la contrainte de cisaillement limite (LSS pour Limiting Shear Stress) et les effets de la transition vitreuse, cette recherche vise à développer des méthodes expérimentales de caractérisation mécanique de lubrifiants ex et in situ. Cela a pour but de développer des modèles pour le comportement des lubrifiants, contribuant ainsi à des solutions tribologiques plus efficaces et à la réduction des émissions de CO₂.

0.2. Utilisation de la spectroscopie Brillouin pour la détection de la transition vitreuse

La spectroscopie Brillouin (BLS pour Brillouin Light Scattering) est une technique non invasive et non destructive basée sur la diffusion inélastique de la lumière, qui permet de mesurer indirectement des modules élastiques et vitesse de propagation du son dans le matériau. Elle repose sur l'interaction entre la lumière monochromatique incidente (photons) et les ondes thermodynamiques (phonons) qui se propagent dans un échantillon. La caractérisation des ondes acoustiques nous renseigne sur les propriétés physiques et mécaniques de l'échantillon. Ces informations sont contenues dans les pics de diffusion inélastique du spectre de part et d'autre du pic central élastique (ou pic Rayleigh, voir Figure

0.4). Cette technique de spectroscopie permet d'effectuer des mesures sur des échantillons au repos ou en mouvement, à condition que la lumière incidente soit focalisée sur des échantillons transparents.

La géométrie de diffusion est un aspect essentiel de la spectroscopie Brillouin, car elle détermine le type d'ondes acoustiques sondées dans le matériau. Les deux configurations les plus courantes sont la géométrie de rétrodiffusion et la configuration en plaquettes [33]. Dans le cas de la géométrie de rétrodiffusion, les ondes lumineuses diffusées dans l'échantillon sont collectées dans la même direction et dans le même objectif de microscope que celui d'où elles proviennent, ce qui permet d'échantillonner les ondes acoustiques longitudinales du matériau [34]. En revanche, la configuration en plaquettes [35] combiné avec la configuration de rétrodiffusion permet aux chercheurs de mesurer à la fois les ondes acoustiques longitudinales et transversales [19,33]. En utilisant la combinaison de ces deux géométries et en analysant soigneusement les spectres obtenus, il est possible d'obtenir des informations sur les propriétés mécaniques et le comportement viscoélastique du matériau, ce qui contribue à une compréhension globale du comportement du lubrifiant dans des conditions extrêmes dans les contacts tribologiques.

Pour analyser les spectres BLS, plusieurs variables et paramètres essentiels sont nécessaires. Le décalage de fréquence Brillouin (ω_b) comme indiqué dans la Figure 0.4, représente le décalage de fréquence de la lumière diffusée et dépend de la vitesse du son (V), de l'angle de la lumière incidente (θ_i), de la longueur d'onde incidente dans le vide (λ_0) et de l'indice de réfraction (n) de l'échantillon. La largeur à mi-hauteur (FWHM) du pic de Brillouin, notée Γ_b , est liée à l'amortissement des ondes acoustiques dans l'échantillon et reflète son comportement visqueux.

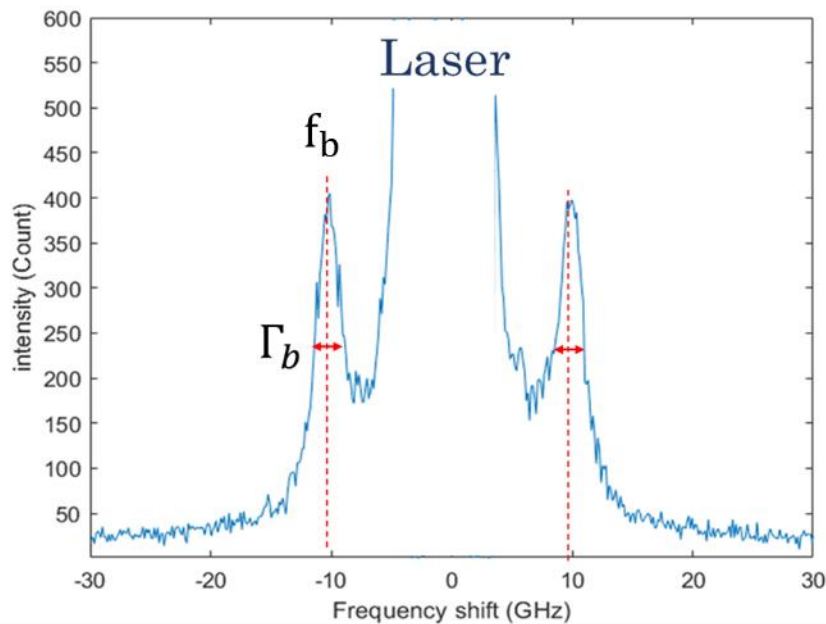


Figure 0.4 : Spectre du benzoate de benzyle sous pression atmosphérique et à température ambiante (22°C) en configuration de rétrodiffusion

Ces paramètres extraits de la spectroscopie Brillouin couplés aux modèles rhéologiques permettent de comprendre la dynamique des matériaux dans les conditions extrêmes de pression et de cisaillement.

Dans le contexte de la spectroscopie Brillouin appliquée aux lubrifiants, le concept de phonons, utilisé à l'origine pour la structure cristalline, est étendu aux liquides. Il représente des fluctuations collectives de densité [36], se déplaçant comme des ondes sonores dans le milieu liquide. Le contexte théorique décrivant les fluctuations de densité se propageant naturellement dans un échantillon suit une approche hydrodynamique linéarisée avec amortissement [37], conduisant à l'expression d'un module longitudinal complexe dépendant de la fréquence $M(\omega) = M'(\omega) - iM''(\omega)$. La partie réelle M' du module représente la réponse élastique du matériau, tandis que M'' est associée à l'amortissement des ondes acoustiques dans l'échantillon.

Les contacts EHD impliquent un fort couplage entre les conditions opératoires de pression, cisaillement et température, qui pourrait rendre difficile l'exploitation de résultats mesurés *in situ*. La stratégie adoptée dans ce travail a donc été de découpler ces conditions et de caractériser leur influence respective individuellement. Pour ce faire, les échantillons de lubrifiants ont été sondés au repos en cellule haute pression, à température contrôlée, et dans un rhéomètre, à pression atmosphérique et température contrôlée. Les résultats obtenus contribueront au développement d'équations constitutives prédictives pour les lubrifiants, conduisant à des solutions tribologiques plus efficaces.

0.3. Méthode expérimental employés

La stratégie expérimentale établie dans ce travail comprenait l'étude de trois fluides : le squalane, le benzoate de benzyle et le glycérol. Ils ont été choisis de par leurs morphologies variées, leurs précédentes caractérisations tribologiques et par leur dynamique moléculaire pour les deux premiers fluides. Le squalane, un alkane linéaire, est considéré comme représentatif d'un lubrifiant. Le benzoate de benzyle, un ester, a été référencé comme fluide modèle. Le glycérol est un composé organique possédant trois groupes hydroxyle correspondant à trois fonctions alcool responsables de sa solubilité dans l'eau et de sa nature hygroscopique.

Des études approfondies ont été menées sur le benzoate de benzyle [38] et le squalane [39,40], en se concentrant sur leurs propriétés rhéologiques et de frottement. Ces deux fluides ont été caractérisés rhéologiquement en utilisant le modèle de viscosité (à bas taux de cisaillement) WLF-Yasutomi modifié en fonction de la température et de la pression. Leur pression de transition vitreuse a pu être estimée à partir de ce modèle. En outre, le comportement du benzoate de benzyle a été largement exploré à la fois en frottement dans un tribomètre bille-plan et au repos dans une cellule haute pression par spectroscopie Brillouin [38,41]. Le glycérol, quant à lui, est un fluide de référence, qui a déjà été caractérisé dans la littérature par spectroscopie Brillouin dans des cellules haute pression jusqu'à 10 GPa, dans des configurations de rétrodiffusion.

Pour la spectroscopie Brillouin, deux technologies distinctes de spectromètre ont été utilisées: le spectromètre tandem Fabry-Pérot à 6 passages (TFP-1) développé par Dr. Sandercock dans les années 1970 et 1980 [42,43], et le spectromètre VIPA (Virtually Imaged Phased Array), technologie plus rapide et en cours de développement. Le spectromètre VIPA offre un avantage remarquable en termes de rapidité d'acquisition, ce qui le rend particulièrement adapté à la réalisation de mesures in situ dans des contacts tribologiques confinés.

Ces spectromètres ont été utilisés dans différents laboratoires, chacun ayant son propre banc expérimental. Le banc d'essais avec spectromètre VIPA a été spécifiquement conçu et monté au LaMCoS pour ce travail de thèse. L'étape de conception de ce banc a représenté une large partie de ce travail de thèse. La difficulté a été de concevoir un montage optique modulable pour pouvoir être couplé à deux bancs expérimentaux ayant chacun leurs caractéristiques géométriques et expérimentales.

Trois unités optiques, appelées A, B et C, ont été conçues pour réaliser des mesures soit en configuration de rétrodiffusion (unité A en Figure 0.5), soit en configuration plaquette (unités B et C en Figure 0.6).

L'unité A en Figure 0.5 a été conçue avec trois étages pour permettre pour permettre simultanément la visualisation du spot laser, la mesure de spectroscopie Brillouin et la mesure de luminescence rubis. De plus son design est adapté aux mesures dans une géométrie de rétrodiffusion pour des expériences à haute pression, au rhéomètre et au tribomètre.

Les unités B et C, représentés sur la Figure 0.6, ont été spécialement conçues pour les géométries obliques, fonctionnent en tandem. Elles joueront un rôle crucial dans la réalisation d'expériences sur la configuration « plaquettes » ou « angulaire », fournissant des informations précieuses sur le comportement des lubrifiants dans des conditions variables. Malheureusement, cette partie n'est pas développée dans cette thèse en raison du manque de temps pour mener une série complète d'expériences en configuration « plaquettes ».

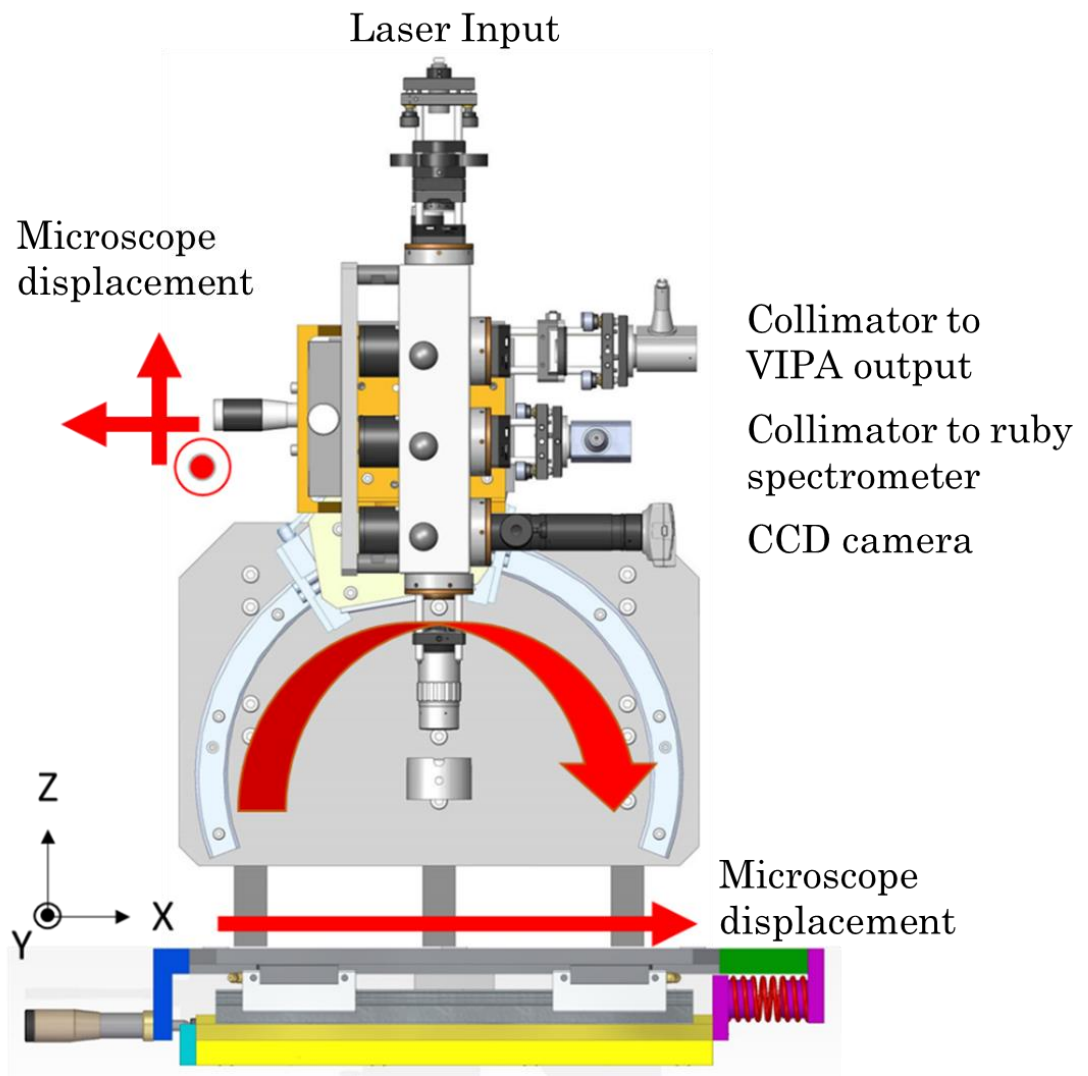


Figure 0.5 : Représentation schématique de l'unité A avec les principales caractéristiques et les déplacements du microscope (flèches rouges)

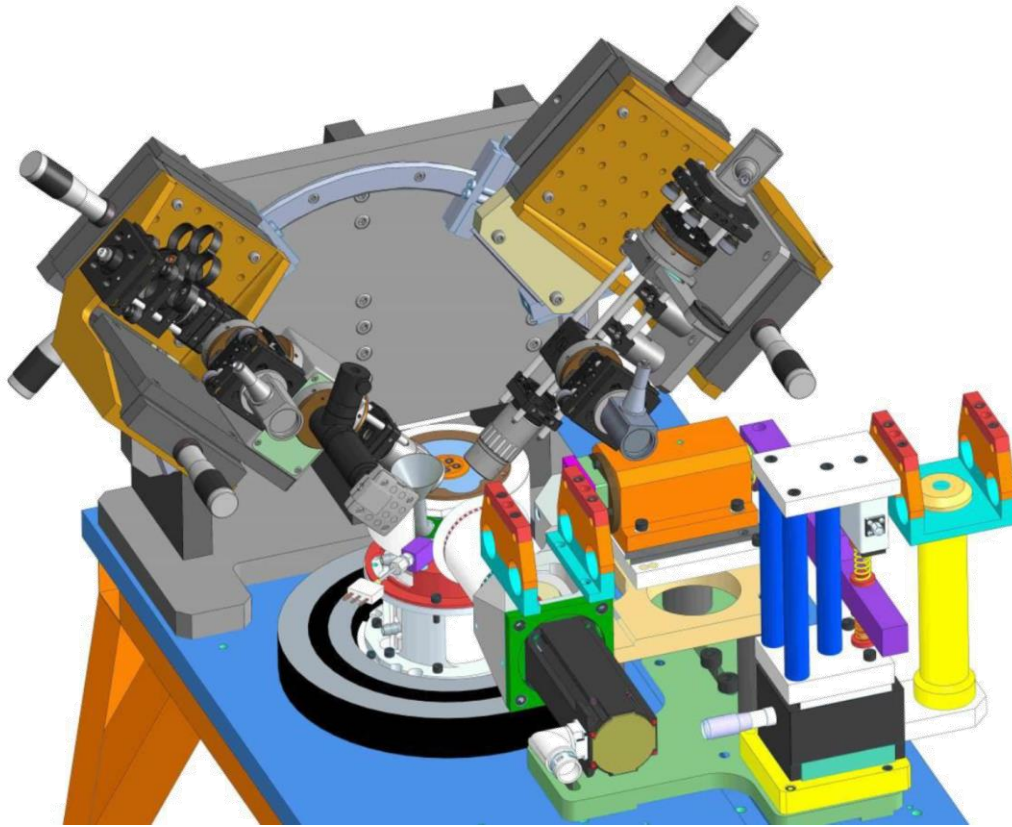


Figure 0.6: Représentation schématique du microscope à configuration angulaire ou en « plaquette » pour les mesures tribo-Brillouin.

Pour réaliser des mesures sur échantillons au repos et soumis à des pressions hydrostatiques variables, des cellules à enclumes de diamant (DAC) ont été intégrées aux bancs de spectroscopie Brillouin. Le principe de fonctionnement de ces cellules est schématisé sur la Figure 0.7. Le fluide est situé entre deux pièces en diamant (deux enclumes sur la Figure 0.7), sur lesquelles une pression est appliquée via une membrane gonflée à l'azote. Deux types de DAC ont été utilisés : l'une avec une conception symétrique classique (deux enclumes en diamant) pour des expériences allant jusqu'à 10 GPa (haute pression), et l'autre avec une ouverture symétrique de 100° (une enclume et une fenêtre en diamant) pour une pression maximale de 1,2 GPa (basse pression). La pression à l'intérieur de l'échantillon a été déterminée en utilisant la sensibilité à la pression de luminescence des rubis introduits dans l'enclume, calibrés dans de nombreuses études [44,45].

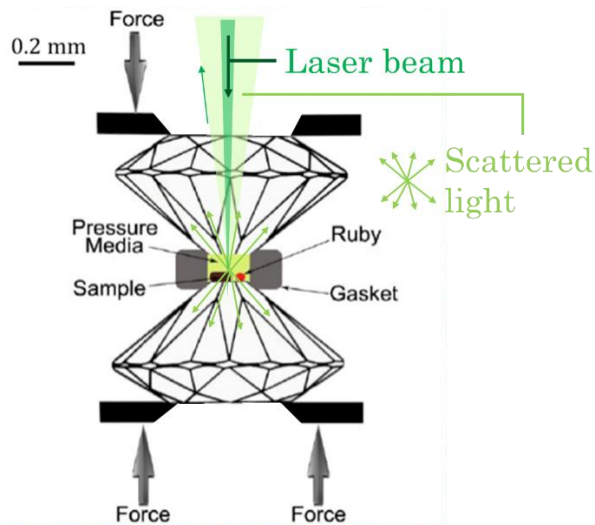


Figure 0.7 : Vue schématique d'une cellule à enclume diamant (DAC). Inspiré de la publication [46].

Pour réaliser des mesures sur échantillons cisailés à pression atmosphérique et température contrôlée, un rhéomètre (Physica MCR301, Anton Paar) a été couplé au banc de spectroscopie Brillouin. Il a permis de réaliser des mesures de viscosité des fluides dans des conditions de taux de cisaillement contrôlé. Ses résultats sont disponibles dans l'annexe E.

Enfin, le banc de spectroscopie Brillouin a été conçu pour être couplé au tribomètre bille-disque JEROTRIB présenté dans [47], et sur lequel des essais de frottement ont été menés avec le benzoate de benzyle et le squalane. Les essais de spectroscopie Brillouin in situ doivent être menés prochainement.

Les données mesurées sur les bancs d'essais présentés ont permis dans le cadre de ce travail et permettront dans la suite de ce projet d'améliorer notre compréhension du comportement des lubrifiants soumis à des conditions extrêmes de pression, de cisaillement et de température.

0.4. Validation du banc expérimental

L'acquisition banc expérimental de spectroscopie VIPA à nécessiter une étape de validation et comparé au banc de spectroscopie TFP-1. Ses comparaisons ont été effectués sur des échantillon macroscopique er en cellule haute pression pour le glycérol. Cette validation concernait à la fois la mise en place du spectromètre Brillouin, le montage optique et le post processus.

Pour garantir une analyse précise des données, le traitement du signal des spectres Brillouin est crucial. Plusieurs étapes d'analyse sont nécessaires pour dériver des spectres Brillouin des paramètres f_b et Γ_b (décrits à la section 0.2) qui soient décorrélés du banc expérimental. La première étape consiste à déconvoluer les spectres mesurés sur chaque échantillon par la fonction instrumentale du banc expérimental mesurée sur un miroir. Cette étape permet de supprimer des spectres l'influence des éléments optiques du montage, notamment l'ouverture

numérique de l'objectif utilisé. En effet, ce paramètre peut avoir une influence non négligeable sur la FWHM des pics inélastiques Brillouin. Ainsi, comme il est montré sur la Figure 0.8, deux spectres pris avec le même microscope mais des objectifs différents (grossissements X10 et X20) ont montré des différences significatives dans les valeurs de FWHM, issues de spectres non déconvolués.

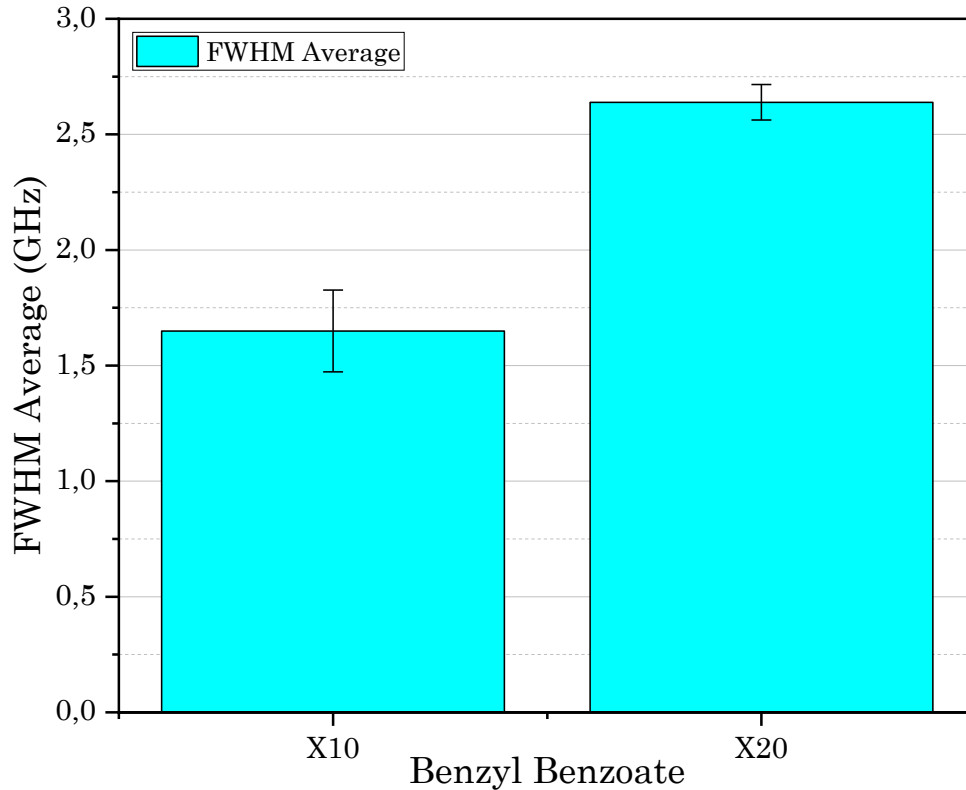


Figure 0.8: Comparaison entre deux FWHM du benzoate de benzyle pris par le même montage VIPA, à l'intérieur du DAC sans pression, avec deux objectifs différents, X10 et X20. Les deux spectres n'ont pas été déconvolués. On trouve un rapport de 0,63 entre ces deux valeurs.

La deuxième étape consiste à ajuster les spectres Brillouin par un modèle représentatif de la forme des pics Brillouin. Deux modèles classiquement utilisés dans la littérature, le fit de Lorentzien et l'oscillateur harmonique amorti (DHO pour Damped Harmonic Oscillator), sont utilisés pour ajuster les spectres Brillouin comme montré dans la Figure 0.9. Le logiciel OriginPro fournit des procédures d'ajustement pour les deux modèles, y compris des ajustements lorentziens multiples qui prennent en compte les contributions des pics de Rayleigh. La comparaison entre les procédures d'ajustement et le logiciel pour déterminer la fiabilité a été effectuée. Bien que les deux procédures d'ajustement donnent des résultats similaires, l'ajustement lorentzien multiple dans OriginPro a été choisie pour décorréler les piques inélastique de la contribution élastique de Rayleigh et avoir des valeurs de largeur à mi-hauteur réalistes.

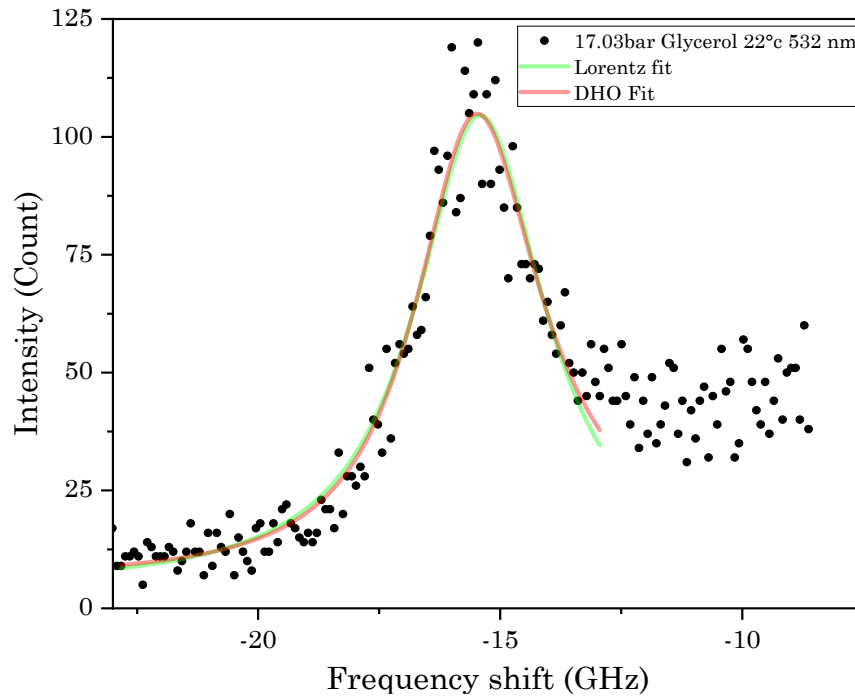


Figure 0.9: Comparaison des ajustements de Lorentz et de DHO simple effectués sur TFP-1 et traités par le logiciel OriginPro

En outre, la symétrie des spectres Brillouin entre les pics inélastiques Stokes et anti-Stokes a été analysée afin d'éviter d'affecter les valeurs de décalage de fréquence et de FWHM pouvant trouver son origine dans les conditions expérimentales et de manipulation. Les configurations TFP-1 et VIPA ont été évaluées et une certaine asymétrie a été observée dans les spectres VIPA. Une des causes supposées pourrait être le mauvais positionnement du green killer sur la raie central Rayleigh et donc d'un mauvais alignement optique ou le changement de longueur d'onde du laser due aux instabilités du courant utilisé. Une méthode d'analyse des spectres a été établie dans le Chapitre 4 en réalisant une moyenne des positions et des largeurs à mi-hauteur des pics Stokes et anti-Stokes pour palier à l'asymétrie.

Enfin, les résultats de spectroscopie Brillouin obtenus sur glycérol au repos et sous pression avec le banc de spectroscopie TFP-1 ont été comparés à des données équivalentes de la littérature [19]. Malgré une évolution similaire de la fréquence Brillouin entre les différents jeux de données, les FWHM dérivées des spectres mesurés avec le banc de spectroscopie TFP-1 ne se superposent pas exactement avec les données des études de Jeong et Oliver. Une des raisons est l'utilisation d'un objectif à plus forte ouverture numérique qui élargit le spectre.

En résumé, ce chapitre a démontré l'importance du traitement du signal et des procédures d'ajustement précises pour extraire des résultats significatifs des mesures de spectroscopie Brillouin. Il a également souligné l'importance de prendre en compte les variations d'installation pour obtenir des données fiables et comparables.

0.5 Résultat haute pression et comparaison aux étude de frottements

La dernière partie de ce travail de thèse exploite les résultats obtenus à la fois en cellule haute pression et dans un rhéomètre.

Pour comprendre l'influence de chaque paramètre sur le comportement du lubrifiant, une approche en trois étapes est adoptée. Des mesures de spectroscopie Brillouin sur échantillons au repos soumis à des hautes pressions avec contrôle de la température sont effectuées pour caractériser leur comportement en pression et température. Les échantillons sont ensuite soumis à un cisaillement dans un rhéomètre couplé au banc de spectroscopie Brillouin VIPA pour observer l'influence du cisaillement sur leur comportement. Cette partie est abordée seulement en annexe. Enfin, des mesures de spectroscopie Brillouin dans un contact sont prévues dans la suite de ce projet pour étudier le couplage de tous les paramètres. A partir de ces mesures, la pression de transition vitreuse (P_g) de chaque fluide est déterminée comme la pression à laquelle une forte transition de comportement est observée. Elle représente la pression critique à laquelle le lubrifiant passe d'un état liquide à un état solide. Cette pression permet d'adimensionner la pression hydrostatique mesurée dans la cellule pour chacun des fluides, comme tracé sur la Figure 0.10.

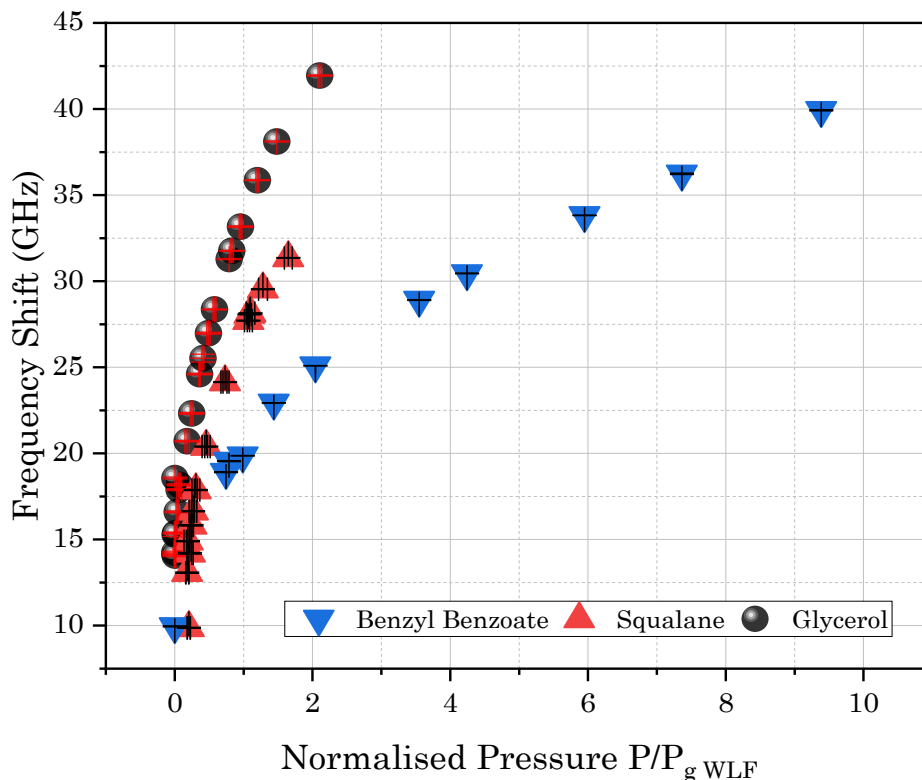


Figure 0.10: Déplacement de fréquence du benzoate de benzyle, du squalane et du glycérol en fonction de la pression normalisée par $P_{g WLF}$, à température ambiante. Tous les résultats ont été obtenus avec le DAC haute pression et l'interféromètre TFP-1.

La dépendance à la pression est étudiée pour le benzoate de benzyle, et il s'avère que les données des configurations TFP-1 et VIPA montrent une évolution similaire de la largeur de raie et du décalage de fréquence, mais qu'il existe des différences dans certaines régions comme montré à la Figure 0.11.

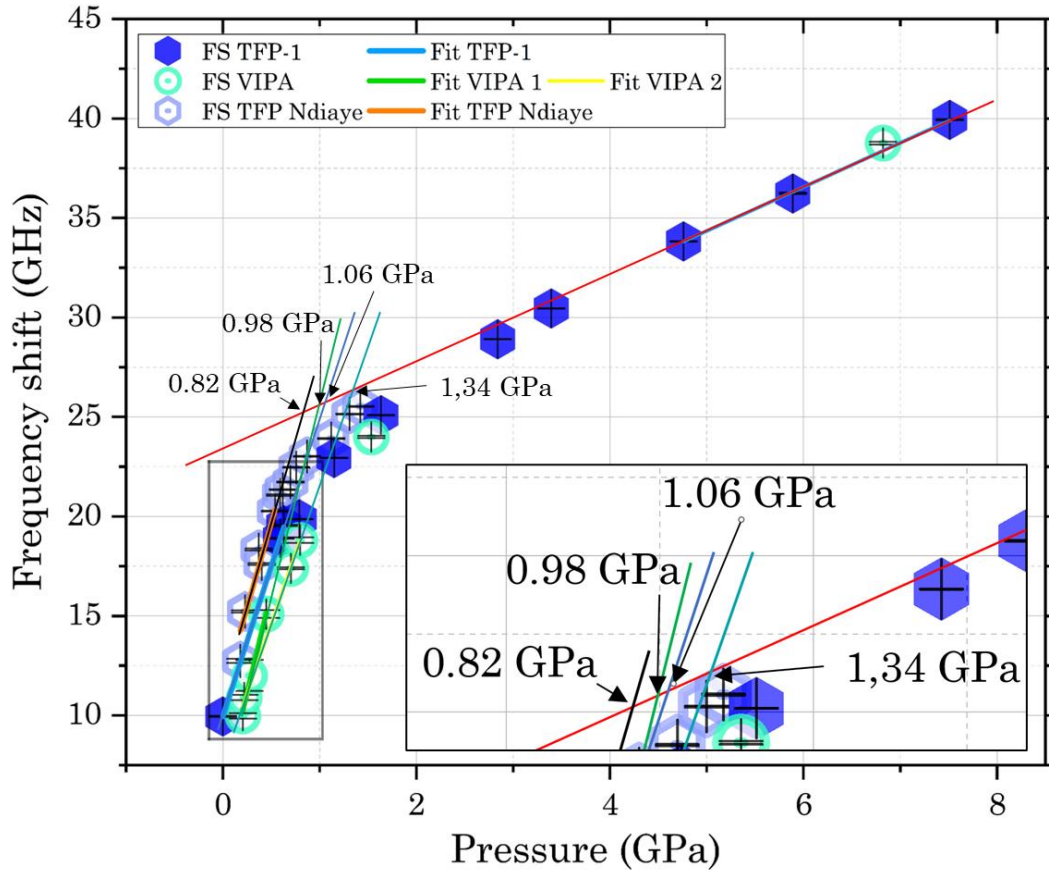


Figure 0.11: FWHM du Benzyl benzoate dans la géométrie de rétrodiffusion à 22°C étude réalisée avec une cellule à basse pression par Ndiaye en utilisant un objectif de microscope X10 [38], représenté par des symboles hexagonaux ouverts bleu clair avec un point central. Les expériences à haute pression de ce travail sur le benzoate de benzyle sont réalisées avec un objectif X20 avec le TFP-1 (hexagone bleu plein) et le VIPA (symboles verts en forme de cercle ouvert avec un point central). La cellule basse pression permet d'être plus précis en dessous de 1 GPa. Les lignes noire, orange et rouge correspondent à l'ajustement linéaire du décalage de fréquence de l'ensemble de données de Ndiaye, la ligne verte à celui de VIPA et la ligne bleue à celui de ce travail sur le TFP-1.

Un zoom sur le décalage de fréquence pour les données du TFP-1 entre 0 et 2 GPa se trouve à l'annexe D.2.

La pression de transition vitreuse extraite des données FWHM est comparée aux prévisions WLF. Le benzoate de benzyle présente des pressions de transition vitreuse proches des prévisions du modèle Williams-Landel-Ferry (WLF). Cependant, la pression de transition vitreuse du squalane et du glycérol est inférieure aux prévisions du modèle WLF, ce qui

suggère des écarts par rapport au modèle classique et indique un comportement complexe de ce fluide dans des conditions extrêmes

Les mesures de spectroscopie Brillouin à haute pression permettent de dériver les contributions de la partie réelle M' et imaginaire M'' du module longitudinal M . M' est obtenu à partir du décalage en fréquence des pics inélastiques Brillouin du lubrifiant en fonction de la pression et de la température. Les données obtenues à partir des mesures de spectroscopie Brillouin montrent une augmentation de M' avec la pression dans la Figure 0.12, révélant une évolution croissante du module élastique du lubrifiant avec la pression. De plus, l'évolution marquée des modules M' et M'' suggère l'existence de deux régimes de comportement asymptotiques des échantillons. Aux faibles pressions, le module longitudinal faible est représentatif d'un comportement fluide viscoélastique. Dans ce régime, le module augmente rapidement avec la pression, donc la réduction de volume de l'échantillon, jusqu'à une pression critique au-delà de laquelle cette évolution ralentit. Dans ce deuxième régime, le module longitudinal élevé est associé aux matériaux au comportement assimilé à un solide de l'échantillon.

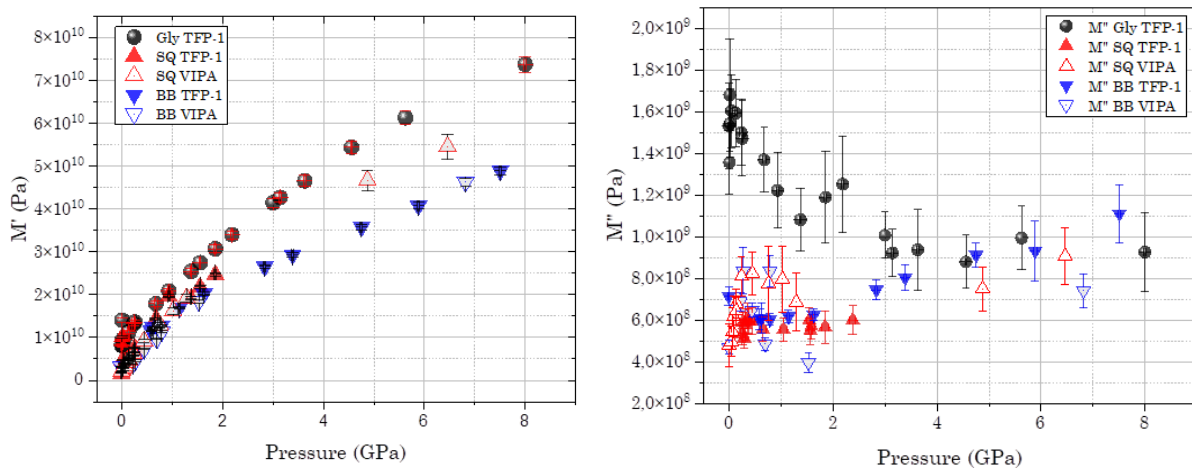


Figure 0.12 : Partie réelle (à gauche) et partie imaginaire (à droite) du module longitudinal du benzoate de benzyle, du squalane et du glycérol sous pression dans la cellule HP, à température ambiante.

Un autre paramètre mécanique important dérivé des spectres Brillouin est le paramètre d'amortissement du fluide (D), qui est lié à la dissipation des ondes acoustiques dans l'échantillon et, par conséquent, associé à la dissipation visqueuse dans le lubrifiant. Le paramètre d'amortissement (D) donne un aperçu du comportement viscoélastique des lubrifiants et de la façon dont ils réagissent aux contraintes de cisaillement.

L'évolution du paramètre d'amortissement (D) en fonction de la pression en Figure 0.13 a été étudiée et il a été constaté que D varie de manière significative en fonction de la pression.

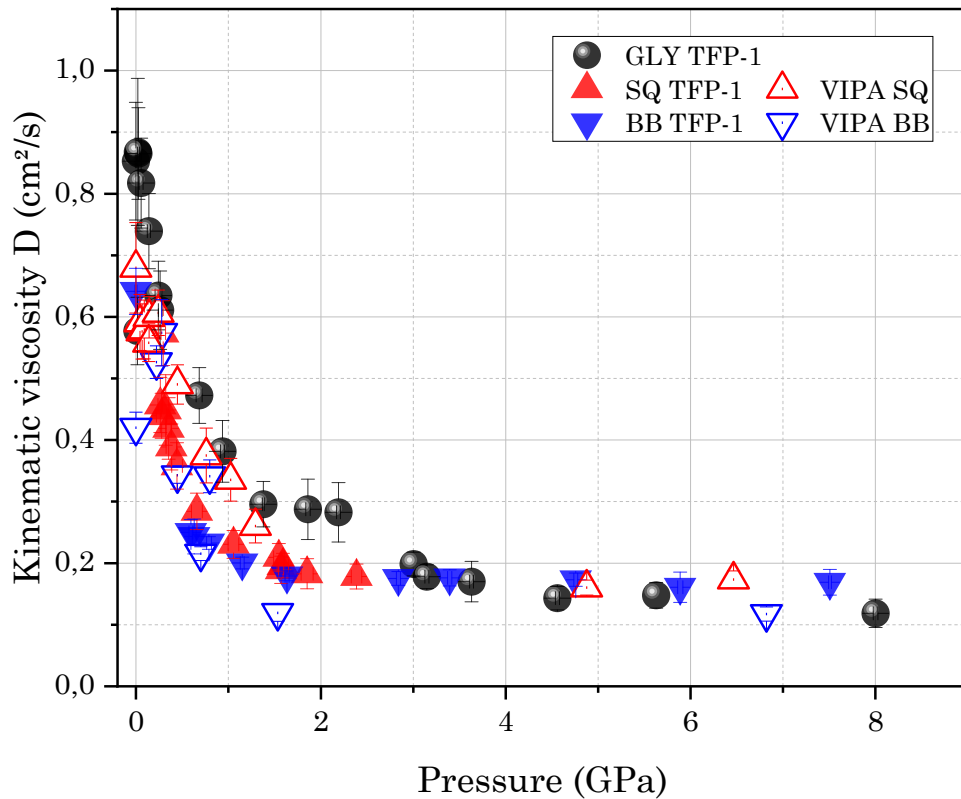


Figure 0.13 : Viscosité cinématique longitudinale du benzyl benzoate, squalane et glycérol en fonction de la pression dans la cellule haute pression, à température ambiante.

L'analyse du paramètre D suggère également la présence d'une transition entre les états viscoélastique et vitreux à des pressions spécifiques, ce qui correspond au concept de comportement de transition vitreuse des fluides.

Le facteur de tangente de perte ($\tan(\delta)$), également connue sous le nom de facteur d'amortissement ou de facteur de qualité, est calculée à partir des spectres Brillouin. La tangente de perte représente le rapport entre le FWHM (amortissement du son) et le décalage en fréquence des pics inélastique (propagation du son) et fournit une mesure du rapport entre la réponse visqueuse et la réponse élastique du lubrifiant comme montré en Figure 0.14.

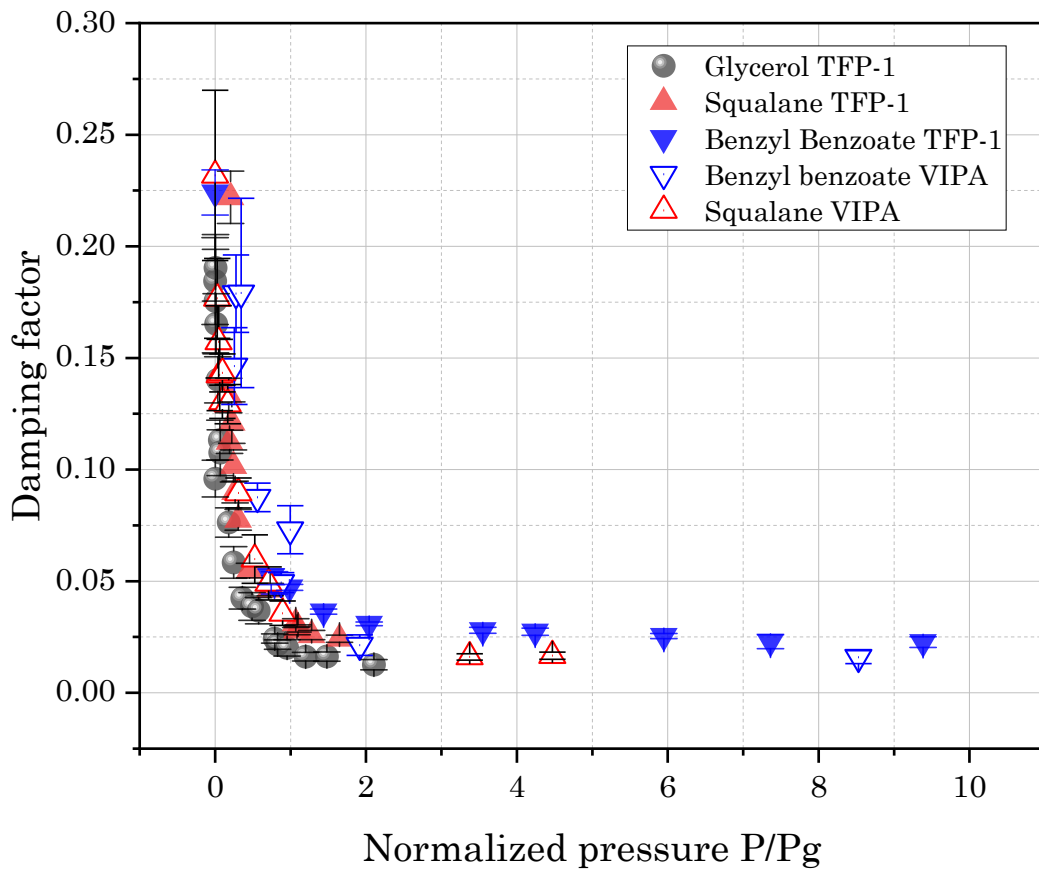


Figure 0.14 : Facteur d'amortissement (facteur de qualité) $\tan\delta = \text{FWHM}/\text{FS}$ de trois fluides, benzoate de benzyle, squalane et glycérol, en fonction de la pression normalisée. Les deux configurations sont représentées, TFP-1 (symboles pleins) et VIPA (symboles ouverts).

L'analyse de la tangente de perte montre que les trois fluides, le benzoate de benzyle, le squalane et le glycérol, présentent un comportement similaire de la tangente de perte malgré leur nature différente. La tangente de perte évolue de manière similaire pour les trois liquides. La très faible valeur de la tangente de perte à des pressions élevées signifie que l'échantillon est dû par l'élasticité et que la dissipation visqueuse est négligeable.

Dans la deuxième série d'expériences, les échantillons sont soumis à un cisaillement dans un rhéomètre couplé au spectromètre Brillouin VIPA pour observer l'influence du cisaillement sur leurs propriétés viscoélastiques [39].

Un écoulement de cisaillement simple est imposé sur une large gamme de taux de cisaillement. Les spectres Brillouin sont enregistrés directement dans la cellule du rhéomètre, en même temps que la viscosité macroscopique mesurée par le rhéomètre, et sont ensuite ajustés avec une triple fonction lorentzienne [106,119,210]. Cette partie n'est pas développée dans cette thèse, néanmoins les résultats sont présents dans l'annexe.

Des mesures de frottement ont été effectuées avec le tribomètre Jerotrib sur la Figure 0.15, et une corrélation a été établie entre le comportement macroscopique et le facteur de dissipation obtenu à partir des spectres BLS.

Les mesures sur le squalane avec le tribomètre Jerotrib ont permis d'établir pour ce fluide la même corrélation entre le frottement macroscopique et le comportement local que celle déjà proposée pour le benzoate de benzyle [38,41]. La pression normalisée $\bar{P}/P_{g:WLF}$ a joué un rôle clé dans le comportement des deux lubrifiants, et les mesures Brillouin couplées au rhéomètre ont fourni des informations précieuses sur cette corrélation. En effet, la Figure 0.15 montre le même changement de régime entre la viscosité apparente relative (dérivée des mesures de frottement dans un contact) et la tangente de perte (dérivée des spectres Brillouin dans une cellule haute pression) autour de la pression de transition vitreuse.

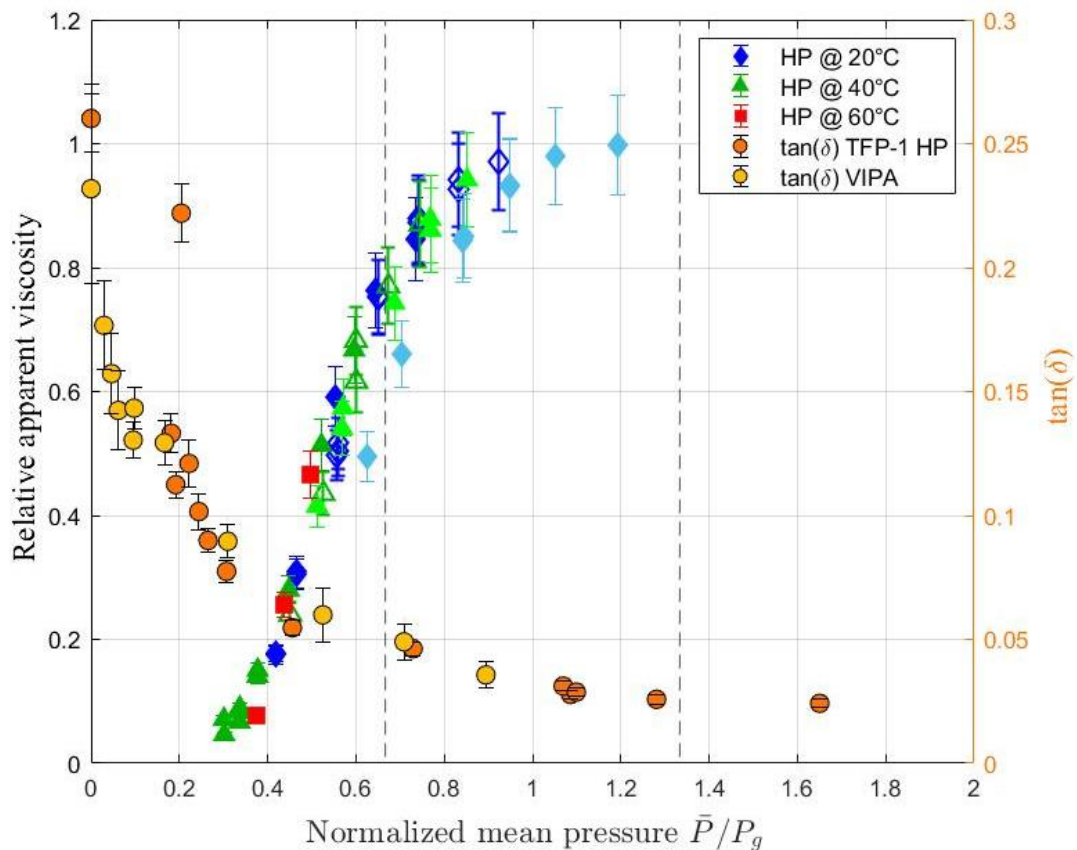


Figure 0.15: Viscosité moyenne relative dérivée des mesures de frottement du squalane prise à 3 températures et à faibles taux de cisaillement (axe de gauche) et facteur de dissipation des spectres Brillouin (axe de droite) par rapport à la pression normalisée $\bar{P} / P_{g:WLF}$ pour le squalane. Pour les viscosités : les symboles pleins de couleurs foncées représentent les surfaces acier-acier, les symboles ouverts représentent les surfaces acier-saphir et les symboles unis de couleurs claires représentent les surfaces en carbure de tungstène (WC-WC).

0.6 Limitations et perspectives

Il est important de considérer les limites associées à ces résultats. Plusieurs points de critique et d'amélioration potentielle ont été identifiés, tant au niveau du dispositif expérimental que de l'analyse des résultats.

Sur le plan expérimental, les limites comprennent l'impossibilité de déduire directement G le module de cisaillement des mesures de spectroscopie Brillouin en raison de la géométrie de rétrodiffusion. La gamme utilisée des taux de cisaillement réalisables dans un rhéomètre est restreinte par rapport à ceux observés dans les contacts.

Les problèmes d'instabilités de laser doivent être solutionner pour permettre une meilleure acquisition des spectres.

Les mesures couplés tribomètre-Brillouin n'ont pas encore donnés de résultats. Un ajustement vertical plus fin ainsi que l'utilisation d'un objectif a plus fort ouverture numérique.

En ce qui concerne l'analyse des résultats, il faut tenir compte de l'hypothèse d'un coefficient de polarisabilité constant en fonction de la pression. De plus les modèles de densités utilisés montrent une différence avec les densités extraites via la spectroscopie Brillouin au-delà de la pression de transition vitreuse.

D'un point de vue expérimental, plusieurs campagnes d'essai sont proposées et ferons suite à cette thèse. Tout d'abord, une campagne impliquant des mesures de spectroscopie Brillouin à l'aide d'une cellule à haute pression dans une configuration de diffusion oblique pour dériver l'indice de réfraction des fluides. Cette expérience comprend la validation de l'hypothèse d'un coefficient de polarisation constant et de la loi de densité des fluides lubrifiants. En outre, une série d'expériences peut être réalisée sur la configuration de rétrodiffusion à l'aide d'une analyse à polarisation croisée VV et VH. Enfin, le nouveau dispositif devrait être couplé au tribomètre pour effectuer des essais in situ, en comparant le comportement du lubrifiant local avec les résultats de l'étalonnage et en étudiant le frottement macroscopique en relation avec la caractérisation du lubrifiant local.

General introduction

In 2010, the International Energy Agency (IEA) issued a cautionary advisory regarding the imperative to undertake substantial efforts aimed at restricting global warming to a threshold of 2°C attributed to industrial activities [48]. It indicated that « the trends that drive growth in energy demand and carbon dioxide (CO₂) emissions associated with climate change continue to surge forward at an unrelenting pace».

Yet, to limit the long-term global average temperature rise to between 2.0°C and 2.4°C, the United Nations Intergovernmental Panel on Climate Change (IPCC) already concluded that by 2050, a minimum reduction 50% in global CO₂ emissions compared to the year 2000 will have to be achieved.

Several recent reports, in particular the one of Holmberg and Erdemir [49] highlight the role that tribology may play as a key technology to reduce energy losses. They estimated that in average 20% of the total energy worldwide is dedicated to overcome friction (103 exajoules (EJ)).

Friction occurs in many industrial sectors, as well as in transportation, which are among the main economic sectors responsible for greenhouse gas emissions. One conventional method to reduce friction, involves the application of a lubricant between two surfaces of the solid bodies in order to separate them, and to concentrate shear in the fluid film. This reduces friction stress in the contact, as well as wear on the solid's surfaces.

Fluids traditionally used to lubricate sliding components are mineral-based oils. They still constitute the largest consumption by volume worldwide. These oils can have complex formulations, since numerous additives are added to optimize lubrication. Some additives are designed to remain in solution to modify the lubricant rheological behavior. Others ensure the lubricant stability and durability. Still others adsorb onto solid surfaces to modify friction in the boundary regime.

Optimizing the lubricated contact operation requires an accurate prediction of the mechanisms responsible for friction, and therefore a thorough understanding of the behavior of the lubricant. Yet, this poses a formidable challenge due to the intricate interplay of mechanical, dynamic, and thermodynamic factors within the contact environment and governing friction (confinement, temperature, pressure and shear rate), making any macroscopic prediction unreliable. Typically, the lubricating fluid film, of the order of one hundred nm thick at the contact center, goes through the contact in less than 10⁻⁴ s. It experiences a pressure rise of more than one GPa and generates shear stresses that can exceed one hundred MPa.

Numerous **rheological models** have been proposed in the literature to characterize the lubricating fluids behavior. They are obtained from rheological measurements carried out on a volume of lubricant, outside of the contact. Implemented in numerical contact models, they enable nowadays a rather good prediction of friction under **moderate operating conditions of pressure, temperature and shear**.

Unfortunately, in the case of highly loaded lubricated contacts (with max pressure of several GPa) described earlier, the severe tribological conditions make any corresponding rheological measurement on the lubricant very strenuous. As a result, up to now, the lubricant behavior at high pressures is still modeled very empirically from **non-predictive models**.

Yet, the most critical in-use mechanisms involve highly loaded lubricated contacts) giving rise to substantial energy dissipation and may ultimately lead to the mixed lubrication regime and a dramatic wear of the surfaces.

This work deals with the prediction of friction in highly loaded lubricated contacts and more specifically on the lubricant response under such conditions.

The initial phase of the overall project involves the development of a non-contact methodology to characterize a lubricant volume under experimental conditions. These conditions are designed to be both i) representative of those encountered in an actual contact and ii) decoupled from each other. This approach has two main objectives:

- To independently discern the influence of each parameter (pressure, temperature and shear) on the lubricant response in the contact,
- to characterize the ex situ behavior of the lubricant under these same conditions. The ultimate goal is to predictive rheological models that can be implemented in a numerical simulation model.

Due to the complex coupling of the contact operating conditions, a promising direction for future research lies in performing measurements directly within the contact. However, the friction coefficient conventionally measured in a contact is a macroscopic quantity, averaged over the whole contact area and therefore containing information about the complex distribution of pressure and film thickness. Therefore, an important step in the future is to couple an experimental tribometry set-up with a means of measuring the local behavior of the lubricant. Such measurements conducted simultaneously with friction tests will make it possible to establish a link between the (thermo)dynamic response of the lubricant and the resulting macroscopic friction.

Due to experimental challenges such as a film thickness of about one hundred nanometers that make any direct measurement virtually impossible and the fast dynamic nature of the contact, we approach the local investigation using a spectroscopic technique called Brillouin spectroscopy coupled with a tribometer based on a transparent disc in contact with a steel ball. The simplified tribo-system coupled to such an indirect non-destructive and non-invasive technique will allow to make in situ real-time measurements in order to investigate the macroscopic values of friction from the analysis and knowledge of the microscopic local behavior of the lubricant.

The thesis work outlined here is particularly dedicated to establishing the foundational framework for this project. It focuses on the development of an adaptable experimental rig capable of accommodating diverse experimental couplings. Additionally, it involves conducting the rheological characterization of some lubricants under the severe conditions of a highly-loaded contact. This study follows on from an earlier doctoral thesis [10,38] in which a synthetic fluid was characterized by friction measurements, Raman and Brillouin spectroscopy over a wide range of operating conditions. The behavior of this fluid at rest was measured and compared with friction results, making it possible to correlate its glass transition pressure and the occurrence of a friction plateau.

The strategy adopted here is to select two lubricating fluids with different behaviors (a lubricant and a model fluid) to make the conclusions, if not universal, at least generalizable to both behaviors. A third fluid is chosen as a reference fluid for Brillouin spectroscopy.

In the first part, the scientific background is set out, both from a tribological (**Chapter 1**) and a Brillouin spectroscopic (**Chapters 1 and 2**).

In the second part, the Brillouin spectroscopy experimental rig, designed to integrate with various experimental devices such as a rheometer (**Appendix E**) or a tribometer, (**Chapter 3**) is established and validated comparing results previously obtained from another experimental rig (**Chapter 4**).

Finally, in the last part of this work (**Chapter 5**), the fluids characterization is presented in relation to pressure, temperature. This characterization is compared with macroscopic friction measurements to extend the correlation previously proposed on a synthetic fluid to lubricants of various natures. This would be a first step towards a general understanding of the mechanisms behind friction.

1. General background about friction in lubricant films

Table of contents

1.1	ENVIRONMENTAL AND ECONOMICAL MOTIVATIONS.....	45
1.2	BASICS OF LUBRICATION	48
1.2.1	REGIME OF LUBRICATION.....	48
1.2.2	A BRIEF OVERVIEW OF A LUBRICATED CONTACT COMPLEXITY	50
1.2.3	TYPICAL FRICTION CURVE.....	51
1.3	FRICTION UNDER HIGH PRESSURE AND SHEAR STRESS.....	54
1.3.1	ORIGIN(S) OF FRICTION PLATEAU	54
1.3.2	GLASS TRANSITION AND RELAXATION TIME	59
1.4	BRILLOUIN LIGHT SCATTERING	63
1.4.1	CHARACTERIZATION OF THE GLASS TRANSITION	63
1.4.2	BRILLOUIN LIGHT SPECTROSCOPY CHARACTERIZATION OF LUBRICANTS	67
1.5	OUTLINES OF THE WORK.....	70

This research addresses critical issues in tribology arising from the energy crisis and global warming. The focus is on highly loaded lubricated contacts where friction and wear significantly impact energy consumption and environmental concerns. The global cost of friction and wear is immense, exceeding 250,000 million euros, with CO₂ emissions surpassing 8 MtCO₂. Approximately 20% of global energy is consumed in overcoming friction, emphasizing the urgent need for efficient lubrication strategies.

The elastohydrodynamic lubrication (EHL) regime, is characterized by high pressures inducing elastic deformation, very thin film and a high shear. However, predicting friction under these conditions is challenging due to the complex behavior of lubricants, due to a strong parameter coupling. A classical ball-on-disc tribometer is employed for friction tests, revealing distinctive regimes.

The existence and origin of the friction plateau in highly pressurized contacts remain a topic of debate. Previous theories proposed a plastic solid or a glassy state of lubricants. Empirical models, like the Limiting Shear Stress (LSS) models, simulate the friction plateau but lack predictability. Addressing these challenges involves direct measurements of velocity profiles in contacts and a comprehensive understanding of lubricant behavior under extreme conditions.

Additionally, Brillouin spectroscopy is a non-invasive technique provides valuable insights into lubricant properties, shear modulus, and relaxation time. Additional informations are needed to compute models such as density, refractive index. The glass transition is observed in the literature as a linear shift to higher values with increasing pressure.

This study contributes valuable insights into the intricate dynamics of lubricated contacts, shedding light on the friction plateau phenomenon and paving the way for more efficient and environmentally friendly lubrication strategies.

1.1 Environmental and economical motivations

The energy crisis, coming from both the increase in prices and global warming, has become a very critical and crucial topic. The International Energy Agency (IEA) warns that efforts must be made to limit the temperature raise by 2°C due to industrialization [48]. These efforts are more and more important as population constantly increases worldwide, which goes in pair with a constant demand of energy consumption. Today, the major part of global greenhouse gas emissions comes from energy production and consumption with 76% of the total emissions (gathering industry, transportation, building, electricity, heat production and other energy, as displayed in Figure 1.1), and only 24% for agriculture, forestry and other land [49](see Figure 1.1).

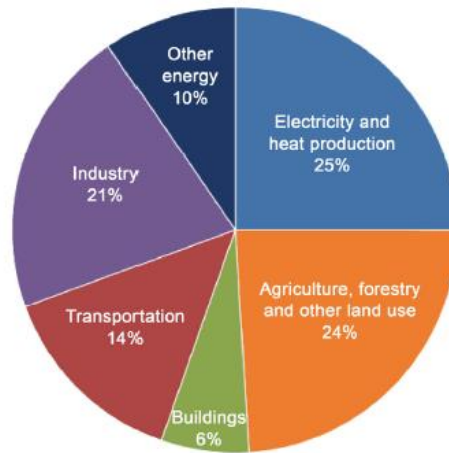


Figure 1.1 : Global greenhouse gas emissions by economic sector [49].

This matches with the economic sectors identified by Holmberg and Erdemir [49] as the main energy consumers, based on the IEA energy statistics (2017) (see Figure 1.2).

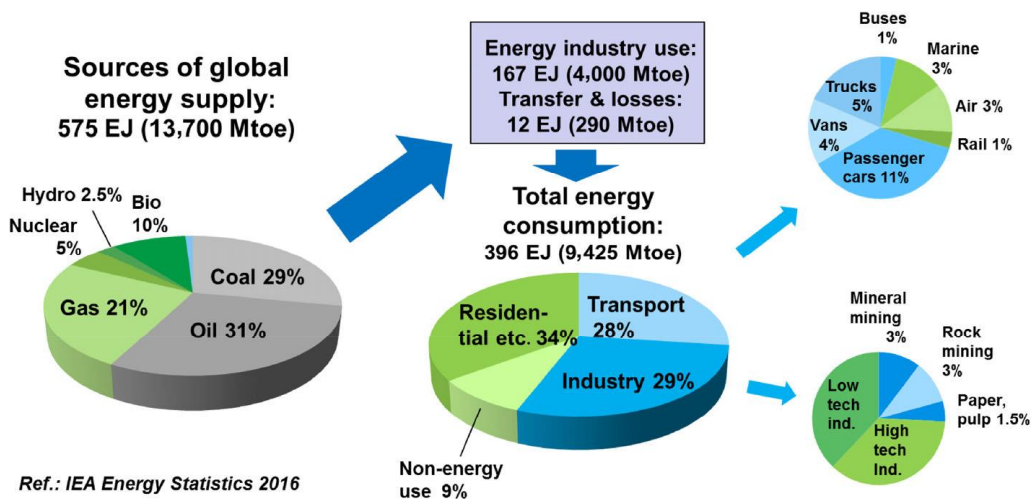


Figure 1.2 : Global energy supply and consumption in main economic sectors (2016). Mtoe = million tons of oil equivalent. Residential etc involves services, agriculture, and forestry. Non-energy use is typical as raw materials [49].

Numerous recent publications focus on essential technologies aimed at reducing energy losses [1–3]. In particular the exhaustive work of Holmberg and Erdemir [49] underscores the field of tribology as potentially improvable. This involves both friction reduction to significantly reduce energy losses and wear prevention to increase mechanical systems' service life. Indeed, the global cost for both friction losses and wear is about 250,000 million euros, and the total CO₂ emission is higher than 8 MtCO₂ (see Figure 1.3).

Besides, Holmberg and Erdemir estimated that in average 20% of the total energy worldwide is dedicated to overcome friction (103 ExaJoule or EJ), while only 1/6 of this energy goes to wear losses (16 EJ) (see Figure 1.3). This leads at the end to an impact of friction on CO₂ emissions which is 6 times higher than that of wear.

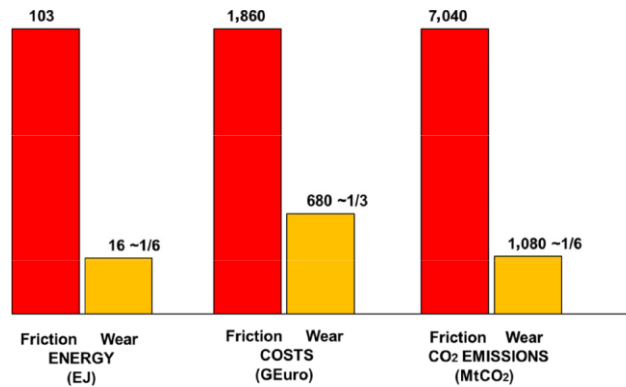


Figure 1.3: Energy consumption, costs and CO₂ emissions due to friction and wear globally [49]

In particular for transportation and Industry, as presented in Table 1.1, wear only represents 10% and 14 % respectively of the energy loss due to friction.

Comparison of energy and costs due to friction and wear for the four economic sectors.

	Energy to overcome friction as part of total energy use	Energy due to wear compared to energy loss due to friction	Costs due to wear compared to costs due to friction
Unit	%	%	%
Transportation	30	10	22
Industry	20	14	35
Energy industry	20	22	53
Residential	10	14	35
Total	20	15	37

Table 1.1 : Comparison of energy and costs due to friction and wear for the four economic sectors [49]

In the analysis displayed in Table 1.2 about the transportation impact, it appears that road vehicles dominate the energy consumption (75%), due to the large number of vehicles in use worldwide.

Key energy and energy efficiency figures in transportation.

	Number of vehicles worldwide	Global energy use	Energy use / vehicle	Part of global transport energy use	Part of global transport by weight and distance	Energy intensity
Unit		EJ/a	GJ/a	%	%	MJ/tkm
Road vehicles	$1,040 \times 10^6$	83	80	75	15	10
Trains	120,000	4	33,000	4	12	0.6
Ships	100,000	12	120,000	11	73	0.3
Airplanes	360,000	12	33,000	11	0.6	35
Total	$1,620 \times 10^6$	110		100	100	2

Table 1.2 :Key energy and energy efficiency figures in transportation [49]

In the domain of road vehicles, the most critical mechanisms occur in rolling element bearings in which load is transmitted through very small contact surfaces, leading to very high local pressures (few GPa). This causes high energy dissipation and may ultimately lead to poorly lubricated contacts, resulting in dramatic wear of the solid surfaces. This is the reason why this work focuses on such highly loaded contacts.

The technical solutions anticipated to reduce friction are numerous. They involve different scales of time and effort. Indeed, some of them are short-term or middle-term solutions, meaning that they can be applied in the next few years and do not require significant modification of the existing mechanical systems. They are mainly related to lubricants characteristics, including nanotechnology-based anti-friction and antiwear additives, low-viscosity oils, vapor phase lubrication, or solid lubricants.

The suggested long-term term solutions are the development of new materials (or material treatment) and surface engineering (including surface treatment, coatings, or texturing), but also new component design (with microsensors and actuators). Also, new methodologies like biomimetics, nanotechnology, and integrated computational material design are anticipated [50–52].

These last solutions involve to re-design and to replace existing components and thus require much more effort. Mechanisms involved in these solutions are multiphysical and multiscale. They require a thorough understanding of the contact and the lubricant behavior for lubricant-related solutions.

Holmberg and Erdemir [49] estimated that the implementation of short term solution under 8 year, that could enable to save 21.5 EJ energy, 455,000 million euros, and 1,460 MtCO₂ emissions (see Figure 1.4). The maximum potential saving is estimated for transportation, which is inline with its actual high level of energy consumption. This saving could then be doubled in the long term (>15 years) and easily reach 46 EJ energy, 973,000 million Euro, and 3,140 MtCO₂ emissions. This would represent 1.39% of the gross national product (GNP) and 8.7% of the total energy consumption. In particular, new tribological solutions related to lubricant engineering in lubricated contacts would help to support the IEA predictions for the reduction of both CO₂ emissions and energy losses.

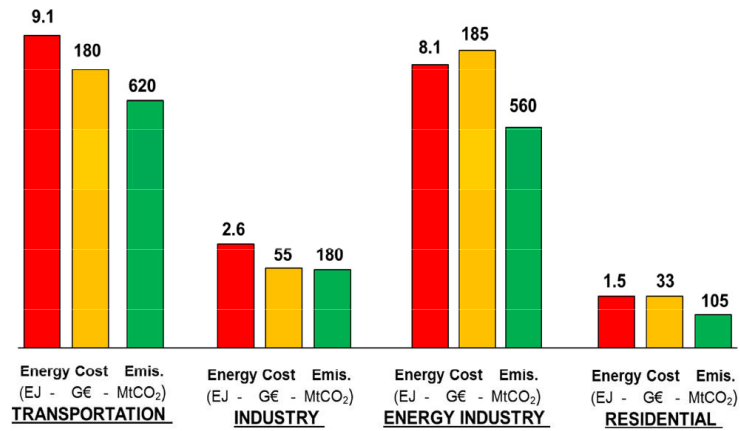


Figure 1.4: Potential annual energy, costs and CO₂ emission savings globally after 8 years of intensive advanced tribology implementation [49]

To resume, it is clear that reducing friction in mechanical systems targeting the transportation sector, and in particular road vehicles, has a major role to play in the next years for both economic and environmental prospects.

1.2 Basics of lubrication

1.2.1 Regime of lubrication

Basically, friction is defined in [53] as « the resistance to the sliding of one solid body over or along another, as solid bodies are ordinarily understood in the macroscopic world”. The magnitude of friction is represented by a coefficient C_f , defined as the ratio between the tangential or sliding force F and the normal force or load W (as shown in Figure 1.5) pressing the two solid bodies together. Friction is widely used as the main performance indicator for industrial contacts like those in rolling element bearings.

In some applications, friction is desirable, as between tires and roads (coefficients in the range of 0.5 to 1.2), or between mechanical parts that are bolted together. However, in most of the applications, friction is rather minimized in order to both reduce the energy consumption of the contact and prevent the wear of the solid bodies in contact.

In many mechanical systems, lubricant is added in the contact to reduce friction. Its purpose is then multiple: firstly, to separate the two solid surfaces and to avoid wear. Secondly, to transfer loads between the solid bodies. Finally, to accommodate the shear due to the sliding velocity between them. It also enables to remove the heat generated by shearing the lubricant in the contact and the wear particles [54,55]. Furthermore, the chemical additives added into industrial lubricants have other features such as preventing from oxidation, corrosion or foam formation.

The lubricant’s ability to separate rubbing surfaces highly depends on the operating conditions.

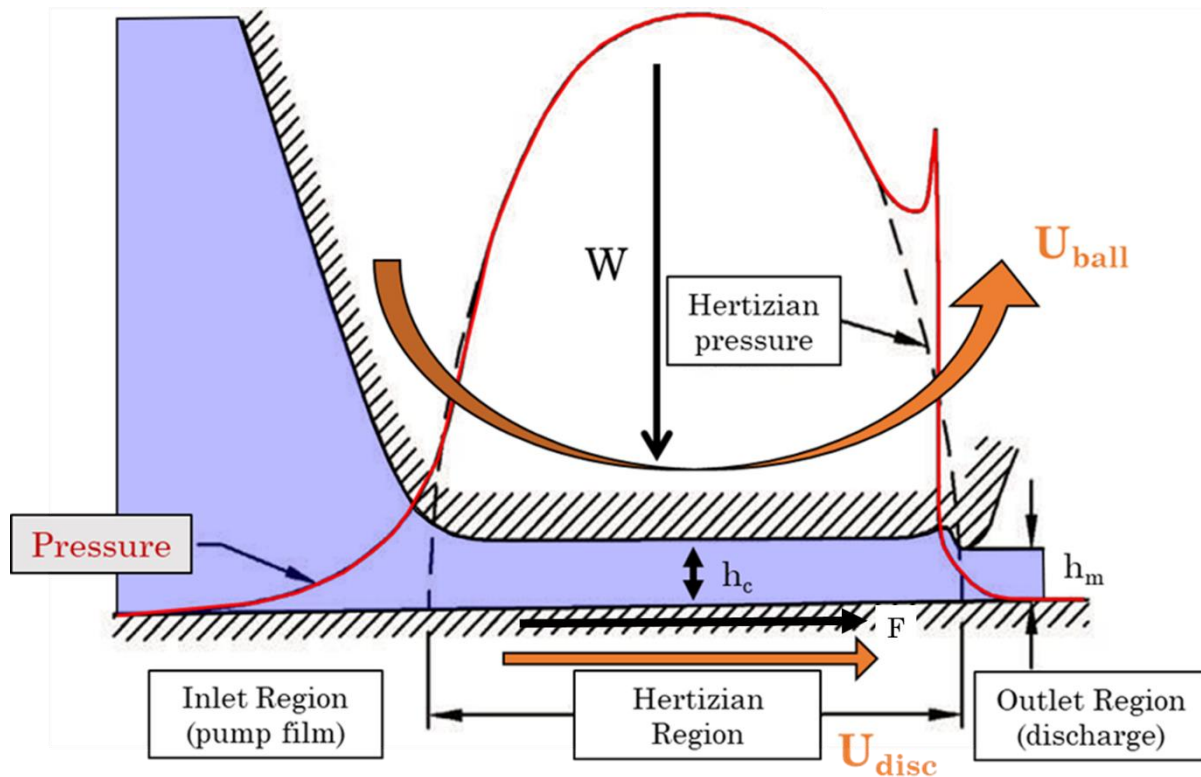


Figure 1.5 : Schematic view of the EHD contact, inspired from [6]. Principal experimental characteristics are explicated. h_c and h_m represents the central and the minimum film thickness respectively. The EHD pressure profile is represented in full red line and the dashed line represents the Hertzian pressure. W is the normal force. The orange arrows represent the rotational velocities U_{ball} and U_{disc} of the solid surfaces, of the ball and the disc respectively. F represents the sliding force.

In the case of highly loaded and highly sheared contacts, the resulting high pressures induce a significant elastic deformation of the solid bodies (generally larger to much larger than the lubricant film thickness). In the meantime, the lubricant (piezo)viscosity [56] together with the imposed entrainment velocity drive enough fluid in the contact so that the solid surfaces are fully separated by a thin film of a typically few hundred of nanometers, under the best conditions. Moreover, the strong hydrodynamic effect enhanced by the pressure influence on the lubricant viscosity. The lubricating regime described here is the ElastoHydroDynamic regime (EHD regime) or EHL for ElastoHydrodynamic Lubrication.

In practice, this regime is typical of non-conformal contacts, as those occurring in gears, rolling element bearings, cam-tappet systems, etc...

In this regime, the lubricant efficiency in reducing friction and wear significantly depends on its rheological properties. For instance, the fuel consumption in a car engines can vary by 5% between a standard oil and an optimized low friction oil [57].

This research is a continuation of the previous work carried out by Serigne Ndiaye [10,38,41] on the investigation of friction occurring in highly loaded circular contacts formed between a ball and a disc, as a representative model of EHD contacts.

1.2.2 A brief overview of a lubricated contact complexity

Models for predicting the lubricant film thickness in ElastoHydroDynamic (EHD) contacts emerged in the 1950s [58,59]. They were based on the strong assumption that the lubricant behaves as a Newtonian fluid [60], with isothermal conditions within the contact, and a pressure viscosity dependence described by the Barus equation [61]. Despite this simple assumptions, they have proven to provide rather accurate film thickness estimations [62] and are still widely used today. Unfortunately, friction prediction is a much more complex problem that still needs to be investigated. The strong assumptions previously stated, and in particular, the Newtonian behavior of the lubricant, lead the EHL theory to overestimate friction measured experimentally [63]. More sophisticated constitutive equations implemented in numerical models at a continuous scale enabled to obtain better predictions at moderate load conditions [64]. However, in the case of contacts submitted to very high loads, strong discrepancies are still observed. The difficulty to predict friction under such operating conditions can be inferred from the combination of: i) the lubricant's complex behavior at high pressure, ii) the complex distribution of these conditions over the whole contact and iii) the strong coupling between operating parameters.

Typically, in EHD contacts, the lubricant travels along a contact of a fraction of a millimeter ($\sim 100\text{-}300\ \mu\text{m}$) in a very short time ($< 10^{-4}\text{s}$), during which it experiences a very brutal pressure increase, up to few GPa in the center of the contact. The resulting central film thickness, conditioned by the lubricant viscosity, ranges between a few tens of nanometers up to a micrometer. This leads to classically considering that friction in lubricated contacts is mainly caused by the shearing of the lubricant film in the highly pressurized contact area. The non-conformal geometry of the contact leads to a steep distribution of pressure, ranging from atmospheric pressure at the interface with air up to the maximum pressure at the center of the contact. This pressure increase occurs along the contact radius of a fraction of millimeter, as estimated by the Herz Theory. This theory considers dry contact without friction and also provides the maximum pressure P_{Hertz} [65], the pressure distribution over the contacts and the elastic deformation of the solid surfaces.

This sharp distribution can strongly influence the thermodynamic behavior of the lubricant. Besides, the non-conformal geometry combined with the surfaces elastic deformation also leads to a strong distribution of thickness across the contact. This directly conditions the shear rate experienced by the lubricant, which also distributes from mean values of $10^5\ \text{s}^{-1}$ – $10^7\ \text{s}^{-1}$ typically at the inlet of the contact (at almost ambient pressure) up to higher values reaching $10^8\ \text{s}^{-1}$ at the contact center in extreme conditions. This may involve a strong dynamic effect on the behavior of the lubricant. On the other hand, such high shear rates generate heat in the confined lubricant because of viscous dissipation. Depending on the operating conditions, the temperature has been estimated to locally increase up to a few tens of degrees [66]. Combined with the thermal properties of the solid bodies, which characterize their ability to conduct or store heat, this leads to a complex temperature distribution inside the confined lubricant.

The complex combination of pressure, temperature, and shear rate distributions impacts the lubricant response. Consequently, this in turn impacts the film thickness and the shear rate, and thus the temperature distribution varies. It results in a very strong coupling inside the contact.

It can also be noted that the nature and geometry of the solid surfaces may bring more complexity by either involving a complex physico-chemical behavior or influencing the no-slip condition at the interface. Non-symmetrical materials may also influence the dissipation of heat in the contact and modify the flow profile.

This complexity highlights the discrepancy between the rheological and tribological approaches. This has long been debated in the literature and is still a topic of discussion [67]. It is more and more admitted in the community that data recorded on a tribometer should not be considered as intrinsic properties, compared to the ones recorded on a rheometer. Macroscopic measurements of the tangential force in a tribometer are averaged over the whole contact area. The resulting friction coefficient provides global information of the energy dissipation through the lubricant shearing. They do not provide any local information on the dependency of the lubricant behavior with pressure, temperature, and shear rate, independently of each other. Therefore, rheological characterization of the lubricant is not enough for friction prediction.

1.2.3 Typical friction curve

A classical friction test in a ball-on-disc tribometer consists in the application of a normal load on one of the solids (for example to the ball) and imposing independently the rotational velocity of each of the two solids. The ball generally dips into a thermostated lubricant reservoir to ensure fully flooded conditions. The tangential force is then measured to derive the friction coefficient C_f . Further details on the tribometer used in this work are given in Chapter 3 (§3.5).

Friction curves depict the relationship between the friction coefficient C_f and the slide-to-roll ratio SRR offering a visual representation of the frictional behavior across varying SRR values. The SRR is calculated as :

$$SRR = \frac{\Delta U}{U_e} = 2 \frac{U_{ball} - U_{disc}}{U_{ball} + U_{disc}} \quad (1.1)$$

$$U_e = \frac{U_{ball} + U_{disc}}{2} \quad (1.2)$$

With SRR which represents the ratio between the sliding and the rolling motion in the contact, U_e the mean entrainment velocity, U_{ball} the ball velocity and U_{disc} the disc velocity, as

represented in Figure 1.5. SRR is equal to zero in pure rolling condition and different from zero in rolling-sliding conditions. Several friction regimes are traditionally identified depending on the SRR value, as shown on Figure 1.6 [68,69]. The first regime (I) is identified as the linear regime, occurring at very low slide-to-roll ratio and displaying a linear increase of the friction coefficient with SRR. In this regime, the slope at the origin defines an effective viscosity [70]. This parameter has the dimension of a viscosity and provides macroscopic information on the dissipative behavior of the whole contact. The second regime (II) is the shear thinning regime where the friction coefficient

Growth rate declines with regard to the SRR. The third regime (III) in Figure 1.6, is the thermal regime, displays a decrease of the friction coefficient at moderate-high slide-to-roll ratio (SRR) due to the viscous heating of the lubricant submitted to high shear rate. Experimentally, for high contact pressures, the friction coefficient may exhibit a plateau-like regime at the end of the shear thinning regime for a given temperature, normal load, and entrainment speed. It means that friction appears to become independent of the sliding velocity. This regime is often related in the literature to the Limiting Shear Stress (LSS) property of the lubricant, defined as its ultimate shear stress or maximum yield shear stress. It was first highlighted by Smith in 1959 [71] and has been widely studied since then [5].

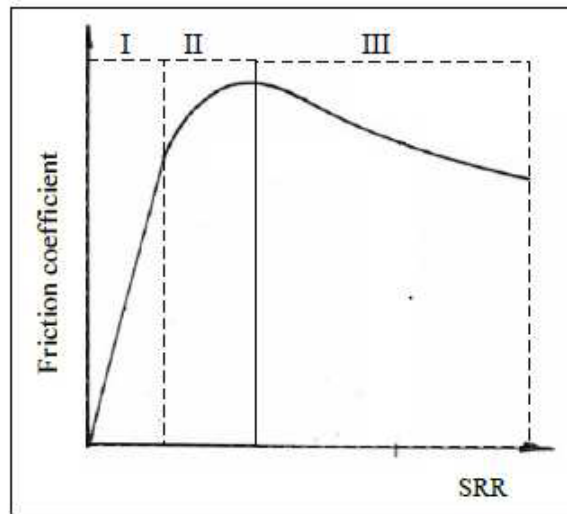


Figure 1.6 : Typical friction curve measured in a tribometer. Friction regimes are identified according to Dyson [69].

From the macroscopic tangential force (or friction force or resisting torque) measured in a tribometer over the whole contact, the mean shear stress versus central shear rate curve may be derived [38].

This conversion requires strong [72] assumptions. First, the mean shear stress $\bar{\tau}$ is obtained by dividing the whole tangential force by the contact area given by the Hertz theory. Then, the central shear rate $\dot{\gamma}_c$ is estimated at the center of the contact, where the maximum pressure and shear stress occur, by assuming a linear velocity profile across the lubricant film. It is derived from the sliding velocity divided by the central film thickness h_c predicted

by one of the available models (a complete comparison is provided in reference [62]). This approach assumes that friction mainly comes from the center of the contact, where the pressure is maximum and the film thickness is representative of the mean film thickness over the contact area.

An example of the resulting mean shear stress vs central shear rate curve is shown in Figure 1.7, two of the three regimes presented by Dyson are identified (I and II). The experimental protocol is described in reference [10]. Operating conditions have been selected to minimize thermal effects in the contact, contrary to the third regime found in Figure 1.6, so that viscous heating does not dominate the lubricant behavior and no significant thermal effect appear. The same trend as that of the friction curve (of Figure 1.6) is obtained. Besides, on Figure 1.7, the third regime, occurring after the shear thinning regime, shows a very slight increase of the shear stress with shear rate, and occasionally an apparent shear stress plateau for the higher contact mean pressure (1.12 GPa) according to the plateau criteria given in [10].

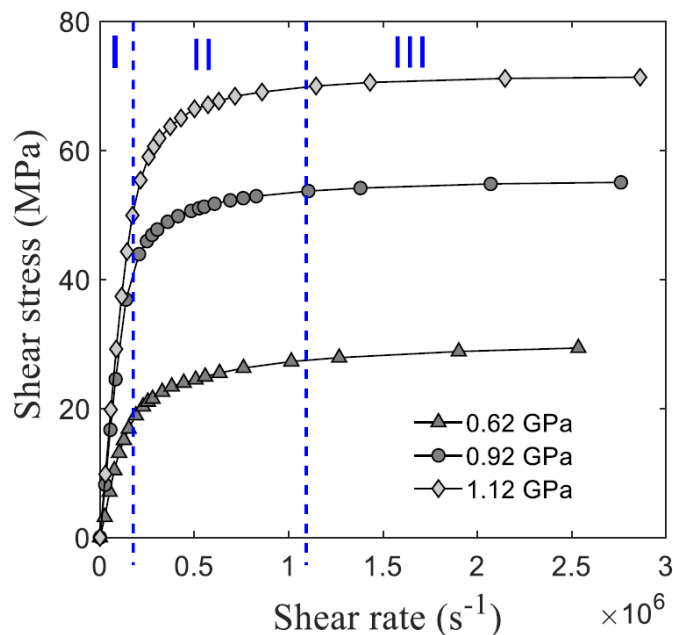


Figure 1.7 : Shear stress vs. shear rate curves for benzyl benzoate at various contact mean pressures, from friction measurements conducted according to the protocol described in [10].

The flattening of the friction curve triggers beyond a critical sliding velocity (or equivalently shear rate) and tends to a maximum value that determines the maximum shear stress that can be transmitted in an EHD contact. Consequently, it limits the energy losses through mechanical contacts, even if the shear rate increases. That is why controlling this plateau-like regime would help to control and reduce friction [73] and then, it would help to support the IEA predictions for the reduction of CO_2 emissions. However, it requires a thorough understanding of the physical mechanisms governing the lubricant response and the contact system under extreme conditions of pressure and sliding velocity. This itself requires an in-depth understanding of the rheological behavior of lubricants submitted to such conditions of high pressure, high shear, and very short flow duration.

Smith [71] suggested that the friction plateau could be attributed to the lubricant acting as a plastic solid when a critical shear stress is reached. He also suggested later that the sliding velocity may accommodate the lubricant through a very thin shear plane of molecular sizes, surrounded by layers of solidified lubricant moving at the velocities of the solid surfaces [74], without providing any direct evidence. Consequently, current models of friction remain empirical by nature and non-predictive. Many other assumptions emerged from the literature since then, which are detailed in the next part.

1.3 Friction under high pressure and shear stress

1.3.1 Origin(s) of friction plateau

The existence and the origin of the friction plateau is still an open debate in the literature. Indeed first, it is not clear whether the friction curve shown for instance in Figure 1.7 (1.12 GPa) exhibits a true plateau or not. Indeed, when examined closely, experimental data with uncertainties, do not show a perfect plateau. This is the case for some of the friction curves reported in Figure 1.7 for which friction data still increase very slightly. Criteria must be selected to define the onset of a plateau, which is very rarely reported or discussed in the literature. For instance, Ndiaye and coworkers [38] defined the onset of a plateau when the relative variation of the coefficient of friction between two successive SRR values became lower than the uncertainty of the measurements. As the friction curves show an increasing shear thinning effect with pressure (in regime II), determining the yield pressure at which friction exhibits a plateau is not straightforward.

The second major debate is whether the friction plateau comes from an intrinsic property of the lubricant (the LSS), so that it could be measured independently from of the contact, or from a combination between the lubricant behavior and the complexity of the contact environment, especially thermal and dynamic effects.

The experimental pieces of evidence required to answer these questions are very difficult to obtain due to experimental limitations in such severe conditions. Complementary data locally recorded inside the lubricant film *in situ* and *in operando* would provide very meaningful information. But it would require access to the inner part of the lubricant film (of ~ 100 nm thick) surrounded by the two-moving solid, and often opaque, surfaces.

Up to now, several assumptions have been drawn in the literature to explain the friction plateau, detailed in reference [63]. Three main assumptions emerge, described below.

In 1959, Smith [71] suggested that the friction plateau was due to the lubricant behaving as a plastic solid. This idea was then shared by several authors [75–77]. Later, exploring it further, many authors described this plastic behavior as a glassy state of the lubricant flowing through a highly pressurized contact [31,78]. This may be today the most popular assumption. It implies that the friction plateau results from an intrinsic property of the lubricants, its ultimate stress in the glassy state. It has already been measured in the literature both rheologically and tribologically as explained in the following.

To characterize the bulk lubricant behavior at high pressure and versus shear rate, rheological measurements have been performed outside of a contact, in a high-pressure rheometer. The first researchers involved were Bair and Winer in 1979 [73] who measured the shear rheological response of a naphthenic mineral oil (N1), a polyphenyl ether (5P4E), and a synthetic cycloaliphatic hydrocarbon (Santotrac 50) under pressures up to 1.2 GPa using three different pressure cells. Their results highlighted the existence of a LSS for the three lubricants, which were measured either in the viscous, elastic or plastic regime depending on the configuration of pressure, temperature, and shear rate. They concluded that in EHD contacts, the LSS should originate from the plastic behavior of lubricants. However, experimental conditions in their high-pressure rheometer are limited to 1 GPa, ultimately 1.2 GPa, and to low to middle shear stresses, or equivalently low shear rates ($<10^3 \text{ s}^{-1}$). Besides, these rheological data have not been compared to friction data. Yet this is essential to discriminate whether the bulk lubricant behavior can alone induce a friction plateau-like regime or whether the complexity of the contact significantly influences friction.

Recent work [41] has bridged this gap by correlating the pressure from which the friction plateau triggers with the lubricant glass transition pressure measured on the fluid at rest. Yet, it should be noted that the orders of magnitude of the lubricant's apparent viscosities derived from the initial slope of the friction curve (in the linear region) are very low ($\sim[10^2 - 10^3] \text{ Pa}\cdot\text{s}$) compared to the reference value of the glass transition viscosity ($10^{12} \text{ Pa}\cdot\text{s}$) classically used in the literature (see §1.3.2). Even if this apparent viscosity should not be considered as a lubricant intrinsic property as it is averaged over the whole contact area, higher values could have been expected to show a true glassy state. This highlights the importance of locally probing the lubricant directly in the contact.

The second tribological approach consisted of directly deriving the limiting shear stress from friction data obtained from lubricated contacts. It was for instance done by Evans and Johnson who used a disc machine [79] on a synthetic polyphenyl ether 5P4E and a traction fluid Santotrac 50. This approach differs from the one of Bair and Winer as measurements in a mechanical contact are macroscopic, averaged over the whole contact, whose complexity has been described in §1.2.2. While it does not necessarily call into question the assumption that friction plateau is due to the lubricant's intrinsic behavior, it does raise the question of the tribological meaning to be given to be a parameter measured in a contact.

Contrary to the first assumption, the second implies that the friction plateau originates from a complex velocity profile inside the contact. The two main profiles proposed in the literature are shear bands forming in the lubricant film [75,80] with specifically plug flow velocity profiles for some authors [81,82] or the occurrence of lubricant slip at the liquid/solid interface [83–85]. These deviations of the velocity profile from the simple case of a linear one with no slippage at the boundaries make any numerical prediction very strenuous.

Shear bands may originate from either mechanical or thermal effects [86]. Both of them have already been characterized in the bulk lubricant, outside of the contact. Mechanical shear bands have been observed by Bair and coworkers in a cell under very slow high-pressure flow [87,88]. They have been shown to develop shear band in the lubricant under isothermal conditions when it is pressurized close to its glass transition and submitted to high shear

stress [86,88]. Later, Bair and coworkers confirmed that mechanical shear bands develop when the lubricant behaves as an amorphous solid under high pressure [87].

On the other side, Bair and coworkers also observed thermally induced shear bands in the lubricant bulk under simple shear [89]. They are described as inhomogeneous and strongly depend on the thermal properties of the solid bodies: they mostly develop in the lubricant layer close to the surface of the lower thermal conductivity [86]. If they occur in a contact, they most strongly influence the value of the LSS, derived from the friction measurements. In an EHD contact, the two types of shear bands may potentially occur, but not simultaneously, depending on the operating conditions [86]. The viscosity sensitivity with temperature of lubricants has been noticed to be too low for thermal shear bands to form in a contact at high temperature. Inversely, pressures must be close to the lubricant glass transition pressure for mechanical ones to develop. In any case, both types of shear bands result from a strong coupling between the intrinsic behavior of the lubricant and the complexity of the contact.

However, none of these characterizations has been directly compared to friction results. On the other hand, some authors have attempted to measure complex velocity profiles directly in a contact. Ponjavik and coworkers [81,90] used a photo-bleached-fluorescence imaging velocimetry technique to visualize the flow of polybutene confined and sheared between a sphere and a flat surface. Their results suggested that there is a critical pressure below which the through-thickness velocity profile is close to linear. Above, the lubricant film may exhibit a plug flow. However, this experimental approach is limited to low contact pressures (< 500 MPa) and to lubricating films sufficiently thick to perform measurements. Besides, the shape of the velocity profile must be anticipated for the photobleached plug to be adjusted on the measurement.

Sperka and coworkers [82] applied a particle tracking velocimetry technique on a mixture of mineral oil with graphite nano-particles to determine the velocity profiles in an EHD contact under sliding conditions. They measured a constant velocity of the nanoparticles flowing through the film thickness, which they interpreted as evidence of a plug flow. They mentioned that this conclusion depends on the particle's distribution and migration in the through-film direction. Besides a relatively low Hertzian pressure of around 0.64 GPa was also applied.

Finally, the last assumption to explain the friction plateau-like regime is the occurrence of strong thermal effects due to the high shear rates inside the lubricant film and resulting in a significant viscosity decrease, as suggested by Crook [68,91].

Indeed, shear heating in a contact was demonstrated in several studies, mostly at high sliding speeds in highly loaded lubricated contacts [10,92]. The shear heating increase with sliding implies that there is no balance or physical process involved and consequently no true friction plateau with respect to the SRR. Friction curves may rather exhibit a plateau-like regime over a limited range of SRR due to the combination of i) the friction increase versus SRR (in the shear thinning regime II of Figure 1.7) and ii) the decrease of lubricant viscosity due to shear heating. Measurements at higher SRR inevitably leads to a friction decrease.

However, some authors showed that thermal effects cannot explain alone the decrease of friction leading to the observed apparent plateau [10,92].

To complete these experimental results, some authors have conducted numerical simulations, especially molecular dynamic (MD) simulations [93–95]. Here again, major assumptions need to be done. In particular, only a small central part of the contact and a rather thin lubricant thickness are simulated, due to the long computational times. Consequently, the complexity of the whole contact cannot be taken into account. Besides the shear rates numerically applied ($> 10^8 \text{ s}^{-1}$) are one order of magnitude higher compared to the ones experienced by the lubricant in a contact ($< 10^7 \text{ s}^{-1}$) (see insert of Figure 1.8). This is due to the very long computational time needed for a sufficiently high momentum to be exchanged between molecules, to cause shear. On the other side, the benefit of this numerical approach lies in its lack of pressure constraints and its capacity to provide detailed information at a localized level across the entirety of the simulation domain. Furthermore, it is a predictive approach as the flow is modeled from inter and intramolecular interactions parametrized through a force field including Lennard Jones and Coulomb potentials. Porra-Vazquez and coworkers [94], have simulated the flow of benzyl benzoate (BB) confined between two rough iron surfaces. They showed that velocity profiles in the confined lubricant are homogeneous and linear. Profiles do not exhibit shear localization, neither at the interface nor in the lubricant bulk, in a large range of pressures crossing the nominal glass transition. This result tends to favor the idea that the friction plateau originates from an intrinsic property of the lubricant associated with its ultimate behavior. On the other side, Xu and coworkers [95], recently ran a finite element simulation at the contact scale to predict friction. The lubricant was characterized with an Eyring model fitted on MD data.

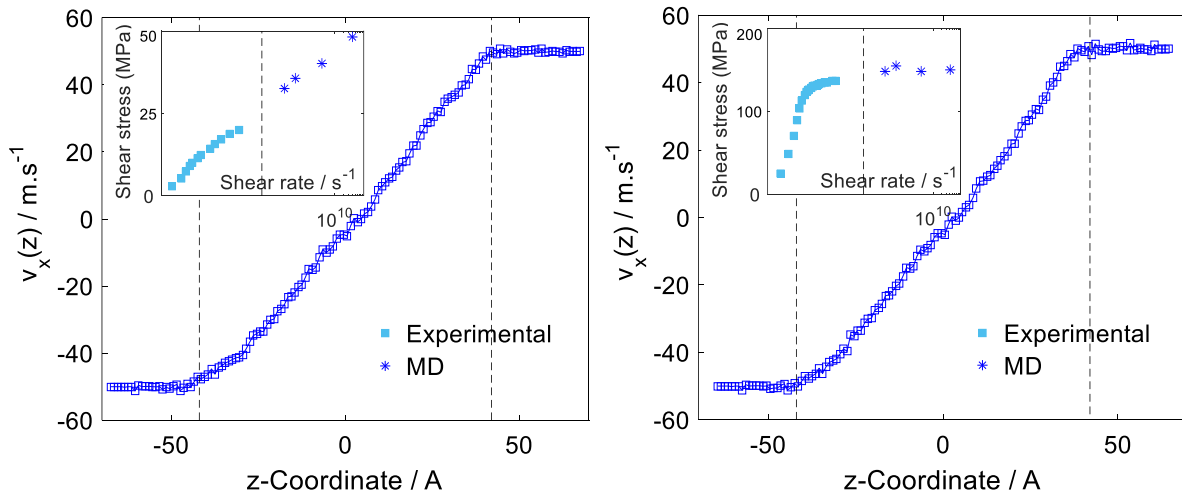


Figure 1.8 : Velocity profiles of benzyl benzoate confined between two rough iron surfaces from [94], at 313 K and 50 m.s^{-1} shear velocity. Normal pressure is 0.5 GPa for the left profile and 2 GPa for the right profile (respectively lower and higher than the nominal glass transition pressure). Dashed lines stand for the lubricant/solid interfaces. Insert: tangential stress vs shear rate, from both experiments (light blue, squares) and MD simulations (dark blue, stars).

They concluded that the heat dissipated in the contact through viscous dissipation plays a crucial role in friction. This, in turn, tends to interpret the friction plateau as a combination

between the lubricant's intrinsic behavior and the thermodynamic complexity of the whole contact.

From all these results, it appears that yet, there is no consensus to explain the origin of the friction plateau. Consequently, no constitutive equation of the lubricant can be built based on its bulk characterization and reflecting the main physical processes occurring in the contact at high pressure and high shear rate. LSS models exist in the literature, that are used traditionally to numerically simulate the friction plateau. However, they are both empirical and non-predictive. Some of them are described in [38], the most widely used being the one of Hirst and Moore [96]

$$\tau_L = \tau_{L0} + \Lambda_p P \quad (1.3)$$

Where τ_{L0} is the limiting shear stress extrapolated to atmospheric pressure and Λ_p is a dimensionless parameter, specific to the considered lubricant and which may depend on temperature, and P is the pressure. Some models include the temperature dependency in the LSS expression, for instance the one of Bair and Winer established from bulk rheological measurements [97]:

$$\tau_L = \Lambda_p(T) * P \quad \text{with} \quad \Lambda_p(T) = \Lambda_1 + \Lambda_2 T \quad (1.4)$$

Or the one from the work of Ndiaye and coworkers [98] derived from friction tests :

$$\tau_L = \tau_{L0} + \Lambda_p P + \Lambda_T T \quad (1.5)$$

where Λ_T is the limiting shear stress temperature coefficient, in $MPa^\circ C^{-1}$.

These models are fitted on experimental data exhibiting a friction plateau, they are thus only valid on the range of operating conditions on which the fit has been performed. Hence, it remains essential to characterize at the local scale the lubricant inside the contact to better understand the physical processes driving friction under extreme conditions.

To overcome these limitations and build a more relevant constitutive equation for lubricants, the first step is to identify the parameters of importance influencing the occurrence of the friction plateau.

After a brief look at friction curves obtained under various operating conditions, and without considering any of the assumptions previously mentioned, it appears that the friction plateau seems to be experimentally measurable beyond a critical pressure and to trigger beyond a critical shear rate (or SRR) [64]. This involves respectively a thermodynamical and a dynamical feature. It was previously established that the critical pressure is associated in the literature to the lubricant glass transition pressure P_g . Moreover, the critical shear rate $\dot{\gamma}_c$ is related to a characteristic time t_c . When derived from rheological measurement, t_c is assimilated to the lubricant relaxation time : $t_R \approx t_c = 1/\dot{\gamma}_c$ [99].

These two notions of glass transition and relaxation time are complex and are explored in the following section.

1.3.2 Glass transition and relaxation time

The glass transition is a transition from an amorphous (liquid) to a solid like material which does not have a defined crystalline structure. It happens when the material is cooled or pressurized rapidly. A glassy material is at non-equilibrium state of matter [7]. To define the solid state in question, it is important to note that glass transition is not a first-order phase transition [100], so that the glassy material does not have latent heat. Indeed, the amorphous microstructure of the liquid remains amorphous during and beyond the transition.

Even if this glass transition is widely studied, it is still not completely understood.

Several definitions are provided in the literature to describe it, some of them are highlighted in the following. This transition involves a strong modification in the lubricant behavior from a liquid state to a glassy state, related to a sudden increase in density, heat capacity, or thermal conductivity. To briefly describe the glassy state, it corresponds to a matter that exhibits mechanical properties close to those of a solid in regard to the observation time of the experiment [7]. Thus defined, it appears that it presents both thermodynamic and dynamic features.

To characterize the transition from a thermodynamical point of view, it is accompanied by thermodynamic peculiarities, mostly defined in relation to temperature. A common parameter used to identify the glass transition is the glass transition temperature T_g which is pressure-dependent. It is defined as the temperature below which a liquid is glassy. Equivalently, the glass transition pressure P_g is defined as the pressure above which a liquid is glassy. This variable is temperature-dependent.

T_g is commonly defined as the temperature at which the heat capacity (or thermal expansion coefficient) exhibits a steep change (*definition 1*), or, more convenient to measure, the temperature at which the sample volume evolution changes its slope [101] (*definition 2*). However, such thermodynamic data are rarely available for lubricants because they are difficult to measure and, because as with any transition process, the glass transition takes place over a range of temperature or pressure, called the “transformation range”. It is thus difficult to precisely determine it. Furthermore, data relating to the glass transition, induced by temperature depends on the sample cooling rate, which further complicates any measurement and any universal constitutive equation to be established, even if this dependency is relatively weak [31,100]. For a liquid to enter the glassy state, it must be rapidly cooled under its glass transition temperature or pressurized above its glass transition pressure, and in both cases quickly enough to prevent a possible crystallization.

In our case, the glass transition is introduced by pressure but its definition remains the same. Even if the glass transition is caused by two different processes, temperature cooling or pressure increase, which lead to the same macroscopic result, the molecular dynamic behind is different. The temperature impacts the kinetic energy of the system, whereas the pressure limits the free volume available to molecules.

Finally, the determination of the glass transition depends on the experimental technique.

The procedure used to establish the pressure-temperature dependency is crucial [102]. Consequently, instead of characterizing it through delicate thermodynamic measurements, the glass transition is rather practically determined from more empirical criteria based on

kinetic features, which are based on a characteristic time: the relaxation time t_{rel} . Indeed, it is widely accepted today that glass transition is of kinetic origin [100,103,104]. Ediger [100] points out that it corresponds to the crossing of an experimental time scale and the time scales for molecular rearrangements. Several relaxation times are described in the literature, which characterizes different physical processes. The two main ones are the structural or α or rotational relaxation, and the secondary or β relaxation [8,105].

Structural relaxation refers to a process where a condensed system, perturbed by external forces or spontaneous fluctuations, temporarily retains a state of imbalance. This state, characterized by movements like rotation or bouncing based on its degree of freedom, is upheld for a specific duration known as the structural relaxation time. This period concludes when the system returns to equilibrium [8]. The rotational relaxation time quantifies the duration required for molecular moments to regain a nearly random distribution after the removal of the external influence. Debye [106] defined the rotational relaxation time “as the time required for the moments of the molecules to revert to practically a random distribution after the removal of the impressed field”. In other words, this relaxation process represents the structural arrangement of molecules, which conditions the flow behavior of the lubricant. It is strongly dependent on both the kinetic energy of the molecules and the degree of freedom in a volume of sample come up. It is thus very sensitive to the temperature and the pressure.

It is the longest relaxation time at equilibrium, i.e. in the absence of shear [107]. It lasts for about 10^{-10} s for large sample volume of liquids but rises at few milliseconds for confined fluids [108].

Depending on the molecules, faster relaxation processes as the secondary or β relaxation processes can occur at the intramolecular scale, due to local fluctuations. They are attributed to intramolecular degrees of freedom, of either vibrational or diffusional nature [8]. They have been noticed to exhibit a simple Arrhenius temperature dependence, weaker than the structural relaxation process [8]. Santucci and coworkers [16] reported that fast relaxation processes are divided into two classes in the literature, depending on their dependence with pressure. The first class gathers the processes that do not shift toward lower frequencies when increasing the pressure, meaning no interplay with the glass transition. They are related to local motions arising from intramolecular degrees of freedom. The second class concerns the processes that do shift with a pressure increase, meaning that they are sensitive to changes in the specific volume and entropy (as the α relaxation). They are called Johari–Goldstein (JG) relaxation processes [109]. While coupling with the α relaxation at a time shorter than 10^{-6} s, they typically decouple beyond. The pronounced impact on fluid flow arises from the phenomenon of structural relaxation, serving as a representative gauge of intermolecular cooperativity. In contrast, the pertinence of beta relaxation processes, acting on the scale of individual molecules, assumes a relatively subsidiary role.

When a liquid enters the glassy state by increasing the pressure, molecular motion strongly slows down because of the presence of neighboring molecules that form a « cage » around each other [103,110,111]. The caging process hinders molecular diffusion, preventing from any structural relaxation to occur. The structural relaxation time can here be simply defined as the time needed for the molecule to escape [112]. Crossing the glass transition, this time becomes significantly longer than those found in most of fluids (of ~ 14 orders of magnitude

) [8] and to any laboratory realistic timescale. Consequently, the sample structure appears frozen, which explains the steep reduction of the expansion coefficient. Typical relaxation times measured beyond the glass transition spread over a wide range of values, between 0.1 and 1000 s for Roland [101], in the scale of minutes, hours, or more for Comez and coworkers [8], which is the scale of observation time required to observe the sample flowing. Therefore a criterion on the value of the relaxation time naturally emerged to determine glass transition [100,101,113]. The common critical duration to exceed for a liquid to become glassy is typically of 100 s [8,9].

Long relaxation times correspond to extended flow durations, resulting in elevated viscosity values. As a consequence, an equivalence criterion has been established in relation to the viscosity of the sample. The (arbitrary) high value of viscosity commonly used as a reference point of the glassy state is $10^{12} \text{ Pa}\cdot\text{s}$ [100,101,114] (*definition 3*).

However, care must be taken as this value is arbitrary and seems to be more appropriate for molten minerals [115] than organic liquids [105]. Some authors consider that the glass viscosity μ_g is much smaller, usually in the range of $[10^7 - 10^{10}] \text{ Pa}\cdot\text{s}$ [116,117]. Schweyer [118] found $\mu_g = 10^8 \text{ Pa}\cdot\text{s}$ for asphalts under pressure. Measurements of viscosity at ambient pressure up to $3.7 \times 10^8 \text{ Pa}\cdot\text{s}$ from the University of Chicago [119] compared with glass transition measurements by transient hot-wire at Umea University [39] have led to a glass transition viscosity of $\mu_g = 1.23 \times 10^7 \text{ Pa}\cdot\text{s}$ for squalane, for an observation time of 0.3 seconds.

It is worth noting that the description of the relaxation processes has so far been established for a fluid at rest. In this context, a pressure increase leads to an increase of the glass transition temperature [120] and to an increase of the α relaxation time [121]. The question of the role of shear may arise. Indeed in a regime of rheo-dependent behavior of a fluid, high shear rates can increase the degree of order of its microstructure and may influence the transition point [122].

Due to the extensive impact of glass transition on a sample's behavior, several physical and mechanical parameters can be assessed to determine the occurrence of this transition. These measurements can serve to characterize the sample's thermodynamic properties, including entropy, free volume, heat capacity, and expansion coefficient [123,124]. Additionally, they can assist in assessing the sample's rheological properties, encompassing dielectric constants, mechanical models, and viscosity [125].

One current instrumental method is the Differential Scanning Calorimetry (DSC) [126] which is used for thermal analysis, focusing on tracking alterations in the physical characteristics of a sample in relation to temperature over time. In essence, this apparatus serves as a thermal analysis tool, uncovering both the temperature and the heat exchange linked to transitions within a material [126].

Dielectric spectroscopy is another powerful tool to study the dynamic of fluids [127]. Measurements are carried out on a sample using two spaced electrodes. The initial sinusoidal voltage is compared to the measured response [128]. This leads to deriving the material

permittivity frequency response of the material. The frequency-dependent permittivity provides information about glass transition.

The relaxation time and the glass transition temperature can be detected through Dynamic Mechanical Analysis (or DMA) [125,129]. It is based on the application of stress oscillations on a viscous sample. The resulting time-dependent behavior of the sample is analyzed to derive the real (in phase) and imaginary (out of phase) parts of its response.

However, those tools either cannot be performed on a liquid under high pressure or be coupled to our tribology set-up.

Inelastic light scattering shows some interest regarding our problematic. In the literature, spectroscopic methods such as Raman scattering or Brillouin spectroscopy appear as promising tools. Those methods require a laser and a transparent material. They both measured specific peaks that are shifted from the initial laser wavelength, generally found at the center of the spectrum. Raman scattering contains various information on molecules in a liquid. More specifically when the analysis is done at near low-frequency, so very close to the laser line peak, Raman scattering shows an interesting feature called the Boson peak that only exists in glasses. It is an excess of density of vibration modes according to reference [130], which creates an additional peak on the normalized density of states of the glassy sample. This peak is also pressure-dependent [131]. Unfortunately, the Raman spectrometer present at LaMCoS does not allow such measurements.

This method can be implemented in a tribology set-up. Nevertheless, additional data such as relaxation time and modulus can not be derived from Raman spectroscopy.

However, among the spectroscopic methods, Brillouin spectroscopy stands out as a particularly promising tool for our study. Brillouin spectroscopy, unlike Raman scattering, offers the advantage of measuring the sound velocity propagation within the sample, which is strongly affected by the structural relaxation process [8]. Consequently, our attention pivots toward the examination of the alpha relaxation process.

Moreover, longitudinal modulus and relaxation time can be derived from Brillouin spectra.

The next part is dedicated to the Brillouin spectroscopy characterization.

1.4 Brillouin light scattering

1.4.1 Characterization of the glass transition

Brillouin spectroscopy has been chosen to conduct experiments inside a lubricated mechanical contact (what we will refer later to « *in situ* » measurements) and a high-pressure device. It has the advantage of being non-invasive and non-destructive (provided that the laser power is carefully regulated to avoid impacting the properties of the sample)). The technique will be extensively introduced and detailed in Chapter 2. Below, the literature on Brillouin spectroscopy, focusing on lubricant characterization and glass transition determination, will be presented.

Several studies have been conducted in the literature on the determination of the glass transition by Brillouin spectroscopy. Most of them have been carried out at atmospheric pressure and by varying the sample temperature [11–15,17,18,132] and only few of them on the influence of pressure [19–21]. It is indeed an experimental challenge to apply and maintain a sample at a given high pressure.

This experimental technique directly measures acoustic waves naturally propagating in a sample. The Brillouin spectrum illustrated in Figure 1.9 exhibits peaks on each side of the Rayleigh central peak, whose frequency shift f_b (or its equivalent, the angular frequency shift ω_b) and linewidth Γ_b (FWHM) are related to the constitutive parameters of the sample.

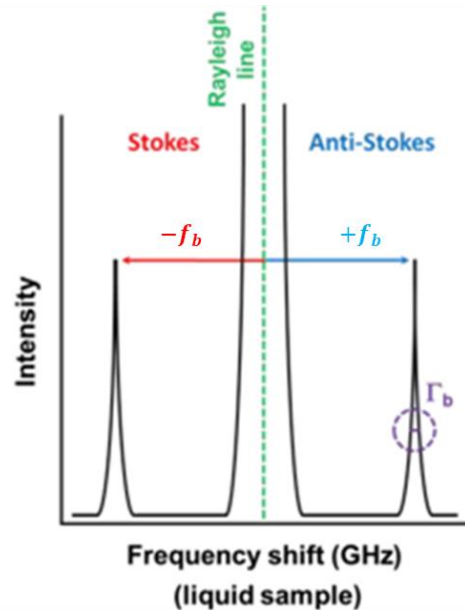


Figure 1.9 : Schematic representation of Brillouin spectra composed of the laser central part called Rayleigh and the light-matter interaction peaks from Stokes and anti-Stokes processes [133].

It was thus possible to derive crucial parameters from the spectra such as the sound velocity and the kinematic viscosity for various fluids: m-toluidine [24], ortoterphenyl and diglycidyl ether of bisphenol-A [25] polybutadiene [18], glycerol [11,13,19] in Figure 1.10, polyethylene [25] in Figure 1.11 and polymethylacrylate [17].

Two other parameters can be extracted such as $M(\omega)$ the frequency-dependent complex modulus of elasticity [11,34,134–136], and the relaxation time [11,13–16]. It must be noted that such measurements are performed at very high effective frequencies, from a few GHz to few tens of GHz for most of the liquids [11].

Ng et al. [22] and Kim et al. [23] identified the glass transition of polyethylene probed by Brillouin light scattering as the slope inflection point in the frequency shift and the FWHM versus temperature (in Figure 1.10). They attributed this inflection point to the onset of long-range coordinated molecular motion near the transition region.

As develop in Chapter 2, the frequency shift f_b and the FWHM Γ_b of the side peaks are associated to the sound velocity and the kinematic viscosity of the sample. The later parameter is defined as the ratio of the fluid longitudinal viscosity to the density.

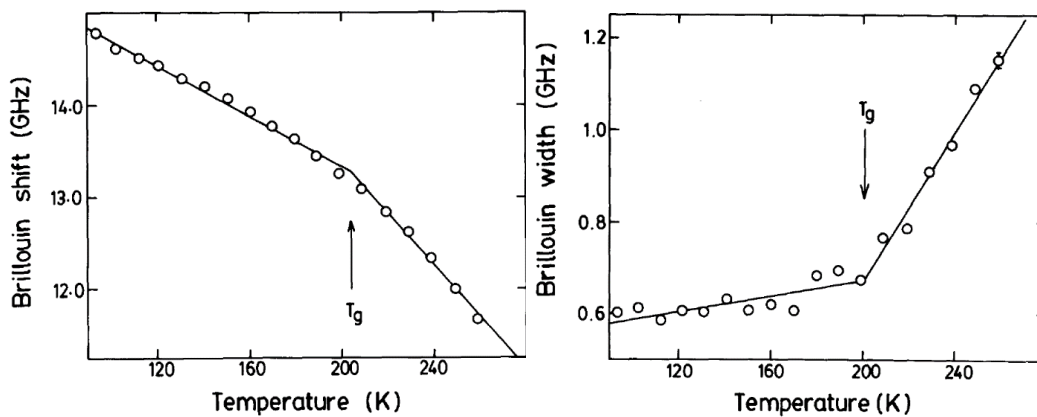


Figure 1.10 : Brillouin shift (left) and width (right) of polyethylene as a function of temperature. The lines are the least square fit. T_g is the glass transition temperature, from [22].

Similarly, other authors [13,24,25] identified the glass transition of several samples. Among them glycerol in Figure 1.11, polybutadiene (PB) from the change in the sound velocity slope (at about 187 K on Figure 1.11 for the glycerol).

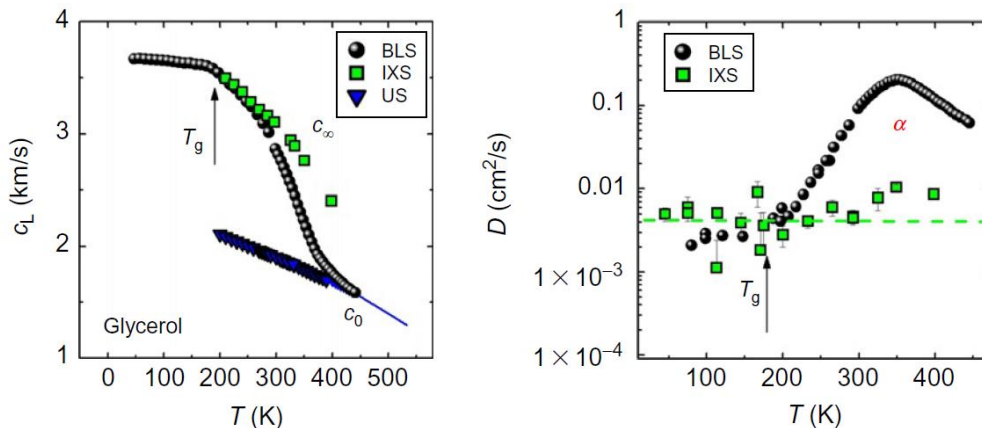


Figure 1.11 : Apparent longitudinal sound velocity (left) and kinematic viscosity $D = \eta_L / \rho(P, T)$ (right), where η_L is the longitudinal viscosity and $\rho(P, T)$ the density determined by Brillouin techniques for glycerol [13] as a function of temperature.

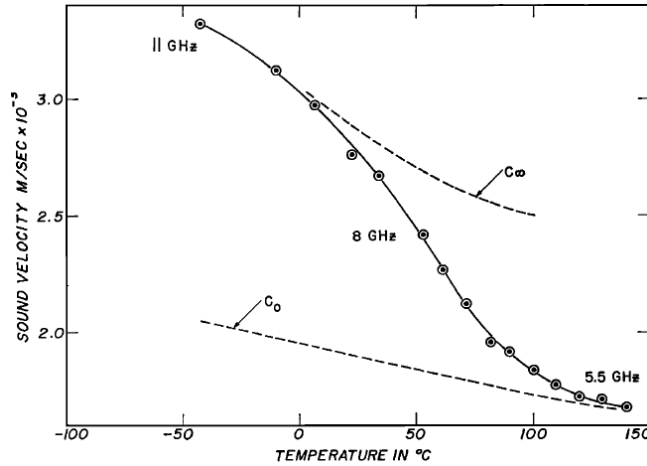


Figure 1.12: Hypersound velocity as a function of temperature in glycerol, from [11].

One way to understand the glass transition is by examining the acoustic properties of the material, such as the sound velocity and attenuation. In Figure 1.11, the sound velocity exhibits a characteristic "S" shape as a function of temperature. This curve is bounded by the limiting high (unrelaxed, c_∞) and low (relaxed, c_0) frequency values of sound velocity, taken by XPS and ultrasound measurements respectively, which is typical of the structural relaxation as highlighted by Comez et al. [8,13]. This is accompanied by a well-defined maximum of the absorption (or attenuation), directly related to the linewidth of the Brillouin peaks and thus to the longitudinal kinematic viscosity.

This maximum occurs when the sample's relaxation time t_{rel} and the characteristic frequency of acoustic excitations ω_b (with $\omega_b = 2\pi f_b$) match each other, a condition given by the parameter $\omega_b t_{rel} = 1$, as shown in Figures 1.13 and 1.14 [11]. The parameter $\omega_b t_{rel}$ enables to take into account both the sample frequency dependence through ω_b and its thermodynamic dependence through $t_{rel}(T, P)$. Pinnow et al. [11], proposed that this parameter reflects the degree of relaxation of the sample and can be used to understand the energy transfers that occur between different modes of density fluctuations in the sample.

To make an analogy it can be assimilated to the Weissenberg number, a dimensionless parameter used to characterize the macroscopic behavior of a fluid under shear [137]. It is defined as the product of the shear rate by the relaxation time of the fluid.

This analysis raises the question of the glass transition identification from sound velocity measurements. Indeed, data derived from Brillouin spectra (sound velocity and kinematic viscosity) are compared to a glass transition temperature T_g of 187 K which is used for the glycerol in [13] and [8], which comes from [138] and corresponds to the value measured by calorimetry techniques. This value is close to the viscosimetric glass-transition temperature of 190 K [139], probably measured at very low frequency. Then it is not clear whether T_g can be directly compared to the sound velocity measured in Brillouin experiments at high frequency, as in Figure 1.11 left. The occurrence of a glass transition on this figure should rather be associated with the change of slope of the sound velocity or with the maximum linewidth. This would correspond in Figure 1.11 right to a glass transition temperature

around 350 K, thus to a sound velocity close to the end of the S shape and to the relaxed c_0 value [11].

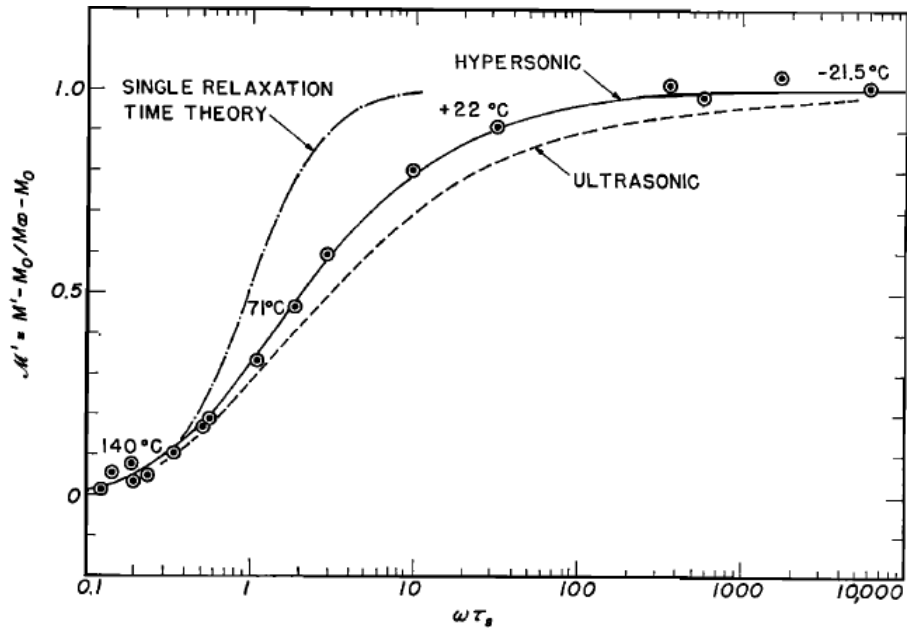


Figure 1.13: Reduced plot of the real part of the longitudinal modulus in glycerol. The dashed line was measured ultrasonically at a frequency of 22 MHz, from [11].

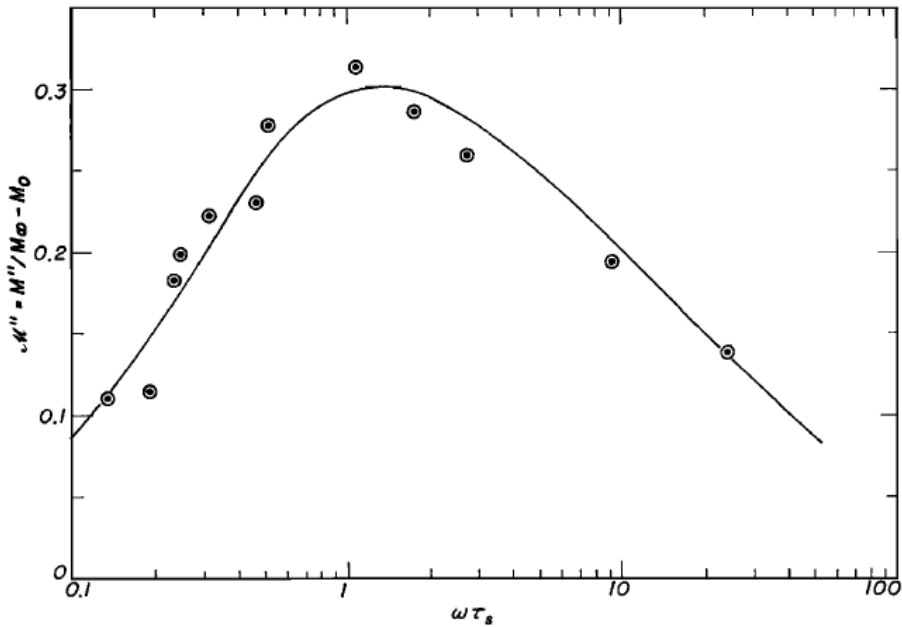


Figure 1.14 : Reduced plot of the imaginary part of the longitudinal modulus of glycerol, from [11].

According to Comez and coworkers [8], a sample at rest in a liquid regime corresponding to $T < T_g$, leading to small values of t_{rel} (and consequently of $\omega_b t_{rel} \ll 1$), the structural relaxation occurs at frequencies lower than the range of frequencies probed in the Brillouin spectrum (GHz). Consequently, it does not contribute significantly to the sample behavior. On the other side, beyond the transition, the rapid slowdown of the sample dynamic freezes the structural relaxation and the Brillouin spectra mainly provide information on the fast

relaxations processes. Indeed, these latter experience a less drastic variation with glass transition due to their small-scale motion, and they survive through the glass transition.

1.4.2 Brillouin light spectroscopy characterization of lubricants

Brillouin spectroscopy has already been used a few decades ago to measure the sound velocity in bulk lubricants at rest versus temperature and pressure. Typically, pressure was generally applied to the lubricant using a high-pressure cell, as detailed described in Chapter 3 of this work. The lubricants tested were of various natures including model fluids (benzyl benzoate [29] ethyl benzoate [12], 5P4E or m-bis (m-phenoxy) benzene [26,28,31] and [30]), pure or blended naphthenic base oil [31], TN68 [27,28], hydrocarbons (MCS-1218 [140]), synthetic oils (PA068 [27,28], DOS Di(2-ethylhexyl) sebacate [21]). The analysis on Brillouin spectra using the frequency shifts and linewidth of the peaks [21], in turn, allowed the determination of sound velocity [12,29,31] in the probed lubricants across a spectrum of temperature and pressure conditions. Data collected have also enabled to derive fluid properties as lubricant density, refractive index and shear modulus [26,28], as well as relaxation time [29,30].

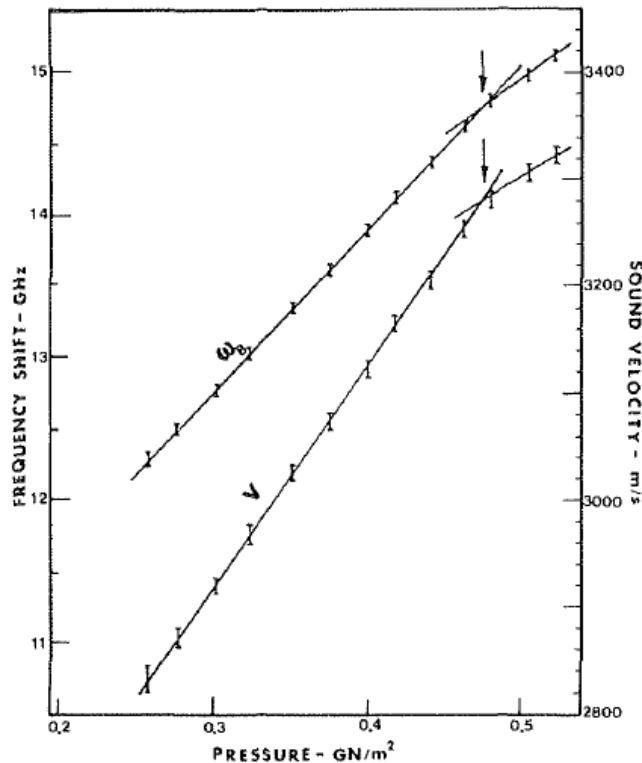


Figure 1.15 : Variation of frequency shift and sound velocity with pressure for a naphthenic base oil at 24°C, from [31]. Arrows on the graph indicate the glass transition pressure.

Alsaad and coworkers [31] studied a naphthenic base oil under varying pressure and temperature conditions. They showed that the sound velocity increases with pressure (for

pressures up to 0.69 GPa) and decreases with temperature (in the range [20°C – 65°C]) (see Figure 1.15 and Figure 1.16). The lubricant glass transition was identified from a change in the slope of the sound velocity versus either pressure or temperature. It was identified at 0.475 GPa for the naphthenic base oil at room temperature, which was in good agreement with previous glass transition measurements from PVT technique (pressure, volume, and temperature) conducted independently. This pressure being in the range of pressures conventionally reached in the EHD regime, it was concluded that the glass transition of this lubricant was likely to occur in a contact.

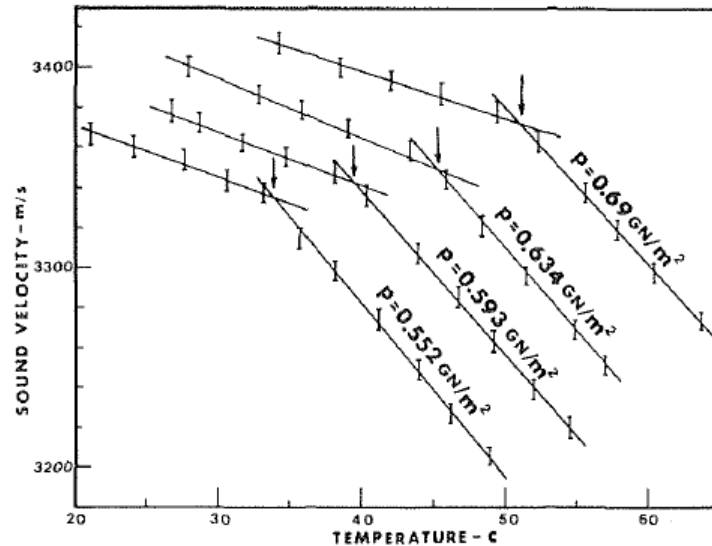


Figure 1.16 : Variation sound velocity with temperature at different constant pressures for a naphthenic oil, from [31]. Arrows indicate the glass transition temperature.

From these data sets, a phase diagram was extracted, reported in Figure 1.17. The glass transition temperature was noticed to shift linearly to higher values with an increasing pressure (over the range of pressure tested). Finally, the loading history of the fluid seemed to only slightly influence the conditions for the occurrence of the glass transition.

Bezot and coworkers estimated the relaxation time of lubricants from the line shape of the spectra, defined as $\Gamma_b = (2\pi t_{rel})^{-1}$, versus temperature, measured in a Helma scattering cell [29]. It has been shown to evolve with temperature similar to the viscosity derived from ultrasonic measurements. Ten years later, Bezot and coworkers [29] anticipate from their results on 5P4E at relatively low pressure ($P \leq 0.3$ GPa) and high temperature ($T \geq 0^\circ\text{C}$) that “in the contact zone, the liquid has no time enough to be in “structural equilibrium” with the other pressure and temperature parameters” [30]. The lubricant maybe assumed to behave like a solid, within the experimental time scale.

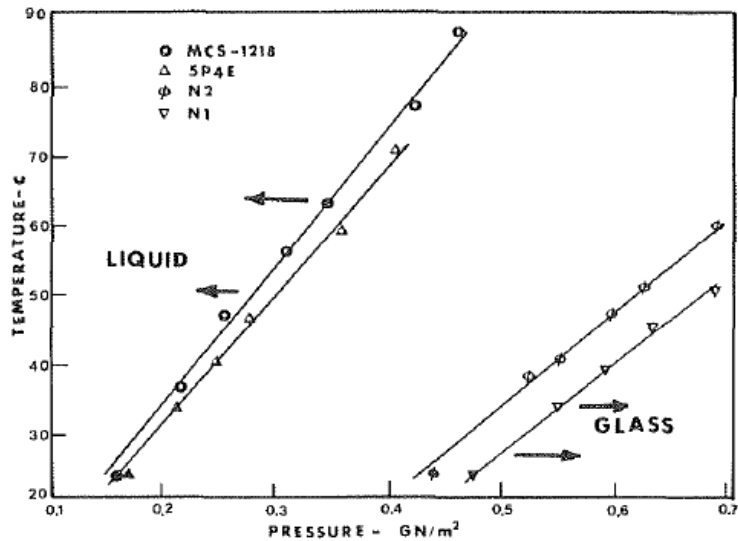


Figure 1.17 : Transition diagram for various fluids (a cycloaliphatic hydrocarbon MCS-1218, a polyphenyl ether 5P4E, a naphthenic base oil N1 and a blended naphthenic oil (N1 blended with 2.2 percent high molecular weight polybutane) N2. Glassy state is to the right and below the transition lines and the liquid state is to left and above the transition lines. From [31].

It must be kept in mind that all these conclusions were drawn on measurements performed on bulk lubricant at rest. Based on the information available, they have not been directly correlated to friction data and may thus not be representative of the lubricant tribological behavior.

A recent study on benzyl benzoate [41] partly filled this gap. Preliminary tests performed with a Fabry-Pérot interferometer on a sample at rest in a high-pressure cell and friction measurements in a rolling-sliding contact have been correlated on a large range of pressures.

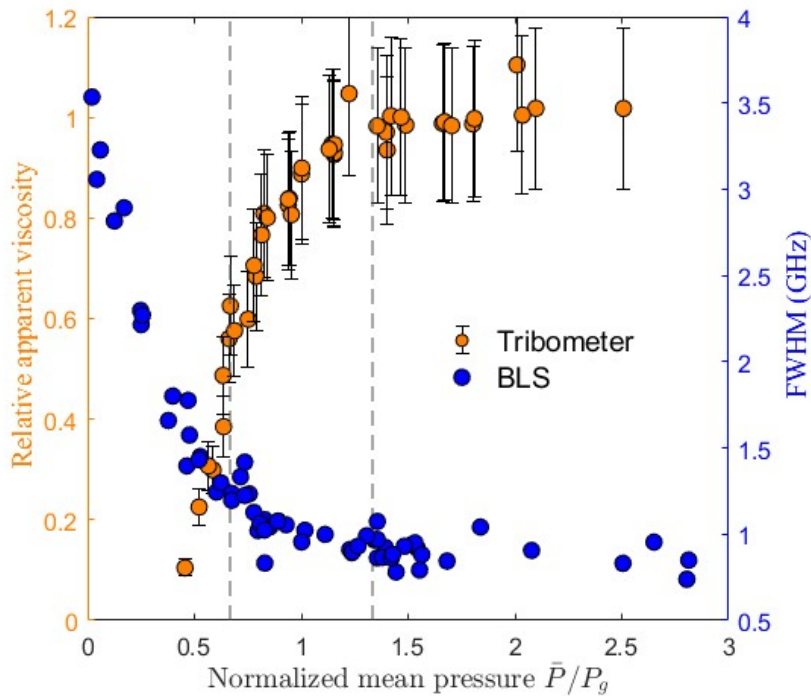


Figure 1.18 : Relative apparent viscosity of benzyl benzoate from friction tests (left axis) and width of Brillouin spectra at rest (right axis) vs. normalized mean pressure(from [41]).

The pressure considered in the contact is the mean pressure \bar{P} , defined as 2/3 of the Hertzian pressure. The line width of the inelastic peaks on the Brillouin spectra (in blue in Figure 1.18) have shown a transition in the lubricant behavior versus pressure in the same range of pressures than an apparent viscosity derived from friction data (in orange in Figure 1.18). This approach has also been validated by molecular dynamic (or MD) simulations [94]. It supports the assumption that the occurrence of a friction plateau can be correlated with the lubricant glass transition.

However, viscosities derived from molecular dynamic simulations [94] ($< 10^3$ Pa.s) are far lower than the arbitrary value of or close to 10^{12} Pa.s which would be expected for lubricants in a glassy state (see 1.3.2). It raises the question of the influence of the strong dynamic experienced by the lubricant in the contact.

Unfortunately, the influence of large shear deformation on the onset of glass transition is rarely explored or discussed the literature. Way and coworkers [141] concluded that applying shear to metallic glasses during their glass transition (versus temperature) changed their behavior from strong to fragile, concept introduced by Angell [142]. This was attributed to the destruction of medium-range and short-range orders in the liquid state. However, the shear rate experienced in this work in [141] (< 300 s $^{-1}$) was far lower than the one experienced by the lubricant in a contact (up to 10^7 s $^{-1}$). Besides, no experimental set-up is representative of the complexity of the contact described in Section 2.2. Therefore, even if these uncoupled approaches can provide essential data to understand the influence of each parameter on the behavior of lubricants, they cannot replace in situ measurements to explain the origin of the friction plateau.

1.5 Outlines of the work

The aim of this work is to gain a better understanding of the behavior of a lubricant in a highly loaded contacts, with the global objective to identify the physical processes driving friction in a lubricated contact and ultimately to propose predictive constitutive equations for lubricants to reduce friction.

The extreme conditions studied here are those found in the EHD regime. In this regime, friction is due to the lubricant shearing, which essentially depends essentially on pressure, temperature, and shear rate. The strategy adopted here is thus to uncouple these parameters in order to understand the influence of each of them.

The experimental tool chosen to characterize lubricants is the Brillouin Light Spectroscopy (BLS), whose theoretical background is extensively described in Chapter 2. The experimental set-ups used during the work are described in Chapter 3. Indeed, two technologies were used. First, a Fabry-Pérot Tandem (TFP-1) interferometer was provided by the Light and Matter Institute (ILM). Secondly, a Virtually Image Phase Array (VIPA) interferometer was installed at LaMCoS. It was designed to couple with either a rheometer, a tribometer or a high-pressure Diamond Anvill Cell (DAC). This set-up was then extensively described and tested in Chapter

4 in term of reliability, stability, accuracy, software and fitting procedure, by comparing its results to those obtained with Fabry-Pérot technology.

The next step was the sample characterization, presented in Chapter 5. The whole study is carried out on 3 fluids chosen for their different behaviors: an hydrocarbon (squalane), a model fluid (benzyl benzoate) and a reference fluid (glycerol), already widely studied in the literature. Thus, the conclusions of the work can be applied to a wide range of fluids used in industry. Pressure and temperature define the thermodynamic conditions applied to the fluid. They were applied to lubricants at rest and varied to highlight the influence of each of them. For this, Brillouin spectroscopy measurements were carried out on a sample in a high-pressure cell which allows both pressure and temperature to be controlled in a finite volume of fluid. Pressure varied from atmospheric pressure to several GPa and temperature from room temperature to 60°C. The results led to identify the nominal conditions of glass transition to occur for each fluid. It was also possible to derive rheological parameters of the fluids from Brillouin spectra, as described in Chapter 2.

However, to go further in the analysis, the density of the fluid versus pressure and temperature was required. For now, we used density models fitted on high-pressure density measurements from the literature (see Chapter 4) as a first approach. However, it is planned as a perspective of this project to conduct Brillouin light scattering measurements in a platelet geometry (see § 2.2.3). This will make possible to measure: i) the transverse waves (which will confirm the appearance of the glass transition) and ii) the refractive index of the material, leading to its density by the Lorentz-Lorenz law.

To complete this characterization in pressure and temperature, the Brillouin spectroscopy setup has been coupled with a rheometer, which allows to characterize the influence of shear rate on the Brillouin response of the fluid (see appendix E). The large sample volume lubricants were tested at atmospheric pressure and at temperatures varying from -10°C to 100°C, and over a range of shear rates up to 10,000 s⁻¹.

The next step of this project will consist in coupling the Brillouin spectroscopy setup with a tribometer to directly probe the lubricant inside the contact. The normal load, the thermostat of the oil tank and the relative velocity of the solid bodies will be widely varied to reach all friction regimes. In each case, Brillouin light scattering spectra will be collected at various positions in the contact area in order to draw a full picture of the lubricant state in the whole contact zone. Friction will be measured simultaneously to directly correlate friction results with BLS data.

2. Introduction to Brillouin spectroscopy

Table of content

2.1	HISTORY AND APPLICATIONS OF BRILLOUIN LIGHT SCATTERING SPECTROSCOPY	75
2.2	VIBRATIONAL SPECTROSCOPY	77
2.1.1	ELECTROMAGNETIC (EM) WAVES	77
2.1.2.	INTRODUCTION TO VIBRATIONS AND PHONONS.....	79
2.1.3.	INELASTIC LIGHT SPECTROSCOPY.....	81
2.2.	BRILLOUIN SCATTERING SPECTROSCOPY	83
2.2.1.	PHOTONS AND PHONONS INTERACTION, THE SCATTERING PROCESS AND GEOMETRY ...	83
2.2.2	BRILLOUIN SPECTRA	86
2.2.3	SCATTERING GEOMETRY.....	88
2.2.4	LIGHT POLARIZATION ON THE BRILLOUIN SPECTRA.....	89
2.3	FROM VISCOELASTIC PROPERTIES OF MATTER TO THE INELASTIC BRILLOUIN	
	SPECTRUM	90
2.3.1	SIMPLE MODEL WITHOUT DAMPING.....	90
2.3.2	LINEARIZED HYDRODYNAMIC EQUATIONS WITH DAMPING.....	92
2.3.3	THE GENERALIZED HYDRODYNAMIC EQUATION FOR SIMPLE FLUIDS	92
2.3.4	THE GENERALIZED HYDRODYNAMIC EQUATION FOR VISCOELASTIC FLUIDS	93
2.4	DENSITY EQUATION FOR DIFFERENT REGIMES.....	94
2.4.1	RELAXED REGIME $\omega t_{rel} \ll 1$ BY DAMPING HARMONIC OSCILLATOR MODEL (DHO).....	96
2.4.2	FOR $\omega t_{rel} \sim 1$ DEBYE AND COLE DAVIDSON MODEL NEAR THE GLASS TRANSITION	97
2.4.3.	FOR $\omega t_{rel} \gg 1$ THE VOIGT MODEL.....	98
2.5.	LOCAL SPECTRUM ANALYSIS	98
2.6.	CONCLUSION	100

This chapter provides an overview of vibrational spectroscopy and Brillouin scattering. The chapter starts with the fundamental concepts of electromagnetism and vibration. Then a section is dedicated to electromagnetic waves interaction with acoustic waves, the underlying principles governing inelastic light spectroscopy.

From there, the focus shifts to Brillouin scattering spectroscopy and the interaction between photons and phonons. The chapter introduces essential parameters from a Brillouin spectrum, exploring their dependence on various factors, including geometry scattering and light polarization.

As the chapter progresses, theoretical models are introduced, ranging from simple, undamped systems to complex viscoelastic fluids, providing insights into material behavior across different spectral regimes. These models encompass damping harmonic oscillator models, generalized hydrodynamic equations, and notable models applicable to systems nearing the glass transition.

This section of the chapter is followed by methods for local spectrum analysis, allowing for the identification of spectral characteristics specific to different materials. Additionally, the concept of relaxation time in a deeper analysis is introduced, offering valuable parameters for understanding dynamic material behavior. At the end of the chapter, an examination of advanced spectral analysis techniques for the extraction of relaxation times is presented from a publication.

2.1 History and applications of Brillouin Light Scattering spectroscopy

The Brillouin spectroscopy technique can measure the stiffness of the material scanned [143]. It is based on constructive interferences between an incident monochromatic light (photons) and propagating thermodynamic waves (phonons) existing in the sample. They involve inhomogeneities in the sample which are due to the change in the position of atoms around their equilibrium position. The resulting acoustic waves carry information about the sample's physical characteristics and mechanical properties such as the sound velocity propagating inside the sample and acoustic attenuation. Brillouin spectroscopy is a powerful technique due to its non-invasive and non-destructive nature for materials. It enables measurements on samples either at rest or flowing, as long as the incident light is focused on transparent samples. It is already used in various application areas, as reported in Figure 2.1 and described below.

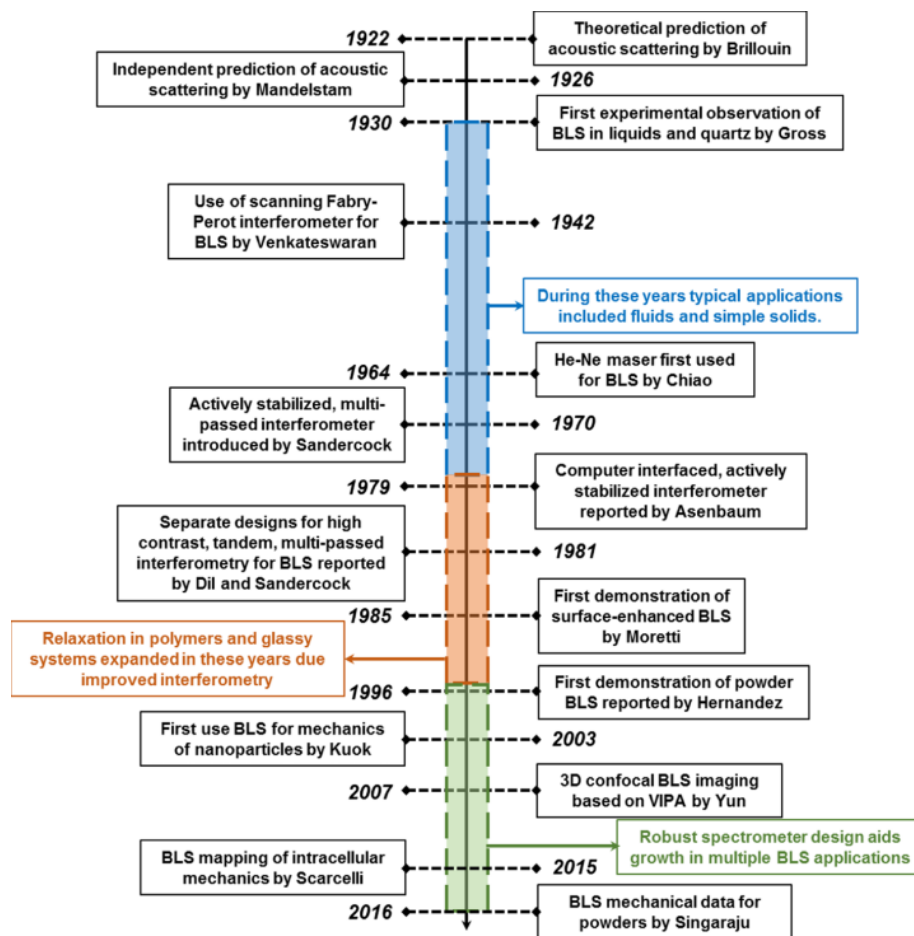


Figure 2.1 : Timeline of Brillouin theory up to its technological development with the Tandem Fabry-Pérot and VIPA-based interferometer. Other dates reported are pioneer studies of different research fields [133].

The light scattered by a sample is collected and analyzed with a high-resolution and high-contrast spectrometer. One well-known spectrometer was developed by Dr. Sandercock from 1970 to 1980 [42,43]. The multi-pass scanning stages Fabry-Pérot Tandem interferometer was first used for condensed matter and phase transition studies [144]. The high contrast provided by the device allows a weak signal measurement and opens the possibility of opaque surface and thin film characterization [145].

In recent years, Brillouin spectroscopy has evolved toward mechanical imaging [146].

Recently, progress in Brillouin microscopy became an emerging tool for mechanobiology. In biological samples, Brillouin spectroscopy is used to bypass the problem of sample fragility which makes difficult any direct contact measurements [147]. Thus, the real-time biomechanical evolution of living cells can be tracked and in situ measurements provide important results to understand the complexity of the interconnected cellular mechanism [33]. In the medical field, this technique has been used to understand the underlying process of tumor growth and drug resistance. Brillouin spectroscopy made it possible to map tumor cells from their viscoelastic mechanical properties [149]. This has been possible with the apparition of a new generation of spectrometers called Virtually Imaged Phased Array etalon or shortly VIPA. It is based on a non-scanning stage using a solid glass or silica that separates wavelengths in one direction. VIPA Brillouin spectroscopy reduces the acquisition time tremendously making this technique particularly suitable for living cell and many more medical applications.

In material science, Brillouin spectroscopy is used to monitor the matter's properties under stress using a simple backscattering configuration. For instance, it was used to determine the elastic modulus of minerals such as diamonds [150], or the viscoelastic properties of materials like glycerol [13] and polymers [151].

In geoscience, seismic propagation is used to study the earth's internal structure, in terms of composition or temperature. As seismic waves are going deeper inside the planet, their prediction and interpretation become more and more difficult. One reason is the increase in mineral density and the temperature change. Brillouin spectroscopy technique enables to study the elastic properties of minerals contained in the Earth's mantle [152]. It helps to understand the complex dynamics of high pressure and temperature of seismic propagation. The complex dynamics of high-pressure and temperature experiments are performed by a Diamond Anvil Cell (DAC) combined with Brillouin spectroscopy and X-ray diffraction [153]. Brillouin spectroscopy gives information about the sound velocity. The density is accessible by Brillouin spectroscopy only when two scattering geometries, the backscattering and an angular geometry, are combined.

Brillouin spectroscopy is of growing interest for lubrication. Several studies provide lubricant rheological characterization to complete tribological data. Viscoelastic properties of 5P4E [30], PA068, and TN68 [28], Di(2-ethylhexyl) sebacate [21], and their pressure and temperature dependencies reveal the potential of this technique for industrial applications.

In the case of ElastoHydrodynamic Lubrication (EHL) studied in this work, the extreme conditions of pressure and temperature applied to the lubricant have already been probed on

benzyl benzoate [41] However, the impact of shear on the physical properties is still understudied.

This chapter focuses on the physical basis of Brillouin spectroscopy and explore how it can contribute to characterizing the behavior of probed samples.

2.2 Vibrational spectroscopy

2.1.1 Electromagnetic (EM) waves

This part is dedicated to the understanding of what is light and specifically a laser source and how it propagates and interacts with matter.

Brillouin spectroscopy technique requires a monochromatic, coherent, and polarized incident light source, called LASER. It possesses a controlled wavelength λ_0 (in nm), a direction of propagation and a particular power distribution. To understand the underlying principles behind a laser, it is essential to grasp the foundational framework of electromagnetism, given by Maxwell's equations.

Maxwell's equations describe light as an electromagnetic monochromatic plane wave. The wave equation of a propagative electric wave in free space [154] is described by:

$$\nabla^2 \vec{E} - \mu_0 \epsilon_0 \frac{\partial^2 \vec{E}}{\partial t^2} = \vec{0} \quad (2.1)$$

where \vec{E} is the electrical field, μ_0 is called the permeability in $[m \text{ kg } S^{-2} A^{-2}]$ or $[N A^{-2}]$ and ϵ_0 in $[F m^{-1}]$ is the permittivity.

The solution of this wave equation is written as:

$$\vec{E}(\vec{r}, t) = \vec{A}_0 \cos(\vec{k} \cdot \vec{r} - \omega t + \phi) \quad (2.2)$$

where \vec{A}_0 is a constant vector, ϕ is the phase angle. The plane wave propagates along the wave vector \vec{k} and the position vector $\vec{r} = x\hat{x} + y\hat{y} + z\hat{z}$ ($\hat{x}, \hat{y}, \hat{z}$ unit vectors). The angular frequency ω is defined as k the wave number defined below and c the speed of light: $\omega = k * c = k / \sqrt{\mu_0 \epsilon_0}$.

When a plane wave propagates in a dielectric medium that is considered isotropic and homogeneous, the plane wave solution of equation (2.2) is written in the complex form:

$$\vec{E}(\vec{r}, t) = \vec{E}_0 e^{i(\vec{k} \cdot \vec{r} - \omega t)} \quad (2.3)$$

Where \vec{E}_0 contained the phase ϕ in equation 2.2.

One key parameter is the wave vector \vec{k} which contains information about both the wavelength and the direction of propagation of the wave. It is inversely proportional to the

wavelength in the vacuum. The scalar of the wave vector is called the wave number k with $|\vec{k}| = k = \omega/c$, expressed in $rad * m^{-1}$. One important relation for the propagating light wave is the dispersion relation that links its velocity c to the angular frequency in free space ω such as:

$$k = \frac{\omega}{c} = \frac{2\pi}{\lambda_0} \quad (2.4)$$

where λ_0 is the light wavelength in vacuum and c is the light velocity in vacuum ($c = 3.10^8 m.s^{-1}$). The angular frequency ω is linked to the frequency f by:

$$\omega = 2\pi f \quad (2.5)$$

When the incident electromagnetic light wave propagates in a medium of refractive index n , n must be considered in (equation 2.4). In this medium, the wavelength is expressed as $\lambda \equiv \frac{\lambda_0}{n}$. From equation 2.4, the velocity of propagation, known as phase velocity v_p becomes:

$$k_x = \frac{2\pi}{\lambda} = \frac{\omega_x}{v_p} \quad (2.6)$$

k_x and ω_x depend on the medium where the light propagates: k_i and ω_i for the incident light (before its interaction with matter), k_s and ω_s for the scattered light (after interaction). Equation (2.3)

For a light wave propagating at $c = 3.10^8 ms^{-1}$, the conversion between spatial and temporal frequencies is straightforward. Thus, the wave propagation velocity:

f (Hz) = $(2\pi)^{-1} k(cm^{-1}) * c(cm s^{-1})$ or f (GHz) = $(2\pi)^{-1} k(m^{-1}) * c(m s^{-1})$. So for a $1 cm^{-1}$ the frequency in GHz is 30 GHz. This data will be used in Chapter 3 to calculate the setup free spectral range.

As mentioned at the beginning of this chapter, the laser used during experiment is vertically polarized, which essentially describes the orientation of the electric field vector of an electromagnetic wave. The laser polarization is linear meaning the electric field oscillates along a single fixed direction as shown in Figure 2.2 [154].

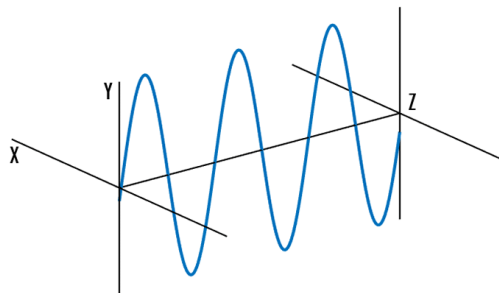


Figure 2.2: Representation of vertical polarization in the Y-Z plan of the electrical field propagating in the Z direction.

The light polarization in Brillouin spectroscopy is an essential feature for spectral analysis.

Lasers are also characterized by a Gaussian or bell-shaped intensity distribution and it is referred to as TEM_{00} which stands for Transverse Electro-Magnetic [155]. This is the fundamental mode (TEM_{00} shape in Figure 2.2 left). This light shape provides a high-intensity and high-resolution light making the resulting Brillouin spectra easy to read.

In the case of VIPA Brillouin setup, the light is coupled to the optical microscope using single mode optical fibers. The light propagating modes in optical fibers are called LP modes, in the figure, the LP_{01} reference the fundamental mode.

Indeed, using a few modes fiber instead of single mode fiber could generate a Brillouin signal presented in Figure 2.3 right side. The fiber Brillouin signal could overlap our sample Brillouin signal which appears in the same range of frequencies. It is therefore essential that the light propagates inside the fiber with maximum efficiency, with less dispersion mode, and keeps the integrity of the initial signal.

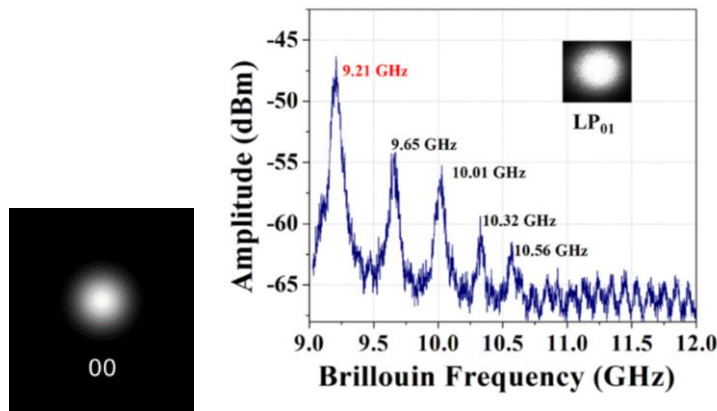


Figure 2.3: (Left) Laser beam shape of TEM_{00} modes. (Right) Brillouin spectra of a few mode fibre at 1055 nm [156]

This part was presenting the basics of optics that will used for Brillouin spectroscopy.

2.1.2. Introduction to vibrations and phonons

Acoustic waves naturally propagate in a material.

In quantum mechanics, acoustic waves are described through the wave motion of quasi-particles called phonons. These are quantized units of vibrational energy that propagate through a material. For crystals at equilibrium states, the system is usually associated with a harmonic oscillator when damping is negligible. the demonstration is given in most crystallography textbooks [144] and in Appendix A.1.

In liquids, atomic and molecular vibrations still exist, but they do not exhibit the same quantized behavior as in crystals. Instead, it is a collective motion of atoms or molecules. In the context of Brillouin spectroscopy, the concept of phonons is extended to liquids by considering the propagation of collective density fluctuations or sound waves within the liquid medium. These density fluctuations are often referred to as "acoustic phonons" or "density waves". They can be characterized by their interactions with the incident light.

Using concepts introduced on light waves in 2.1.1, the acoustic wave propagation in a medium can be described by a dispersion relation similar to equation 2.4. Usually, this curve is in the function of the angular frequency ω and the wavevector of the phonon \vec{q} describing the direction and magnitude of this wave-like motion.

The dispersion curve of the phonon $\Omega = V * q$ represented in Figure 2.4 shows the evolution of the wave number of the phonon q within the first Brillouin zone (the primitive cell in reciprocal space of the crystal lattice, bounded between $-\frac{\pi}{a}$ and $\frac{\pi}{a}$, where a is the atom distance in the molecule) in function of the frequency Ω . Two types of phonons branches are represented: optical and acoustic modes. Brillouin spectroscopy probes acoustic waves from the central part of the Brillouin zone, represented as a yellow square on Figure 2.4, for q closed to 0. In this zone, the acoustic branch in solid blue and green lines is superimposed with the light dispersion curve (dashed orange line).

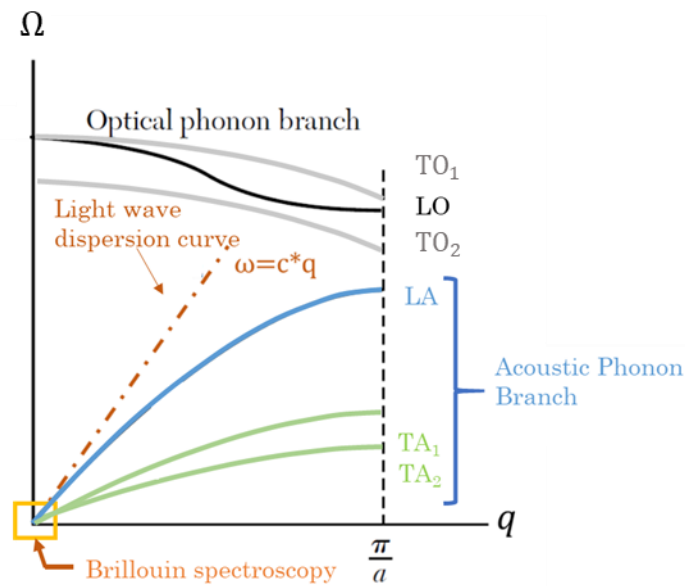


Figure 2.4: Dispersion curve representation of phonons on the First Brillouin Zone. It is composed of an optical branch LO and TO, , and the acoustic branch, LA and TA, where the light dispersion curve (dashed orange line) is superimposed [157].

In liquid media, the phonon propagation is not as straightforward as in crystalline solids due to a lack of long-range order. Transverse waves require a relatively rigid medium to transmit their energy. In means that liquids that do not possess viscoelastic behavior do not have shear mode, only the longitudinal acoustic wave exists [158].

For a liquid becoming glassy, the same logic is applied as for crystalline solids. For p atoms present in the unit cell, it exists $3 * p$ branches, for the two atoms system, there are 6 branches. 3 acoustic branches are named Longitudinal (LA) and two Transversal Acoustic (TA) waves, and $3p - 3 = 3$ optical one, longitudinal (LO) and two transversals (TO) optical that can be analyzed by Raman spectroscopy. In Figure 2.5, in the case of acoustic waves are in phase with each other, whereas the optical are in opposition of phase. The LA and TA waves propagate respectively at the sound velocities V_L and V_T , which are accessible by Brillouin spectroscopy. The longitudinal sound waves and the \vec{q} vector are in the same direction, contrary to the transversal waves where \vec{q} is perpendicular to the direction of atoms' oscillation as illustrated in Figure 2.5.

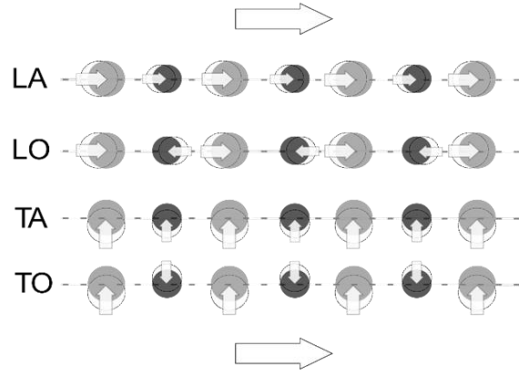


Figure 2.5: The molecular motion of longitudinal optical and acoustic waves are illustrated [159]. Longitudinal and transversal acoustic are named respectively LA and TA, and longitudinal and transversal optic branches, LO and TO respectively.

Those notions are important to understand how inelastic light spectroscopy works. This is detailed in the following.

2.1.3. Inelastic light spectroscopy

To perform spectroscopy measurements, the sample is illuminated by monochromatic light, the scattered light is then analyzed by a spectrometer. The resulting spectra is divided into 3 parts as so in Figure 2.6 below, the center called the Rayleigh peak corresponds to the elastic scattering of the light. The Stokes and anti-Stokes peaks are located symmetrically apart from the Rayleigh center. ω_o , ω_B and ω_R are respectively the Rayleigh, Brillouin, and Raman angular frequency. Each process is sensitive to temperature variation, denoted ΔT .

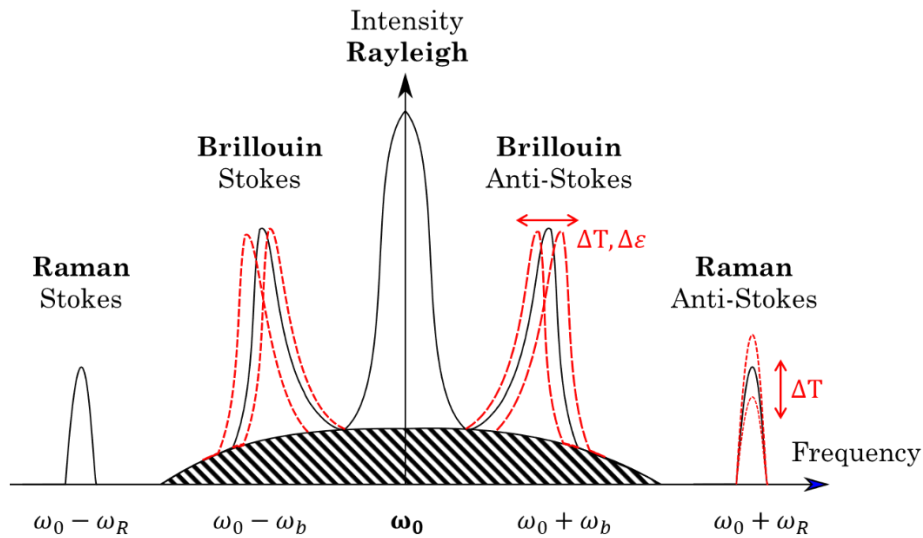


Figure 2.6: Typical spectra of the Brillouin and Raman scattering spectra in function of the angular frequency [160], $\Delta\varepsilon$ is the longitudinal strain variation, ΔT is the temperature variation [161]. The dashed part at the center represents the Mountain contribution that is related to structural relaxation [162].

Those inelastic processes be explained by the light and matter interaction creating in the sample the polarization of the electron cloud. As illustrated in the Figure 2.7, the energy of the light, used does not promote the electron to an excited state but in at a virtual level. The scattering process involving only the electron cloud is referred as the Rayleigh elastic scattering. In another hand, the inelastic scattering, the Stokes and anti-Stokes, involved in this case also the displacement of the nucleus.

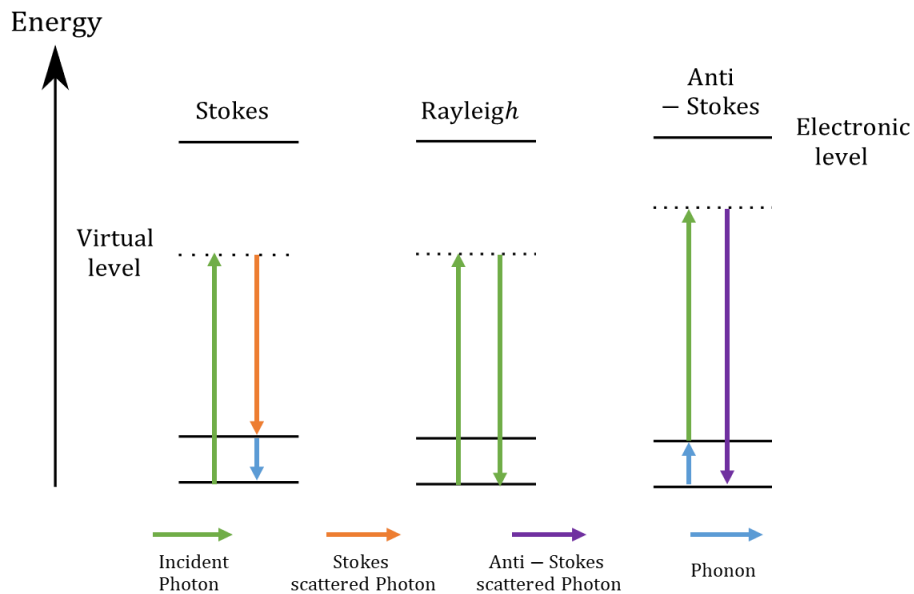


Figure 2.7: Stokes, anti-Stokes, and Rayleigh processes involving the interaction between photon and phonon. The energy exchange is indicated by the colored arrows.

The quantum description of scattering process take considers the interaction between photons (Section 2.1.1) and phonon (Section 2.1.2), following the momentum conservation principal:

$$(\omega_s - \omega_i)\hbar = \pm\hbar\Omega \quad (2.7)$$

$$\vec{k}_s - \vec{k}_i = \pm\vec{q} \quad (2.8)$$

The laser is characterized by the angular frequency is referred to as ω_i that propagates in the \vec{k}_i direction. The phonon (Ω, \vec{q}) is either annihilated or created when is interacting with an incoming photon. The scattered light is described by (ω_s, \vec{k}_s) . In equations 2.7 and 2.8, the “+ sign” is related to the created phonon, and the “− sign” is for the annihilated one.

Typically, the photon energy is around 1 eV, and the $q \approx 10^{-3}\text{\AA}$ [163].

Raman spectroscopy provides information on the chemical composition of a samples, whereas Brillouin spectroscopy reports a collective behavior of molecules for both through the interaction of an electromagnetic light with an acoustic wave in the material.

Even if both Raman and Brillouin spectroscopy are based on inelastic light scattering, Raman spectroscopy probes optical phonon corresponding to a frequency between 1 to 150 THz which corresponds to an order of $10 - 1000\text{ cm}^{-1}$ [33]. Brillouin spectroscopy probe frequencies situated between 5 to 1000 GHz ($0.1 - 6\text{ cm}^{-1}$), which corresponds to a ratio of energy transfer between the laser and the phonon about 10^{-5} [164].

The aim of the present work is to characterize the behaviour of a sample microstructure submitted to extreme conditions of pressure and shear. That is why the following section focuses on the Brillouin spectroscopy.

2.2. Brillouin scattering spectroscopy

2.2.1. Photons and phonons interaction, the scattering process and geometry

The Brillouin inelastic light scattering process, first introduced by Smekal [165], can be described in different ways, a classical and quantum mechanics approach. The complete demonstration of the dielectric fluctuation relationship to the scattered intensity is found in Appendix A.2 [166].

It exists two kinds of processes that lead to scattering process, dielectric or density fluctuation. The nature of the material determines which contribution is dominant.

For a solid at rest, atoms that constitute any material are in permanent movement, their position oscillates around the equilibrium position due to thermal agitation. The spatial displacement of atoms creates an oscillation of the electronic cloud that affects the dielectric susceptibility and the dielectric constant ϵ . Therefore, when an incoming monochromatic electromagnetic light passes through the transparent material with heterogeneities, it

scatters the monochromatic light in all directions [167]. The total electrical field E at a large distance \vec{R} from the scattered volume is the sum of the incident and scattered electromagnetic field: $E = E_i + E_s$. The scattered field E_s is affected by the density and dielectric constant fluctuation, the incident and scattered light polarization $\vec{d}r_i$ and $\vec{d}r_s$ respectively. Then the scattered light can be written in terms of:

$$E_s(\vec{q}, \vec{k}_s, \vec{k}_i, \omega_i, \delta\varepsilon_{is}, \vec{d}r_i, \vec{d}r_s) \quad (2.9)$$

The scattering wave vector \vec{q} is the difference between \vec{k}_s the scattered light wave vector and \vec{k}_i the incident light wave vector, and $\delta\varepsilon_{is}$ is the dielectric fluctuation function.

For a fluid, the density fluctuations are the main contribution [161].

The created propagating acoustic waves associated to the density fluctuations in all directions of space result in a grating-like pattern of varying densities and so of modulated dielectric constant. Therefore, the material possesses regions with different densities and hence of dielectric constants, separated periodically by a distance Λ [144] which corresponds to the wavelength of the acoustic wave. It is related to the phonon wavenumber q by the Bragg law [158]:

$$\Lambda = \frac{2\pi}{q} \quad (2.10)$$

Those regions with different densities are the support for constructive interferences between the incident light and acoustic waves, which depend on the angle between the incident and the scattered light θ , as presented in Figure 2.8 [166].

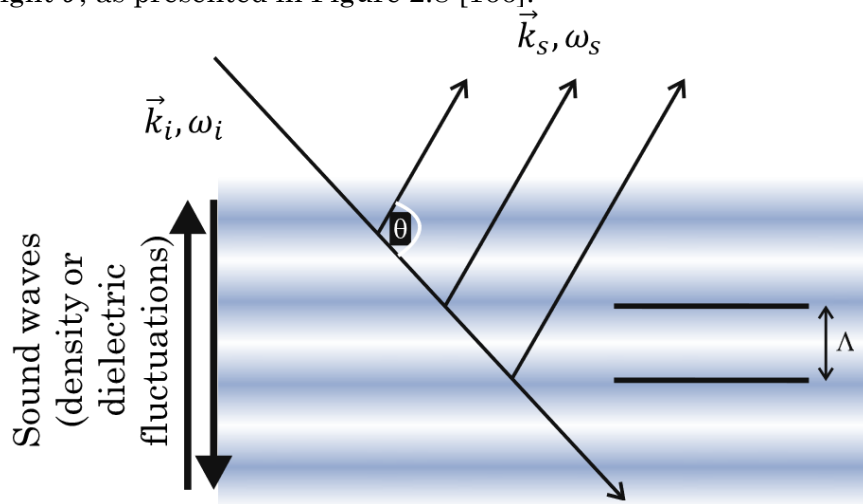


Figure 2.8 : Representation of the incident and scattered wave vector \vec{k}_i and the phonon wavelength Λ scattering on Bragg planes created from propagating acoustic plane waves from [158].

The maximum reflected light intensity from constructive interferences:

$$2n\Lambda \sin \frac{\theta}{2} = \lambda_0 \quad (2.11)$$

Where λ_0 the wavelength is taken in vacuum and n the refractive index. The typical geometry used for the measurements is called backscattering configuration, corresponding to $\theta = \pi$.

The length of the probed phonon is directly linked to its refractive index n and the λ_0 wavelength of the laser used. In our case having a laser wavelength at 532 nm for benzyl benzoate ($n=1.57$) at room pressure and 20°C in the backscattering configuration:

$$\Lambda = \frac{\lambda_0}{2n} = \frac{532 \text{ nm}}{2 * 1.57} \approx 168 \text{ nm} \quad (2.12)$$

From equation 2.8, the norm of this phonon wavevector depend θ the between the incident and the scattered light, and the precedents quantities [164] :

$$q = \|\vec{q}\| = \sqrt{\|\vec{k}_s\|^2 + \|\vec{k}_i\|^2 - 2\|\vec{k}_s\| * \|\vec{k}_i\| \cos(\theta)} \quad (2.13)$$

The energy transfer between phonons and photons is very small, the ratio tends to 10^{-5} . Therefore, it is assumed that $\|\vec{k}_s\| \approx \|\vec{k}_i\|$, the expression of the norm of the scattering wavevector written in equation 2.15 can be simplified as:

$$q = 2\|\vec{k}_i\| \sin\left(\frac{\theta}{2}\right) = \frac{4\pi n}{\lambda_0} \sin\left(\frac{\theta}{2}\right) \quad (2.14)$$

Equation 2.14 is referred to as the Bragg condition. It can be noted that the quasi-staticity comes from the discrepancy between acoustic wave velocity ($\sim 10^3 - 10^4 \text{ ms}^{-1}$) and light velocity (10^8 ms^{-1}) [166].

The phonon wavevector \vec{q} indicates the direction of acoustic propagation. It is imposed by the geometry between the incident and scattered wavevector \vec{k}_i and \vec{k}_s as shown in Figure 2.9. The easiest scattering configuration used to probe longitudinal acoustic waves is the backscattering geometry.

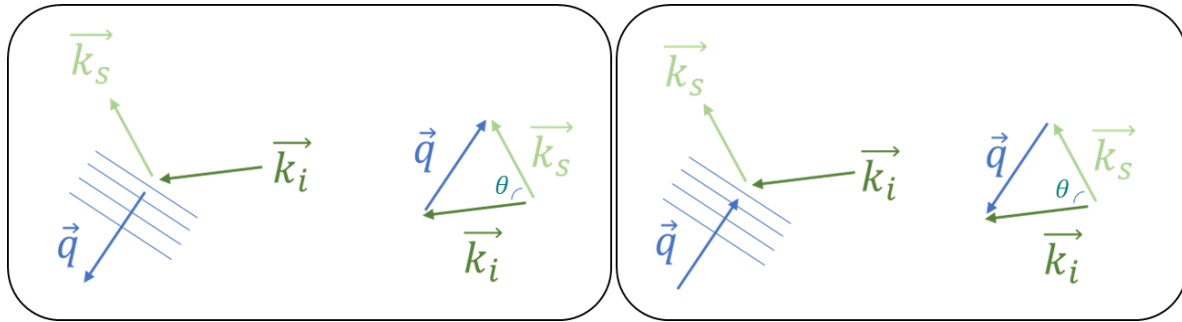


Figure 2.9 : Representation of the incident and scattered wave vector \vec{k}_i and \vec{k}_s and the phonon \vec{q} with an anti-Stokes process on the left side and the Stokes process on the right side [168].

The Figure 2.9 illustrate equations 2.7 and 2.8. The relationship between the phonon angular frequency Ω , the wavelength of the density planes and the velocity of the phonon, which is the dispersion relation of phonon, using equation 2.10 is:

$$\Omega = 2\pi * \frac{V}{\Lambda} = V * q \quad (2.15)$$

with V the sound velocity in the sample. From equation 2.15, the phonon frequency $f_{phonon} = \Omega/2\pi$, can be expressed from section 3.2.2:

$$f_{phonon} = \frac{V}{\Lambda} = V * \frac{q}{2\pi} \quad (2.16)$$

V can either be the sound velocity of transversal waves V_T or longitudinal waves V_L .

In the same way the angular Brillouin frequency shift ω_b is expressed from the angular frequency phonon in equation 2.7 [169]:

$$\omega_b = (\omega_i - \omega_s) = \Omega \quad (2.17)$$

$$\omega_b = V * q \quad (2.18)$$

Using equations 2.5, 2.14, and 2.18 the final Brillouin frequency shift $f_b = \omega_b/(2\pi)$ is [170]:

$$f_b = \pm \frac{2 n V}{\lambda_0} \sin \frac{\theta}{2} \quad (2.19)$$

In the last equation, the Brillouin frequency shift depends on the sound velocity in the sample V , the light angle θ , the incident wavelength λ_0 and the refractive index n of the sample. For all experiments, the sample will be compressed and affected by temperature as shown in Figure 2.6. Therefore, an accurate sound velocity can be computed only if the refractive index of the material in the function of pressure and temperature is established accurately.

2.2.2 Brillouin spectra

The Brillouin frequency shift f_b of the light wave, previously described in (2.19), can be identified on Brillouin spectra for different acoustic wave polarizations.

As an example, Figure 2.10 below shows the possible spectra obtained from a solid. The intensity of each peak is not representative of reality. The three pairs of peaks on each side of the central Rayleigh peak (R) are the result of three acoustic wave polarizations that propagate at different velocities: one longitudinal (compressional) mode (QL) and two transverse (shear) modes (QT). The first longitudinal mode has a polarization vector collinear to the direction of propagation. It is the most energetic mode, with the highest intensity [171], and it is observed in the so-called backscattering geometry (developed in the next section).

The two transverse modes have a polarization vector which is orthogonal to their propagation [171]. They are also orthogonal to each other. These modes are less energetic and thus more difficult to detect. The three peak pairs are only observed in anisotropic solids where acoustic waves can propagate at different velocities in different directions. Moreover, transverse waves can not be detected with the backscattering geometry configuration mentioned previously. For that, the light collection geometry (or configuration) has to change from backscattering to an angular one. This feature is discussed in the next section.

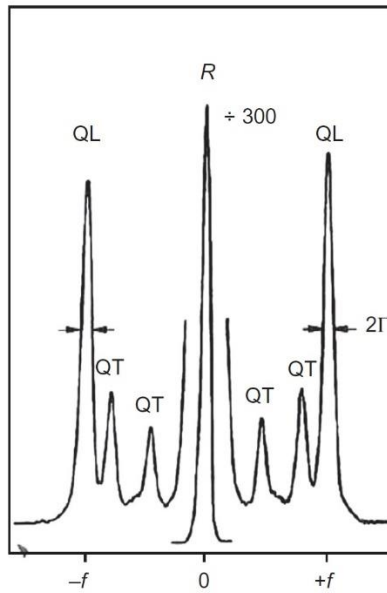


Figure 2.10 Typical Brillouin spectrum of a solid versus frequency shift from the reference [170]. R is the Rayleigh central peak, QT represents the slow transversal acoustic phonons, QL longitudinal phonons.

Isotropic solids show two peak pairs, one longitudinal mode, and one shear mode. This is because the two shear modes in isotropic media propagate at the same velocity.

However, in ideal fluids (which means no viscoelastic behavior), Brillouin spectra exhibit only a single peak pair, the one representative of the longitudinal acoustic mode. Indeed, transverse waves require a relatively rigid structure to be able to propagate in a sample. This is due to the nature of a shear wave, where particles move in a direction perpendicular to the wave propagation. The network between particles must be strong enough for the shear wave to propagate and for the particles not to simply slide past each other. Nevertheless, it is noted in [167] that in viscoelastic fluids, if the acoustic modes couple to molecular structural relaxations, transversely polarized sound modes can be detected at sufficiently high frequencies. One example is a study on glycerol under pressure that shows the transversal wave signal on the Brillouin spectra when is going through its glass transition [134].

Each Brillouin peak is characterized by two parameters: the Brillouin peak shift ω_b can be correlated to the sample behavior such as the sound velocity V in the sample and the Brillouin peak width Γ_b , called the full width at half maximum (FWHM), to the viscous behavior through rheological models. This will be detailed in Section 2.3.

As mentioned, different geometry of light collection is needed to collect the proper information about acoustic waves.

2.2.3 Scattering geometry

Brillouin spectroscopy is dependent on the scattering geometry through the angle θ in equation (2.21) and on the incident light polarization discussed below. The backscattering configuration is used to probe the longitudinal acoustic waves [34] of the material. In this configuration, scattered waves are collected in the same direction and the same microscope objective from which they originate as shown in Figure 2.11 left. The angle θ is equal to 180° so that from equation (2.19):

$$f_b = \pm \frac{2 n V}{\lambda_0} \quad (2.20)$$

Other configurations are needed to probe anisotropy and transversal acoustic waves as the platelet one displayed in Figure 2.11 right.

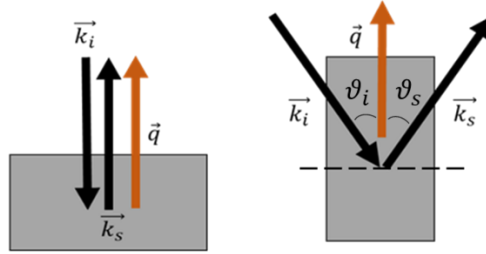


Figure 2.11: Geometry configurations for Brillouin spectroscopy technique: (left) backscattering geometry, (right) platelet configuration ($\theta_i = \theta_s$) [33].

Angular geometries with any angle incident light is able to couple with transversal acoustic waves. The intensity of transversal Brillouin peaks is maximized for a 90° scattering geometry [172]. Moreover, the scattered light from the transverse phonon is depolarized compared to the longitudinal acoustic waves conserving the scattered light initial polarization [145].

Using the combination of these two geometries through the expressions of the sound velocity in equation 2.19 [19], and by applying the Snell Descartes law for the platelet geometry, the refractive index of the sample can be derived:

$$n(T, P) = \frac{\omega_B(\pi) \sin\left(\frac{\theta}{2}\right)}{\omega_B(\theta)} \quad (2.21)$$

where θ is the scattered angle between the incident and the scattered light in platelet geometry, defined as: $\theta = \theta_i + \theta_s$.

From equation 2.21, the characteristics of refractive index $n(T, P)$ can be related to the sample density by the Lorentz–Lorenz equation or also called Clausius-Mossotti equation [19]:

$$\frac{n^2 - 1}{n^2 + 2} = \frac{4\pi}{3} \frac{\rho}{M_w} N_a \alpha \quad (2.22)$$

where M_w is the molecular weight in kg/mole, N_a is the Avogadro's number equal to $6.022 * 10^{23} \text{ mole}^{-1}$, ρ the density in $\text{kg} * \text{m}^{-3}$ and α the polarizability in m^3 . We make the hypothesis that the polarizability α is considered constant with pressure, as already considered in the literature [173]. The value of polarizability for each fluid we study will be derived from direct measurements of both the fluid density and its refractive index at atmospheric pressure and fixed temperature. These data are inserted in equation (2.22) to calculate the fluid polarizability.

The influence of polarizability on the refractive index calculation is considered.

From the data given in the glycerol pressure study by Jeong in 2015 [19], the refractive index was calculated using the polarizability from the force-field-based molecular calculation ($8.93 * 10^{-24} \text{ cm}^3$) and compared to the refractive index from Lorentz-Lorenz calculation using the experimental result of the polarizability at ambient condition ($8.17 * 10^{-24} \text{ cm}^3$). A difference of $0,62 * 10^{-24} \text{ cm}^3$ implies a shift about 6 % ($\sim 0,1$) on the calculated refractive index.

As mentioned in equation 2.11 the scattered electromagnetic wave is in function incident and scattered light polarization vectors, \overrightarrow{dir}_i and \overrightarrow{dir}_s . Depending on the nature of sound waves, LA or TA, which interact with light, the scattered light has different polarization. This feature is discussed in the next part.

2.2.4 Light polarization on the Brillouin spectra

To identify the longitudinal or transversal nature of the waves inducing the inelastic peak, a pair of polarizers and analysers can be mounted on the microscope.

The analyzer is placed in the way of the collected light, before the spectrometer, to filter the outgoing polarization.

Two main configurations of polarizer and analyser can be used, VV (V: vertical) or HH (H: Horizontal) means that the orientation of the polarizer remains the same. The scattered light corresponding to the longitudinal acoustic phonon keeps the same polarisation as the incident electromagnetic wave [174]. The second configuration, VH or HV the set of polarizers, are crossed by 90° . The polarization of the light interacting with a transversal acoustic wave is depolarised [134], meaning that the polarization gets out of the initial orientation. So a cross-polarizer increases the contrast by removing the longitudinal contribution.

By applying the previous formula, a first characterization of the lubricant is possible.

Thus, the Brillouin spectrum is fully identified. Using models from the literature, physical properties and parameters can be derived. The next part will be dedicated to the literature and explanations about those models based on the description of the density fluctuations. Indeed, the damping harmonic oscillator model is used to extract rheological and physical properties such as the modulus and relaxation time of the material. Those elements are crucial in the characterization of glass-forming systems.

2.3 From viscoelastic properties of matter to the inelastic Brillouin spectrum

As stated earlier (§2.1.2), acoustic waves are associated with density fluctuations. The theoretical background describing density fluctuations naturally propagating in a sample has first been suggested by Landau & Placzek [175] then followed by Mountain [176]. It assumes a low thermal conductivity of the sample which enables decoupling thermal diffusion, acoustic mode propagation and damping. In fact, density fluctuations only contribute to the low-frequency region of the spectrum, giving rise to the Rayleigh peak centered at zero frequency and with a linewidth of about 0.1 GHz [13]. The lower resolution limit (~0.1 GHz) of Brillouin spectroscopy does not allow to resolve them [37].

Density fluctuations propagate following a hydrodynamic mechanism of sound propagation in fluids [177]. In the Brillouin literature, the density equation is referred to as the hydrodynamic equation. It is derived from the linearization of the three hydrodynamic equations of i) continuity, ii) Navier Stokes, and iii) energy transport. More complex models are provided as the section continues by introducing the relaxation process in equations. It needs then to be completed by constitutive equations of the fluids which are introduced in the following.

2.3.1 Simple model without damping

To model the evolution of density fluctuations in a simple homogeneous fluid, the simplest model is analogous to solve an undamped spring by a simple harmonic oscillator. For liquid, the fluctuation is dominated by collisions. The fluctuation is considered slow enough compared to the system and considered at local equilibrium for wavenumber and frequencies that are sufficiently low [8,178]. It represents the ideal case of the sample with negligible viscosity. The equation of motion is written as follows:

$$\frac{\partial^2 \rho(q, t)}{\partial t^2} + \omega^2 \rho(q, t) = 0 \quad (2.23)$$

From that last equation, the elastic longitudinal modulus M is written:

$$M(\omega) = \frac{\rho \omega^2}{q^2} \quad (2.24)$$

It must be noted that the modulus M derived from Brillouin spectra is related to the uniaxial deformation of a sample whose cross-section does not change. In other words, the material is not allowed to expand sideways, thereby altering its density and/or volume. This must be kept in mind when Brillouin measurements are compared to more traditional rheological measurements whose mechanical conditions are not equivalent. For instance, the Brillouin longitudinal elastic modulus M is different from the Young's modulus E measured by AFM.

Four moduli are mainly used to describe the mechanical behaviour of a material, as shown in figure 2.12. Knowing two of them is sufficient to characterize the material, the other two moduli being derived from the first ones. For example, the longitudinal modulus M is linked to the shear (G) and the bulk (K) moduli as follows:

$$M = K + \frac{4}{3}G \quad (2.25)$$

The bulk modulus K is related to the compressibility, as shown in Figure 2.12. It is derived from the ratio of stress radially applied to the resulting relative change in volume. G is the shear modulus. One difference to keep in mind between M and E is the order of magnitude. M generally, lies in the GPa range and is probed at GHz frequency, whereas E rather lies in the kPa range, and is probed at Hz-kHz frequencies. The bulk and Young modulus are more studied by other techniques such as AFM.

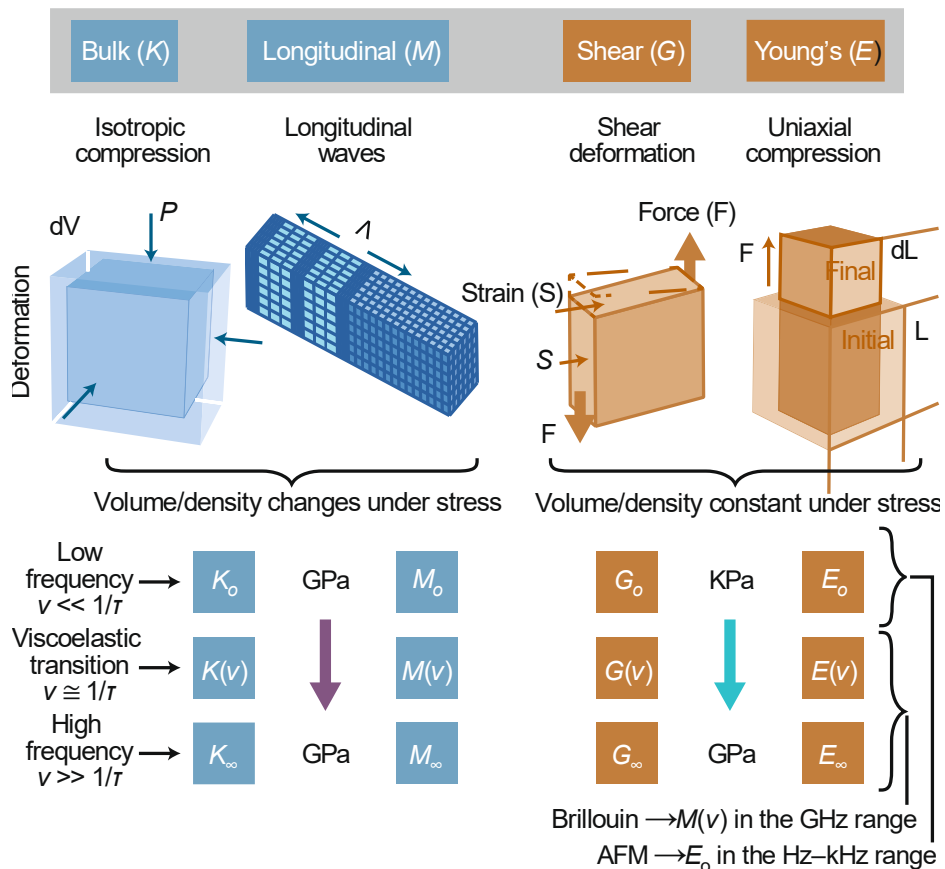


Figure 2.12 : Elastic moduli definition and schematics found from reference [143]. In our Brillouin light scattering study, we focused on the longitudinal modulus M and in the perspective work the shear modulus G .

This model is too simple to describe our viscoelastic sample. In order to take into account the lubricants' viscous effect, the density fluctuation with a damping contribution of the sample is introduced in the next part as the linearized hydrodynamic equations [179].

2.3.2 Linearized hydrodynamic equations with damping

A more realistic model of a simple homogeneous fluid includes the damping of the acoustic waves inside the probed media. The longitudinal complex modulus M is expressed as $M = M_0 + i\omega\eta_L$ where η_L is the longitudinal viscosity in Pa.s.

The equation of density fluctuations can be described by the linearized hydrodynamic equation as follows [37,179] :

$$\frac{\partial^2 \rho(q, t)}{\partial t^2} + \left(\eta_L \frac{q^2}{\rho_M} \right) \frac{\partial \rho(q, t)}{\partial t} + \left(M \frac{q^2}{\rho_M} \right) \rho(q, t) = 0 \quad (2.26)$$

where $\rho(q, t)$ is the density fluctuations propagating inside the media along the wavenumber q expressed in equation 2.6. M is the longitudinal elastic modulus in Pa, is written as: $M_0(\omega_0) = \rho_M \omega_0^2 / q^2$, with $\omega_0 = V_0 q$ and $V_0^2 = M / \rho_M$. The viscosity is expressed as $\eta(\omega_0) = \rho_M \Gamma_0 / q^2$ and ρ_M is the static mass density. The longitudinal viscosity is expressed as: $\eta_L = \frac{4}{3} \eta_S + \eta_B$, with η_S and η_B the shear and the bulk viscosity respectively.

2.3.3 The generalized hydrodynamic equation for simple fluids

During a Brillouin scattering experiment, for simple fluids, meaning a structureless fluid where transverse waves does not couple with the density fluctuation. Only longitudinal modes are visible on the spectrum, forming a peaks triplet spectrum. Thus, the resulting isotropic part of scattered spectrum [174], denoted as $I(q, \omega)$, where ω is the frequency shift relatively to the laser frequency, is directly proportional to spectrum of density fluctuations $\rho^2(q, t)$. All the demonstrations are found in [37,167].

The correlation function of density fluctuations, which describes the statistical correlation between density fluctuations in the material as a function of both the wave vector \vec{q} and time t , in equation 2.27 is related to the dynamic structure factor $S(\vec{q}, \omega)$ by:

$$\langle \rho_q(0) \rho_q(t) \rangle = S(\vec{q}, \omega) \quad (2.27)$$

In another words, the dynamic structure factor contained information of the space and time Fourier transform of the density correlation function. The fluctuation-dissipation theorem [180] relates the correlation function to the imaginary part of the susceptibility $\chi(\vec{q}, \omega)$. The susceptibility refers as the capacity of a material can be magnetized when exposed to an external magnetic field, the imaginary part describe dissipative processes in the sample [167].

$$S(\vec{q}, \omega) = \frac{2 k_b T}{\omega} \sum_{p=1}^3 \text{Im} \chi(\vec{q}, \omega) \quad (2.28)$$

with $\chi(\vec{q}, \omega)$ the complex frequency-dependent susceptibility, k_b the Boltzmann constant and T the temperature.

The dynamic structure factor S is proportional to the intensity of the scattered light and the factor i_s representing the intensity of the incident light. The spectral scattered light distribution accessible by Brillouin spectroscopy [181]:

$$I(\vec{q}, \omega) = A_{i_s} \cdot S(\vec{q}, \omega) \quad (2.29)$$

Thus, using equations 2.28 and 2.29, the energy dissipated by the system through oscillations is closely related to the imaginary part of the Fourier transform of the susceptibility [8,37,167,179]:

$$I(\vec{q}, \omega) = \frac{I_0}{\omega} \text{Im} \chi(\vec{q}, \omega) \quad (2.30)$$

The spectral scattered light distribution for the Brillouin spectrum is expressed from the equation of motion (2.26) and the equation 2.30:

$$I(q, \omega) = \frac{I_0}{\omega} \text{Im} \left[-\omega^2 + \frac{M}{\rho_M} q^2 - i\omega \frac{\eta_L}{\rho} q^2 \right]^{-1} \quad (2.31)$$

$$I(q, \omega) = \frac{I_0}{\omega} \frac{\frac{\omega \eta_L q^2}{\rho}}{\left(\omega^2 - \frac{M q^2}{\rho_M} \right)^2 + \left(\frac{\omega \eta_L q^2}{\rho_M} \right)^2} \quad (2.32)$$

This equation is complexified for viscoelastic fluids. The longitudinal modulus M is expressed as $M = M' + i\omega\eta_L$.

The next part is dedicated to the generalized hydrodynamic equation that highlights relaxation processes and introduces the characteristic relaxation time t_{rel} of the structural relaxation.

2.3.4 The generalized hydrodynamic equation for Viscoelastic fluids

The line shape of the Brillouin triplet is described by the dynamic structure factor $S(q, \omega)$ (equations 2.28), that contains information about their time evolution and inter-particle correlations. For viscoelastic fluids, the harmonic solution $\rho(q, t)$ changes the shape of the modulus expressed before into a complex frequency dependant modulus [37]:

$$M^*(\omega) = M'(\omega) - iM''(\omega) \quad (2.33)$$

Where $M^*(\omega)$ is referred as the generalised modulus used for sample experiencing glass transition or solid-like approach. It is composed of M' , the elastic contribution of the longitudinal modulus, also called the storage longitudinal modulus. It is associated with the material's ability to store energy elastically. The generalised modulus possesses an imaginary part M'' called loss modulus is associated with viscous dissipation. The “+” or “-” sign between M' and M'' in equation 2.33 depends on the author's convention. This present work will follow the convention “-” chosen in reference [37].

From the previous equations 2.26, 2.32 and 2.33:

$$I(q, \omega) = \frac{I_0}{\omega} \frac{\frac{[M''(\omega) + \omega \eta_L]q^2}{\rho}}{\left[\omega^2 - \frac{M'(\omega)q^2}{\rho}\right]^2 + \left[\frac{(M''(\omega) + \omega \eta_L)q^2}{\rho}\right]^2} \quad (2.34)$$

In literature, $M''(\omega) + \omega \eta_L$ may reduce and expressed as $M''(\omega)$ [8,16,17]. Equation (2.34) becomes:

$$I(q, \omega) = \frac{I_0}{\omega} \frac{M''(\omega) q^2 / \rho_M}{\left[\omega^2 - \frac{M'(\omega)q^2}{\rho_M}\right]^2 + \left[\frac{(M''(\omega))q^2}{\rho_M}\right]^2} \quad (2.35)$$

The expression of the real and imaginary part M' and M'' are frequency-dependent. Thus, for the expression (2.35) to be fitted on a Brillouin spectrum, their evolution versus ω must be known, so a longitudinal modulus model must be introduced. The following authors used the positive complex modulus convention. The most general model is derived from the generalization of the hydrodynamic equations [8,13,148], where the influence of the relaxation process on the longitudinal modulus is identified as ΔM such as:

$$M(\omega) = M_\infty + \Delta M + i\omega\eta_\infty \quad (2.36)$$

M_∞ and η_∞ represents the solid-like unrelaxed modulus, called also high-frequency longitudinal modulus. ΔM depends on the nature and the complexity of the relaxation process. In the next part, the complex modulus expression is provided for the three regimes of behavior: the liquid-like regime, the glass transition and the solid-like regime.

2.4 Density equation for different regimes

The expression of the modulus depends on the diffusion regime and the model applied. Figure 2.13 displays the contributions M' and M'' for a sample that experiences alpha-relaxation associated with the local maximum of the loss modulus. The parameter $\omega_b t_{rel}$, which is mentioned in the context of the glass transition in Section 1.3.2, enables to describe the sample behavior in terms of its relaxation time and characteristic frequency. In this sense, $\omega_b t_{rel}$ is reminiscent of the Deborah number, as they both describe the degree of relaxation of a material. Indeed, De is the ratio between the relaxation time and the characteristic time

of observation. The different regimes defined by De can be reached by varying either the frequency or the relaxation time. The central region can be described by $De = \omega \times t_{rel} = 1$.

Specifically, Pinnow et al decomposed the density fluctuations into oscillatory and non-oscillatory modes and showed that the energy transfer between these modes depends on $\omega_b t_{rel}$. For $\omega_b t_{rel} \ll 1$, the relaxed regime, energy transfer between the two modes can easily occur, implying structural rearrangements completely coupled with the oscillations and macroscopic fluid-like behavior of the sample. However, for the unrelaxed one $\omega_b t_{rel} \gg 1$, energy transfer cannot occur between the two modes (oscillatory and non-oscillatory), and the oscillatory mode is not coupled to the relaxational process, involving a solid-like behavior of the sample. Finally, $\omega_b t_{rel} = 1$ represents the maximum acoustic wave absorption.

On this Figure 2.13, 3 regimes can be distinguished: the liquid (relaxed) regime at low frequencies, the solid (unrelaxed) regime at high frequencies and the transition one in between, around alpha-relaxation ($\omega t_{rel} = 1$). M' increases with frequency, up to a plateau value corresponding to $M'_\infty = \rho V_\infty^2$, where M'_∞ is the unrelaxed or high-frequency longitudinal modulus V_∞ is the sound velocity at a solid-like state. On the other hand, at low frequency, the adiabatic longitudinal modulus M_0 , for a simple fluid is related to the adiabatic sound velocity V_0 and the density by $M'_0 = \rho V_0^2$.

In the same figure, the red line shows the loss modulus M'' across frequencies. Its evolves tremendously. In liquid state, it is described by the relaxed viscosity η_0 and the angular frequency $M''_0 = \eta_0 \omega$. In the unrelaxed regime, it is described by the unrelaxed modulus $M''_\infty = \eta_\infty \omega$.

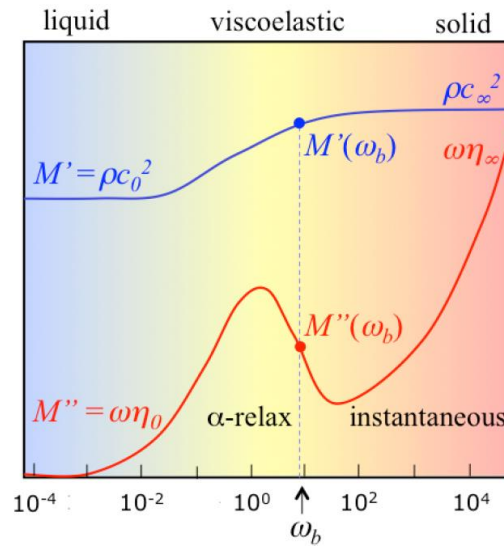


Figure 2.13: Qualitative representation real and imaginary parts of the longitudinal modulus from liquid to solid behavior depending on the angular frequency taken for reference [148].

In between those two asymptotic regimes, at moderate frequencies, the sample experiences an alpha relaxation, which involves a non-monotonous behavior of M' . The alpha relaxation is related to the relaxation time t_{rel} . It depends on pressure and temperature conditions. Note that the relaxation time is denoted t_{rel} in this work to avoid any confusion with the shear stress τ defined for tribological tests.

2.4.1 Relaxed regime $\omega t_{rel} \ll 1$ by damping harmonic oscillator model (DHO)

$\omega t_{rel} \ll 1$ defines the relaxed regime. It occurs either in the (very) low-frequency region of the spectrum or for very low relaxation time (high temperature and low pressure). The sample behaves like a relaxed fluid.

Using this new formalism on the first regime of the ideal fluid regime, i.e. for $\omega t_{rel} \ll 1$, described earlier in 2.3.4, the relaxation contribution ΔM in equation 2.36 becomes:

$$\Delta M(\omega \rightarrow 0) = (M_0 - M_\infty) + i\omega(\eta_0 - \eta_\infty) \quad (2.37)$$

Then, the complex modulus expression is: $M(\omega) = M_0 + i\omega\eta_0$.

In this case, the damping harmonic oscillator model (DHO) [13,134,174,182] links those quantities by expressing the power spectrum $I(\omega)$ in function of Γ_b the Full Width Half Maximum (FWHM) and ω_b the Brillouin shift. Thus, the equation of motion of density fluctuations described in equation 2.28 can be rewritten:

$$\ddot{\rho}(q, t) + \Gamma_0 \dot{\rho}(q, t) + \omega_0^2 \rho(q, t) = 0 \quad (2.38)$$

with ω_0 is the oscillation frequency of the undamped system, very close to the one of the damped systems, and Γ_0 the damping coefficient.

By identification of equation 2.35 and 2.38 becomes [148]:

$$I(\omega) = \frac{I_0}{\pi} \frac{\Gamma_0 \omega_0^2}{(\omega^2 - \omega_0^2)^2 + (\Gamma_0 \omega)^2} \quad (2.39)$$

By comparison with equation (2.35), the complex elastic modulus in this regime can be expressed as a function of the linewidth Γ_0 and angular frequency shift ω_0 .

$$M'_0 = \frac{\rho_M \omega_0^2}{q^2} = \rho_M V^2 \quad (2.40)$$

$$\eta_0 = \frac{\rho_M \Gamma_0}{q^2} = \text{and } M''_0 = \omega_0 \eta_0 \quad (2.41)$$

M_0 and η_0 describe the relaxed longitudinal modulus and viscosity.

However, in a contact, the high-pressure conditions induce a strong viscoelastic behavior of the sample that could not be fully represented by the DHO model. Indeed, close to the glass transition, relaxation processes strongly couple with the acoustic waves and have to be included in the expression of $\Delta M(\omega)$. In this case, the expression of the modulus M is more complex. The simple form of the DHO model can still be applied at high pressure to obtain values for the ‘‘apparent’’ sound velocity and attenuation [34,183].

2.4.2 For $\omega t_{rel} \sim 1$ Debye and Cole Davidson model near the glass transition

The acoustic energy absorption reaches a maximum for $\omega_b t_{rel} \sim 1$. Indeed, it occurs when the acoustic mode propagating in the material (and characteristic of its behavior) matches the material internal degree of freedom (which drives the relaxation time) [13]. It results in a maximum linewidth of the Brillouin peak, or equivalently a maximum apparent attenuation D (equation (2.44)) or viscous modulus M'' [17].

The condition $\omega t_{rel} \sim 1$ defines the transition regime. In this regime, the sample is still described in the literature by the apparent sound velocity and the apparent attenuation (or kinematic viscosity) D [13]:

$$D = \Gamma_b / q^2 \quad (= \eta_L / \rho) \quad (2.42)$$

However, in this regime, as relaxation processes play an important role in the sample behavior, this latter may highly depend on frequency. Consequently, a simple fluid behavior, enabling application of the DHO model cannot be used anymore and the relations (2.40) and (2.41) no longer hold. Instead, the relaxation contribution ΔM of the longitudinal modulus M should take into account relaxation processes. It can be modeled by a single exponential function, the Debye relaxation model:

$$\Delta M = \frac{M_0 - M_\infty}{1 + i\omega t_{rel}} \quad (2.43)$$

However, it should be noted that, according to [13], the α relaxation is not perfectly a single frequency process. Instead, this process tend to stretch the dispersion zone, i.e. the transition zone between the asymptotic relaxed (low frequency) modulus and the asymptotic unrelaxed (high frequency) modulus [13]. The ΔM function shape is then closer to the Cole Davidson (CD) relaxation function. It is a power-law expression using the stretching parameter β varying between 0 and 1:

$$\Delta M = \frac{M_0 - M_\infty}{(1 + i\omega t_{rel})^{\beta_{Debye}}} \quad (2.44)$$

This corresponds to the Debye model with a stretching parameter of 1, meaning no stretching of the dispersion zone. This CD model is fitted to a spectrum when no evidence, in the transition regime, of a strong secondary relaxation process is coupled to density fluctuations. Indeed, it must be kept in mind that the Cole Davidson model does not take into account the possible presence of additional processes faster than structural relaxation [13]. Yet, for some fluids, a single exponential is not sufficient. In this case, several contributions of the different relaxation processes can be added, which is equivalent to sum as many ΔM contributions as relaxation processes. An example is provided in appendix A.3.

2.4.3. For $\omega t_{rel} \gg 1$ the Voigt model

The condition $De = \omega t_{rel} \gg 1$ defines the unrelaxed regime. It occurs either in the high-frequency region of the spectrum or for high relaxation time (low temperature and high pressure). The sample macroscopically behaves like a solid [148].

The relaxation contribution ΔM of the longitudinal modulus M vanishes, and the expression (2.36) becomes:

$$M(\omega) = M_\infty + i\omega\eta_\infty \quad (2.47)$$

with:

$$M'(\omega) \cong M_\infty \text{ and } M''(\omega) = \omega\eta_\infty = \omega\eta_L \quad (2.48)$$

which corresponds to a Voigt model. The spectrum is fitted by the combination of equation (2.42) and (2.48) leads to access M_∞ and η_∞ .

As presented in this previous part, fitting models are essential to extract mechanical properties and relaxation time from Brillouin spectra. The spectrum analysis is developed in the next section.

2.5. Local spectrum analysis

The most common spectrum analysis in the literature is the local fit of the spectrum. A simple behavior of the sample is assumed, following for instance a Voigt model, characterized by a modulus and a viscosity. These parameters, already defined in (2.40) and (2.41), are calculated from the peak frequency ω_b and FWHM Γ_b (representative of the acoustic waves damping), which are obtained by fitting the spectrum in a narrow frequency region around the Brillouin peak as shown in Figure 2.14. The most commonly used function to fit the peak of the spectrum are the Lorentzian and the DHO model. Using a Lorentzian makes it possible to represent the asymmetry of the inelastic peaks [37,161].

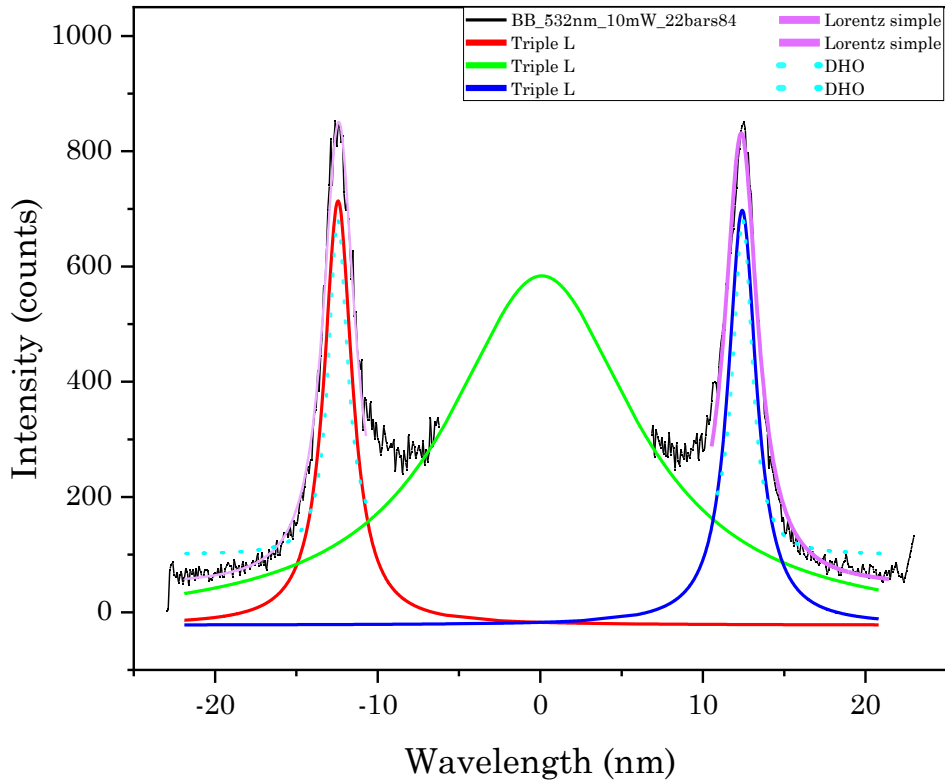


Figure 2.14 : Fit of a spectrum performed on benzyl benzoate by 3 different fitting functions: Lorentz, Lorentz multiple fit and DHO model.

It should be noted that the frequency peak position f_b and FWHM directly extracted from the Brillouin spectrum (in GHz) correspond to $\omega_b/2\pi$ and $\Gamma_b/2\pi$ in the DHO model. In the dynamic behavior of viscoelastic material, the general cooperative processes of molecules are affected by the material structural relaxation [8], causing additional acoustic damping. This coupling could be responsible for Mountain Peak situated at the center of the Brillouin spectrum [13]. This signal creates a supplementary background on low frequencies (few GHz) [162,184].

In the glassy regime (below the glass transition temperature for data plotted versus temperature), the relaxation time increases of several orders of magnitudes (see chapter 1). Thus, structural alpha (α) relaxation occurs at very low frequencies, lower than 1 Hz, and consequently lower than frequencies that can be probed in Brillouin spectroscopy (in the GHz region). It is then expected that there is no significant (and measurable) contribution of the α relaxation on the spectra in this glassy regime [8].

To highlight the different regimes that can be experienced by a material, and to characterize them, a third quantity can be calculated from M' and M'' : the $\tan(\delta)$, which is the dissipation factor, defined as the inverse of the quality factor Q :

$$\tan(\delta) = \frac{M''}{M'} = \frac{1}{Q} \quad (2.49)$$

It is a dimensionless parameter that corresponds to the ratio of the viscous to elastic response of a viscoelastic material, so the energy dissipation potential of the material. In other words, it represents a measure of sound damping or attenuation. The greater the $\tan(\delta)$, the more dissipative the material whereas the lower the value of $\tan(\delta)$, the more elastic the material. For an oscillator, it is the reciprocal of the quality factor, which represents the « quality » or durability of the oscillation. This parameter is of great interest for the simplicity of its expression. Indeed, both $M'(\omega)$ and $M''(\omega)$ are relevant for both relaxed and unrelaxed regimes. The ratio between the two parameters is equivalent to the ratio between Γ_b and ω_b which dispense with the density dependency of $\tan(\delta)$.

$$\frac{1}{Q} = \frac{M''}{M'} = \frac{\Gamma_b}{\omega_b} \quad (2.50)$$

The dissipation factor varies in $[0, +\infty[$. The value of 0 ($\delta = 0^\circ$) corresponds to the ideal case of an elastic solid. Then, its value tends to $+\infty$ ($\delta = 90^\circ$) in the ideal case of a purely viscous fluid. The case of elasticity perfectly balancing viscosity occurs for $\tan(\delta) = 1$. It occurs at the glass transition point. Thus, liquid phase involves a $\tan(\delta) > 1$ and solid phase involves a $\tan(\delta) < 1$.

The sound velocity as shown in Figure 1.12, the change in the slope of sound velocity is representative of the glass transition of the material [8].

This parameter leads to highlighting the different regimes for which the sample is governed by viscous damping (relaxed regime, sound diffusion) or elasticity (unrelaxed regime, sound propagation).

2.6. Conclusion

This chapter introduced the concept of Brillouin spectroscopy, which is an experimental approach already used in many fields of physics to characterize materials. It showed that the light-matter interaction leads to the shift in the energy of the probe laser called the Brillouin shift. From Brillouin spectra, the position and the full width at half maximum give information about the physical properties of the samples probed. The scanning angle plays an important role on the wave vector. Information can be extracted from models adapted to the regime experienced by the sample. The liquid or relaxed regime is described by the Damping Harmonic Oscillator (DHO), where the system can be considered at equilibrium. When the sample experiences a glass transition, its modulus can be described by Debye or Cole Davidson's models. Finally, the unrelaxed regime is described by the Voigt model. The next chapter will describe the experimental setups and methods developed in the present work to characterize samples in extreme pressure and wide shear conditions.

Within this chapter, the focus shifts from theory to practical implementation, providing descriptions of the various components within the experimental methodology. A complete description of each sample being investigated is provided.

3. Experimental method

Table of content

3.1.	SAMPLE DESCRIPTION	103
3.1.1.	FLUIDS AND RHEOLOGICAL MODEL DESCRIPTION	103
3.1.2.	DENSITY MODEL	105
3.2.	BRILLOUIN SET-UP	107
3.2.1.	FABRY-PÉROT BRILLOUIN SPECTROMETER	108
3.2.2.	VIPA SPECTROMETER.....	110
3.3.	MICROSCOPES.....	113
3.3.1.	ILM SET-UP	113
3.3.2.	LAMCoS SET-UP.....	114
3.4	HIGH-PRESSURE CELLS	118
3.4.1	HIGH-PRESSURE CELLS DESIGN	118
3.4.2	DETERMINATION OF THE PRESSURE INSIDE THE DAC	120
3.5.	TRIBOMETER SET-UP.....	123
3.6	CONCLUSION	126

In Chapter 3, the experimental set-up for the study is detailed. It first covers the selection of fluids for analysis. Then, the second section introduces two Brillouin spectrometer technologies: the Fabry-Pérot Brillouin Spectrometer existing at Institut Lumière Matière (ILM), Université Lyon 1 (ILM) and the VIPA Spectrometer developed at LaMCoS during the thesis. A part will be dedicated to the microscopes used, high-pressure cell design, pressure determination methods, and finally the tribometer set-up. The discussion provides insights into the optical construction of inelastic light scattering spectrometers, emphasizing advantages and disadvantages of each set-up. The chapter concludes with an introduction to spectra treatment, which is elaborated on in the subsequent chapter.

3.1. Sample description

Three lubricants were selected for this experimental study: squalane, benzyl benzoate, and glycerol.

3.1.1. Fluids and rheological model description

The choice was based on the morphological shape and their physical properties. Benzyl benzoate and squalane were extensively studied rheologically and tribologically at LaMCoS laboratory, as well as with molecular dynamic simulation [94,95] and study in Brillouin-Raman spectroscopy [41].

Squalane [39] is a typical glass-former fluid characterized using both experimental and computational approaches [185]. The limiting shear stress (LSS) of squalane was also investigated experimentally at LaMCoS, however the results are not yet published.

This organic lubricant is a linear alkane, composed of a carbon chain $[(CH_3)_2CH(CH_2)_3CH(CH_3)(CH_2)_3CH(CH_3)CH_2CH_2-]_2$, (CAS 111-01-3) provided with a 96% purity from Sigma Aldrich. As a flexible broadly linear molecule, it has commonly been employed as a model lubricant in tribological experiments [93]. It has been rheologically described with a modified WLF-Yasutomi viscosity model versus temperature and pressure (equation 3.1), over [0.1 – 1400] MPa and [20 – 65] °C, according to the methodology described in [186]. Coefficients of the WLF law (equations 3.2 and 3.3) are provided in [105] and reported in Table 3.1. μ_g is fixed at 10^{12} Pa.s (see chapter 1.3.2).

$$\mu_{WLF}(T, P) = \mu_g \exp \left[\ln(10) \times \frac{-C_1(T-T_g(P))F(P)}{C_2+(T-T_g(P))F(P)} \right] \quad (3.1)$$

$$T_g(P) = T_g(0) + A_1 \ln(1 + A_2 * P) \quad (3.2)$$

$$F(P) = (1 + B_1 * P)^{B_2} \quad (3.3)$$

where $\mu_{WLF}(T, P)$ is the low shear stress viscosity at temperature T and pressure P , $T_g(P)$ is the glass transition temperature at pressure P . F is the dimensionless relative thermal expansion of the free volume. Parameters (A_1 , A_2 , B_1 , B_2 , C_1 and C_2) are fitted parameters.

Equation 3.2 predicts the glass transition temperature T_g as a function of pressure. This equation can be reversed to obtain an estimate of the glass transition pressure at a given temperature. The glass transition pressure P_g for squalane at 20°C and 25°C is then estimated at $P_{gSq}(20^\circ C) = 1.45$ GPa and $P_{gSq}(25^\circ C) = 1.53$ GPa respectively. At 40°C and 60°C, temperature probed in friction curve, the glass transition pressure is respectively $P_{gSq}(40^\circ C) = 1.78$ GPa and $P_{gSq}(60^\circ C) = 2.15$ GPa. Inversely, at atmospheric pressure, the glass transition temperature predicted by the model is -88.68°C. This can be compared with the differential scanning calorimetry (DSC) measurement which has been performed at atmospheric pressure (under helium atmosphere) from -130°C to 50°C at +10°C/min. Results

are displayed in Figure 3.1, illustrate the heat flow (or specific heat) given by DSC. The specific heat exhibits a first sharp drop starting at -101.9°C which corresponds to the onset of the sample glass transition. It is accompanied by an endothermic peak somehow involving an enthalpy recovery from the glassy state, corresponding to a latent heat of -1.622 J/g . The deviation in the glass transition temperatures may be inferred to the measurement uncertainties in the two experimental approaches to the fact that the transition occurs over a temperature range and not at a specific value and finally to the extrapolation at a viscosity of $10^{12}\text{ Pa}\cdot\text{s}$ considered in the rheological model.

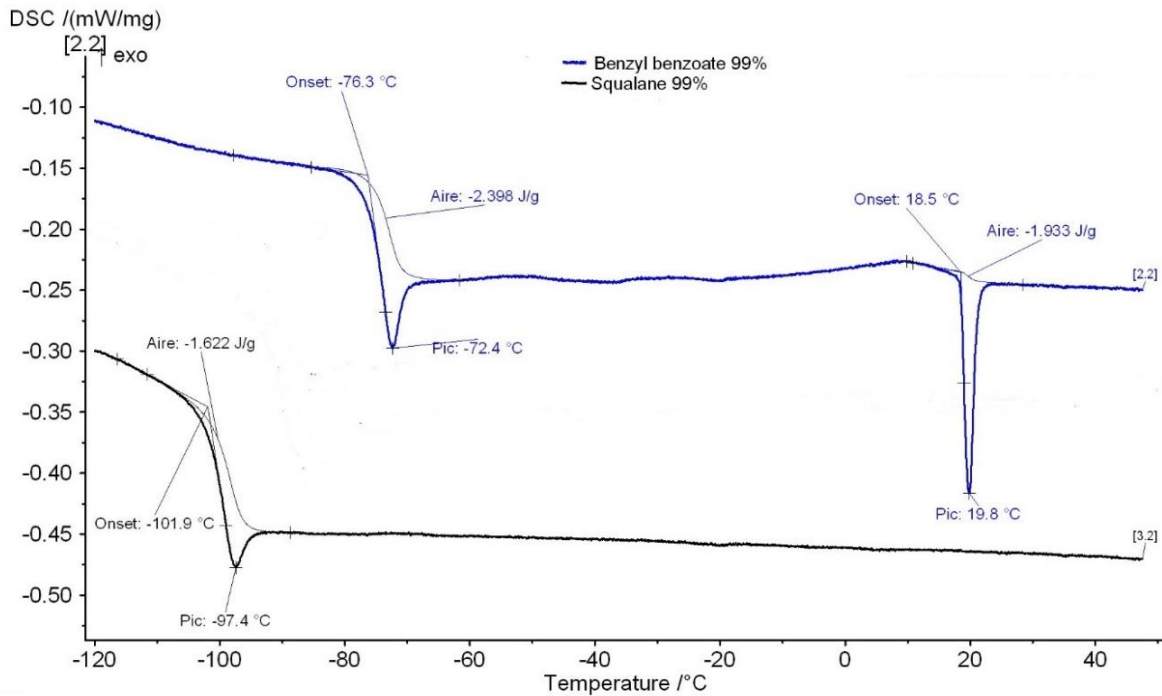


Figure 3.1 Enthalpy of the squalane and the benzyl benzoate measured with differential scanning

Benzyl benzoate, which is used as numerical model fluid, is an ester of benzyl alcohol and benzoic acid. It is a double-cycle carbon with the following chemical composition $\text{C}_6\text{H}_5\text{CO}_2\text{CH}_2\text{C}_6\text{H}_5$. The sample is provided by abcr GmbH company which guaranties its purity at 99% (CAS 120-51-4). It is composed by two benzene rings. This leads to high friction coefficients, so a high capacity to transmit power [93]. As well as squalane, benzyl benzoate has been rheologically characterized. Its behavior has been modeled with a modified WLF-Yasutomi viscosity model (eq. 3.1 – 3.3) over the range of $[0.1 - 700]\text{ MPa}$ and $[40 - 130]^{\circ}\text{C}$, as provided in [38] and reported in Table 3.1. Its rheological study method is described in reference [186] and the results are presented in reference [10]. The glass transition temperature of -81.7°C predicted by the model can be compared to the value of -76.3°C derived from DSC measurements as shown in Figure 3.1 [41]. Besides its rheological characterization, the pressure and temperature dependence of the limiting shear stress was also established by friction measurement and correlated to the thermodynamical response probe by Brillouin spectroscopy [38,41]. In the same way as for the squalane, the glass transition pressure of the

benzyl benzoate is estimated from the modified WLF-Yasutomi model at $P_{g_{BB}}(20^\circ\text{C}) = 0.8 \text{ GPa}$, $P_{g_{BB}}(40^\circ\text{C}) = 1.0 \text{ GPa}$ and $P_{g_{BB}}(60^\circ\text{C}) = 1.2 \text{ GPa}$.

	T_g0 ($^\circ\text{C}$)	A1 ($^\circ\text{C}$)	A2 (GPa^{-1})	B1 (GPa^{-1})	B2	C1	C2 ($^\circ\text{C}$)
Squalane	-88.69	263.8	0.3527	13.73	-0.3426	11.66	39.17
Benzyl benzoate	-81.73	400.19	0.363	5.391	-0.399	16.00	14.55

Table 3.1 Parameters of the modified WLF-Yasutomi viscosity model for benzyl benzoate [38] and squalane [105].

Finally, the last liquid, Glycerol is a tri-alcohol and water-friendly molecule $\text{HOCH}_2\text{CH}(\text{OH})\text{CH}_2\text{OH}$, (CAS 56-81-5) with a 99.5% purity from Sigma Aldrich. This fluid was characterized up to 10 GPa by Brillouin spectroscopy coupled with a high-pressure set-up in backscattering [19]. It will serve as reference for relaxation time, and refractive index dependency calculation on pressure and temperature. It's glass transition pressure at 22°C is taken at $P_{g_{GLY}}(22^\circ\text{C}) = 4.15 \text{ GPa}$ from reference.

To be able to fully describe those fluids in the EHD contact, their density in function of pressure has to be predicted.

3.1.2. Density model

The Tait equation of state (equations 3.4 and 3.5) depicts the volume dependence on temperature and pressure.

$$\frac{V_{Tait}}{V_R} = \frac{\rho_R}{\rho} = (1 + a_v(T - T_R)) * \left[\left(1 - \frac{1}{1 + K'_0} \right) \ln \left[1 + \frac{P}{K_0} (1 + K'_0) \right] \right] \quad (3.4)$$

$$\text{With } K_0 = K_{00} \exp(-\beta_K T) \quad (3.5)$$

where V_{Tait} and ρ are the volume and the density, respectively, at temperature T and pressure P . V_R , T_R and ρ_R are respectively the volume, temperature and density at the reference state of the fluid (here, 40°C and at atmospheric pressure). a_v is the thermal expansion defined for volume linear with temperature. K_0 is the isothermal bulk modulus at $P=0$. K_{00} is K_0 at zero absolute temperature, K'_0 is the pressure rate of change of isothermal bulk modulus at $P=0$, β_K is the temperature coefficient of K_0 .

This equation has been employed in [95], [38] and [94] to describe relative volume in function of pressure and temperature for both benzyl benzoate and squalane. The coefficients of this law have been obtained by fitting density measurements performed in the range of $[40 - 105]^\circ\text{C}$ and $[0.1-400] \text{ MPa}$ for benzyl benzoate and $[40 - 100]^\circ\text{C}$ and $[0.1-378] \text{ MPa}$ for squalane. Coefficients of the law come from [187] for benzyl benzoate and [188,189] for squalane. To convert relative volume data into density, the reference density at 40°C of 1.1023 g/cm^3 for benzyl benzoate comes from [38] and a value of 0.7958 g/cm^3 for squalane comes from [189].

	BENZYL BENZOATE	SQUALANE
K'_0 [l]	10.439	11.74
K_{00} [GPa]	13.707	8.658
β_T [K^{-1}]	0.006107	0.006232
a_v [C^{-1}]	7.474E-04	0.000836
ρ_R [kg/m^3] @40°C	1102.3	795.8
SD [%]	0.07	0.05

Table 3.2: Tait model parameters were employed to derive the density as a function of pressure. SD is the standard deviation.

Using the Tait equation, density of benzyl benzoate and squalane were extrapolated, including conditions where a glass transition may occur.

As mentioned previously, for benzyl benzoate and squalane, the Tait model is fitted on density measurements performed over low ranges of pressure. This density model for benzyl benzoate has already been compared to results from dynamic molecular simulations in [94] for pressures up to 2 GPa. Data are in good agreement, with a relative difference of order of 2% at 2 GPa for the three temperatures tested, which validates the Tait law up to this pressure. The same validation is presented here with squalane in Figure 3.2. The maximum relative error for the three temperatures tested is also of order of 2%.

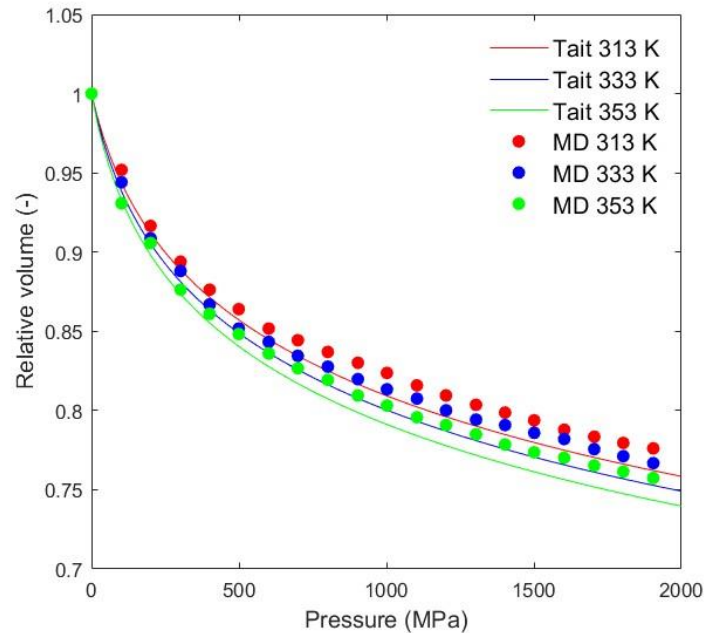


Figure 3.2 : Comparison between the Tait density predictions for squalane sample and results from molecular dynamic simulation [94].

A simplified Tait equation has been also fitted for the glycerol in literature, considering no dependence with temperature. Coefficients of the law are determined at 22.5 °C in [190]. They were fitted on experimental data of relative volume taken in the range of [0-1176] MPa

from [191]. The reference density at 20°C comes from [192]. Coefficients of the law are determined at 22.5 °C in [190].

When the density is estimated, the refractive index n of the fluids may be derived with the equation of Lorentz-Lorenz or called Clausius-Mossotti [19] (2.24). It will then be used to calculate the phonon scattering wavevector \vec{q} according to (2.14). For that, it is assumed that the coefficient of polarizability of the Lorentz-Lorenz equation is constant with pressure over the range of tested pressures, as found in [55,58,59,173]. Its value is taken from [19] for the glycerol. For benzyl benzoate and squalane, it is adjusted so that the refractive index resulting from the Lorentz-Lorenz law at 20°C and atmospheric pressure matches the measured refractive index in the present study with a refractometer ABBEMAT 300 (Anton Paar), at 20°C and atmospheric pressure. This calculation also requires the fluid density at the same conditions. The density measured at 20°C and atmospheric pressure with a densimeter Anton Paar DMA4500M were used. Table 3.3 summarizes key material characteristics: ρ is the density, n the refractive index, α the polarizability and P_g the glass transition pressure.

Material	ρ [g/cm ³] @ 20°C and P_{atm}	n @ 20°C and P_{atm}	α [cm ³]	P_g [GPa] by WLF @ 20°C
Benzyl benzoate	1.119	1.5694	24.67*10 ⁻²⁴	0.8
Squalane	0.8094	1.4521	55.88*10 ⁻²⁴	1.446
Glycerol	1.262 [179]	1.4758	8.17*10 ⁻²⁴ [19]	3.8

Table 3.3 : Measurements of density and refractive index at 20°C and atmospheric pressure for the three fluids and glass transition pressure estimated by the WLF model. α the polarizability is calculated at atmospheric conditions.

3.2. Brillouin set-up

The following part is dedicated to the description of the experimental set-ups used to conduct Brillouin spectroscopy measurements. The principle of the Brillouin light scattering was described earlier in Chapter 2. We might just recall that two parameters will be extracted from the Brillouin spectrum: f_b the frequency shift and Γ_b the full width at half maximum (FWHM). To give an order of magnitude, a fluid at atmospheric pressure has a frequency shift in the GHz range. A Brillouin frequency shift peak at 10 GHz is equivalent to 0.3 cm⁻¹ in wavenumber, and the diffusion peaks are actually at a distance of 10 pm from the incident laser wavelength (Rayleigh). Therefore, it requires spectrometers that fully filter the contribution of the elastic scattering (i.e. with a very high rejection of the Rayleigh scattering) despite the very small distance to the inelastic light scattering. The two most widely used instruments for Brillouin spectroscopy are the Fabry-Pérot-based spectrometer and more recently the VIPA (virtually imaged phased array)-based spectrometer. These two spectrometers were used in this work. A schematic view of the whole experimental set-up is given in Figure 3.3 showing the simplified light path through the equipment. A monochromatic laser is coupled to an optical microscope to focus the beam on the sample and

collect the backscattered light. The output beam is collected toward the Fabry-Pérot or the VIPA spectrometer. Finally, the signal is recorded by a detector and software associated with the spectrometer equipment. Each component of both set-ups will be described separately in the following sections.

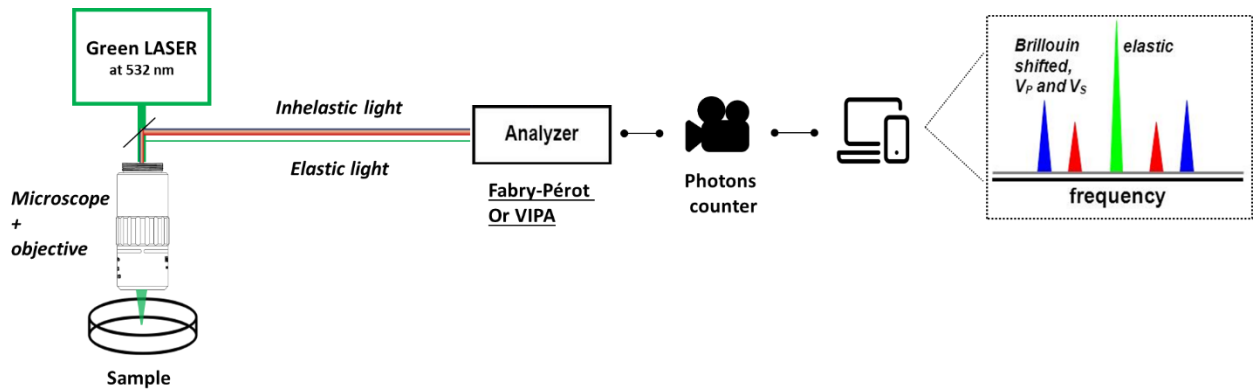


Figure 3.3: Schematic of the whole experimental set-up, from the laser to the Brillouin spectra

3.2.1. Fabry-Pérot Brillouin spectrometer

In the seventies, J.R. Sandercock et al. [193] started to develop the Brillouin spectrometer based on the combination of two Fabry-Pérot (FP) interferometers, working in tandem. It is commercially called the 6-pass tandem Fabry-Pérot (TFP-1, Table Stable Ltd) Brillouin spectrometer. A scheme of the TFP-1 is given in Figure 3.4.

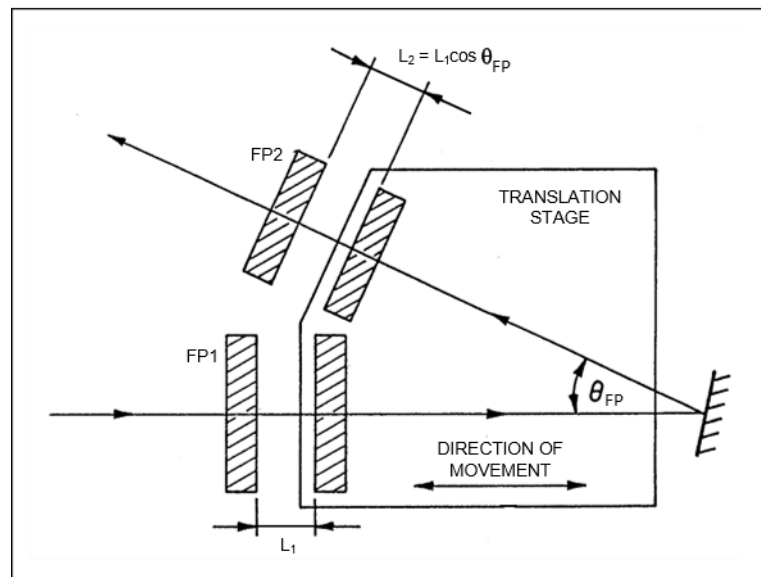


Figure 3.4 : Optical path inside the 6-passes Fabry-Pérot Brillouin spectrometer noted FP1 and FP2. The angle between this two FP is called θ_{FP} . This graph is taken from the user manual [194].

The TFP-1 is based on two Fabry-Pérot interferometers arranged in series with a slight angle in their relative orientation that conditions the transmitted wavelength depending as mentioned previously on the spacing L in the Fabry-Pérot, the finesses F , and the wavelength

used. The two FP have to satisfy a certain length $L_2 = L_1 \cos \theta_{FP}$ to be able to transmit light in the tandem mode.

This spectrometer is based on the ability of the Fabry-Pérot interferometer to distinguish two sequential peaks from the MHz to the GHz. This interferometer is an optical cavity made from two perfectly parallel and flat semi-reflective mirrors that have 95% reflectivity. The quality of the spectrum is determined by the finesse $F = \Delta\lambda / \delta\lambda$ where $\Delta\lambda$ is the distance between the transmitted laser peaks and $\delta\lambda$ its width, combined with other parameters like the cavity and the pinhole size. Those parameters are presented in Figure 3.5. The finesse F system depends on the mirror's reflectivity R and L the mirror spacing: $R_{FP} = F * 2L / \lambda$. At 532 nm, the typical finesse is about 60. For a given distance L between both mirrors, only some wavelengths will be transmitted. The transmittance [- or in %] [154] is expressed as :

$$T_{FP} = \frac{\tau_{0_{FP}}}{1 + \left(4 * \frac{F^2}{\pi^2}\right) * \sin^2\left(\frac{2\pi L}{\lambda}\right)} \quad (3.7)$$

where $\tau_{0_{FP}}$ is the maximal transmission of the system, its value is inferior to 1, which determines losses in the system. λ is the wavelength of the laser transmitted.

In this later configuration (Figure 3.4), both mirrors are mounted on a translatable stage. First, the scan is ensured by piezoelectric transducers that shift around 2.5 μm from the rest position. Secondly, the mirror spacing sets the Free Spectral Range (FSR), which is the spectral window of the experiment, equal to $2 * \Delta\lambda$. The mirror spacing is generally between 30 μm and 30 mm, which corresponds to the analyzed range between 2.5 GHz and 2.5 THz. The proper mirror spacing and scan have to be set according to the Brillouin signature of the sample.

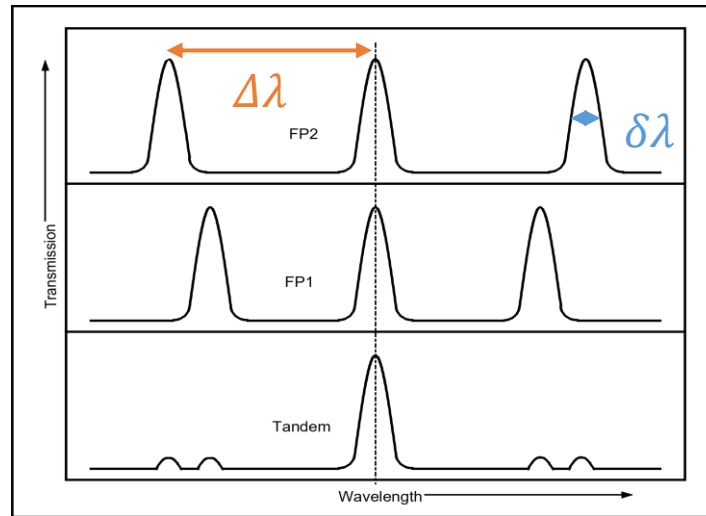


Figure 3.5: Transmission spectra of the FP cavities 1 and 2 and the final tandem spectrum. This graph is taken from the user manual [194].

For the first FP, the cavity length named L_1 conditions the light that is transmitted through constructive interferences. Only the wavelength λ that validates the following equation is transmitted through the cavity:

$$L_1 = \frac{1}{2} p \lambda \quad (3.8)$$

Where p , an integer, corresponds to the number of wavelengths that will be transmitted.

Similarly, the same logic applies to the second FP:

$$L_2 = \frac{1}{2} d \lambda \quad (3.9)$$

where d is an integer.

The resolution depends on the FSR set previously and also the acquisition channel. In our experiments, each spectrum is recorded on 1024 data points. To reduce acquisition time, 512 or 256 data points are accessible but in the detriment of the resolution.

The associated camera is an avalanche photodiode iDus DU 401 CCD BVF, with a thermo-electric cooling to -100°C , that allows reducing significantly the dark current down to 0.003 electrons/pixel/sec at maximum cooling. Moreover, the quantum efficiency, which is the capacity of an imaging device to convert incident photons into electrons, is around 95% at 532 nm.

Even if the performance of the Tandem Fabry-Pérot allows to probe extremely small samples, the acquisition time remains quite high. For thin confined films, this time varies between 30 min and one hour. In situ conditions/experiments in lubricated films requires a Brillouin spectrometer able of recording a signal in the shortest time possible in order to minimize the lubricant heating due to high shearing in the contact.

3.2.2. VIPA spectrometer

The VIPA spectrometer is a new generation of interferometers used for Brillouin spectroscopy. It is based on an etalon, which is a transparent glass block described later in this section. The system used is built by LightMachinery (Light Machinery, Hyperfine HF-8999-532). A schematic of the designed etalon is given in Figure 3.6.

The etalon has two walls perfectly parallel and flat. Two coatings with different reflectivity are deposited on the surface of each wall: one to produce a total reflection and the other one to allow a partial transmission. On the pure reflecting face of the etalon, a window without coating located at the bottom of the block allows the incoming light from the microscope (and from the sample) to be focused inside the etalon by a cylindrical lens. As a result, each wavelength contained in the incoming light is transmitted by the VIPA with a different angle θ_λ .

Then, the various orders of interferences and wavelengths are dispersed only in the vertical direction (unlike the FP etalon). Then, because orders of the transmitted light can overlap, a cross-dispersing element is added. The light is dispersed in the horizontal direction by a reflective grating. The resulting pattern of white light is shown in Figure 3.7. This grating is located after the VIPA and before the camera (Figure 3.8).

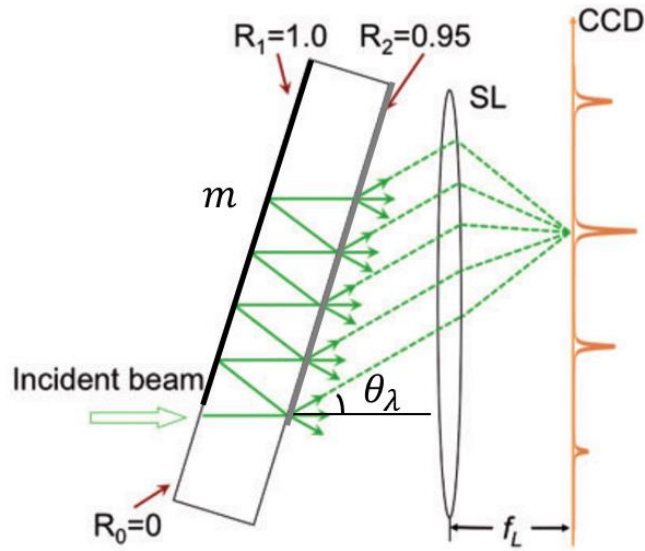


Figure 3.6 Schematic of the VIPA etalon principle on the left, the spherical lens in the middle, and the CCD camera on the right. The refractive index n of the etalon, θ_λ the angle of the transmitted beam. The m correspond to constructive interferences [195]. R_1 and R_2 correspond to the reflectivity of each surface. R_0 is the window with 100% transmittance.

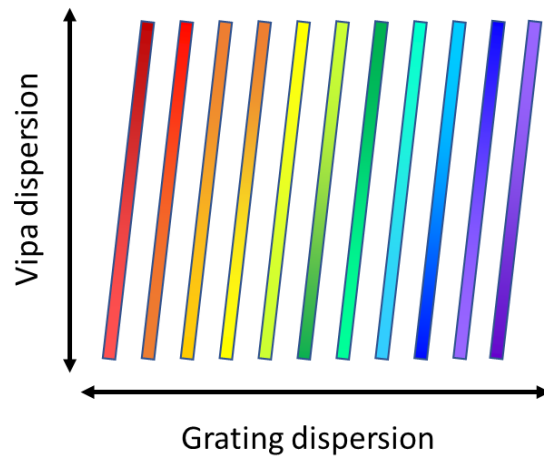


Figure 3.7: Schematic of the white light dispersion made by the VIPA vertically and by the grating horizontally. The color bars represent the wavelength dispersion with a continuous source (white light) *Image Credit: LightMachinery.*

This grating is located after the VIPA and before the camera (Figure 3.8).

The FSR is essentially determined by the thickness of the etalon and the material used. The etalon provided by Lightmachinery is 1.686 mm thick with a reflective index of 1.4607, leading to a FSR of 60 GHz, [531.94 ; 532.06] nm or $\pm 2.0\text{cm}^{-1}$ with a resolution of 0.2 GHz and a finesse of 13.5.

The acquisition of the Brillouin signal is done by a sCMOS camera Iris9, 9 Megapixel, air-cooled, with a quantum efficiency of 73% at 532nm. It is designed for low luminosity

measurements with a dark current of $0.5e^-/\text{pixel}/\text{second}$ and a read noise of $1.5e^-$. The acquisition time range is between 0.0025 s to 20 seconds. The spectrometer includes two tunable 30 dB Rayleigh suppressors named Pump Killer and consist of an air-spaced etalon. The etalon used for pump suppression has (nominally) a finesse of 15, 83% of reflectivity, 4.5 GHz of transmission bandwidth, and a FSR of 70 GHz. One is included in the main spectrometer box as shown in Figure 3.8. Another one is installed on the side of the spectrometer. The pressure inside the suppressor, to minimize the central Rayleigh peak, is controlled by the software.

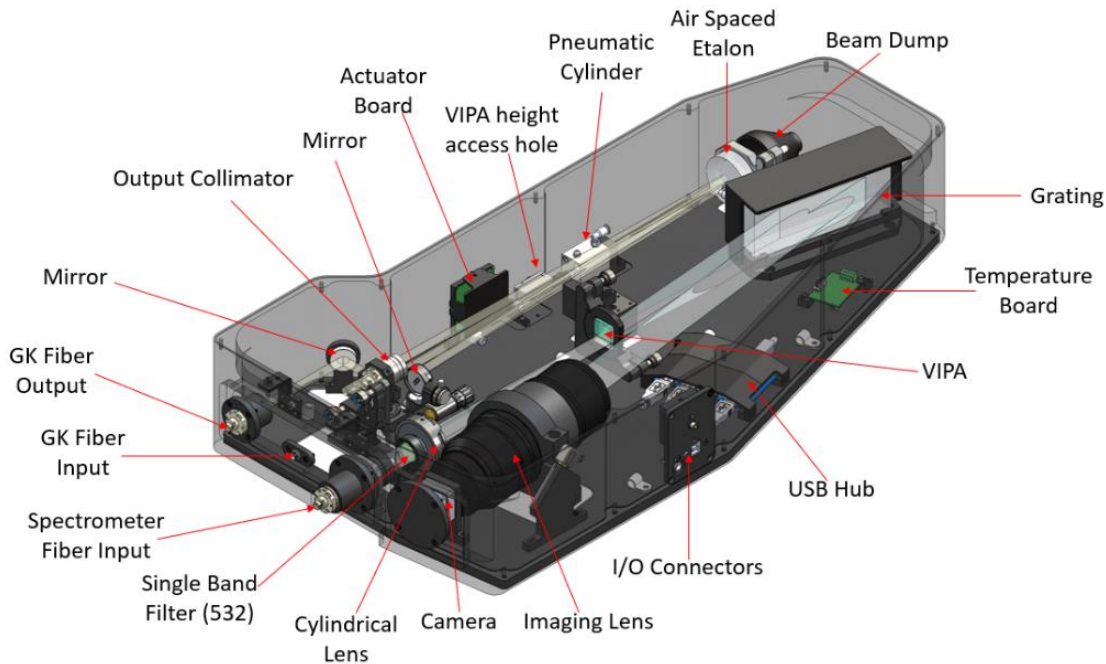


Figure 3.8 : Sectional view of the VIPA spectrometer with the optical path from the light machinery website *Image Credit: LightMachinery.*

This technology enables the rapid acquisition of a Brillouin spectrum, in few seconds, which is faster compared to the TFP interferometer. It is therefore very interesting for further in situ measurements in a fluid confined in a tribological contact. Therefore, the VIPA technology was further chosen over Fabry-Pérot because of the fast data acquisition. However, as the VIPA technology was implanted during the thesis, both results obtained with TFP and VIPA spectrometers will be given in the following chapters. A comparison between the two techniques will be done. Some advantages and drawbacks of both spectrometers are listed in Table 3.2.

A comparative study in 2020 from the ILM team reveals a similar feature as mentioned in Table 3.4 [196]. The uncertainty reported in the article is about 5 MHz for the frequency shift and 20 MHz for the FWHM in both techniques. The frequency shift is quasi-identical in both techniques but the linewidth can have about 75 MHz difference.

Fabry-Pérot		VIPA	
Advantages	Drawbacks	Advantages	Drawback
-High contrast (150 dB)	-Long acquisition time (30) min	Fast acquisition (\leq s)	-Contrast (80 to 120 dB)
-High stability in time	-Expensive vibration isolator system		-Optical fibers signal in the spectra
-Tunable FSR			-Fixed FSR
-Accumulation for weak signal			-Unstable laser position on the spectrum (Require an expensive correcting software)
			-Limited acquisition time (20s)

Table 3.4 : Advantages and drawbacks of each spectroscopy technique.

3.3. Microscopes

As previously mentioned, both TFP-1 and VIPA spectrometers were used. The TFP-1 spectrometer is located at the Matter and Light Institut (ILM) at Lyon 1 University, whereas the VIPA spectrometer is located at LaMCoS (Laboratory of Mechanics of Contacts and Structures), INSA of Lyon. Consequently, the whole experimental configuration is different between both techniques and will be described in the following part.

3.3.1. ILM set-up

The first set-up provided by the ILM is composed of an inverted bioscience microscope Nikon eclipse TI-U with a 20 \times Mitutoyo objective lens (N.A. 0.35) to obtain a \sim 10 μ m laser spot diameter in air. The set-up is well described in [196]. In the case of inverted microscopes, the objective is located under the sample. A beam splitter 50/50 is situated on the base of the system to separate the incoming and the scattered light. The Fabry-Pérot and microscope are directly coupled (without an optical fiber).

The monochromatic source is provided by a continuous wave at 532 nm Diode-pumped solid-state laser (DPSS) Torus (from Laser Quantum), that possesses a spectral linewidth of 1 MHz, a noise below 0,25% RMS and a power stability of less than 1% RMS. Later, in May 2020, it was replaced by a 532nm DPSS Excelsior laser (from Spectra-Physics). The spectral linewidth is less than 10 MHz (0,01 pm), the noise <0.2% RMS and it has the same power stability as the Torus one. Both lasers have a vertical polarization and a single longitudinal mode. The wavelength is situated in the green color because the intensity of the scattered light has a dependency of λ^{-4} .

3.3.2. LaMCoS set-up

The second set-up has been designed and developed during the present work at LaMCoS. It is composed of a microscope, a laser, and the VIPA spectrometer, all indirectly coupled with several single-mode optical fibers.

The tailor-made microscope can be coupled with different other tools such as high-pressure cells, a rheometer and a tribometer, and secondly to work with the both geometry configurations for Brillouin spectroscopy (backscattering and platelet, see Figure 2.11). during this thesis, the coupling with high-pressure cells and an optical rheometer in the backscattering configuration was successful and will be described in the following section. However, several attempts with the tribometer and the platelet geometry needed some additional work and technical improvements to provide results. This part will be detailed in the perspective section of this work.

The microscope is composed of three optical units referenced A, B, and C. These units can be coupled or not, according to the whole experimental design.

During the thesis, the coupling with high-pressure cells and an optical rheometer with the unit A in the backscattering configuration was successful and will be described in the following section. However, several attempts with the tribometer and the platelet geometry needed some additional work and technical improvements to provide results. This part will be detailed in the perspective section of this work.

Unit A:

Unit A is detailed in Figure 3.9. This unit is dedicated to backscattering Brillouin spectroscopy and can be coupled with high-pressure cells, a rheometer and a tribometer. It is composed of 3 stages to send back the beam to a camera (for optical observation), the VIPA (Brillouin spectroscopy) and the Ocean spectrometer (pressure calibration with ruby luminescence when a high-pressure cell is used, see section 3.4). Each optical output is equipped with an XY slip plate for coarse adjustment of 1mm and a tilting stage with a sensitivity of 7 mrad/rev.

The output beam collimator toward the Brillouin VIPA spectrometer is realized by a protected silver reflective collimator installed on a tilting adjustment. It is a light, achromatic and compact solution using a parabolic mirror.

The optical visualization of the area of interest is done with a white light coaxial lamp combined with a color Alvium 1800 U CMOS USB camera with a 2064x1544 pixels resolution on a 7.12x5.32 mm² detector. The light is then focused by a precision eyepiece adaptor Navitar X1.

For the ruby luminescence part, a similar silver reflective collimator is used.

The input laser is filtered by a notch filter at 532 nm followed by a half-wave plate to clear the polarization that shifted inside the optical fiber. It is a 488-633 nm FC/APC mono-mode fiber (SM450 3 μ m core) with an attenuation ≤ 50 dB/km at 488 nm, which is a 4 m long. Even

if the fiber is quite long, the laser coupling in the backscattering geometry, using a mirror is beyond than 30% into the mono-mode fiber.

Unit A is attached to the microscope structure with a micro-positioning XYZ stage (Figure 3.10) allowing a translating stroke of 40 mm, which is compatible with the required translation in the DAC, rheometer or tribometer configurations. Unit A together with the XYZ stage can slide on a circular track (arch) attached to a metallic support. It enables to tilt the microscope around the sample. Finally, the metallic support can also slide onto an additional translating stage of 40 mm in X (Figure 3.9) for a faster displacement in DAC, the rheometer (along a radius), or the tribometer (in the fluid entrainment direction) while keeping the optical alignment.

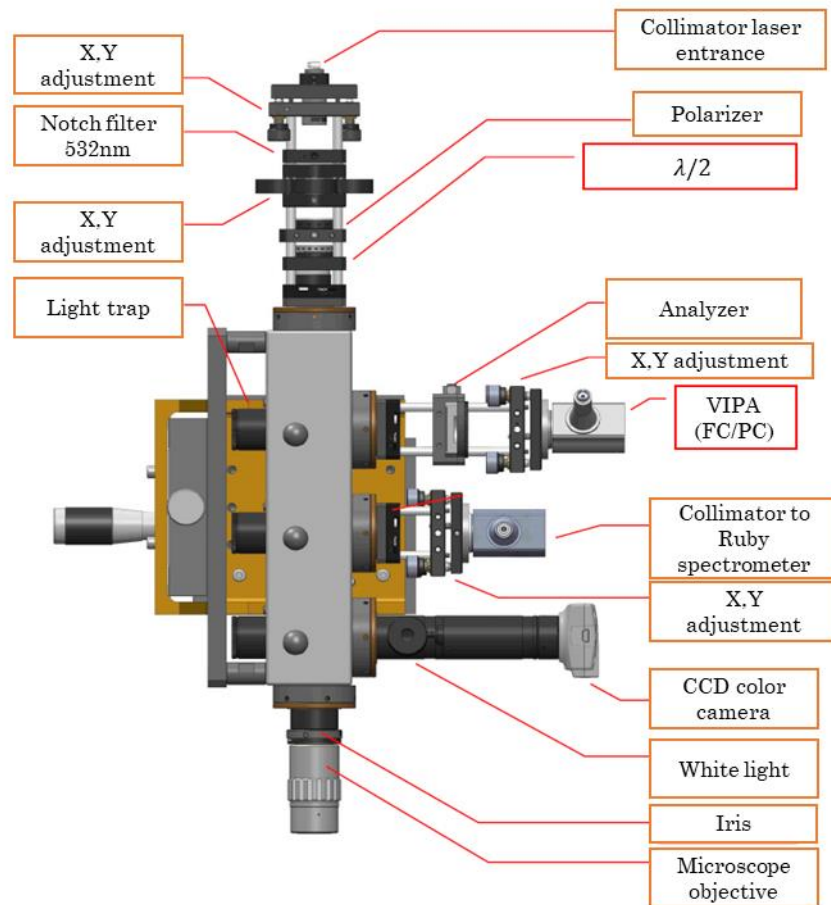


Figure 3.9 : The microscope unit A is represented with the description of all its elements.

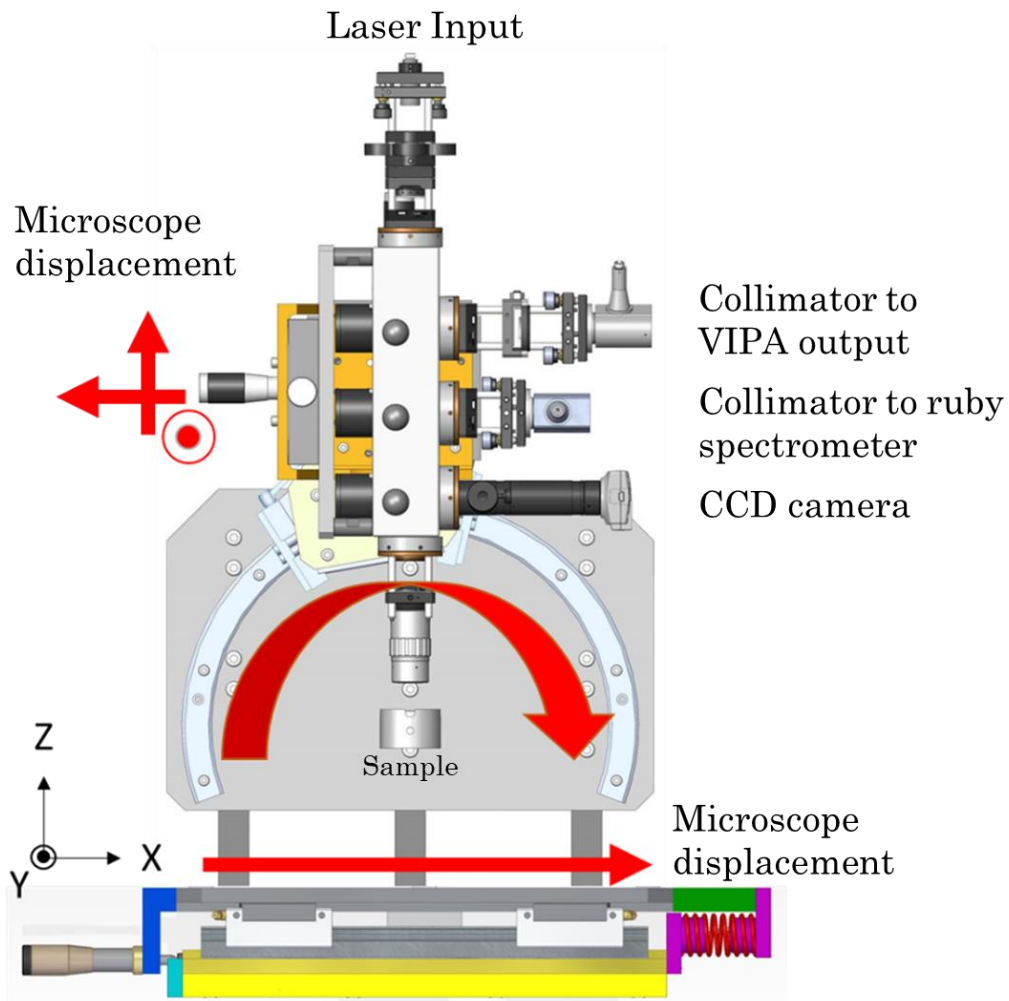


Figure 3.10 : The microscope Unit A is attached to an arch segment of 220° . It possesses 3 degrees of freedom from 3 linear stages of 40 mm travel represented by 3 red arrows. An additional linear stage in the X direction translates the complete support (Unit A on the Figure).

The spot size in the backscattering geometry was measured using the Brillouin spectroscope and squalane. The resulting spot size with a x10 (MY10X-803) and x20 (MY20X-804) long-distance Mitutoyo objective with a working distance of 34 mm and 20 mm respectively is below $10\ \mu\text{m}$ in diameter. However, the resolution of the linear stage is higher than $5\ \mu\text{m}$. The method used to measure the spot size with precision is detailed in the Appendix B and inspired from Jubault et al [197].

Unit B and C:

Unit B and C were designed to work in tandem for oblique geometries (platelet configuration). The arch was designed to hold the two units B and C. Unit C is the laser injection unit (optical visualization and VIPA/ruby luminescence outputs to do angled backscattering for the tribometer set-up which could help avoiding the Rayleigh contribution in the spectrum) and unit B is the collection one (VIPA and ruby luminescence outputs). A scheme of this configuration is given in Figure 3.11. The inclination is monitored by two dual-axis inclinometers $\pm 45^\circ$, which display angles at $\pm 0,001^\circ$ and installed behind each platform. Laser input and optical visualization of the Unit C is the same that of the Unit A. More detail about the unit B and C is accessible in Appendix C.

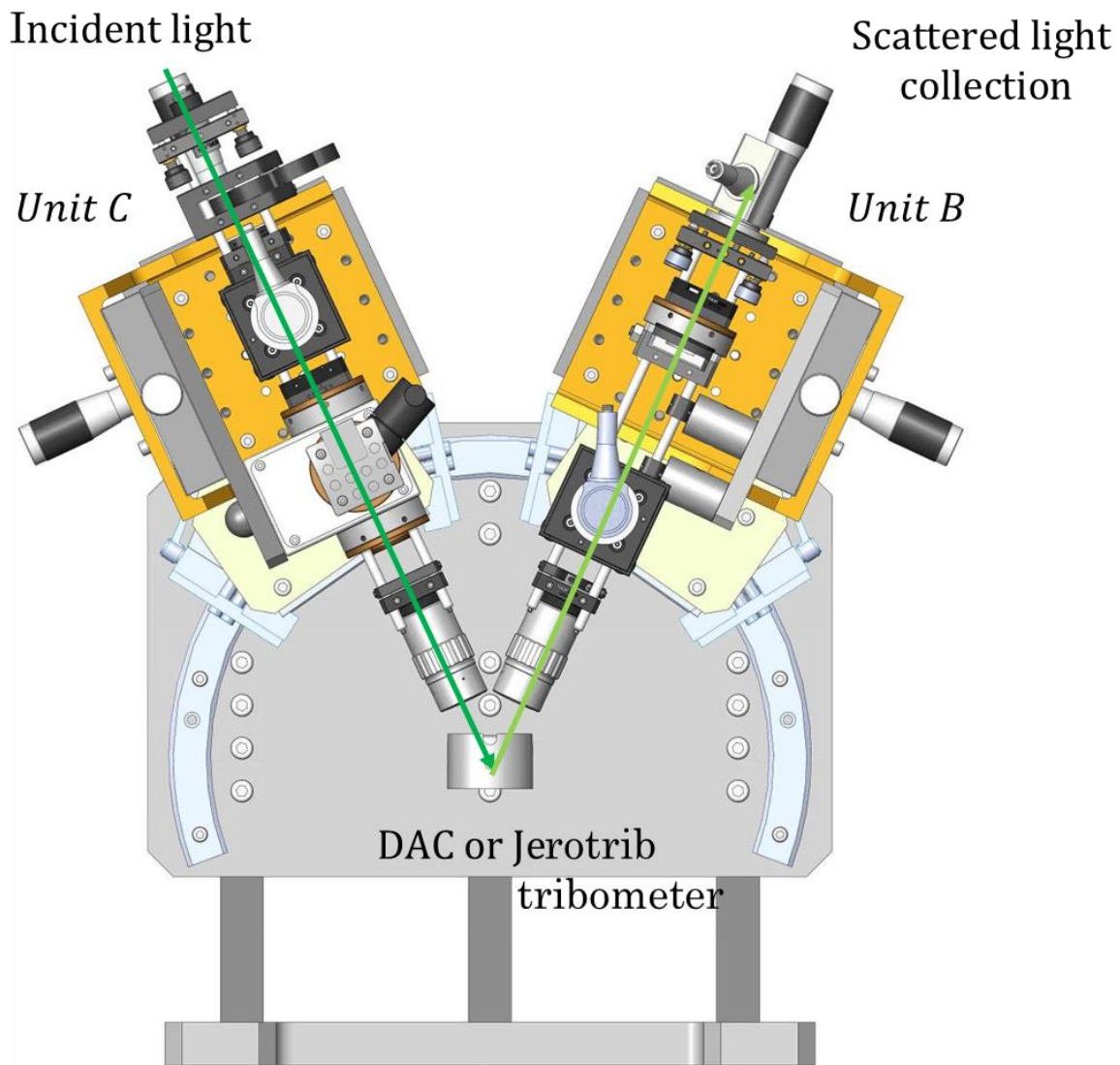


Figure 3.11 : Schematic of the oblique set-up. The left bloc (Unit C) is designed to inject the incident light, visualization, and ruby spectra analysis. The Unit B on the right is created to collect the inelastic scattering.

As explained in Section 2.2.3, this configuration is very interesting since it is not dependent on the refractive index. In addition, Brillouin spectroscopy coupled with a high-pressure cell allows extracting the pressure and temperature dependence of the refractive index, thus the density, according to the equation 2.21. It is important to extract the refractive index and the density as a function of pressure and temperature as presented in Section 2.2.3. Moreover, the oblique orientation gives access to the transversal mechanical properties and signature of glassy materials [198].

This part (3.2 and 3.3) presented the optical microscopes and spectrometers, used during the study. First in the Light and Matter Institute provided an inverted microscope connected by air to a tandem Fabry-Pérot interferometer TFP-1 working at 532 nm in Sections 3.2.1 and 3.3.1. Then LaMCoS set-up equipped with the microscope built for backscattering (A unit) and angular measurement (B and C units) were presented in Section 3.3.2. It is coupled with optical fiber to the VIPA-based interferometer in Section 3.2.2.

Sections 3.4, 3.5 present the high-pressure devices (P, T), and the tribometer ($P, T, \dot{\gamma}$) set-ups that will be coupled to the spectrometer. The rheometer ($\dot{\gamma}, T$) description is available in appendix E.1.

3.4 High-pressure cells

3.4.1 High-pressure cells design

To identify the pressure and temperature dependence of the glass transition in the lubricants, a Diamond Anvil Cell (DAC) was coupled to the Brillouin spectroscopy set-ups.

Two types of DAC were used in this work. The first one is equipped with two diamond anvils with a classical symmetrical design (Le Toullec type) allowing experiments up to 10 GPa (referenced as “high pressure” in the next chapter). The second one is equipped with a diamond anvil and a diamond window with 100° symmetrical aperture (M-DAC-BHP, Betsa). Given the diamond anvil culet size (1.4 mm), the maximum pressure achievable is 1.2 GPa (referenced as “low pressure” in the next chapter).

Benzyl benzoate, squalane, and glycerol were characterized using the Toullec high-pressure (< 10 GPa) diamond anvil cells whose characteristics are reported in Table 3.5. Only the benzyl benzoate was studied with both DAC, the low-pressure (< 1,2 GPa) and the high-pressure DAC.

A cross-section view of the DAC (Le Toullec) is given Figure 3.12. No cross-section view of Betsa cell is provided since the DAC structure is identical, only the diamond anvil of the bottom part is replaced by a flat diamond window.

	Low-pressure DAC (Betsa)	High-pressure DAC (Le Toullec)
Diamond characteristics	Type Ia, standard design, (100)-oriented, ultra low birefringence	Type Ia, standard design, (100)-oriented, ultra low birefringence
Maximum pressure	1.2 GPa	10 GPa
Hole size for visualization	500 μm	200 μm
Fluid volume	0.1 μL	0.004 μl
Diamond window	4 mm diameter and 0.6 mm in thickness	N/A
Diamond anvil height	<1.95 mm	2 mm
Culet size diamond anvil	1.40 mm	0.60 mm
Gasket size and material	washer shaped 400 μm thick, 4 mm diameter, nickel	square shaped 200 μm thick, 5,2 mm x 5 mm, stainless steel 301

Table 3.5 : Characteristics of the two DAC used.

The DAC is composed of two diamond anvils separated by a hollow steel gasket, where the tested fluid is confined, ensuring the cell sealing. Each diamond was properly aligned to generate a hydrostatic pressure in the sample. The anvils are supported by tungsten carbide seats, mounted on two plates (in purple on Figure 3.12). The lower plate is screwed on the cover and is the fixed part. The upper plate can move vertically thanks to four steel guides sliding inside the fixed plate. The motion is induced by a force generated by an inflated membrane represented by two orange rectangles in Figure 3.12. The gasket is initially indented between the two diamond anvils and then drilled at the center of the indented area. A photo of the drilled gasket is shown in Figure 3.13. A gasket holder is used to keep the gasket in the same position during the indentation process and the sample-filling process.

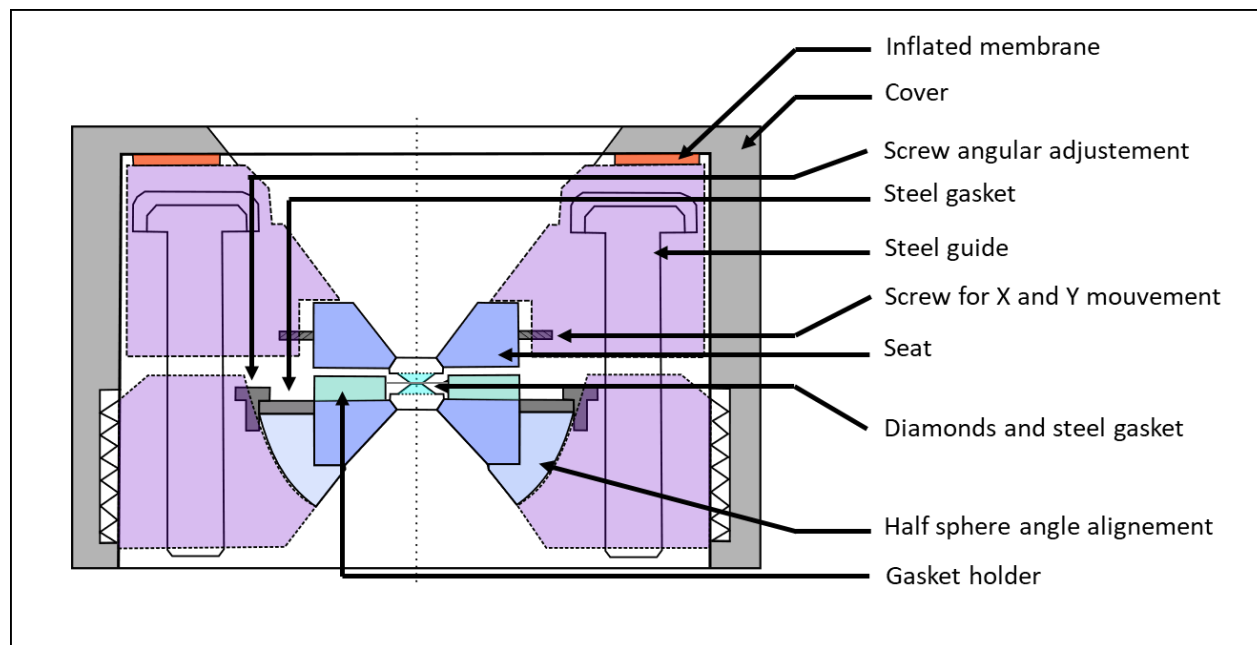


Figure 3.12 : Sectional view of the double diamond DAC (HP Toullec).

The hole is about 200 μm in diameter. In the case of the low-pressure cell (Betsa), the gasket is drilled without being pre-indented to obtain a 500 μm diameter hole.

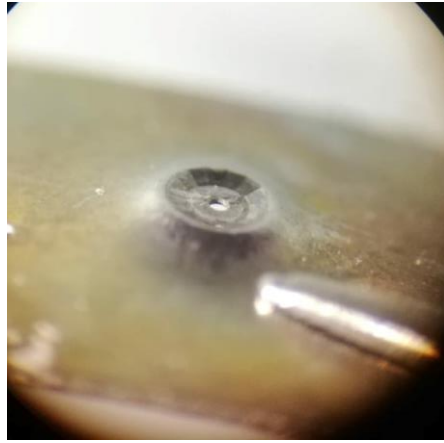


Figure 3.13 : Side view of the steel gasket taken by a binocular microscope. The indentation by the two diamonds is visible. The hole at the center measures 200 μm in diameter.

The temperature of the sample is measured thanks to a thermocouple placed as close as possible to the confined fluid (by touching the gasket). The temperature is then measured with a precision of ± 1 K.

3.4.2 Determination of the pressure inside the DAC

The pressure inside the sample is given by the luminescence of microparticles (3-50 μm diameter) of ruby introduced into the gasket hole. An example of the sample and the ruby deposited in the gasket hole is given in Figure 3.14.

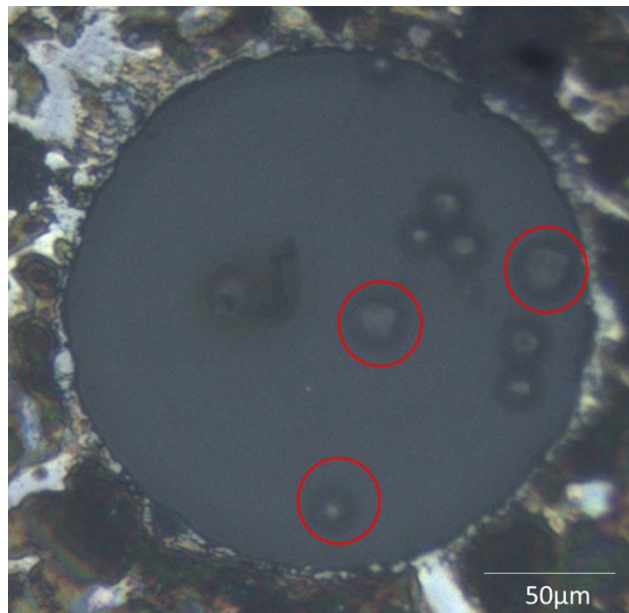


Figure 3.14 : Example of a loaded DAC with squalane and isolated rubies circled in red in a diamond anvil cell. The hole is 200 μm in diameter. Each ruby is around 10 to 20 μm in diameter.

Ruby doped with Cr^{3+} provide a double peak luminescence between 691 and 694 nm as shown in Figure 3.15. According to a previous work about pressure calibration with ruby published in 1992, the R1 peak is more reliable and easy to use [45]. The photoluminescence shift of the R1 peak was calibrated under hydrostatic pressure by Moa and al. (1986) [44] and with temperature correction by Datchi and al. (2007) [199]. The pressure is given with a precision of +/-50 MPa.

The ruby luminescence signal was recorded with dedicated spectrometers.

For the ILM set-up, an Andor Technology - SHAMROCK - SR-303I-A Spectrograph that has a tunable grating for light diffraction is used.

For the LaMCoS set-up, a high-resolution Ocean Optics spectrometer HR4000 with a [640 - 730] nm spectral window, using a linear Toshiba CCD array of 3648 pixels. The grating used is the H11 1800 lines/mm combined with a 5 μ m slit at the spectrometer entrance that enables a 0.05 nm f on the FWHM according to the constructor specification. The spectrometer is connected to the microscope with a 400 μ m diameter fiber (0.22 NA). The detector is protected by a long pass filter at 550 nm to cut the backscattering of the laser beam.

Due to possible small room temperature fluctuations leading to a possible drift of the spectrometer detector, small errors on the ruby peak position could be observed, resulting however in rather large errors in pressure estimation. Therefore, a Neon spectral lamp (using the narrow peak at 703.24 nm) was used as a reference to correct the ruby peak position for each spectrum. Ruby and neon peaks were adjusted by multiple Lorentz fits to determine the wavelength positions. A typical obtained spectrum is shown in Figure 3.15. R2 and R1 correspond respectively to the first and the second peak of the ruby luminescence and the fit result is provided in Table 3.6. Here, the neon peak is measured at 702.64 nm instead of 703.24 nm. Then, R1 peak position will be corrected according to the difference between these two values.

It is important to select an isolated ruby to avoid the measure the luminescence response of a ruby bundle. For the experiments conducted with the VIPA set-up, in order to improve the accuracy of the pressure measurement, at least 3 isolated rubies were used to calibrate the pressure in the DAC. It enables to take into consideration the possible dispersion of the pressure inside the DAC, in particular when hydrostatic conditions are no longer valid.

The pressure inside the DAC is increased thanks to the inflator linked to the membrane. The pressure in the membrane is increased by step of 0.01 bar every second and stabilized at the desired pressure during 30 min [38]. Then ruby spectrum is recorded to determine the pressure. Moreover, the ruby spectrum was recorded before and after Brillouin measurements for a given pressure. An average of the two measures is calculated to take into account a potential variation of pressure between the beginning and the end of the Brillouin spectrum recording.

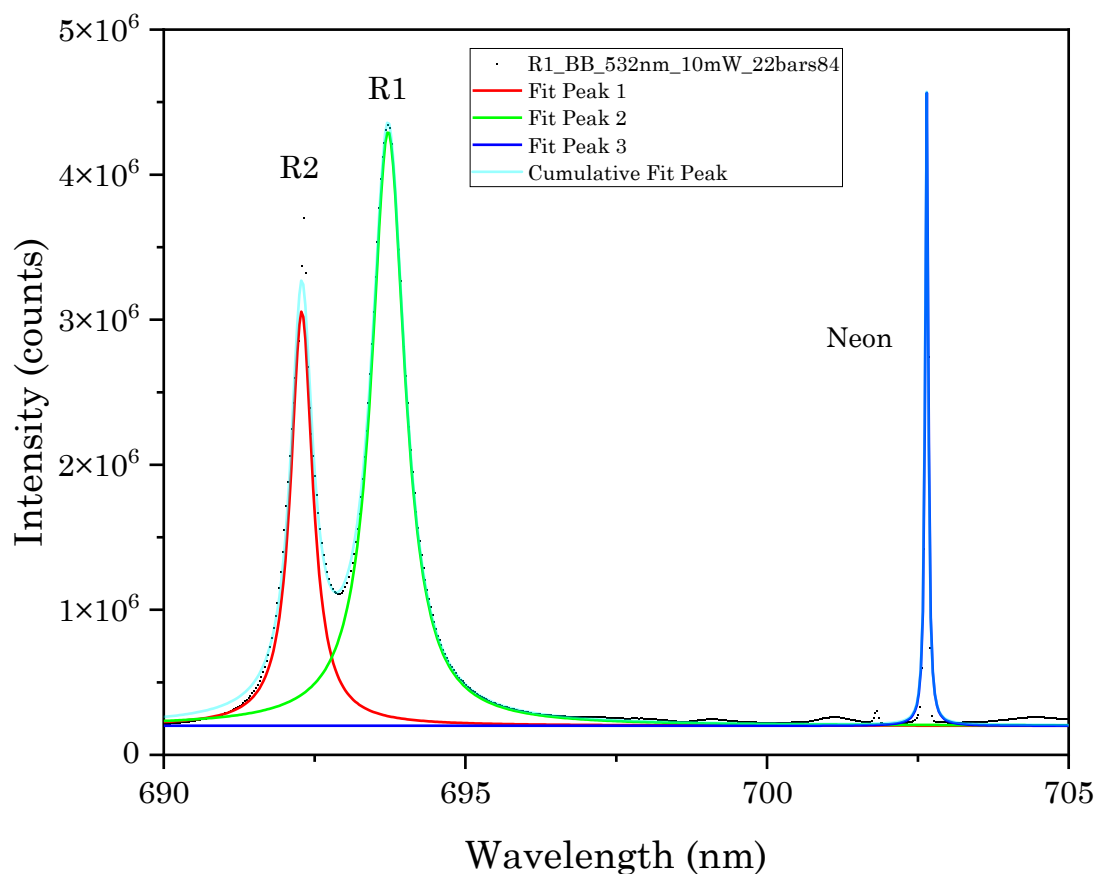


Figure 3.15 : Extraction of the position of each peak of the ruby luminescence R1, R2 and the neon spectral lamp peak. Each peak was fitted using Lorentz function.

Model	Lorentz					
Equation	$y = y_0 + (2*A/\pi)*(w/(4*(x-xc)^2 + w^2))$					
Plot	Peak1(Intensity)	err	Peak2(Intensity)	err	Peak3(Intensity)	err
y0	200327.29231	1652.90791	200327.29231	1652.90791	200327.29231	1652.90791
xc	692.28719	0.00155	693.72006	0.00134	702.64803	0.000408954
w	0.44197	0.00467	0.67523	0.00409	0.06114	0.000959458
A	1984098.0553	15575.39472	4345663.59721	19566.02406	419527.20838	5021.95875
Reduced Chi-Sqr	2,315E+09					
R-Square (COD)	0.9945					
Adj. R-Square	0.99445					

Table 3.6 : fitting of 3 Lorentz from Figure 3.15

3.5. Tribometer set-up

The tribometer used in this study is a ball-on-disc tribometer called Jerotrib. It is already described in [47]. A schematic side view of the ball-on-disc contact (left) and a picture of the set-up during the experiment (right) are represented in Figure 3.16. The ball diameter is 25.4 mm and the radius of gyration may be accurately adjusted between 30 to 36 mm thank to an optical microscope located above the contact. To study a large range of contact pressure, three sets of material configurations were used: a AISI52100 steel ball against either a AISI52100 steel disc or a sapphire (Sapph) disc, and tungsten carbide (WC) ball against a WC disc.

The lower normal loads experiments were conducted with steel ball and steel disc, the intermediate normal loads with steel ball and sapphire disc, and the highest normal loads were reached with tungsten carbide (WC) ball and disc. The mechanical properties of both specimen and the fluids are given in Table 3.7.

Solid	Ball		Disc		
Material	Steel	WC	Steel	Sapphire	WC
Young modulus [GPa]	210	610	210	360	610
Poisson's Ratio [-]	0.3	0.258	0.3	0.34	0.258
Thermal conductivity [W/mK]	16	29.3	46	40	29.3
Specific heat [J/kg K]	470	194.7	470	750	194.7
Density [kg/m ³]	7850	14850	7850	400	14850
Fluid	Squalane		Benzyl Benzoate		
Thermal conductivity [W/mK]	0.14		0.13		
Specific heat [J/kg K]	1040		2058		

Table 3.7 : Mechanical properties of solid specimen and fluids used for tribological test.

The ball dips into the lubricant reservoir to ensure fully flooded conditions of the contact.

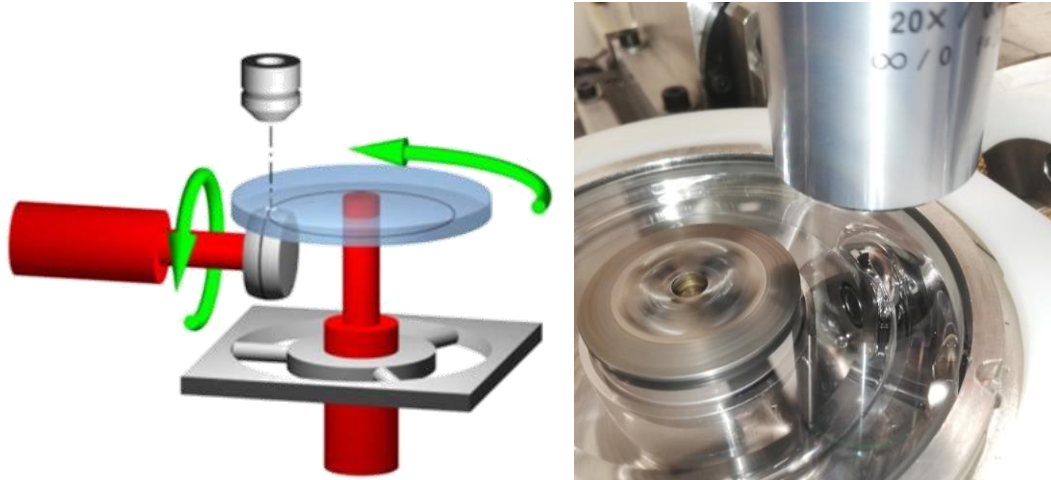


Figure 3.16 : Jerotrib tribometer schematic side view on the left-hand side. The lubricant reservoir is not represented on the schematic but is visible in the right image. Rotational axis of the ball and the disc are represented by green arrows. On top of both pictures, the microscope objective is positioned in the backscattering configuration.

The two specimens (ball and a disc) are driven independently with two motors equipped with optical encoders to apply any desired SRR with high accuracy. The slide to roll ratio (SRR) is classically defined as the ratio of the relative velocity of the solids and the entrainment velocity as already described in equation 1.1 and 1.2 from Section 1.2.3. The maximum SRR range was between [-50% - 0 - + 50%].

The entrainment velocity, defined as the mean velocity of the solid bodies, was chosen to minimize the thermal dissipation while ensuring to work in the full film lubrication regime. Those ranges were chosen to avoid shear heating which is one of the two reasons for thermal dissipation. The second reason for thermal dissipation is the to film thickness thermal reduction coefficient which influence the friction response. It was chosen above $\phi_T > 0.96$ [200]. A minimal central film thickness of order of 100 nm calculated from Chittenden equation [201] was targeted to ensure a lubrication parameter above 3 to prevent from direct contacts between asperities from three sets of materials used. It is defined as h_m/Σ

with $\Sigma = \sqrt{\sigma_{ball}^{RMS^2} + \sigma_{disc}^{RMS^2}}$. This lubrication parameter was calculated using the following measured roughnesses: $\sigma_{Steel\ ball}^{RMS} \sim 5\text{ nm}$, $\sigma_{Steel\ disc}^{RMS} \sim 10\text{ nm}$, $\sigma_{Sapph\ disc}^{RMS} \sim 8\text{ nm}$, $\sigma_{WC\ disc}^{RMS} \sim 20\text{ nm}$. The Chittenden film thickness equation for circular and elliptical contacts was discussed and recommended in [62]. The maximal entrainment velocities were adjusted to limit the shear heating in the sample, as described in [98].

Jerotrib allows to measure both friction and film thickness. The maximum applied normal load can reach 400 N. The normal force F_z and the tangential -or friction- forces F_x are simultaneously recorded with a maximum uncertainty of 0.8% and 0.3% respectively. Therefore, a friction coefficient with an uncertainty of $\Delta C_f / C_f = 1.1\%$ can be derived. Positive and negative SRR were probed and were systematically averaged to deliver mean values. Furthermore, some tests have been repeated, and lead to a mean relative standard deviation of 2.8% with a rather low dispersion, as stated in [10].

The maximum pressure found in the contact, named the Hertzian pressure P_H , is estimated by the Hertz theory:

$$P_H = \frac{3F_z}{2\pi a_H^2} \quad (3.12)$$

With a_H the contact radius, also expressed by the Hertz theory:

$$a_H = \left(\frac{3F_z R_{eq}}{2E_{eq}} \right)^{\frac{1}{3}} \quad (3.13)$$

R_{eq} and E_{eq} are the reduced radius of curvature and the reduced Young modulus of the solid bodies (ball on disc), defined as:

$$R_{eq} = \frac{1}{\left(\frac{1}{R_1} + \frac{1}{R_2} \right)} \quad (3.14)$$

$$E_{eq} = \frac{2}{\left(\frac{1 - \nu_1^2}{E_1} + \frac{1 - \nu_2^2}{E_2} \right)} \quad (3.15)$$

with R_1 and R_2 the radii of curvature of the solid bodies, (E_1, ν_1) and (E_2, ν_2) their respective Young modulus and Poisson coefficient.

From the Hertz pressure, the mean pressure \bar{P} in the contact can be derived as two third of the Hertzian pressure $\bar{P} = 2P_H/3$.

Normal force was chosen so that the mean pressure in the contact \bar{P} extends on either side of the glass transition pressure P_g of each fluid, determined by the modified WLF- Yasutomi rheological model (see 3.1). Therefore, friction was measured under nominal liquid and glassy condition.

Two lubricants were used for friction experiments: benzyl benzoate and squalane at 20°C, 40 °C and 60°C (oil reservoir temperature). A large range of normal loads was applied [31-401] N corresponding to Hertzian pressure of [0.79 - 3] GPa.

The experimental protocol followed by the benzyl benzoate and describe in reference [38,41] was also applied to squalane.

3.6 Conclusion

This chapter provides a comprehensive overview of the techniques and tools employed to investigate the behavior of lubricants under extreme pressure and shear conditions in ElastoHydroDynamic (EHD) contacts.

Initially, the selection of fluids for this study, namely benzyl benzoate and squalane, was guided by their distinct morphological shapes and physical properties. These fluids have been extensively investigated both rheologically and tribologically at LaMCoS laboratory, and also employing molecular dynamic simulations. Pressure of glass transition was investigated with the WLF-Yasutomi model. The modified Tait equation of states used as the density model was applied and extrapolated beyond the glass transition pressure. Other models were used as the Lorentz-Lorenz equation to extract optical properties from the density model, resumed in Table 3.3.

The Brillouin Light Spectroscopy technique seems to be an indispensable tool due to its non-invasive and non-destructive nature, allowing measurements on samples at rest or in motion, as long as they are transparent. The set-up includes a high-resolution and high-contrast spectrometers, such as the multi-pass Fabry-Pérot interferometer called TFP-1 and the VIPA etalon-based spectrometer. Both are enabling accurate measurement of weak signals and providing valuable insights into the material's acoustic properties.

Two experimental set-ups were presented. The inverted bioscience Nikon Eclipse microscope TI-U is presented with all optical elements. Then the set-up developed during the PhD is composed of microscopy units A, B and C, enabling to observe and analyze the behavior of lubricants with the possibility of an angular scan direction. The combination of microscopy with Brillouin light spectroscopy, rheometer, and tribometer measurements offers a comprehensive approach to studying lubricant behavior under extreme conditions.

By employing Brillouin light spectroscopy in conjunction with a Diamond Anvil Cell (DAC), static experiments will be conducted at high-pressure and temperature. A description of the DAC and the protocol to extract the pressure was presented.

The tribometer is another critical experimental set-up used in this study. It is employed to perform friction measurements in a ball-on-disc contact. The tribometer allows to investigate the correlation between the macroscopic behavior of the lubricant under extreme pressure and temperature conditions and the friction regime. By correlating the friction measurements with the Brillouin spectra data.

Overall, the instrumental set-up chapter establishes the foundation for studying lubricant behavior under extreme conditions. The next chapter will then establish the procedure that would be used to derive from spectra both frequency shift and linewidth.

4. Fitting, Software, and Setup Validation

Table of content

4.1.	INSTRUMENTAL FACTOR	129
4.1.1.	DECONVOLUTION	129
4.1.2.	NUMERICAL BROADENING	129
4.2.	VALIDATION OF THE PRESSURE EXTRACTION PROCESS	130
4.2.1.	EXPERIMENTAL SET-UP	130
4.2.2.	RUBY STANDARD DEVIATION	131
4.2.3.	BRILLOUIN STANDARD DEVIATION	133
4.3.	DATA PROCESSING: FITTING PROCEDURE	134
4.3.1.	SOFTWARE AND FITTING PROCEDURE	134
4.3.2.	SINGLE VERSUS MULTI-FIT LORENTZ PROCEDURE ON ORIGINPRO.....	138
4.3.3.	FITTING PROCEDURE: SINGLE LORENTZ VERSUS DHO FOR EACH SOFTWARE.....	141
4.3.4.	DIFFERENCE BETWEEN SINGLE LORENTZ GHOST AND MULTI-LORENTZ ORIGINPRO	144
4.4.	ASYMMETRY OF THE SPECTRA.....	146
4.4.1.	ASYMMETRY ON THE GLYCEROL SAMPLE AT LOW PRESSURE.....	146
4.4.2.	ASYMMETRY BETWEEN STOKES AND ANTI-STOKES OF THE INELASTIC PEAKS UNDER PRESSURE FOR BOTH SOFTWARES	147
4.4.3.	ASYMMETRY BETWEEN STOKES AND ANTI-STOKES INSIDE THE DAC UNDER PRESSURE FOR BOTH SOFTWARES	151
4.5.	VALIDATION OF THE PROCEDURE AND SET-UP	153
4.5.1.	COMPARISON BETWEEN VIPA AND FABRY-PÉROT MEASUREMENTS	153
4.5.2.	COMPARISON WITH LITERATURE: FLUID REFERENCE UNDER PRESSURE	154
4.6.	CONCLUSION	156

In the previous chapter, two optical devices were described. Each set-up includes a laser, an optical microscope and a Brillouin spectrometer. Each element in one device is different from its counterpart in the other device. The Brillouin spectrometers are either a conventional 6-pass tandem Fabry-Pérot (TFP-1) or a more recently developed VIPA interferometer. The VIPA-based spectrometer allows reducing the acquisition time significantly compared to the TFP-1 interferometer. However, this technology is still under development, with efforts being made to enhance its reliability and reproducibility of the measurements. Moreover, lasers and microscopes are also different in both set up. Indeed, a new microscope was designed to be able to perform angle scattering measurements at LaMCoS. The following chapter is dedicated to the signal processing of the Brillouin spectra from the two set up. Indeed, it is critical to get similar results on the principal parameters using different spectrometers and optical microscopes. This chapter will focus on the impact of the set-up used, in particular the microscope and spectrometer, as well as the fitting method and software impact on the final result.

4.1. Instrumental factor

4.1.1. Deconvolution

As stated earlier, the two parameters that will be extracted from the Stokes and anti-Stokes peaks of the Brillouin signal are the frequency shift and their Full Width at Half Maximum (FWHM). The Rayleigh contribution is reduced for both interferometers. Even if attenuated, is still visible in the spectrum. Before extracting physical parameters from the fit of the Brillouin spectra, some signal treatment has to be taken into consideration. Since the light travels through many optics and interacts with them, it is necessary to ensure that the final spectra are not distorted, particularly the FWHM. As explained in the literature [202], the Brillouin spectra exhibit broadened peaks due to the instrumental limitation. This contribution called instrumental function is evaluated for each set-up and has to be deconvoluted.

The laser signal is supposed to have an extremely small linewidth. The laser signature identified as the central Rayleigh peak on the spectrum is broadened by the set-up optical path. As result, this signal is used to determine the instrumental function. Several methods exist to determine the instrumental function contribution [183]. This can involve utilizing a solution of dispersed latex particles, employing a diffusive surface, or directly extracting it from the measured spectra. Because of the low coupling of the build microscope and the VIPA spectrometer, a mirror was used. This first approach method will be reconsidered and changed in the next studies after some microscope improvements. The obtained signal is the convolution of the spectrum with the intensity of the instrumental function (as a function of the frequency shift) taken with this method. The Rayleigh signal is fitted by a Lorentz function. As in the paper published in 2020 [196] about VIPA-based spectroscopy, the deconvolution of two Lorentz functions becomes a linear deconvolution:

$$\Gamma_B = \Gamma_{measured} - \Gamma_{IRF} \quad (4.1)$$

Where Γ_{IRF} is the instrumental response function, Γ_B is the FWHM and $\Gamma_{measured}$ is the unprocessed FWHM.

The resulting deconvoluted FWHM Γ_B is the subtraction of the measured FWHM by the instrumental function Γ_{IRF} . This procedure allows a more accurate representation of the true underlying peaks. As mentioned in the comparison paper [196] between VIPA and TFP-1 interferometers, this deconvolution is not necessary for the TFP-1. This assumption was applied during the rest of the study even if other works used the deconvolution method for this Fabry-Pérot interferometer [184,203,204].

4.1.2. Numerical broadening

Another aspect to take into consideration is the influence of the numerical aperture (NA) on the peak linewidth, even if the backscattering configuration is less affected by this enlargement for high numerical apertures. According to reference [202], this contribution is of the order of 0.1 GHz for a 0.5 NA objective. The peak displacement is more sensitive for other configurations such as a 90° geometry where the relative peak displacement can reach more than 10 % for a 0.5 NA, which represents ~0.45 GHz.

There are different ways to fit the Brillouin spectrum in order to extract the key parameters. Brillouin shift and Rayleigh may be adjusted with a Lorentzian or a DHO fit, and different combinations can be used for each option. More details will be given in the next chapter where a comparison between both experimental set-up (TFP-1 and VIPA) is also conducted.

4.2. Validation of the pressure extraction process

4.2.1. Experimental set-up

All pressure dataset from TFP-1 experiments were calculated from the only ruby present in the DAC. In the pursuit of characterizing and improving accuracy in high-pressure experiments, the homogeneity of pressure within the DAC cell has to be verified. This section presents the methods employed to assess and characterize pressure uniformity, a factor that can profoundly influence the reliability of experimental results.

Traditionally, ruby fluorescence provides a convenient means to estimate pressure in DAC experiments. Lately, the introduction of three (or more) ruby spheres into the sample chamber, with their fluorescence properties changing predictably under pressure, offered a valuable benchmark. By capturing the ruby spectra before and after the Brillouin spectra, the average of the pressure readings from these distinct points provides a representative measure of the pressure experienced by the sample as explained in Section 3.4.2. This technique, widely adopted, inherently insures a uniform distribution of pressure throughout the DAC volume, an assumption that may not hold true under all experimental circumstances as shown in [205]. To address this issue, the analysis of pressure dispersion was investigated, specifically examining the standard deviation of the pressure measurements. The evaluation of pressure standard deviation becomes particularly pertinent when dealing with very high-pressure conditions, where some a rather large dispersion has been observed [206], at large pressure where the sample properties depart from those of a liquid. It is important that the overall results calculated are based on the initial dataset.

An experiment with squalane sample under pressure was designed to answer this question using a ruby spectrometer combined with Brillouin measurements provided by the VIPA spectrometer. Figure 4.4 is the image of a gasket hollow of 200 μm in diameter of the DAC filled by squalane and 7 ruby spheres (yellow circles). The homemade microscope placed on a micro displacement stage allows to map the sample in the DAC. 12 areas (blue circles) have been chosen for the Brillouin analysis. The protocol of pressure determination is detailed in Chapter 3 Section 3.4.2.



Figure 4.1 : Microscope image taken with the VIPA set up of the DAC, loaded with ruby microspheres (black point) immersed in squalane at ambient conditions. The yellow circles indicate the ruby sphere's location, blue circles the locations where the Brillouin spectra were taken. The outer circle represents the boundaries of the 200 μm hole inside the steel gasket.

4.2.2. Ruby standard deviation

Previously, the dispersion of ruby luminescence in air was tested by Seoudi. 7 ruby particles were placed on the top of a diamond and recorded. The standard deviation has been calculated, and the dispersion found was equal to ± 50 MPa [206].

In Figure 4.2, the standard deviation (SD) has been calculated using 5 rubies (R0, R1, R3, R4 and R5) immersed in squalane to correspond to the ruby distribution found in the study of Seoudi [206]. Rubies situated on the edges position inside the DAC were excluded from the calculation.

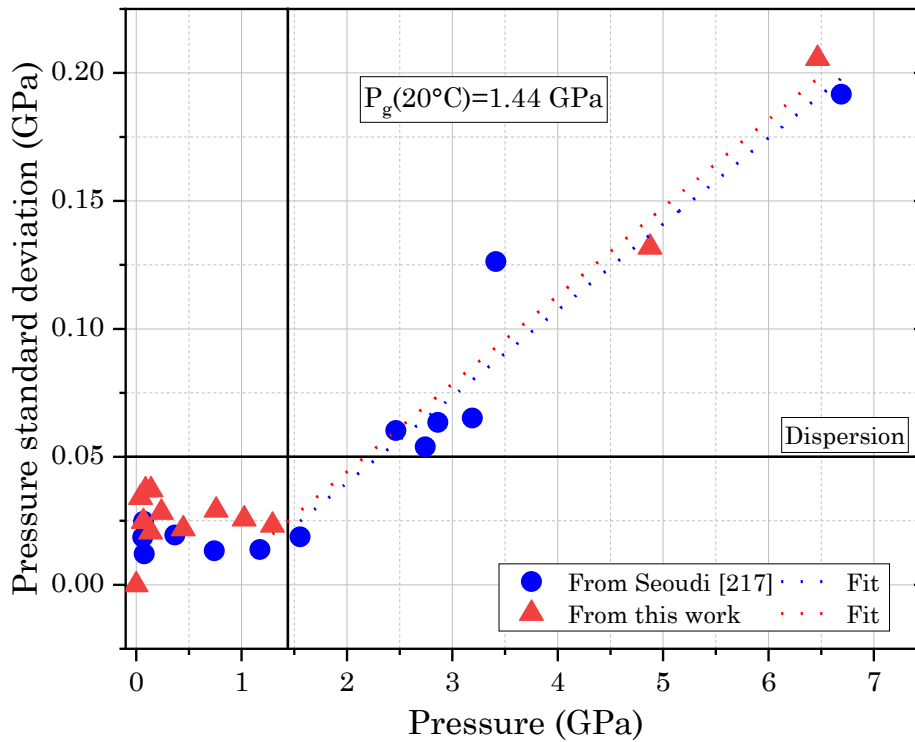


Figure 4.2 : Standard deviation (SD) on pressure measured on 5 ruby spheres immersed in squalane at 22°C inside the Toullec 11 DAC, compared with the results obtained with the same fluid at the same temperature in reference [206].

The Ruby's SD of our experiment is higher than the values found by Seoudi under similar conditions below 1.5 GPa. Nevertheless, The standard deviation are lower than than 50 MPa uncertainty on the pressure measurements obtained in air (horizontal line) given in section 3.4.2 [206]. Then, beyond a certain value, it strongly increases up to 200 MPa at 7 GPa of average pressure. The standard deviation is modulated (less than 3% of the pressure average) but still four times higher than the pressure uncertainty, it is significant. It means that beyond this value, the pressure distribution is no longer perfectly homogeneous.

4.2.3. Brillouin standard deviation

In Figure 4.3 the standard deviation for the Brillouin frequency shift measured in squalane in 5 to 10 areas in Figure 4.5 in blue circles is provided.

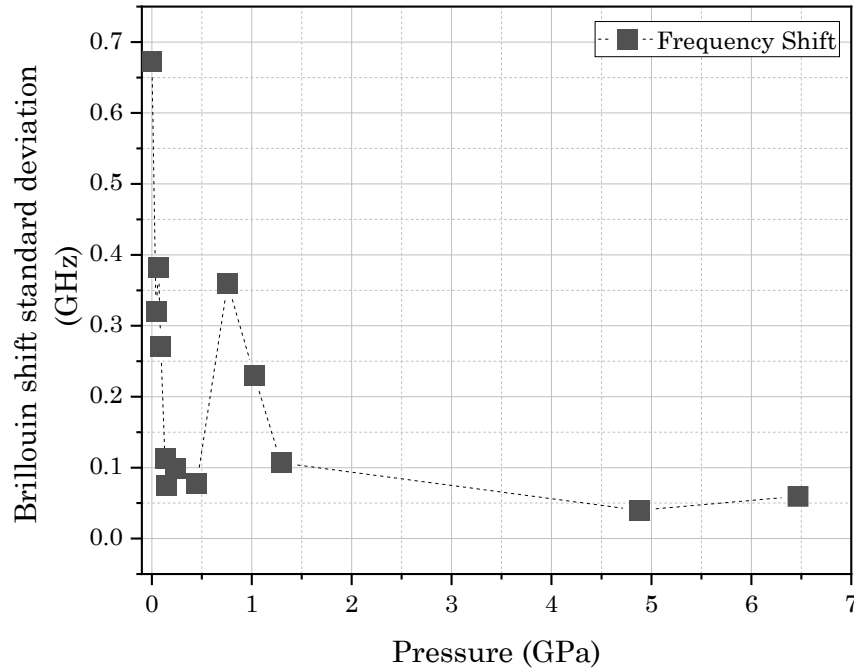


Figure 4.3 Standard deviation from the frequency shift measured on squalane at 22°C inside the Toullec 11 measured by VIPA spectrometer taken between 5 and 10 points in the DAC calculated across pressure.

The Brillouin SD shows a discontinuity of around 1 GPa. The SD, after the same value found for the ruby standard deviation, reduces to 0.1 GPa.

Surprisingly, the Brillouin standard deviation data do not corroborate with the ruby standard deviation. It was indeed expected that both sets of data would evolve similarly. It seems from Figure 4.6 that the dispersion of Brillouin data measured on various spots of the diamond anvil evolves in similar ways to the linewidth. One main feature that could influence the high values of Brillouin standard deviation data situated at low average pressure is the proximity of Brillouin elastic Peaks with the central Rayleigh peak. This closeness increases the probability of fitting errors.

The standard deviation of the pressure across the DAC will be use in the results section.

4.3. Data Processing: Fitting Procedure

4.3.1. Software and fitting procedure

The characteristics of a Brillouin spectrum recorded in benzyl benzoate is shown in Figure 4.1. This spectrum was recorded at ambient pressure and 22°C with the VIPA set-up in the DAC, in backscattering configuration. It is composed of different parts already presented in Figure 2.6 in Section 2.1.3 and Figure 2.10 in Section 2.2.2. As explained in Section 2.5, the Mountain peak appears at the center of the spectrum, as a supplementary component under the sharp Rayleigh central peak. To make accurate Lorentzian fitting, this contribution has to be fitted simultaneously with the Brillouin shift.

As mentioned in Chapter 2, two models are commonly used to fit Brillouin spectra, either using a Lorentzian model or a DHO model. The DHO model has been previously used to fit the glycerol under pressure [13], polymers [17], biological sample [148]. In other hand, the Lorentzian multi fit and single fit was used with OriginPro.

To compare the different fitting processes (as well as the software) independently on the spectrometer used, two sets of high-pressure experiments were conducted with the two different interferometers and microscopes configurations. This part will identify the best-fitting method proposed in the literature, followed by the comparison between the two set-up, using the tree fluids under pressure. In the following, the typical value of the FWHM of the Stokes and anti-Stokes lies between 2.20 GHz for squalane and 3.2 GHz for glycerol, their maximum position is found between 8.5 GHz for squalane and 16 GHz for glycerol, at ambient conditions.

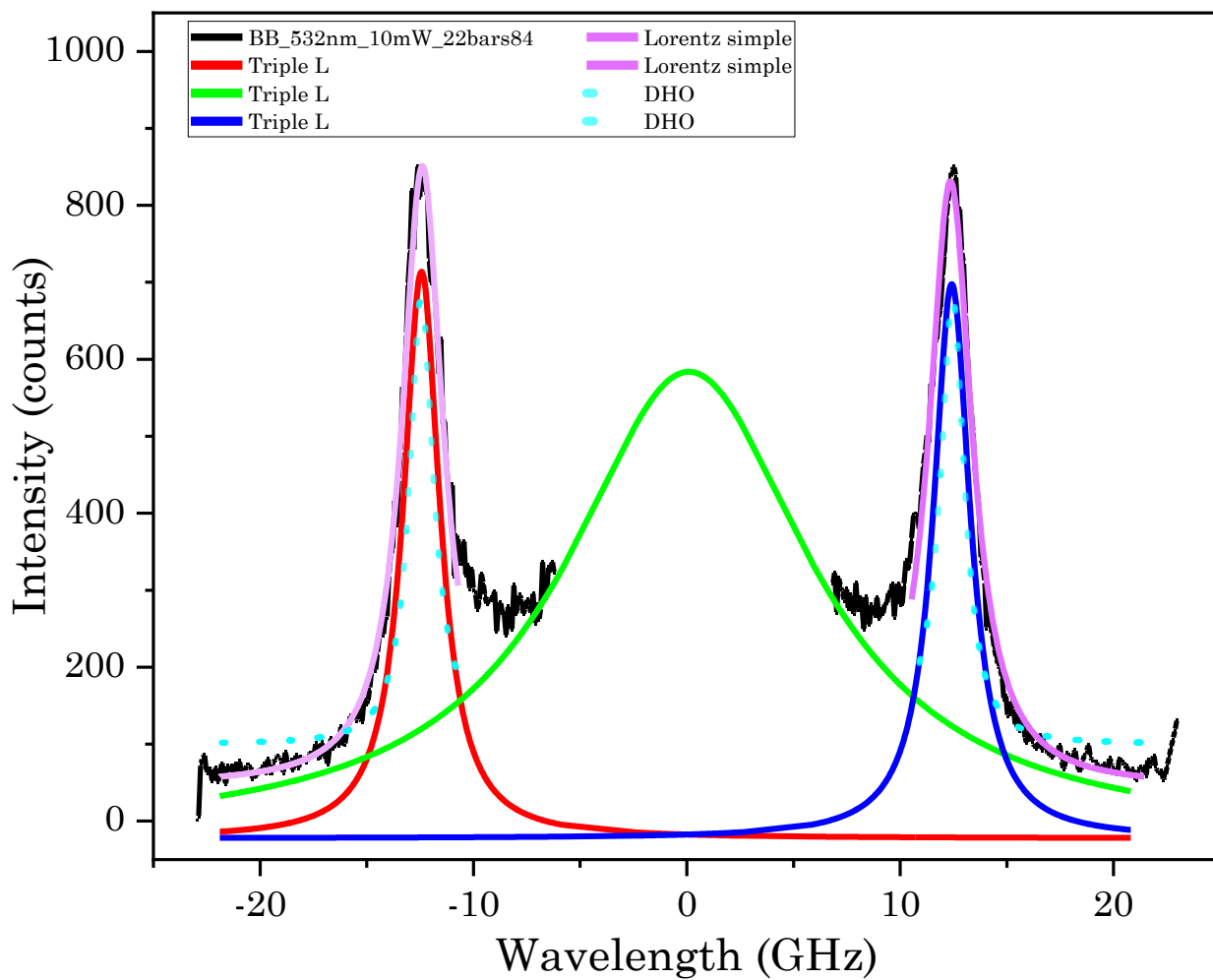


Figure 4.4: Brillouin spectrum of benzyl benzoate at 22°C fitted by OriginPro with a multi and single Lorentz and a DHO model.

Model	Triple Lorentz		
Equation	$y = y_0 + (2*A/\pi)*(w/(4*(x-xc)^2 + w^2))$		
Plot	Peak1(Intensity)	Peak2(Intensity)	Peak3(Intensity)
y0	-22,46515 ± 8,63141	-22,46515 ± 8,63141	-22,46515 ± 8,63141
xc	-12,435 ± 0,01092	0,0951 ± 0,08163	12,41715 ± 0,0112
w	2,07046 ± 0,04322	13,88577 ± 1,72053	2,09234 ± 0,04377
A	2394,29499 ± 50,81593	13221,53044 ± 353,61819	2366,92755 ± 50,01482
Reduced Chi-Sqr	517,02125		
R-Square (COD)	0,9887		
Adj. R-Square	0,98839		

Model	DHOfromGHOST (User)		Model	Lorentz	
Equation	$B+(4*I*\gamma*f_0*f_0)/(4*\pi*((x*x-f_0*f_0)*(x*x-f_0*f_0)+(4*x*x*\gamma*\gamma)))$		Equation	$y = y_0 + (2*A/\pi)*(w/(4*(x-xc)^2 + w^2))$	
Plot	Intensity	Intensity	Plot	Intensity	Intensity
f0	-12,48423 ± 0,06085	12,49906 ± 0,05867	y0	46,04478 ± 3,21546	43,80571 ± 3,86663
HWHM	0,68838 ± 0,09939	0,68801 ± 0,09692	xc	-12,39489 ± 0,01074	12,35798 ± 0,01271
I	5000 ± 581,71891	5000 ± 577,16594	w	2,31532 ± 0,04035	2,441 ± 0,04869
B	100 ± 14,34386	100 ± 14,50528	A	2927,48115 ± 45,70349	3019,35928 ± 55,25052
Reduced Chi-Sqr	14833,32346	14374,59437	Reduced Chi-Sqr	526,07152	672,59719
R-Square (COD)	0,76317	0,77174	R-Square (COD)	0,99157	0,98906
Adj. R-Square	0,75725	0,76573	Adj. R-Square	0,99136	0,98878

Table 4.1 : Fitting parameters used in Figure 4.4 for the multi-Lorentz, Lorentz and DHO.

The Lorentzian expression is given in Equation 4.1 for the OriginPro software and Equation 4.2 for the GHOST software, which is provided with the TFP-1 to record Brillouin spectra. GHOST can also be used to fit the spectra with 3 models: single Lorentz, single Gauss and DHO. OriginPro is an advanced analysis software for peak fitting, signal and numerical data processing. In particular, it is possible to fit data using a multi peak analysis.

$$y = y_0 + \left(2 * \frac{A}{\pi}\right) * \left(\frac{w}{4 * (x - xc)^2 + w^2}\right) \quad (4.2)$$

where y is the intensity (in counts), y_0 is the baseline offset (in counts), xc is the wavelength at the center of the peak (nm), w is the Full-Width Half Maximum (nm) and A is the area under the peak (arbitrary unit).

The Lorentz and DHO fitting equations 4.3 and 4.4 are already implemented in the GHOST software [207] as presented in Figure 4.5. DHO equation was also implemented manually in OriginPro (Figure 4.4). Equation 4.2 and equation 4.3 are equivalent since $I = A$, $xc = f_0$ and $w = 2\Gamma_b$.

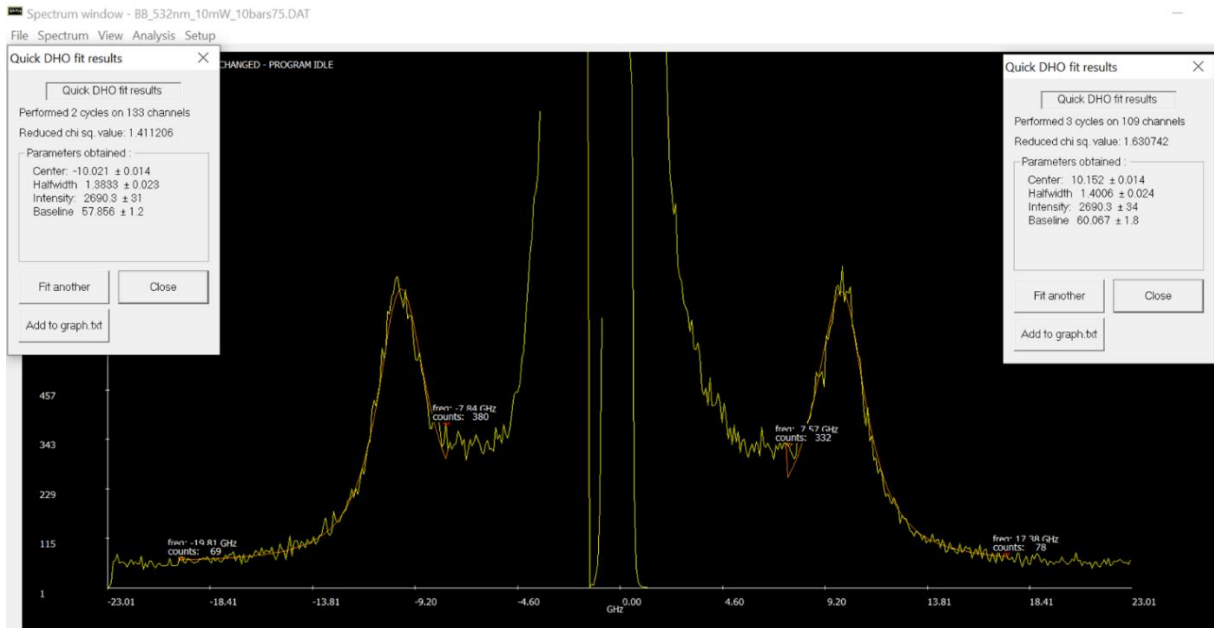


Figure 4.5: DHO fitting procedure on GHOST software, benzyl benzoate inside the DAC at 22°C and very low pressure, on the TFP-1 spectrometer.

$$I_{Lorentz} = B + \frac{I}{\pi} \frac{\Gamma_{HWHM}}{(f^2 - f_0^2)^2 + \Gamma^2} \quad (4.3)$$

$$I_{DHO} = B + \frac{I}{4\pi} \frac{4\Gamma_{HWHM}f_0^2}{(f^2 - f_0^2)^2 + 4f^2\Gamma^2} \quad (4.4)$$

Where B is the baseline (in counts), I is an intensity arbitrary factor (in counts), Γ_{HWHM} is the Half Width at half maximum in GHz and f_0 the peak frequency according to the GHOST manual version 6.75.

As shown in Figure 4.5, the different models used to fit the spectra led to some differences in the final results. Therefore, a comparison between the different ways to analyze the spectra will be detailed in this chapter. Then, the next section (§ 4.2) will be dedicated firstly to evaluate and compare the fitting procedures to choose the most accurate, and secondly to compare measurements between the TFP-1 and the VIPA spectrometers.

The following will be dedicated to the validation of the experimental procedure both with the TFP-1 and the VIPA devices. The analysis concerns the fitting procedure, the pressure extraction, the spectra symmetry, and the reliability of the new VIPA and microscope set-up compared to the data obtained on the TFP-1 spectrometer.

4.3.2. Single versus Multi-Fit Lorentz Procedure on OriginPro

OriginPro provides different kinds of fitting procedures using the Lorentz model: single and multi-peaks. Table 4.2 summarizes a comparison between a 3-Lorentzian deconvolution called “multi” (taking into account simultaneously both inelastic peaks and the central one) and a single Lorentz fit (meaning two separate Lorentzian fit of each inelastic peak). The glycerol was studied under pressure with the TFP-1 configuration. As shown in Figure 4.4, the spectrum is composed of the central and the two inelastic peaks. The intensity of the central peak is around 100 times higher than the inelastic ones, making impossible the multi-fitting process of the two inelastic peaks. In order to solve this issue, the central peak height is cut off. The resulting fit might be depended on the way the central peak was cut off. Therefore, the multi fit was repeated 3 times for 3 different central peak maximum values.

	Adjust ed R- square	Av. of S & AS Freque ncy Shift (FS, GHz)	2 SD on FS (GHz)	Av. S & AS FWH M (GHz)	2 SD on FWHM (GHz)	Difference between the multi and single fit		
						FWHM (GHz)	FS (%)	FWHM (%)
Multi 1	0.75	28.36	0.043	0.82	0.12	0.06	0.21	7.26
Multi 2	0.77	28.36	0.041	0.81	0.12	0.055	0.19	6.74
Multi 3	0.85	28.36	0.022	0.76	0.06	0.0012	0.004 1	0.14
Single	0.9	28.36	0.025	0.76	0.08			

Table 4.2: Comparison between single and multiple Lorentz on OriginPro software for the spectrum of glycerol at 2.19 GPa for the same range but playing with the Rayleigh intensity cut-off.

The differences between the multi and single fits are very small: less than 0.01 GHz for the frequency shift (FS) and about 0.06 GHz for the FWHM. These values are close to the uncertainties of the measured values: between 0.02 and 0.04 GHz for the FS and between 0.06 and 0.12 GHz for the FWHM. The differences in percentages are also given. They correspond to a maximum of 0.21% for the FS and 7.3% for the FWHM. Therefore, we can conclude from Table 4.2 that for the multiple fit procedures to be equivalent to the single fit, the R^2 has to be larger than 0.8 to be under one percent difference on the FWHM.

The same analysis was extended on the two other fluids, glycerol and squalane. The spectra were still recorded with the TFP-1 configuration but at two pressures: the results are detailed in Tables 4.3 ,4.4 and 4.5.

Squalane		Multi Lorentz	2 SD (GHz)	Single Lorentz	2 SD (GHz)
0,29 GPa	FS	9,872	0,031	9,791	0,040
	FWHM	2,191	0,109	2,631	0,133
1.55 GPa	FS	28,140	0,016	28,139	0,019
	FWHM	0,809	0,045	0,830	0,060
Glycerol		Multi Lorentz	2 SD (GHz)	Single Lorentz	2 SD (GHz)
0,056 GPa	FS	15,362	0,062	15,249	0,061
	FWHM	2,539	0,196	3,228	0,213
1,37 GPa	FS	24,599	0,028	24,597	0,025
	FWHM	1,019	0,083	1,046	0,085

Table 4.3 : Extended analysis on glycerol and squalane using OriginPro at different pressures on TFP-1. The single Lorentz fit is compared to the multi-Lorentz fit.

According to Table 4.3, the multi-Lorentz standard deviation is lower than the single Lorentz for the squalane sample at low and high pressure. It is important to highlight that the performance of the TFP-1 spectrometer was compromised during the glycerol experiments due to the aging detection system reaching the end of its operational life. Consequently, random peaks sporadically appear in the spectra, thereby diminishing the quality of the multi fit. Despite these challenges, it remains noteworthy that the standard deviation is still more favorable for the multi-Lorentz than the single Lorentz when applied to the FWHM.

Table 4.4 are reported only the absolute and relative (%) differences between single and multi fits presented in Table 4.3 on the FS and the FWHM.

	Abs Difference FS (GHz)	Abs Difference FWHM (GHz)	% FS to the single Lorentz	%FWHM to the single Lorentz
Squalane 0.29 GPa	0.081	0.44	0.83	16.7
Squalane 1.55 GPa	0.001	0.021	0.026	2.55
Glycerol 0.056 GPa	0.11	0.69	0.75	21.4
Glycerol 1.37 GPa	0,00136	0,0267	0,0055	2,56

Table 4.4: Extended analysis performed in Table 4.2 on glycerol and squalane at different pressures on TFP-1. Difference between the multi and single fit.

From Table 4.4, the relative differences are small except for the FWHM at low pressure where the relative differences are of 21% and 17 %, for glycerol and squalane respectively. The origin of these higher values at low pressure can be explained by the central Rayleigh and the Mountain peak contributions rather close to the Stokes and anti-Stokes peaks. Obtaining a more precise fit becomes challenging when dealing with insufficiently separation between peaks using a single Lorentz.

As a conclusion, at low-pressure, the fitting of these experiments is problematic due to the interactions between the Rayleigh central part and the inelastic peak which become particularly intricate. The multi-peaks Lorentz fitting method allows us to disentangle these components, providing a detailed and accurate representation of the FWHM. The standard deviation of the multi-peak Lorentz is in most cases lower than for the single Lorentz.

The same analysis is done on the VIPA spectra at different pressures for 2 fluids: squalane (SQ) and benzyl benzoate (BB). Only the FWHM is analyzed. Indeed, in the case of the VIPA acquisition, there is a drift of the Rayleigh peak during the spectra recording. To correct this, as shown in § 4, the spectra axis is recorded in nm instead of GHz (frequency shift). Then, the Rayleigh position is extracted using the half mean distance between Stokes (S) and anti-Stokes (AS) peaks and converted in GHz. The results are summarized in Table 4.4.

FWHM SQUALANE	Fit	Av. of S & AS FWHM (GHz)	Diff. between multi and single fit (FWHM, GHz)	Dif. between multi and single fit (FWHM, %)	Adjusted R-square
0.089 GPa	Multi	2.270	0.318	12.3	0.910
	Single	2.588			0.980
0.445 GPa	Multi	2.043	0.106	5.46	0.980
	Single	1.937			0.990
4.87 GPa	Multi	1.318	0.175	11.7	0.980
	Single	1.492			0.980
FWHM BENZYL BENZOATE	Fit	Av. of S & AS FWHM (GHz)	Diff. between multi and single fit (FWHM, GHz)	Dif. between multi and single fit (FWHM, %)	Adjusted R-square
0 GPa	Multi	2.535	0.931	26.9	0.980
	Single	3.466			0.990
0.27 GPa	Multi	1.691	0.227	11.8	0.990
	Single	1.918			0.990
2.44 GPa	Multi	1.714	0.021	1.22	0.980
	Single	1.736			0.98

Table 4.5 : Comparison between the fitting procedure of single and multi-Lorentz fit for VIPA spectrum for benzyl benzoate and squalane.

Due to the fiber connection between the microscope and the VIPA interferometer, a pair of silica inelastic peak appear at 532.197 and 532.257 nm (see Appendix D.1). During the pressure experiment, the pressurized lubricant Brillouin signature overlap the silica signal.

As seen in Table 4.5, when the inelastic peak is in the range of the silica peak, e.g. for the squalane sample at 4.87 GPa, the same problem arises as for the central Rayleigh peak fitting.

To summarize, examining Table 4.2, it is evident that the single Lorentz fit proves comparable to the multiple Lorentz fit when the adjust R^2 is above 0.85. The analysis conducted on the TFP-1 spectrometer in Tables 4.3, reveals that higher pressure levels exhibit a diminished disparity between these two fitting methodologies. A similar trend is observed with the VIPA spectrometer, as shown in Table 4.4, holding true until the inelastic peak closely approaches the silica peak of the VIPA's optical fiber signal. Across all investigation, the single Lorentz fit is less accurate at low pressure.

The next analysis is still completed using the single Lorentz fit on the same area of the spectra due to the inability of the GHOST software to provide multiple peaks fit simultaneously.

4.3.3. Fitting Procedure: Single Lorentz versus DHO for Each Software

In this section, a comparison between the Lorentz and DHO fitting procedures is presented. Each software provides both DHO and Lorentz fitting procedures. The goal is to assess the consistency of the software in producing similar values with two distinct fitting approaches.

Both GHOST (provided with the TFP-1) and OriginPro software will be compared. As mentioned before, only a single Lorentz model is available in the GHOST software. Both employ the same solver method. For comparison purpose, here the single Lorentz is considered. All the spectra were recorded in TFP-1 here in order to compare only the fitting process.

An example of DHO and single Lorentz fits, done with OriginPro on Glycerol at 22°C and ambient pressure is presented in Figure 4.3. This experiment was conducted at ambient conditions where the Stokes and anti-Stokes are close to the Rayleigh and Mountain contributions.

The resulting frequency shift and FWHM are given in Figures 4.6 for the anti-Stokes and Table 4.7 for the Stokes.

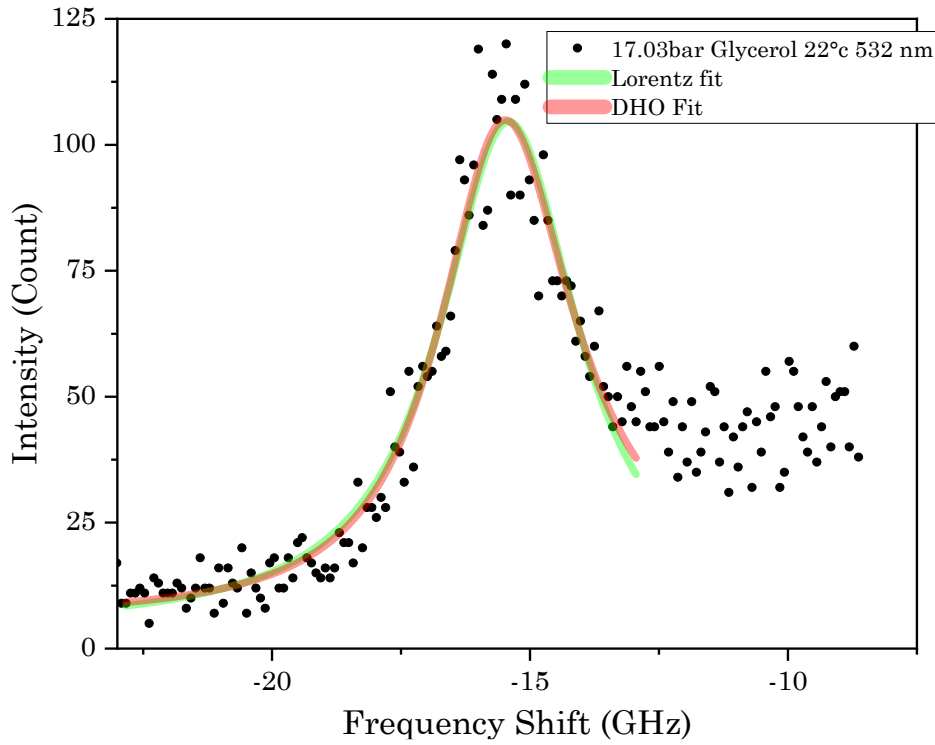


Figure 4.6: Comparison of Lorentz and DHO fits performed on TPF-1 on the anti-Stokes peak and processed by the OriginPro software.

anti-Stokes	Frequency shift and SD (GHz)	FWHM and SD (GHz)
Lorentz (GHOST)	-15.39 ± 0.034	2.85 ± 0.105
Lorentz (OriginPro)	-15.42 ± 0.025	2.94 ± 0.087
DHO (GHOST)	-15.59 ± 0.034	2.87 ± 0.11
DHO (OriginPro)	-15.62 ± 0.024	2.94 ± 0.084

Table 4.6: Anti-Stokes comparison between the DHO and single Lorentz fits made on GHOST and OriginPro softwares on Glycerol at 17.03 bar and 22°C (TFP-1 spectrometer, results presented in Figure 4.3). The final result is expressed with one standard deviation σ obtained from the fitting procedure.

Stokes	Frequency shift and SD (GHz)	FWHM and SD (GHz)
Lorentz (GHOST)	15.15 ± 0.037	3.2 ± 0.130
Lorentz (OriginPro)	15.18 ± 0.031	2.99 ± 0.136
DHO (GHOST)	15.39 ± 0.037	3.18 ± 0.13
DHO (OriginPro)	15.37 ± 0.032	2.95 ± 0.128

Table 4.7 : Stokes comparison between the DHO and single Lorentz fits made on GHOST and OriginPro softwares on Glycerol at 17.03 bar and 22°C (TFP-1 spectrometer, results presented in Figure 4.3). The final result is expressed with one standard deviation σ obtained from the fitting procedure.

Considering then the anti-Stokes peak in Figure 4.6, both DHO and Lorentz fits were applied on one spectrum with GHOST and OriginPro softwares. Regarding the frequency shift, slight variations are observed when DHO and Lorentz are compared. The difference is 0.2 GHz for GHOST (DHO-Lorentz) and 0.2 GHz for OriginPro. When considering fits obtained from the same equation, the disparity is even smaller, about 0.03 GHz for the Lorentz (GHOST-Origin) and 0.03 GHz for the DHO. The Full Width at Half Maximum (FWHM), a very low value (0.2 GHz maximum) is observed when comparing DHO and Lorentz fits within a given software. However, the most significant difference is 0.07 and 0.09 GHz for the DHO and the OriginPro softwares respectively for a given equation.

Examining in Table 4.7 the Stokes peak, for the Stokes frequency shift, there is a difference of 0.24 GHz for GHOST (DHO-Lorentz) and 0.19 GHz for OriginPro, both superior to a SD. For a given equation when comparing the fits obtained with OriginPro and GHOST, the Lorentz (GHOST-Origin) is 0.03 GHz and for the DHO 0.02 GHz. The standard deviation found for the frequency shift is low compared to the absolute value.

The FWHM Stokes shows similar values using the same software. For the GHOST software, there is a difference of 0.02 GHz (DHO-Lorentz), and for the OriginPro software 0.04 GHz. For the same equation, the values found with the different software are a difference of 0.21 GHz for the Lorentz fit and 0.23 GHz for the DHO model.

Moreover, the FWHM shows a higher value of the standard deviation compared to the frequency shift. The standard deviation represents a non-negligible percentage of the FWHM value (around 5%), one reason is the presence of the central Rayleigh and Mountain contribution close to the inelastic peaks making more difficult the fit.

All values are resumed in Tables 4.8 and 4.9.

Anti-Stokes	FS difference (GHz)	Comparison to the SD	FWHM difference (GHz)	Comparison to the SD
DHO (G/O)	0.03	≤ SD	0.07	< SD
Lorentz (G/O)	0.03	≤ SD	0.09	< SD
Stokes	FS difference	Comparison to the SD	FWHM difference (GHz)	Comparison to the SD
DHO (G/O)	0.02	< SD	0.23	> SD
Lorentz (G/O)	0.03	≤ SD	0.21	> SD

Table 4.8 : Frequency shift (FS) and the Full Width at Half Maximum (FWHM) absolute difference calculated for each fitting model for the Stokes and anti-Stokes peaks.

Anti-Stokes	FS difference (GHz)	Comparison to the SD	FWHM difference (GHz)	Comparison to the SD
DHO - Lorentz (O)	0.2	> SD	0	< SD
DHO - Lorentz (G)	0.2	> SD	0.02	< SD
Stokes	FS difference	Comparison to the SD	FWHM difference (GHz)	Comparison to the SD
DHO - Lorentz (O)	0.19	> SD	0.04	< SD
DHO - Lorentz (G)	0.24	> SD	0.02	< SD

Table 4.9 : Absolute difference on fitting model calculated for each for the Stokes and anti-Stokes peaks.

Tables 4.8 and 4.9 reveals that the frequency shift and the Full Width at Half Maximum are influenced by the fit and the software, particularly in the case of GHOST software. However, with the OriginPro software, the impact on FWHM is less pronounced, showing values that are closely aligned. Notably, the FWHM from OriginPro these values fall below the spectrometer resolution (200 MHz), as determined from its Free Spectral Range (FSR).

In summary, a maximum deviation of 0.24 GHz is observed among different fits and software. The Stokes Full width at half Maximum (FWHM) seems to be affected by the software on the Stokes section whereas the frequency shift (FS) for both Stokes and anti-Stokes is impacted by the fit used. In fact, the frequency shift difference is higher than the standard deviation for both Stokes and anti-Stokes, as seen in Table 4.9. Moreover, there is a clear asymmetry between the Stokes and anti-Stokes found on the frequency shift position as presented in the Table 4.9 below.

In this example, a substantial impact has been observed in comparing fitting methods applied to the frequency shift within a given software. Furthermore, notable differences in Full Width at Half Maximum (FWHM) are observed, particularly for the Stokes peak, when comparing the same fitting method from both software's.

4.3.4. Difference between single Lorentz GHOST and multi-Lorentz OriginPro

The previous results were conducted at low pressure on glycerol. In the following, the comparison between Lorentz and DHO with two software (OriginPro and GHOST) is extended to glycerol and squalane at various pressures, from spectra taken with the TFP-1 spectrometer. The results are shown in Tables 4.10 and 4.11. The 2 SD (standard deviation) is the total error accumulated by the fitting procedure and the averaging between Stokes and anti-Stokes results.

Diff. between GHOST and OriginPro (DHO)	FS (GHz)			FWHM (GHz)		
	Value (GHz)	2 SD (GHz)		Value (GHz)	2 SD (GHz)	
		GHOST	Origin Pro		GHOST	Origin Pro
Squalane 0.30 GPa	0.0024	0.0410	0.0353	0.1220	0.127	0.106
Squalane 0.44 GPa	0.0069	0.0393	0.0213	0.0047	0.104	0.0661
Squalane 1.55 GPa	0.017	0.0294	0.0204	0.1290	0.0696	0.0645
Glycerol 0.05 GPa	0.041	0.0789	0.0587	0.306	0.279	0.194
Glycerol 1.38 GPa	0.0381	0.0397	0.0259	0.0901	0.106	0.874

Table 4.10: Comparison between GHOST and OriginPro for the DHO fitting with their associated Standard Deviation (SD).

Diff. between multi Lorentz (OriginPro)/ Single Lorentz (GHOST)	FS (GHz)			FWHM (GHz)		
	Value (GHz)	2 SD (GHz)		Value (GHz)	2 SD (GHz)	
		GHOST	Origin Pro		GHOST	OriginPro
Squalane 0.30 GPa	0.076	0.041	0.031	0.96	0.063	0.109
Squalane 0.44 GPa	0.026	0.0393	0.0271	0.685	0.0526	0.0806
Squalane 1.55 GPa	0.012	0.0295	0.0155	0.458	0.0348	0.0447
Glycerol 0.05 GPa	0.234	0.0763	0.0621	0.710	0.152	0.196
Glycerol 1.38 GPa	0.034	0.0397	0.0400	0.530	0.0536	0.0117

Table 4.11: Comparison between the single Lorentz GHOST and OriginPro for the multi-Lorentz fitting, with their associated Standard Deviation (SD).

Regarding the frequency shift (FS) differences, whatever the fluid (squalane or glycerol) and whatever the equation (DHO or Lorentz), they are most of the time lower than the standard deviations estimated on the peak fitting. Exceptions are found for FWHM at low- and high-pressure glycerol and squalane with the single and multi-Lorentz fits using Origin Pro. One explanation is the range of data used during the fitting process. In fact, the GHOST software carries only single Lorentz fit, selecting manually a small portion of the inelastic peak, which influence deeply the result accuracy of the fit.

Note that there is a small FS asymmetry on the Stokes and Anti-Stokes peaks, and that the fit of the former is less accurate than for the latter. These relatively small deviations can explain some higher relative differences. In conclusion, the software used to fit has few effects on the final results on the frequency shift. However, as the FWHM of the Brillouin peaks becomes narrow and far from the Rayleigh peak, minor deviations may occur.

To conclude previous Sections 4.2 and 4.3, with the OriginPro software, the single and multi-Lorentzian fits on data obtained from the TFP-1 were compared. It seems that the multi-Lorentz model is more appropriate to take into account the central Rayleigh part on the inelastic peak. However, at or high pressure, the single Lorentz expression seems to be more accurate due to the smaller range of data needed.

Then the performance of both softwares were examined with the Lorentz and the DHO equations. The frequency shift seems to have been less affected by the choice of the software, unlike the FWHM for which rather large differences have been observed. To understand the origin of these differences, the reliability of both fitting expressions was compared for each software. According to Figure 4.4, the OriginPro software shows a better similarity in the frequency shift than the GHOST software.

4.4. Asymmetry of the Spectra

4.4.1. Asymmetry on the glycerol sample at low pressure

Table 4.12 compare the values of FS and FWHM presented in Tables 4.6 and 4.7, there is a clear asymmetry between the Stokes and anti-Stokes values using both software's.

Comparison abs(Stokes/ anti- Stokes)	GHOST		OriginPro	
	FS (GHz)	FWHM (GHz)	FS (GHz)	FWHM (GHz)
Lorentz	0.24	0.35	0.24	0.05
DHO	0.2	0.31	0.25	0.01

Table 4.12 : Comparison between Stokes and anti-Stokes absolute values fitted by GHOST and OriginPro with Lorentz and DHO models.

To conclude, the disparity between DHO and Lorentz is more pronounced when using the GHOST software compared to OriginPro, suggesting that the former may be less reliable, especially concerning FWHM.

For these reasons, the subsequent section will expand this comparison to experiments conducted under pressure conditions, but using the multi-Lorentz fit instead.

4.4.2. Asymmetry Between Stokes and Anti-Stokes of the Inelastic Peaks Under Pressure for Both Softwares

According to the diffusion theory, Stokes and anti-Stokes peaks should be symmetrically shifted to the Rayleigh peak. It means the frequency shift (distance from the Rayleigh) is expected to be the same for the Stokes and anti-Stokes peaks and the FWHM has to be the same. Because a spectrum is a combination of the fluid response and of many optical components' response, it is mandatory to check the symmetry of the spectrum recorded both with the TFP-1 and the VIPA. As seen in Tables 4.5 and 4.6, the values of the Stokes and anti-Stokes peak are different. For that purpose, the symmetry of Brillouin spectra made on benzyl benzoate and squalane (TFP-1 and VIPA) and for Glycerol (TFP-1) was analysed.

For the VIPA spectrometer, the frequency shift is not displayed because of the procedure to acquire the Rayleigh central peak position. Indeed, the main difference between the TFP-1 and the VIPA acquisition method is on the spectra x-axis. With the TFP-1 spectrometer, the software provides direct symmetrical peak position and linewidth, in GHz. In the VIPA spectra, a drift of the scattered light across the CMOS detector, over a short period of time (few second to minute), is observed. It may be due to thermal fluctuation and/or laser power instabilities. The consequence is the inability to set a reference point to convert data from nm to GHz. Therefore, the mean distance between the Stokes and anti-Stokes peaks is used to define the Rayleigh position (at 0 GHz). Moreover, the combination of two pump-killers for low-pressure experiments reduces the intensity of the Rayleigh peak of the spectra which disable to directly convert into GHz (see Figure 4.12). In the following figures, the term doublet represents the absolute value of the difference of FS and FWHM between Stokes and anti-Stokes.

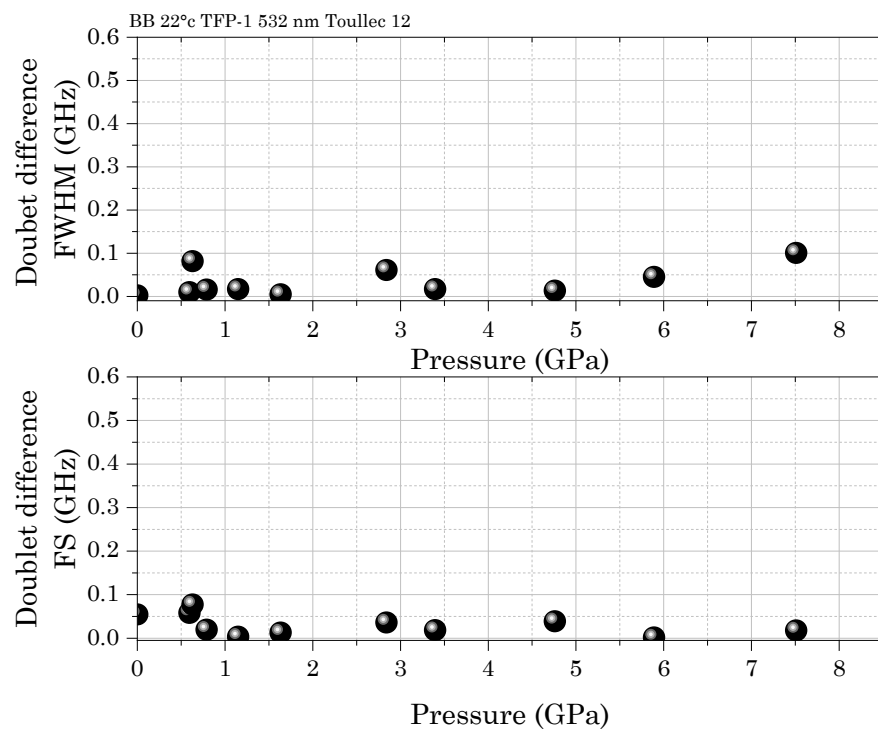


Figure 4.7: Differences in the FWHM (top) and frequency shift (FS, bottom) of the doublet for benzyl benzoate under pressure. All analyses were done using the TFP-1 spectrometer and the multi-Lorentz fitting procedure. All datas were recorded between 450 and 850 cycles.

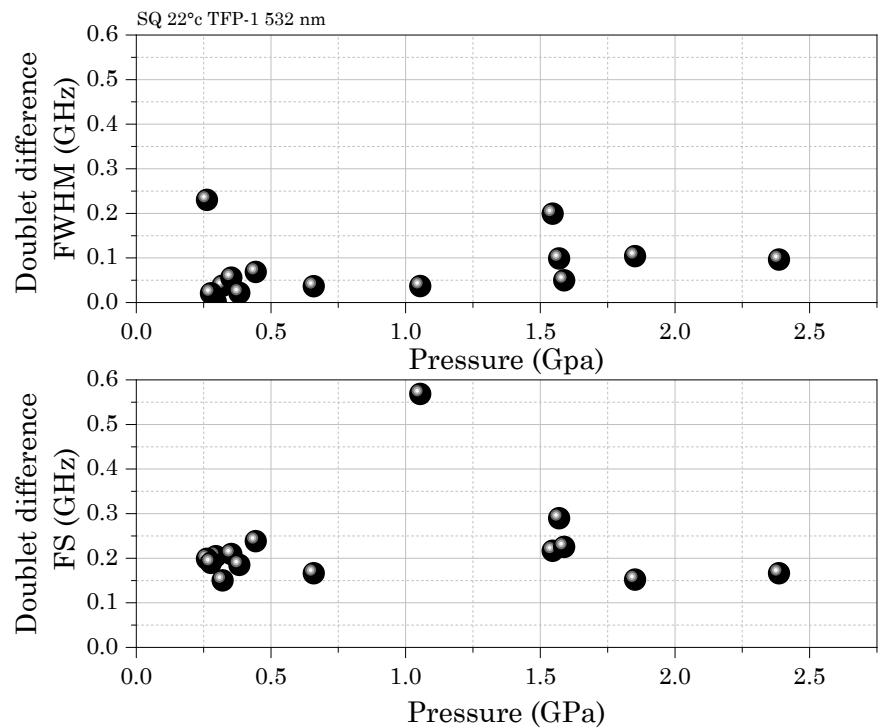


Figure 4.8: Differences in the FWHM (top) and frequency shift (FS, bottom) of the doublet for squalane under pressure. All analyses were done using the TFP-1 spectrometer and the multi-Lorentz fitting procedure. All datas were recorded by an accumulation of 500 cycles.

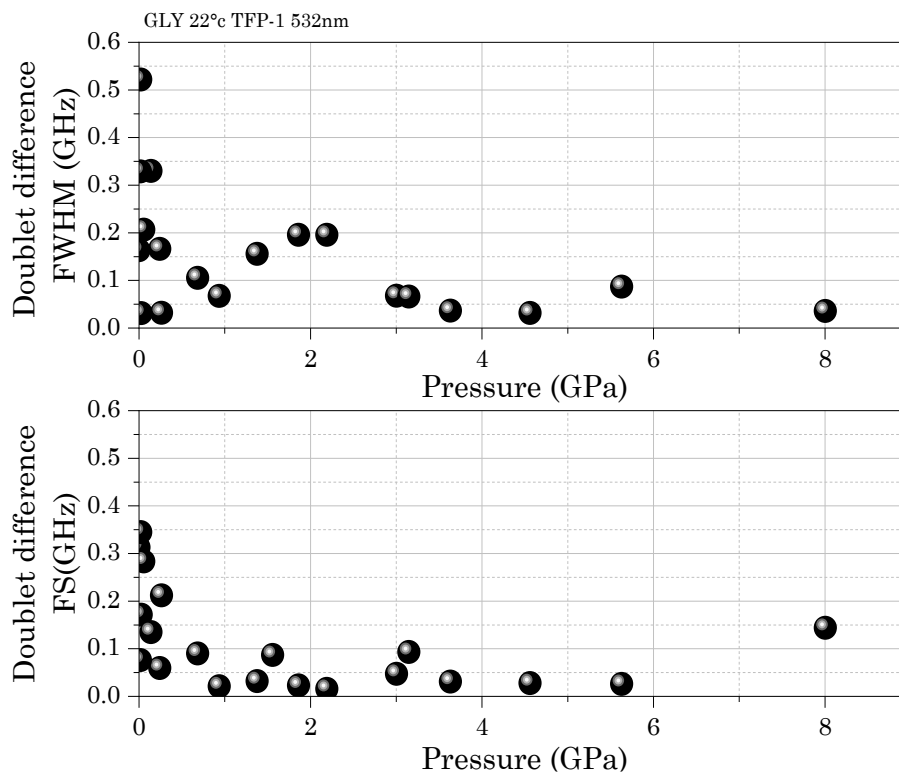


Figure 4.9: Differences in the FWHM (top) and frequency shift (FS, bottom) of the doublet for glycerol under pressure. All analyses were done using the TFP-1 spectrometer and the multi-Lorentz fitting procedure. All data were recorded with 1000 cycles.

Figures 4.7, 4.8, and 4.9, the maximum difference on the FWHM reaches 0.10 GHz for the benzyl benzoate, 0.23 GHz for the squalane, and 0.55 GHz for glycerol. It does not follow any clear trend for benzyl benzoate and squalane. The spectra accumulation for all data from the TFP-1 does not determine the difference between Stokes and anti-Stokes

The doublet difference for glycerol decreases as the pressure increases.

The VIPA analysis was conducted on the FWHM because all data have been recorded in nm, and the frequency shift is calculated using the mid-position between Stokes and anti-Stokes peaks.

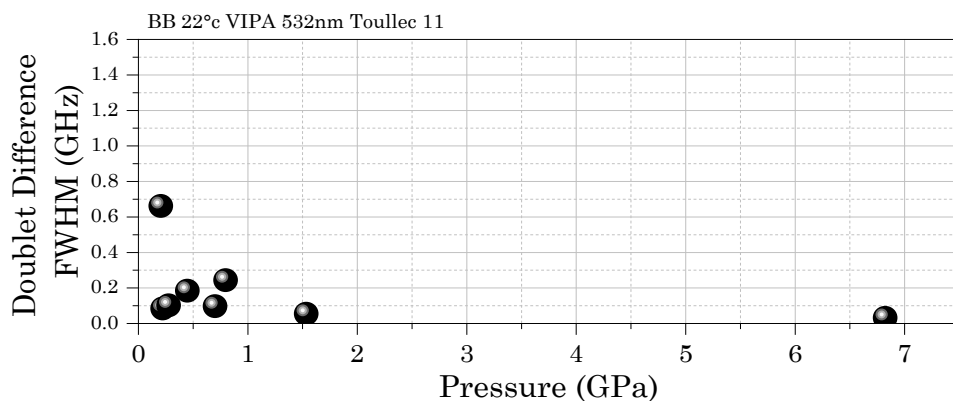


Figure 4.10 : Differences in the FWHM of the doublet for benzyl benzoate under pressure. All analyses were done using the VIPA spectrometer and using the Lorentz fitting procedure. All dataset were recorded 1750ms averaged 10 times and 3750 ms averaged 8 times for the highest pressure.

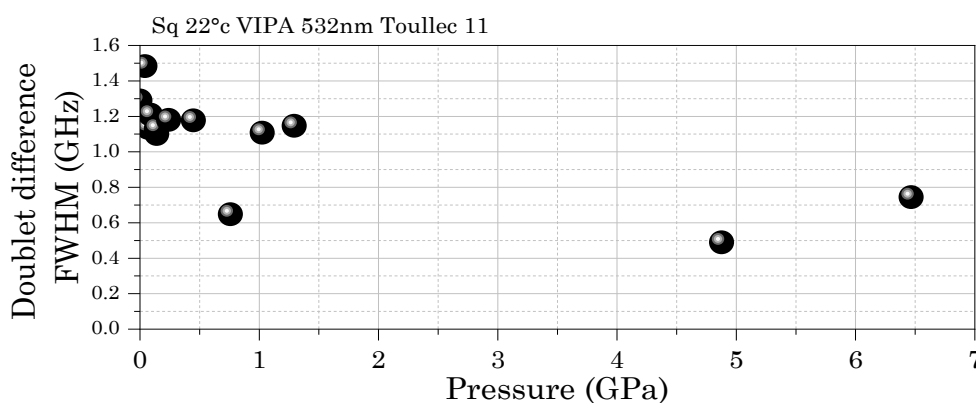


Figure 4.11 : Differences in the FWHM of the doublet for squalane under pressure. All analyses were done using the VIPA spectrometer and using the Lorentz fitting procedure. All datas were recorded between 1500 ms and 8500 ms non-averaged.

Both benzyl benzoate and squalane were examined using identical tools, employing a comparable acquisition time and procedure. However, while the benzyl benzoate series underwent averaging procedure during the acquisition, meaning that a series of spectra of the same sample was averaged and combined over one spectrum through the VIPA software, the squalane spectrum was recorded without this processing step. The analysis conducted on the VIPA spectrometer indicates that the averaging applied to the spectra appears to diminish the doublet difference. To sum up this part, the FWHM as affected than the frequency shift compound in both TFP-1 and VIPA.

4.4.3. Asymmetry Between Stokes and Anti-Stokes Inside the DAC Under Pressure for Both Softwares

The FWHM doublet difference presented in Figures 4.10 and 4.11 for benzyl benzoate and squalane clearly shows important values at low and medium pressures. This is mainly due to the fluctuation of the light position on the detector during the acquisition, and the optical misalignment of the set-up as shown in Appendix D.1 Figure D.1 and in agreement with reference [196] from which Figure 4.12 exposed asymmetrical features with a VIPA spectrometer.

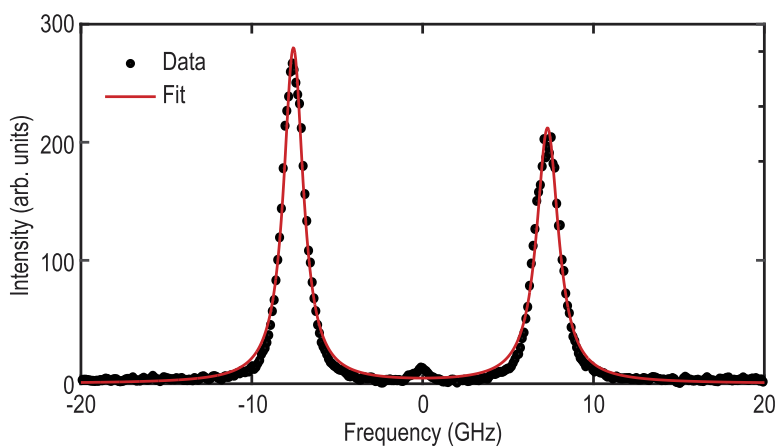


Figure 4.12: Figure from reference [196]: spectrum of pure water measured with a VIPA spectrometer at room temperature which shows asymmetrical intensities between the Stokes and anti-Stokes peaks. The central Rayleigh contribution is attenuated due to the use of dual-pump-killers.

Then the influence of the position of the probed sample inside the diamond anvil cell on the linewidth is investigated.

The previous analysis is extended to the influence of the localization on the measurement of the asymmetry in the doublet for high-pressure experiments. Coming back to the squalane experiments using the VIPA set-up, Brillouin spectra for four pressures on squalane have been taken in 12 localizations (from Z0 to Z10) represented in blue in Figure 4.4. The analysis is presented in Figure 4.13.

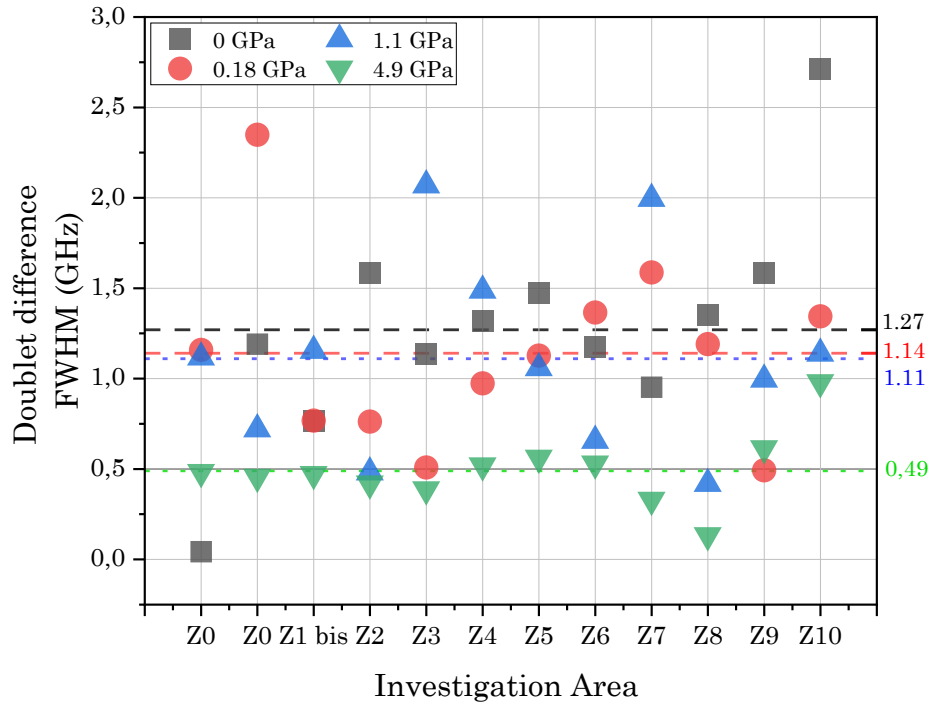


Figure 4.13: Doublet difference (on Stokes and anti-Stokes peaks) in the FWHM of squalane obtained with the Toullec 11 cell using the VIPA set-up. Horizontal lines correspond to the average value of the doublet differences (in GHz) for each pressure.

From Figure 4.13, depending on the measurement localization, the FWHM shows important disparities that are larger than the VIPA spectrometer resolution (0.2 GHz). The average value of the doublet difference tends to decrease with increasing pressure, as shown in Table 4.9. For high pressure, the doublet difference and its standard deviation tend to be smaller than at low pressure.

Pressure (GPa)	0	0.18	1.1	4.9
Averaged doublet difference (GHz)	1.27	1.14	1.11	0.49
Standard deviation (GHz)	0.59	0.49	0.51	0.19

Table 4.13 : Summary of the analysis of Brillouin spectra recorded at 12 distinct positions using the VIPA spectrometer. The standard deviations and the average doublet differences are averaged over all the measurement areas for each pressure.

To conclude, this analysis shows that the VIPA spectrometer more asymmetry than the TFP-1, especially when the spectrum is unaveraged. The cause may be due to a misalignment in its optics and an important instability of the spectra position during the acquisition.

The FWHM and the frequency shift will be averaged values from Stokes and Anti-Stokes peaks and the final error will be calculated by the sum of the fitting errors on the doublet measurement.

For the rest of the work, all spectra will be analysed by OriginPro and the multi-Lorentz fit, to analyse as best as possible the spectroscopic parameters at low pressure which will be used as reference values to establish the pressure (and temperature) influence

4.5. Validation of the Procedure and Set-up

4.5.1. Comparison Between VIPA and Fabry-Pérot Measurements

To verify the fitting procedure gives similar results to those of the literature, Figure 4.14 presents data from Jeong et al. [19] on glycerol under pressure taken from a six-pass tandem Fabry-Pérot with a laser source at 532nm. The microscope is an Olympus BX-41 equipped with a microscope objective of 0.25 NA. The frequency shift evolution found here seems coherent with their results, whereas the FWHM extracted from the TFP-1 present higher values, above 4 GPa our FWHM values are about 0.25 GHz larger.

Several differences have to be highlighted to understand the difference on the FWHM.

In the Jeong reference, the glycerol was filtered through a microfilter before being analysed by Brillouin spectroscopy to eliminate possible dust and impurities. In addition, glycerol is a water-friendly molecule. A review from 2019 [208] shows that a mixture of glycerol and water tends to increase the linewidth by 0.1 GHz if the mixture is at 90/10 glycerol/water. But, this effect does not explain alone the 0.25 GHz difference.

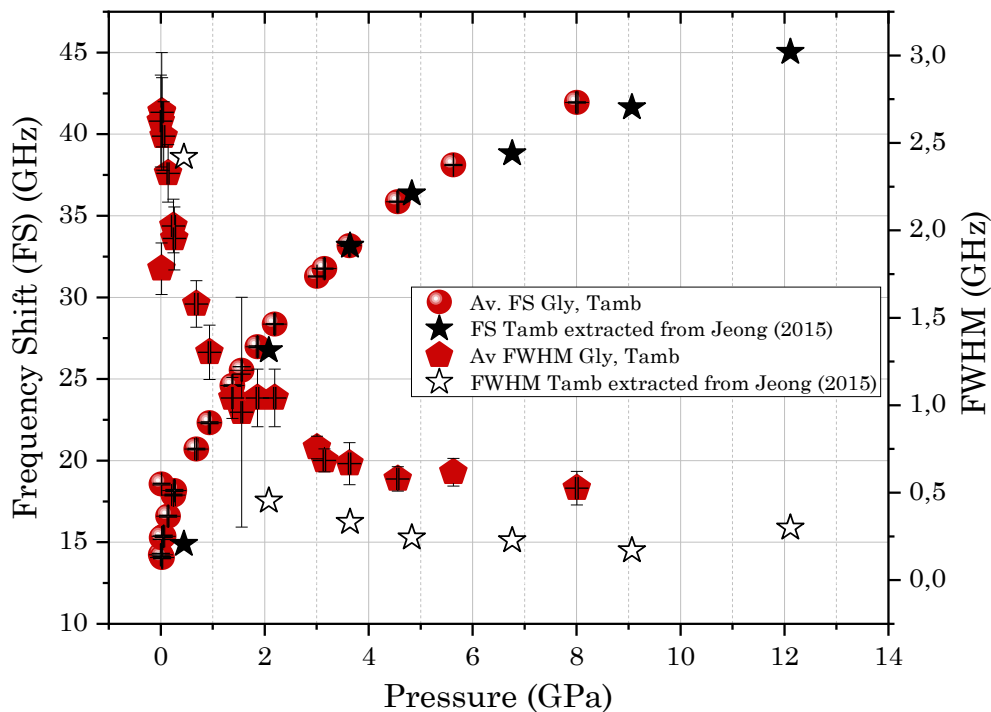


Figure 4.14: FWHM and frequency shift of glycerol under pressure with the Lorentz fitting procedure from TFP-1. Those results are compared to the results of Jeong et al. (2015) [19].

The microscope and objectives used by Jeong et al. are obviously different from those used in the work. The numerical aperture of the objective was of 0.25, and a 10 mm diameter circular aperture was put in front of the collection lens to reduce the aperture broadening effect. In fact, our objective has a numerical aperture of 0.42. According to reference [202], the greater the numerical aperture the wider the FWHM, which might explain to some extent the discrepancy between the two set of results. In fact, according [202], the Full Width at Half Maximum (FWHM) experiences an increase of approximately 0.16 GHz when transitioning from a Numerical Aperture (NA) of 0.25 to a NA of 0.42 in a backscattering configuration."

4.5.2. Comparison with Literature: Fluid Reference Under Pressure

The signal recorded by the Brillouin spectrometer is the signature of the sample but also of the spectrometer (including all optical components) itself. As presented in Section 4.1.2 about the numerical aperture effect, the impact of the objectives on the spectrum is explored. Indeed, the FWHM is a way to characterize the properties of a material, it is crucial to determine the influence of the spectrometer on this parameter. As an example, in Figure 4.15, the FWHM is measured for two different objectives, a x10 with a 0.28 NA and x20 with a 0.42 NA (§ 3.3.2) keeping all the other conditions the same: benzyl benzoate at ambient pressure and temperature, VIPA set-up with a DAC. As expected, when the numerical aperture increases, the FWHM becomes larger.

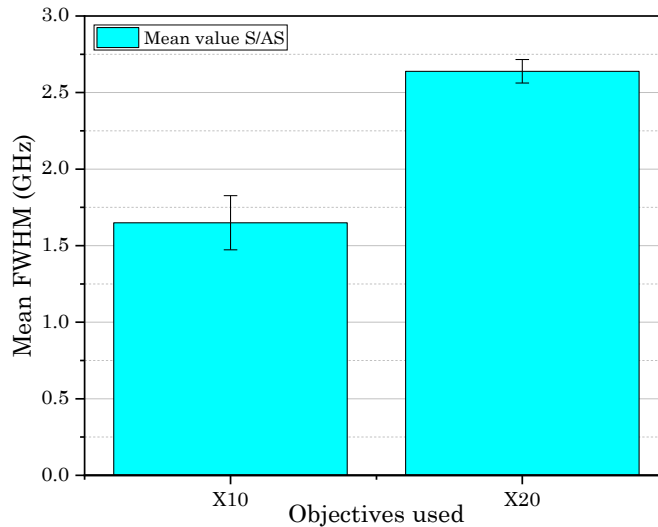


Figure 4.15: Mean value of the FWHM of benzyl benzoate taken by the same VIPA set-up, inside the DAC at ambient pressure, but with two different objectives, x10 and x20. Both spectra were not deconvoluted.

According to Figure 4.15, we can conclude that the FWHM for the same sample changes significantly depending on the objective used. The FWHM obtained with the x20 objective is

63 % larger than one given by the x10 objective. The deconvolution method is thus needed on the multi-Lorentzian fit to reduce the effect of broadening and to give accurate FWHM values.

From this statement, the same processing is used to compare results from the TFP-1 and two VIPA spectrometers (at ILM and our set-up). This analysis is summarized in Figures 4.16 for benzyl benzoate and 4.17 for squalane. The microscope used for the Fabry-Pérot measurement was equipped with a x20 objective, as well as the two VIPA spectrometers. Benzyl benzoate and squalane were placed in a beaker to be characterized. This sample are referred as large sample volume response (LSV). All measurements done by the VIPA set-ups were deconvoluted by their respective instrumental function at ambient condition of pressure and temperature.

The instrumental functions used for the VIPA spectrometers from ILM and LaMCoS are $I_{IRF_0} = 0.792$ GHz, from reference [196], and $I_{IRF_{LaMCoS}} = 1,039$ GHz respectively. Results from the TFP-1 spectrometer are not deconvoluted.

This comparison between the three set-ups shows, after the same post-processing, similar values of frequency shift and FWHM for both fluids.

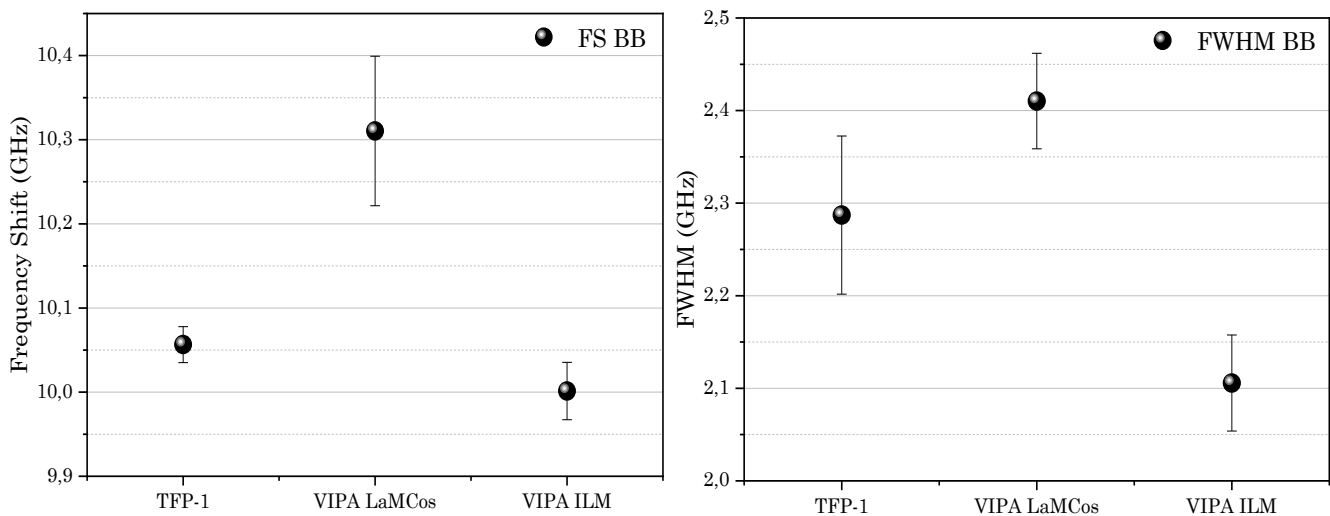


Figure 4.16: Measurements on benzyl benzoate conducted with three Brillouin spectroscopy set-ups, working with the same 532 nm wavelength.

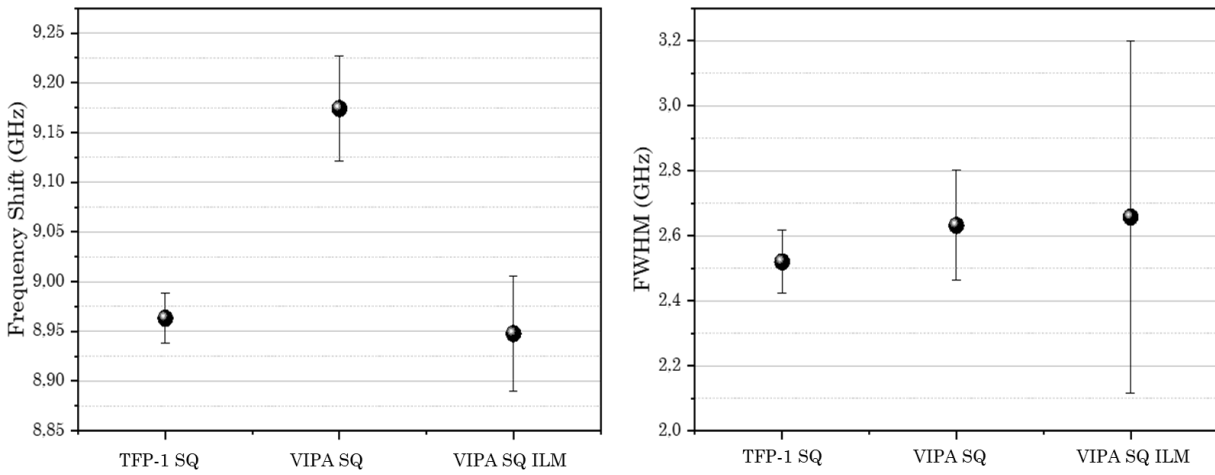


Figure 4.17: Measurements on squalane conducted with three Brillouin spectroscopy set-ups, working with the same 532 nm wavelength.

4.6. Conclusion

To conclude this chapter, the first part was dedicated to the fitting procedure and the software. Then knowing that the TFP-1 and the VIPA spectrometers do not have the same operating system, we had to choose which software, GHOST or OriginPro, is more reliable for the fitting procedure.

On one hand, the GHOST software provides Lorentz and DHO fitting models which are rather single expressions. The OriginPro software offers the Lorentz and the multiple Lorentz fitting functions. In the first phase, we found that the single and multi-Lorentz fits are equivalent if $R^2 > 0.8$.

Then both Lorentz and DHO fitting equations were compared from different softwares on 3 samples, benzyl benzoate, squalane, and glycerol at different pressures. It was observed that the Full Width at Half Maximum (FWHM) obtained from TFP-1 spectra, employing Lorentz or DHO equations, exhibits larger differences. Thus, we try to find which software provides the best similarities between both fitting procedures. OriginPro seems to give the best results, based on lower differences on both the frequency shift and the FWHM.

In a second part, the symmetry of the spectra was analysed using TFP-1 and VIPA set-up. This step was important and necessary to avoid any optical misalignment that might influence the frequency shift and the FWHM values. This analysis reveals that the VIPA spectrometer generates a significant deviation between Stokes and anti-Stokes FWHM certainly due to the instability during the acquisition and also optical misalignment. For the TFP-1 device, the distortion is lower. There is no clear tendency of the influence of the pressure on the asymmetry for both spectrometers.

In the third part, the fitting procedure was tested for glycerol versus pressure and the results were compared with a paper from the literature. We found a good agreement for the frequency shift but the FWHM measurements showed a rather large discrepancy, of around 0.25 GHz. Even if the reference paper does not provide information about the lens used in that analysis, the hypothesis behind the larger values is based on the numerical aperture of our objective and the missing pinhole that the reference work used to reduce the undesirable effect of the objective. This last element shows the importance of the impact of the set-up parts on the optical broadening.

This phenomenon was confirmed using a unique microscope but with two objectives of different numerical apertures. The results show a larger FWHM value using the x20 objective compared to the one obtained with x10 objective of lower numerical aperture.

This analysis was followed by the VIPA set-ups analysis at atmospheric pressure on large sample volume samples with the deconvolution method, and compared to the results obtained with the TFP-1 spectrometer. This method shows similar results on the 3 set-ups for the frequency shift and the FWHM. Nevertheless, the latter is more influenced by the optical parts of the set-up used.

All results presented in the Chapter 5 will be analyzed using the OriginPro software in combination with the multi-Lorentz fitting expression. Then the final results are the average of Stokes and anti-Stokes values for the frequency shift and the FWHM, deconvoluted for the VIPA set-up by the instrumental function.

5 High-pressure experimental results and comparison to friction measurements

Table of content

5.1	DETERMINATION OF THE TRANSITION PRESSURE IN A HIGH-PRESSURE CELL BY BRILLOUIN SPECTROSCOPY	161
5.1.1	OPERATING CONDITIONS	161
5.1.2	PRESSURE DEPENDENCE	162
5.2.	LIQUID BEHAVIOR UNDER PRESSURE COMPARED TO THE GLASS TRANSITION	166
5.2.1.	GLASS TRANSITION PRESSURE DETERMINATION.....	166
5.2.2.	EVOLUTION OF BRILLOUIN PARAMETER IN FUNCTION OF THE GLASS TRANSITION PRESSURE.....	177
5.3.	EVALUATION OF MECHANICAL PARAMETERS.....	183
5.4	CORRELATION WITH FRICTION MEASUREMENTS.....	191
5.6.	RESULTS CONCLUSION.....	195

In a non-conformal contact in the EHD regime, the lubricant is submitted to major constraints. It mainly experiences a very strong and very sharp increase in pressure (from P_{atm} to $P > 1 \text{ GPa}$) due to the convergent geometry of the contact inlet which leads to a strong increase in shear rate, up to very high values of $\sim 10^5$ to 10^7 s^{-1} , due to the flow velocity profiles in that region. The level in shear rate is similar at the center of the contact, due to the very thin film thickness of the lubricant ($\sim 100 \text{ nm}$). Finally, a high shear rate leads to significant heating that can result in a temperature increase of several tens of degrees at the center of the contact where the maximum high pressures occur. It is therefore crucial to understand the influence of each parameter on the behavior of the lubricating fluid to establish a robust constitutive equation on the range of stresses experienced by the lubricant in a contact. The first difficulty of lubricant characterization comes from the extreme orders of magnitude of pressure and shear rate in a contact, which are difficult to reach experimentally and simultaneously. The second difficulty comes from the strong coupling of all these parameters including temperature inside a contact.

The approach taken in this work is to uncouple these three parameters to identify their respective influence on the behavior of the lubricant. Three steps are necessary. In the first set of experiments, high-pressure measurements with temperature control combined with Brillouin measurements were carried out on the samples at rest. Pressure and temperature dependencies of lubricant properties were extracted. Then, these samples were placed in a rheometer coupled to the Brillouin spectrometer to observe the possible influence of shear on their properties. This part is discussed in the appendix E. In a second step, these results were compared to friction measurements performed in a ball-on-disc contact to establish a correlation. Finally, the last step expected in this project, but not yet carried out, will be to make in situ Brillouin spectroscopy measurements to take into account the coupling of all these parameters.

This chapter presents and analyzes the Brillouin spectroscopy measurements performed with the spectroscopy set-up described in Chapter 3 (using either the tandem Fabry-Pérot or the VIPA interferometer), compared and validated in Chapter 4. Data were exploited and interpreted following the protocol given in Chapter 4. Tests were carried out on the 3 fluids selected in Chapter 3: benzyl benzoate (BB), squalane (SQ) and glycerol (GLY). As specified in this previous chapter, superimposing data from benzyl benzoate and squalane will make possible to compare the behavior of lubricants of different molecular structures.

5.1 Determination of the transition pressure in a high-pressure cell by Brillouin spectroscopy

5.1.1 Operating conditions

Benzyl benzoate, squalane, and glycerol were characterized using the Toullec high-pressure (< 10 GPa) diamond anvil cells whose characteristics are reported in Table 3.5. Only benzyl benzoate was studied with both DAC, the low-pressure (< 1,2 GPa) [41] and the high-pressure DAC.

As explained in Section 3.4.2, micro-ruby doped chromium particles were introduced in the DAC to monitor the sample pressure. Each pressure increase is followed by a rest time of about 30 min. Then, the ruby luminescence is recorded before and after each Brillouin spectra.

The final pressure is the average pressure between two measurements corrected by the neon shift. The measurement error is the sum of the fitting errors in all steps.

Each lubricant has been introduced in the DAC using a micropipette in the cleaned hollowed steel gasket. The DAC is carefully closed and a thermocouple of type K with a precision of 1°C is installed around it. The temperature is stabilized at around 22°C.

The 532 nm laser power on the sample is limited to 10 mW to ensure that the lubricant stays unaffected.

For the Tandem Fabry-Pérot interferometer used at ILM, the inverted microscope is equipped with a long-distance X20 objective with a numerical aperture of 0.42. Most of the Brillouin spectra were recorded with more than 600 repetitions of between 0.25 and 0.5 s for each measurement that are accumulated to ensure a good signal-to-noise-ratio (SNR) as presented in Appendix E.1. The pinhole combination on the spectrometer is 600-700 μm with a mirror spacing of 6 mm. There is no deconvolution on those spectra.

For the VIPA spectrometer with two pump-killers the acquisition time is done in single take between 2000 ms at low pressure up to 10 000 ms at high pressure. The averaging function of SpectraLock was used in the benzyl benzoate experiments cases on the final spectra due to the instabilities of the laser. Then, the spectra are deconvoluted by the instrumental function to avoid the spectra broadening using Equation 4.1 introduced in Section 4.1.1. In backscattering configuration, the width Γ_{IRF} found of the laser passing inside the build microscope presented in Section 4.5.2, is about 1 GHz. The initial line bandwidth of the Torus laser is about 1 MHz according to the datasheet given. The broadening was limited by the use of a low numerical aperture objective [202].

VIPA experiments on benzyl benzoate and squalane were performed with the Toullec 11 DAC and the build microscope with the Mitutoyo X20 apochromatic long-distance objective. Every spectrum was recorded by the original software provided by Light Machinery.

In both cases, as justified in Chapter 4, Brillouin spectra are fitted with the multiple Lorentz formula provided by the OriginPro software.

5.1.2 Pressure dependence

In this section, an exploration into the pressure-dependent properties of benzyl benzoate, squalane and glycerol is undertaken. The investigation particularly focuses on discerning changes in the Full Width at Half Maximum (FWHM) and frequency shift (FS) as a function of pressure.

Benzyl benzoate was studied in backscattering geometry at 22°C and typical results are reported in Figure 5.1, were the imposed pressure ranges between 0 and 7.5 GPa.

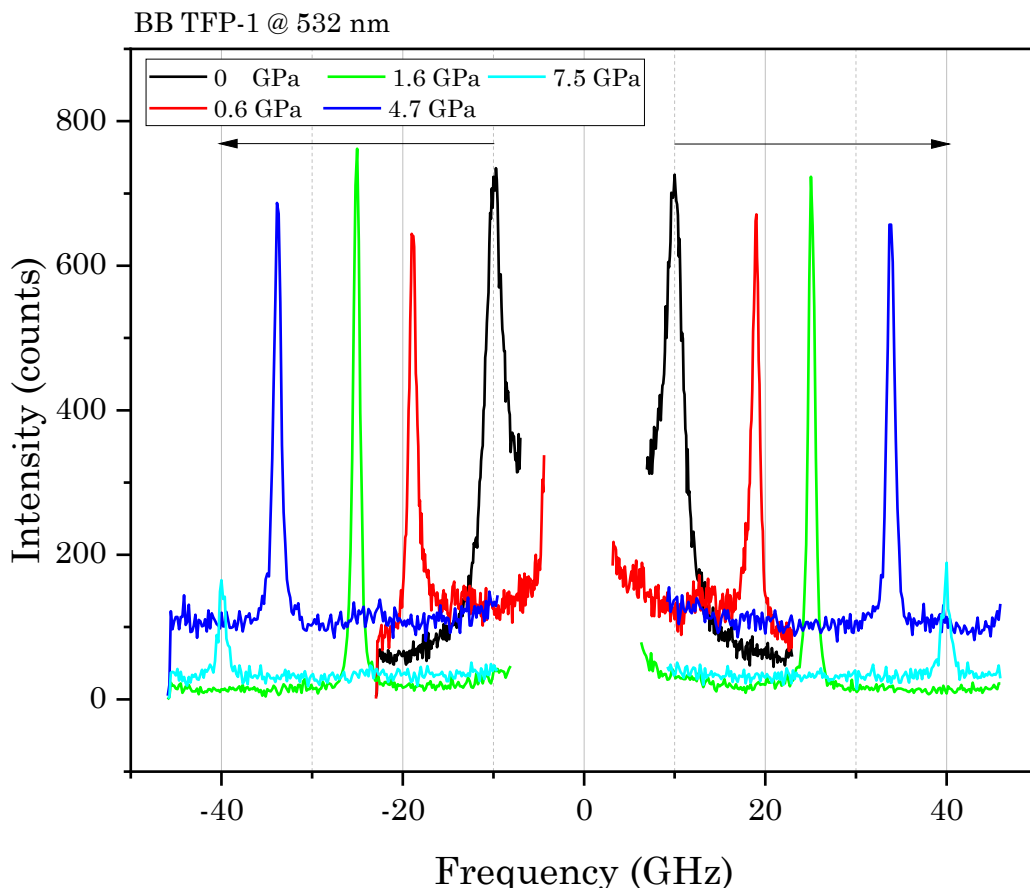


Figure 5.1: benzyl benzoate at 22°C spectra from TFP-1 at 532 nm using the Toullec 12 DAC. Arrows on the top of the peaks indicate the frequency shift progression. The Rayleigh contribution at the center has been masked.

As the pressure increases, the frequency shift of the lubricant spectra, which is initially near 10 GHz at room pressure, reaches 40 GHz at 7.5 GPa. The FWHM of the inelastic peaks also changes from 2.3 GHz at room pressure to 0.9 GHz at 7.5 GPa. These evolutions are not linear, as shown in Figure 5.2.

The evolutions as a function of pressure for the 3 fluids are superimposed in Figures 5.2 and 5.3 for the frequency shift and the FWHM, respectively. Additional measurements from Large

Sample Volumes (or LSV) are identified by an empty symbol. The final result on glycerol is compared to a similar study done by Jeong [19] (stars symbols).

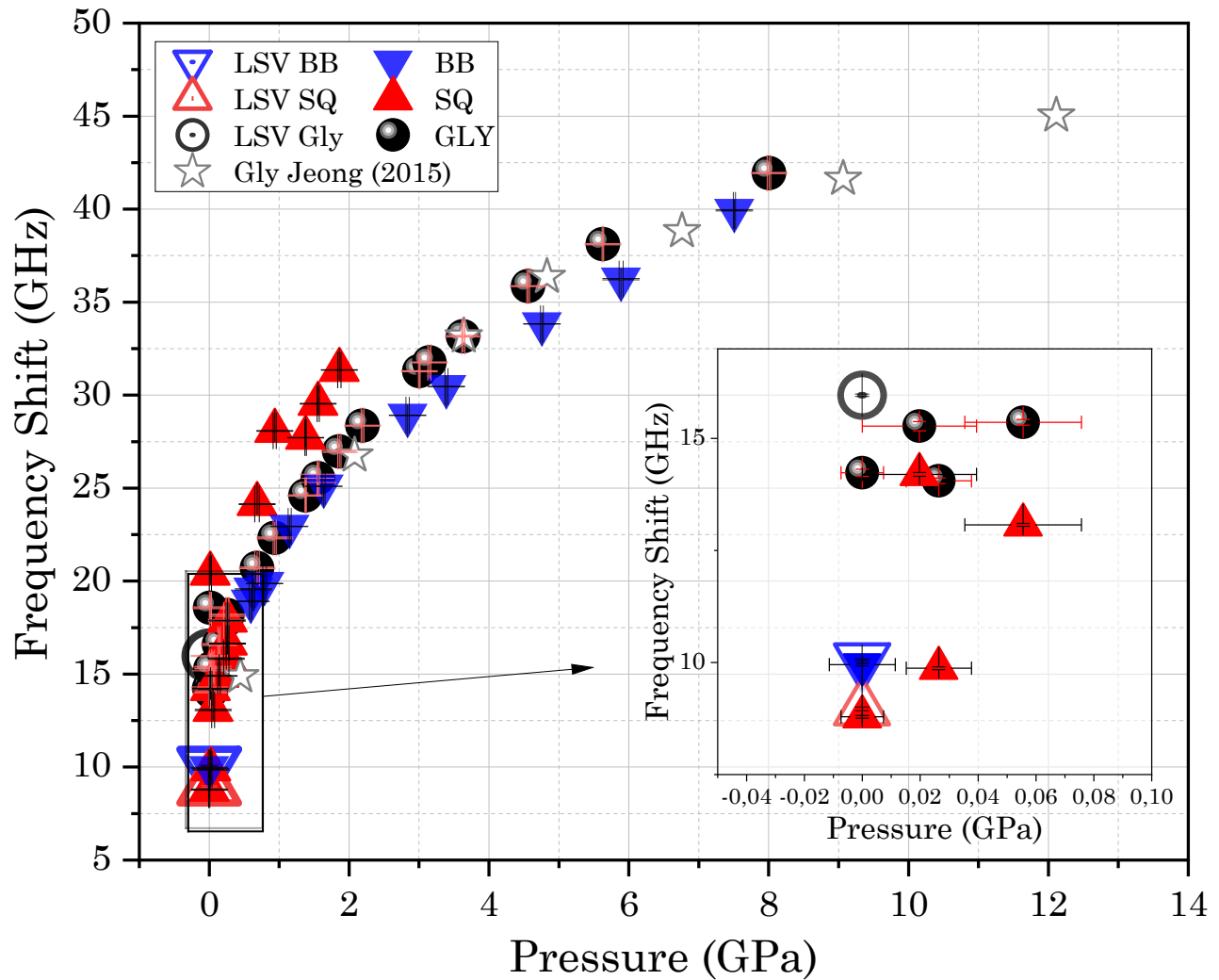


Figure 5.2 : Frequency shift of benzyl benzoate, squalane and glycerol in the backscattering geometry vs. pressure in the Toullec DAC, at room temperature. All data were obtained with the Tandem Fabry-Pérot interferometer TFP-1. A zoom on the right side shows on the Large Sample Volume (or LSV) measurements (open symbols).

Looking at Large Sample Volume (or LSV) dataset in Figure 5.2, those values are close to the values measured at atmospheric pressure in a high-pressure cell. It means closing the DAC does not create a significant additional pressure.

All fluids frequency shift increases rapidly at low pressure, in the range of [0 – 1] GPa. Then for pressure over 2 GPa, the frequency shift increase rate seems to reduce over pressure.

In more detail, in the [0 – 0.7] GPa range of pressure, benzyl benzoate frequency shift increases by 9 GHz in 0.6 GPa (15 GHz/GPa), which is similar to the variations experienced by the glycerol sample. Nevertheless, the glycerol sample seems to be less impacted by the increasing pressure by showing a 7 GHz rise for a 0.7 GPa increase (10 GHz/GPa). The

squalane sample seems to be more pressure sensitive by increasing by 15 GHz while increasing the pressure by 0.7 GPa (21.4 GHz/GPa).

At pressures between [0.7 – 1.7] GPa, the evolution rate of each sample is the following: benzyl benzoate 5.2 GHz for an increase of 0.9 GPa (5.8 GHz/GPa), squalane 5.5 GHz for an increase of 1 GPa (5.5 GHz/GPa) and glycerol about 4.8 GHz for an increase of 0.88 GPa (5.45 GHz/GPa). All in all, these values are very close.

Finally, between [4 – 8] GPa, both benzyl benzoate and glycerol show another reduction of the frequency shift increasing rate. For benzyl benzoate, it dropped to 2.2 GHz/GPa and for glycerol to 2 GHz/GPa.

Note that the frequency shifts of the 3 samples tested in this work are similar to the one provided by [31] for a naphthenic base oil and reported in Figure 1.13.

In Figure 5.3, the FWHM of all samples seems to follow the same L shape, with a rapid drop up to 2 GPa and the occurrence of a plateau-like value at higher pressures.

In more detail and with the same methodology used for the frequency shift, between [0 – 1] GPa, the FWHM decreasing rate for benzyl benzoate is around 2 GHz/GPa, 1.5 GHz/GPa for glycerol, and 3.1 GHz/GPa for squalane. Between [1 – 3] GPa, the FWHM decreasing rate for benzyl benzoate is 0.02 GHz/GPa, 0.2 GHz/GPa for glycerol, and 0.3 GHz/GPa for squalane. Finally, between [4 – 8] GPa, the FWHM decreasing rate almost stabilized approximatively about 0.02 GHz/GPa for glycerol, which is lower than the error bar calculated. The benzyl benzoate sample behaves differently, the value increases again by approx. 0.01 GHz/GPa, but still this variation is lower than errors.

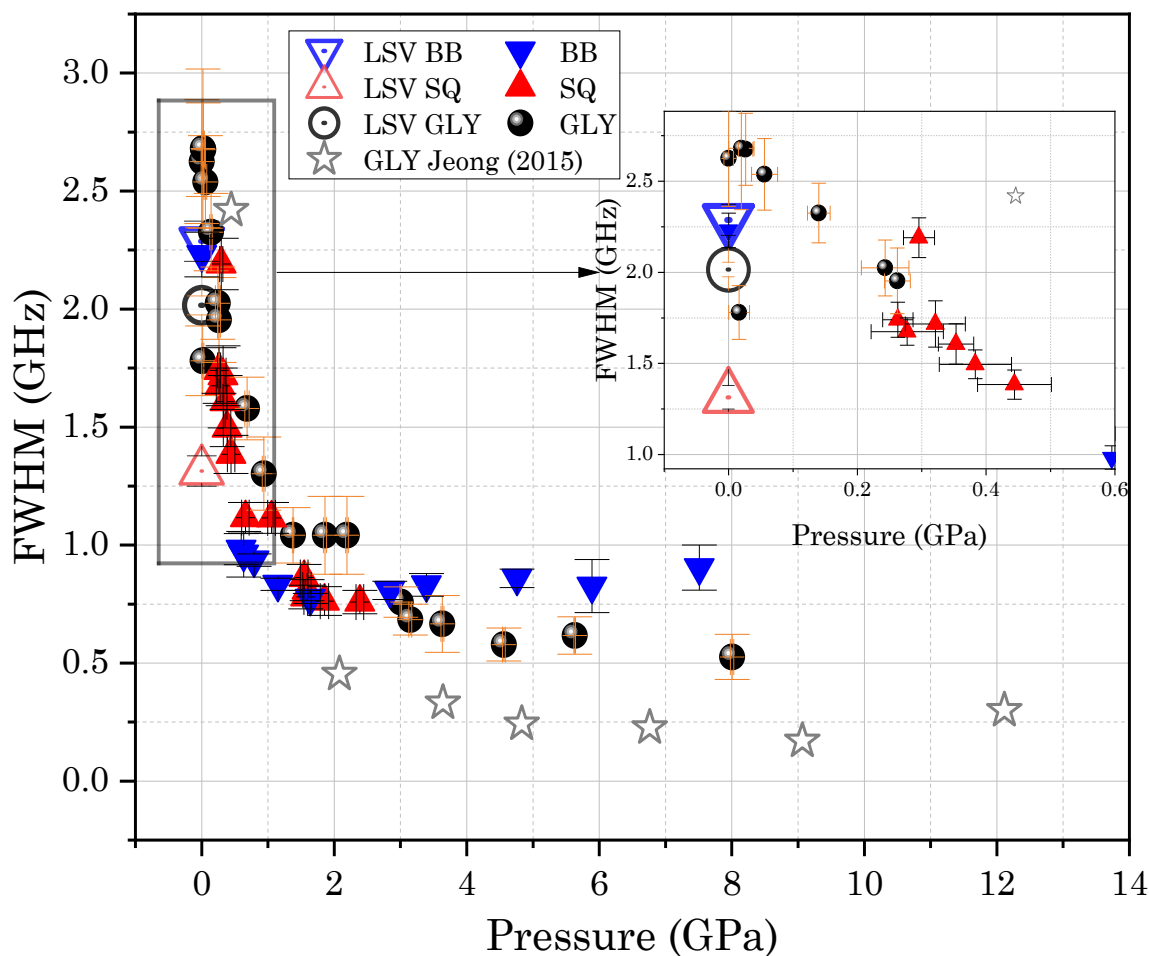


Figure 5.3 : FWHM of benzyl benzoate, squalane and glycerol vs pressure in the Toullec DAC, at room temperature. All results were obtained with the Tandem Fabry-Pérot interferometer. A zoom on the right side shows the result of Large Sample Volume (LSV) measurements (open symbols).

The glycerol FWHM can be considered in our study to reach a plateau beyond 4 GPa. Nevertheless, this shows a significant difference compared to the published values from Jeong 2015. As mentioned in [19,209], the numerical aperture of the lens used in the Jeong and al. study was 0.25 NA which is lower than the one used in this study (0.42 NA). In addition, as seen in Sections 4.1.2 and 4.5, the larger the numerical aperture, the larger the dispersion of the linewidth. The dynamic of compression could affect the overall thermodynamic behavior, and so the pressure of the glass transition [210]. This study on the dynamics of compression combined with inelastic light scattering is recent. Unfortunately, this point was not studied in this work due to the lack of time.

However, our dataset exhibits a favourable alignment with the frequency shift observed in the Jeong study.

The transition from the liquid-like to the glassy regimes is reminiscent of the glass transition explained in Chapter 1 (§ 1.3.2). It can therefore be analyzed with regard to the relaxation processes in the sample. Comez and coworkers [8] described a comparable evolution of the spectra of several molecules (PB, DGEBA, oTP and m-toluidine) as a function of temperature.

They found a strong temperature dependence of the linewidth for temperatures above the glass transition temperature, so when the material is liquid because it is dominated by structural (α) relaxation. Conversely, for temperatures below the glass transition temperature, the structural relaxation time is very long and therefore accessible at very low frequencies only, lower than the range of frequencies of the spectrum (lower than 1Hz according to [8]). Over this range of (low) temperatures, there is no significant contribution of the structural relaxation on the GHz region, which explains the very low and constant value of the linewidth. The same analysis can be proposed here with pressure. Indeed, on one side lowering the temperature of a sample temperature reduces the thermal energy of the molecules. On the other hand, increasing the pressure leads to a jamming of the sample volume. This results in both cases in a reduction of the mobility of the molecules, therefore a slowing down of the dynamics of relaxation [19].

The next part will highlight the impact of the glass transition pressure on physical properties such as sound velocity, storage and viscous moduli.

5.2. Liquid behavior under pressure compared to the glass transition

5.2.1. Glass transition pressure determination

The investigation initially focused on benzyl benzoate, employing two DACs, the low-pressure Betsa as used by Ndiaye [38], and the high-pressure Toullec 12 utilizing the same interferometer (TFP-1) and laser wavelength (Torus at 532 nm).

Ndiaye in his thesis in 2017 initially used a Gaussian fit [38]. All data presented, from this study and from S. Ndiaye, has been treated with the multi-Lorentz fit described in section 4.3. Indeed, the Gaussian fit could create an important deviation on the linewidth since the inelastic peak is asymmetric. Vertical error bars in Figures 5.4 to 5.10 represent the uncertainty due to the fitting of the BLS spectra with a multi-Lorentzian function. Uncertainties on the pressure determination, detailed in Section 3.4.2, are also reported by horizontal error bars.

Figure 5.4 is a comparative analysis performed between high-pressure from this work and low-pressure data extracted from Ndiaye's earlier study in 2017 [38]. Another set of high-pressure measurements done in this work with the new microscope and the VIPA spectrometer are added to the figure. It appears that the evolution of both the frequency shift and the FWHM (Figure 5.6) from TFP-1 data-sets shows close values with the same pressure dependency over the range of pressure chosen even if the. However, notable differences have to be discussed.

In Figure 5.4 and the zoom in Figure 5.5, the frequency shift of benzyl benzoate under pressure follows a similar trend for the three sets of data as explained in Section 5.1.2.

However, a slight shift of the frequency shift between 0 and 2 GPa between all experimental results can be noticed. In fact, they are not perfectly superimposed. The VIPA frequency shift is shifted toward high pressure by 0.1 to 0.2 GPa, compared to our measurements with the TFP-1 interferometer.

In the tests carried out, several main differences are identified. First, ruby spectrometers used in the TFP-1 and the VIPA experiments are not the same as presented in section 3.4.2, but the same pressure calculation procedure is applied. This point will be later discussed in Section 5.3. Secondly, the microscopes are not identical, even if the microscope objectives have the same numerical aperture and the lasers are identical. However, the ruby pressure procedure may differ from Ndiaye procedure in the determination of the reference ruby luminescence. Indeed, In the Ndiaye publication, the reference ruby wavelength is taken for a membrane pressure that shifts the R1 peak. In other hand, in this work, the reference ruby is taken when the membrane is closed and non-pressurized.

Moreover, the difference in DAC set-up could partially explain this point, as presented in Table 3.3 in Section 3.1.

As mentioned in Section 1.4.1, the glass transition is identified as the change of slope in Brillouin spectra as a function of temperature or pressure. The glass transition pressure extraction method is conducted by computing linear fits on the edges of the pressure domain and extrapolating to make those lines cross each other. In Figures 5.4 to 5.7, linear fits represented as dashed or solid lines are computed on both sides of the slope change zone. In Figure 5.4, four fits are performed on the dataset, with two corresponding to VIPA experiments.

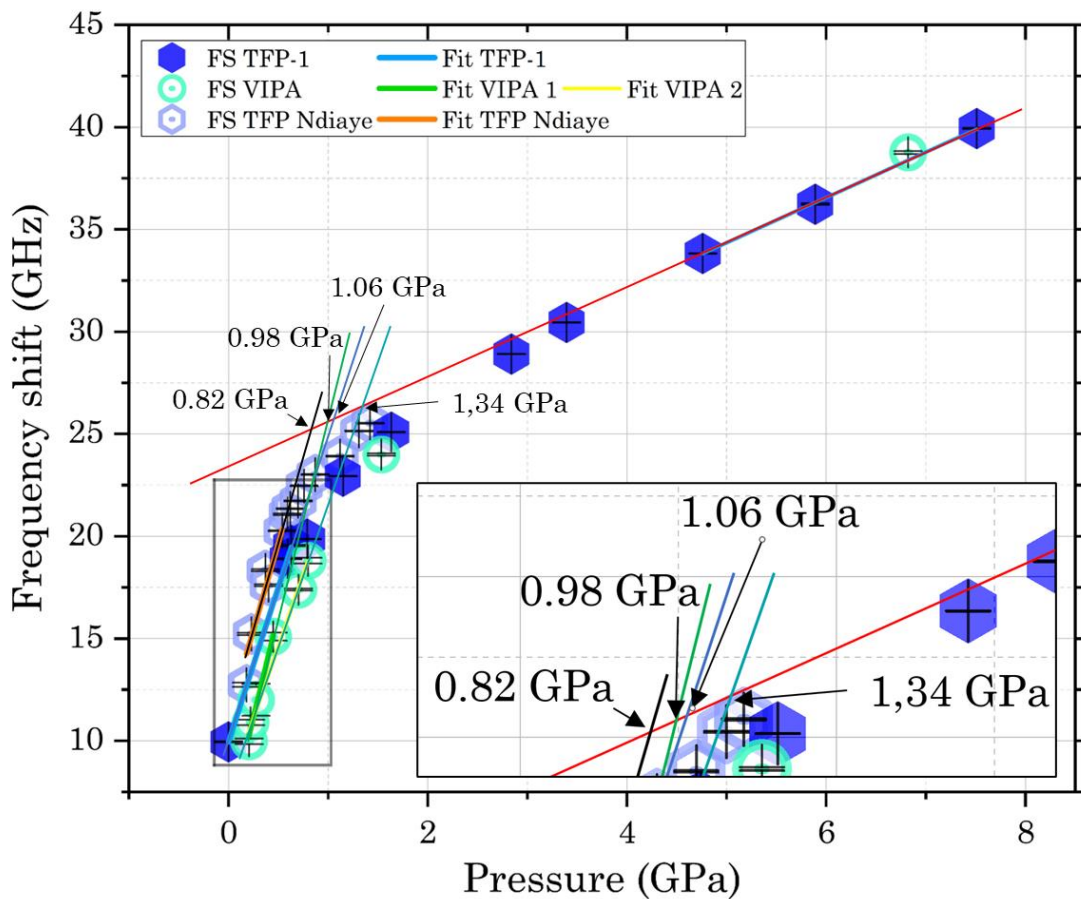


Figure 5.4: Benzyl benzoate frequency shift in the backscattering geometry at 22°C. The high-pressure experiments from this work are performed with an X20 objective with the TFP-1 (blue full hexagon) and VIPA (green open circle symbols with a central dot). The low-pressure cell allows small incremental pressure steps below 1 GPa. The study performed with the low-pressure cell by Ndiaye using a X10 microscope objective [38] is represented by light blue open hexagon symbols with a central dot. The black, orange and red lines correspond to the linear fit of the frequency shift of the Ndiaye dataset, green from VIPA, and blue from this work on the TFP-1. A zoom for TFP-1 data between 0 and 2 GPa is given in Appendix D.2.

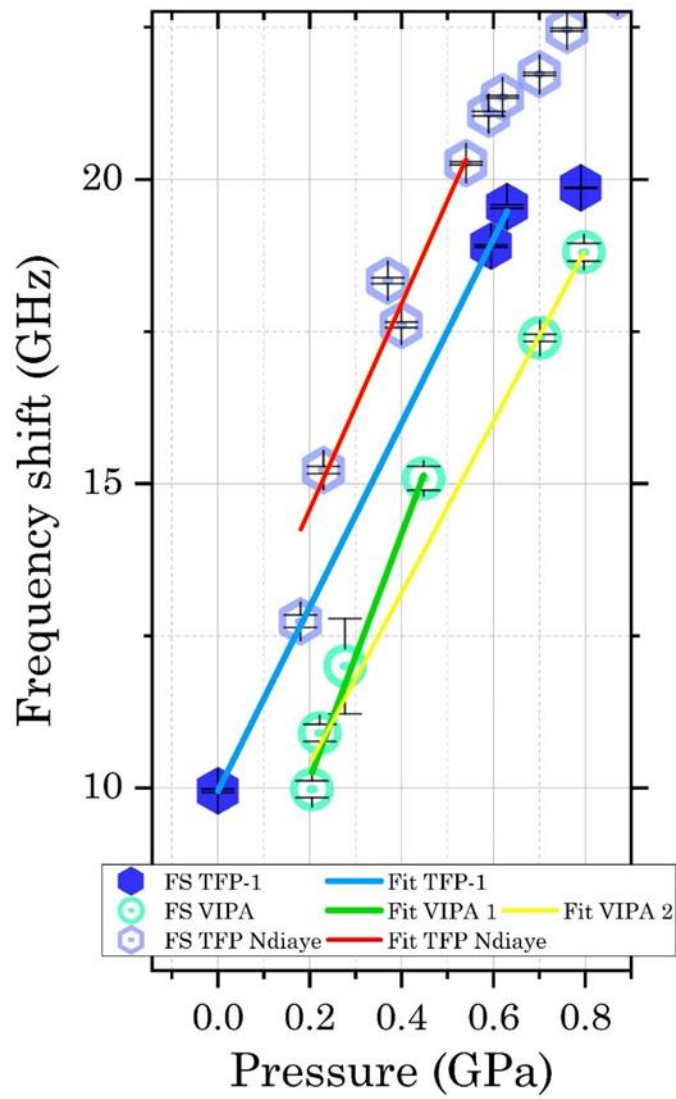


Figure 5.5 : Zoom on the low-pressure area of Figure 5.4. Four fits were tested on this work TFP-1 (blue), the Ndiaye dataset (red) and VIPA dataset (green and yellow).

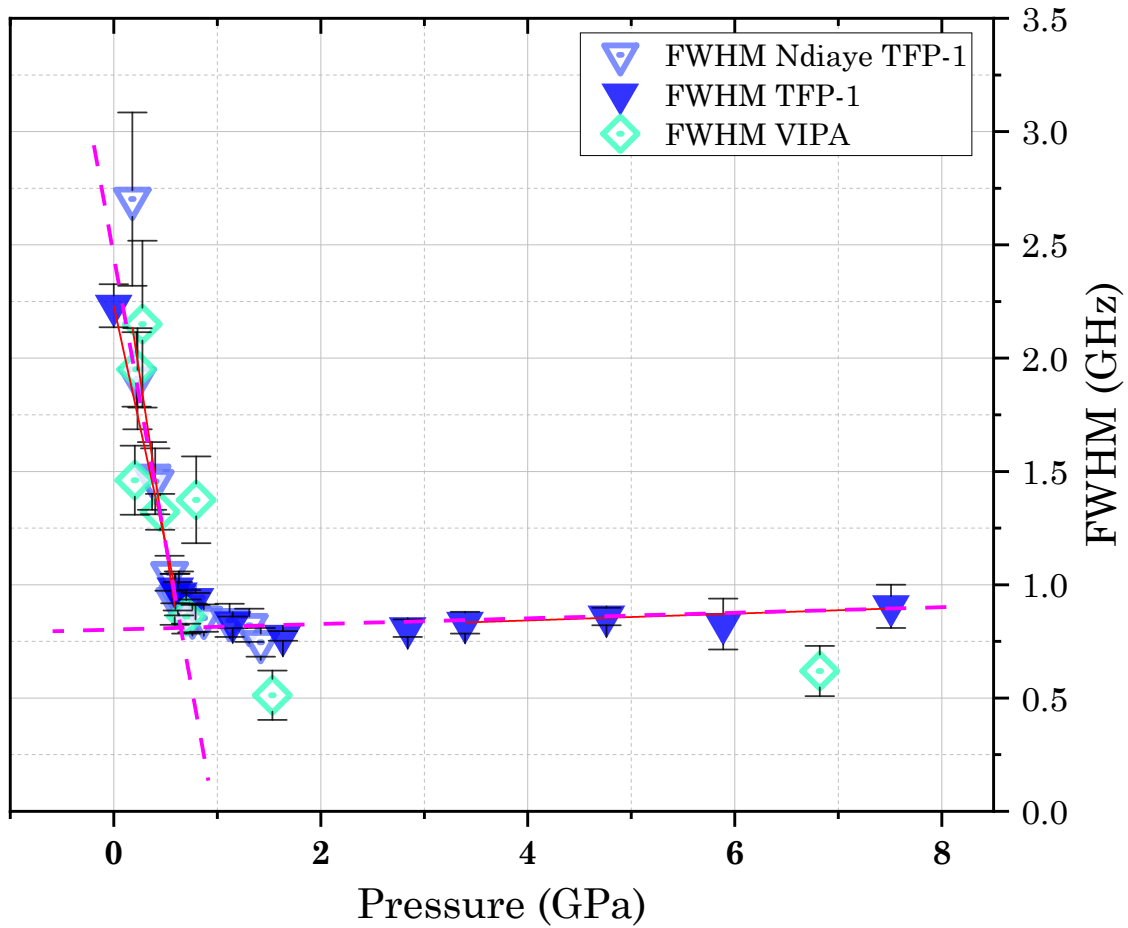


Figure 5.6 : Benzyl benzoate FWHM in the backscattering geometry at 22°C study performed with low-pressure cell by Ndiaye using a X10 microscope objective [38] (light blue upside down open triangle shape with a central dot) and fitted by the triple Lorentz. High-pressure experiments on benzyl benzoate are performed on this work with an X20 objective on the TFP-1 (dark blue upside-down open triangle shape with a central dot) and VIPA (green open diamond shape and central dot). The DAC characteristics are resumed in Table 3.4. The low-pressure cell allows small incremental pressure steps below 1 GPa. The dashed pink line corresponds to the linear fit of the FWHM, situated before and after the slope change.

The FWHM shows a more clear and more distinct change of slope compared to the frequency shift.

The glass transition pressure for benzyl benzoate is identified from the crossing of the fitting lines in Figure 5.4 for the frequency shift, $p_{g;FS} \approx [0.82 - 1.06]$ GPa, and of the pink dashed lines in Figures 5.6 for the FWHM: $p_{g;FWHM} \approx [0.6 - 0.8]$ GPa. Figure 5.6 and the Appendix D.3 presents an enlarged view of the low-pressure domain and linewidth of benzyl benzoate under pressure of Figure 5.7 respectively.

Those glass transition pressures are close to the predicted value by the modified WLF model at 20°C of 0.8 GPa.

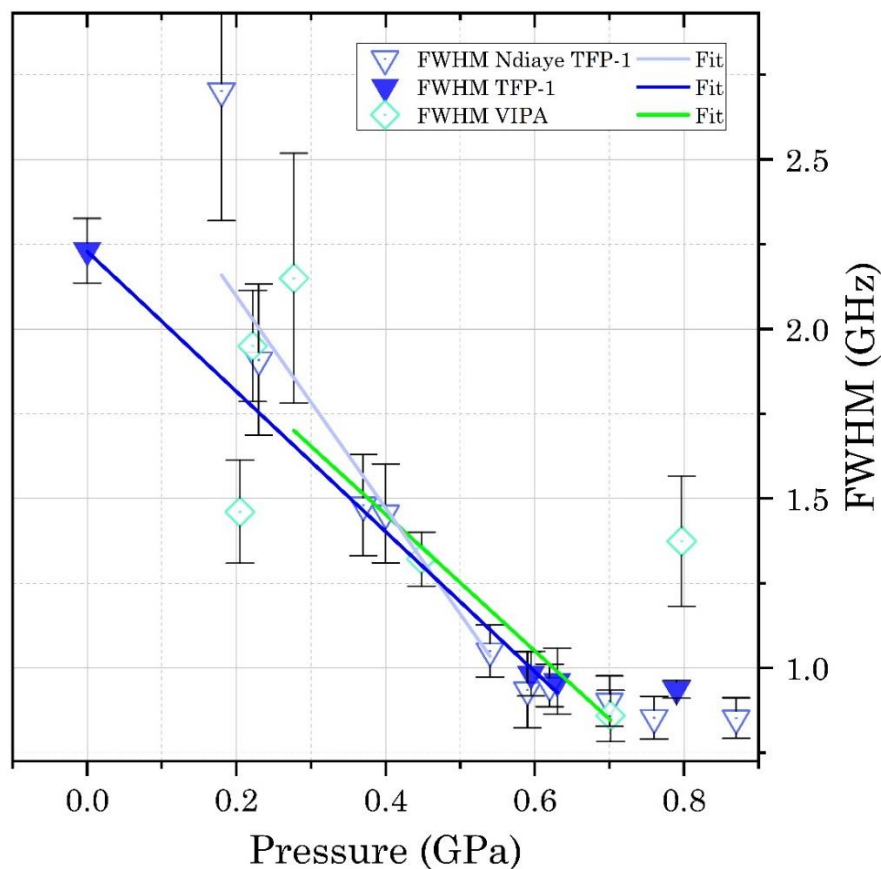


Figure 5.7 : Zoom of the Figure 5.6 between 0 and 0.9 GPa. Linear fits on each dataset were performed, light blue for data from Ndiaye with the low-pressure cell and dark blue and green from this work for TFP-1 and VIPA interferometers, respectively, from the high-pressure DAC.

Moreover, the glass transition pressures extracted from the linewidth and the frequency shift seem to be lower and higher, respectively, than the WLF glass transition pressure prediction.

This procedure for the glass transition determination has been duplicated on the squalane linewidth in Figure 5.8 and frequency shift in Figure 5.9. For glycerol, its frequency shift is displayed in Figure 5.10 and its linewidth in Figure 5.11.

Two other characteristic pressures, P_t and P_p , obtained from the BLS linewidth are indicated in Figures 5.8, 5.10 and 5.11. The transition pressure, P_t , marking the transition between the first (liquid) and the second region (glass transition) of the pressurized fluid behavior, corresponds to the first (i.e. at the lowest pressure) crossing of the fitting lines. Values derived from Figures 5.8 and 5.10 are 0.45 GPa for squalane and 1.03 GPa for the glycerol. In Figures 5.8 and 5.10, the third region at high pressure, P_p , corresponds to the very beginning of the plateau of the linewidth, corresponding to the solid “like state” (or glassy). Values derived from those figures are 1.59 GPa for squalane and 3.47 GPa for glycerol. These values are surprisingly comparable to the glass transition pressures P_g either predicted by the WLF model for squalane or taken from the literature for glycerol (in Table 3.3 in Section 3.1).

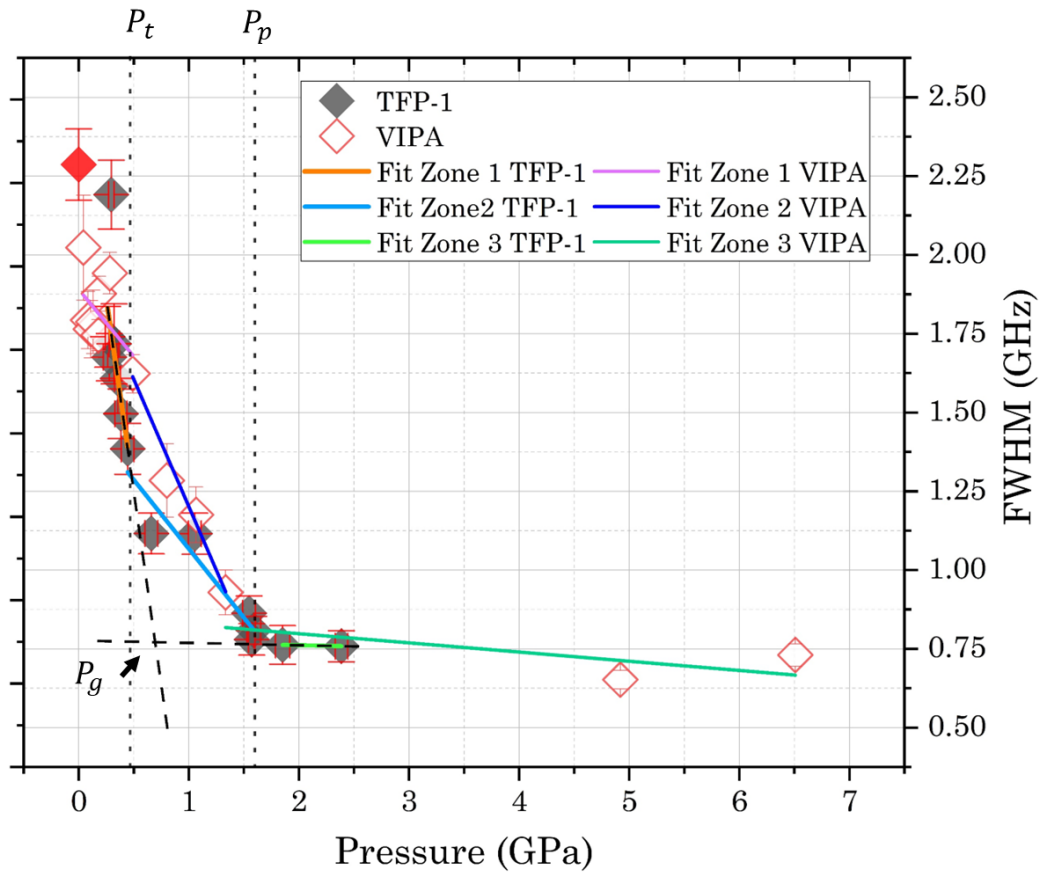


Figure 5.8: Squalane FWHM obtained with by the TFP-1 taken at 22°C and at different pressures. Linear fits are represented by dotted lines and separate different regimes characterized by $P_g = 0.7 \text{ GPa}$, $P_t = 0.45 \text{ GPa}$ and $P_p = 1.59 \text{ GPa}$.

In Figures 5.8 to 5.11, three distinct regimes are found, and particularly for the linewidth evolution with pressure. P_g is identified for all fluids. For squalane $P_{g_{FWHM}} = 0.7 \text{ GPa}$ and $P_{g_{FS}} \approx [0.7 - 1.17] \text{ GPa}$ and for glycerol in Figures 5.10 and 5.11 $P_{g_{FS}} = 2.32 \text{ GPa}$ and $P_{g_{FWHM}} = 1.49 \text{ GPa}$. This glass transition is separated by a transition zone between them identified and edged by P_t and P_p . The first regime, at low pressures, shows a strong dependence of the spectrum (frequency shift but especially linewidth) with pressure. Pressure increases the frequency shift, and strongly decreases the linewidth. The second regime is reached around intermediate pressures. Indeed, squalane shows a transition phase between 0,5 GPa and 1,5 GPa, highlighted in Figure 5.8. This range of values is compared to the Figures 4.2 and 4.3 showing a change in the standard deviation of the pressure and of the frequency shift inside the DAC at a value close to the predicted glass transition pressure ($P_g(20^\circ\text{C}) = 1.44 \text{ GPa}$). The P_p value seems to corroborate with the significant change in the homogeneity of the DAC, adding another prove of a glass transition.

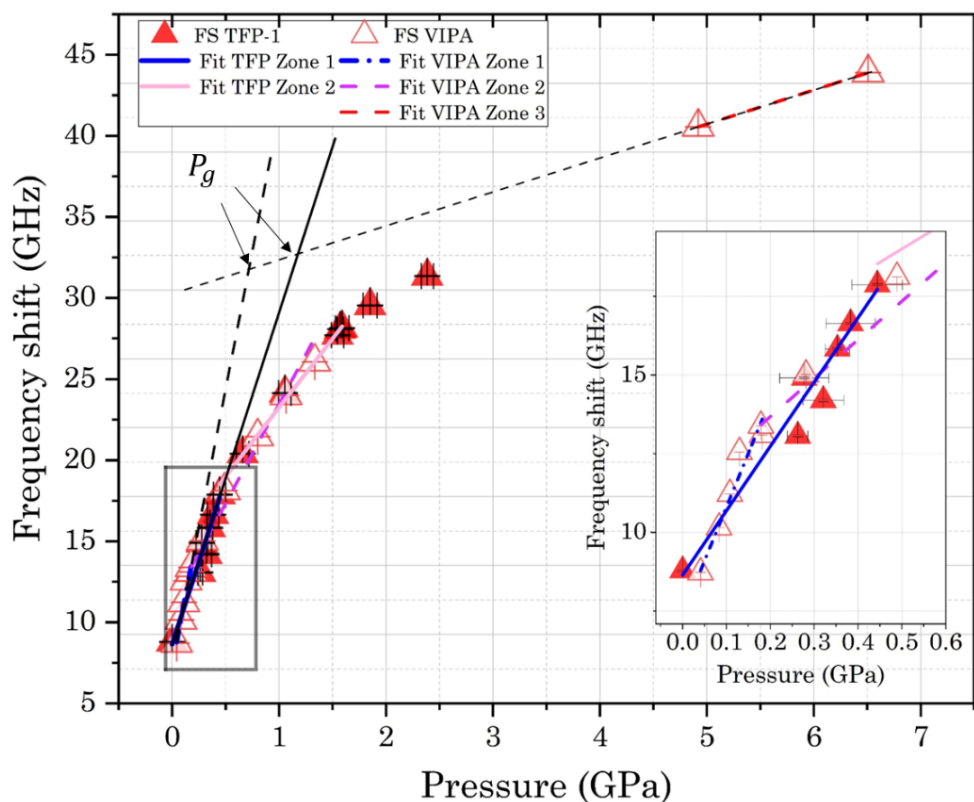


Figure 5.9 : Squalane frequency shift obtained with by the TFP-1 taken at 22°C and at different pressures. Linear fits are represented by dotted or solid lines and which lead to $P_{g_{FS}} = 0.71 \text{ GPa}$ and $P_{g_{FS}} = 1.17 \text{ GPa}$, respectively.

The same behavior occurs between 1 GPa and around 3.5 GPa for glycerol. It is characterized by a weaker dependence of the spectra with pressure. The frequency shift increases further with pressure, following a weaker slope, while linewidth stabilizes to a very low value ($< 1 \text{ GHz}$).

As shown in Figures 5.8 to 5.11, squalane and glycerol show large transition regions between the liquid-state and the solid-like state. By comparing the glass transition pressure to the literature values, there is a disagreement concerning glycerol. This is due to the variety of methods available to determine the glass transition and possible differences in the experimental protocols.

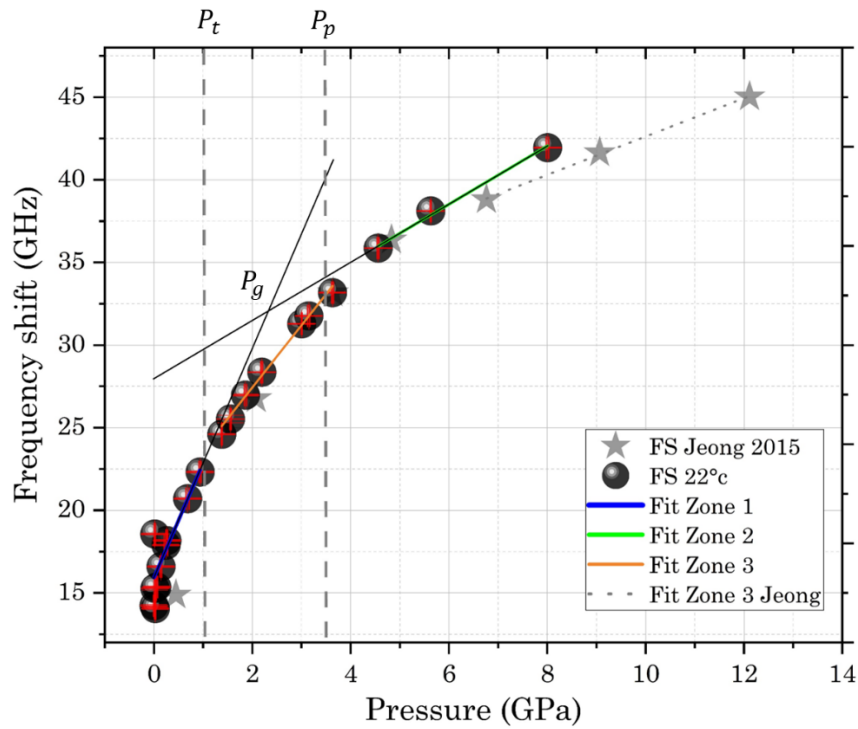


Figure 5.10 : Glycerol frequency shift and FWHM taken by the TFP-1 and data extracted from [19]. Linear fits represented by vertical dotted lines separate different regimes identified by P_t and P_p .

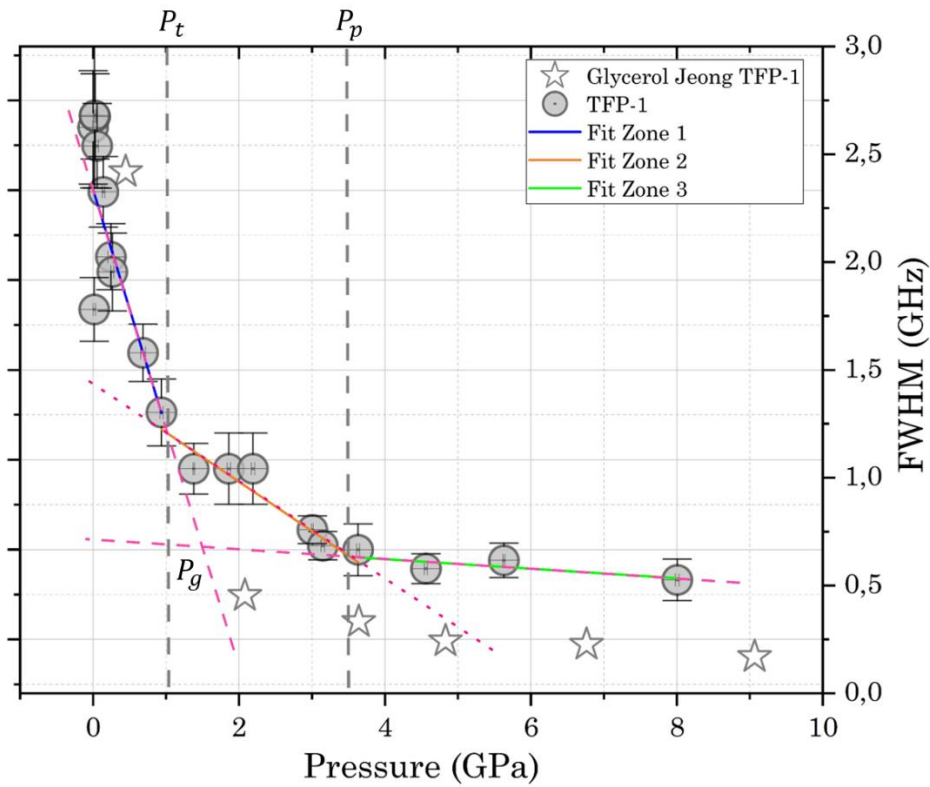


Figure 5.11 : Glycerol FWHM taken in the backscattering geometry by the TFP-1 and data extracted from [19]. Linear fits represented by dotted lines separate different regimes identified by P_t and P_p .

Indeed, a publication by Oliver reports a glycerol glass transition pressure at 25°C around 4,5 GPa [205], using Brillouin spectroscopy. In Figure 5.12 extracted from Oliver publication, a plateau regime appears earlier, around 3.5 GPa, and corresponds to the P_p value previously reported. Moreover, another experimental feature is the occurrence of a non-hydrostatic pressure when the pressure exceeds 5.5 GPa. This feature is not present in our experiments nor in the Jeong 2015 publication.

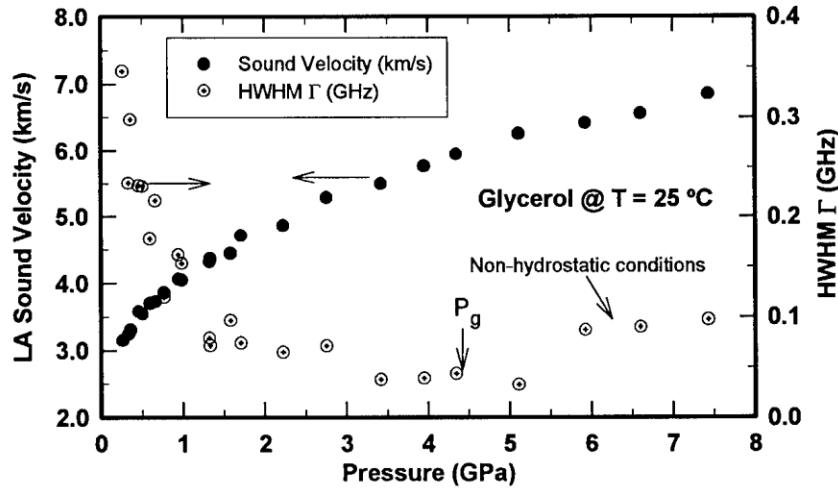


Figure 5.12: Figure extracted from the W. Oliver [205]. It represents high-pressure HWHM Brillouin measurements on glycerol in backscattering geometry and 25°C, and also the longitudinal sound velocity (which varies like the frequency shift).

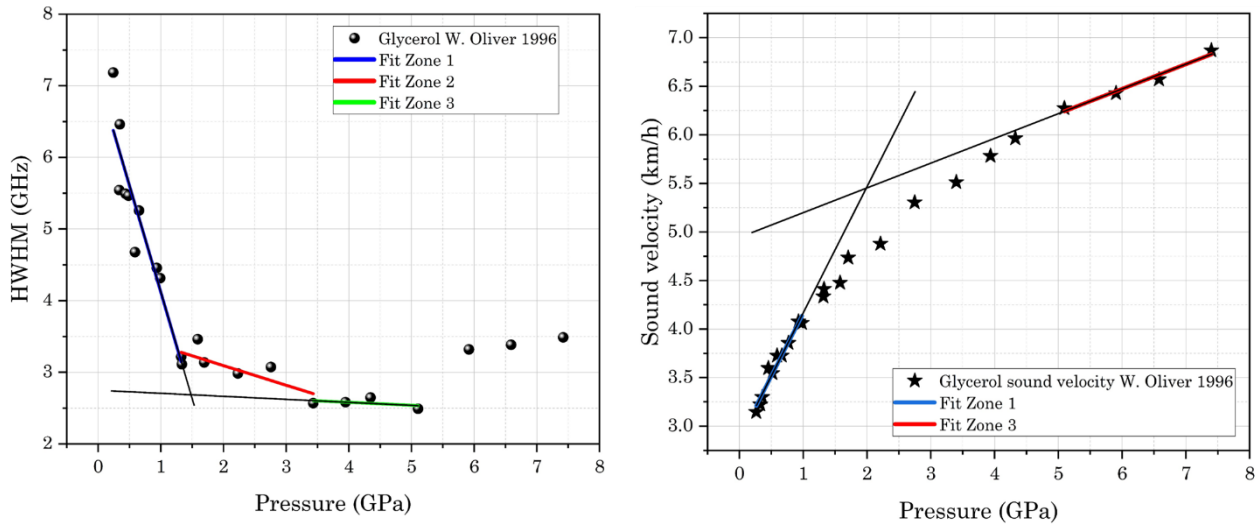


Figure 5.13: HWHM (left) and sound velocity (right) versus pressure, extracted from Oliver [205]. Fits are provided for three zones on the HWHM and at the edges of the pressure domain for the sound velocity.

With the method described previously, the glass transition pressures are of $P_{g_{HWHM}} = 1.48 \text{ GPa}$ (Figure 5.13 left) and $P_{g_{SV}} = 1.98 \text{ GPa}$ (Figure 5.13 right). The values extracted from

the HWHM is close to the one found with the FWHM in this study. However, the sound velocity, which is calculated from the frequency shift, shows a significant deviation (of ≈ 0.34 GPa). The average pressure error dataset made during this study is under 0.1 GPa but no error bars are given by Oliver. In addition, neither frequency shift nor refractive index from Oliver work have been reported, so their values cannot be compared. Furthermore, It has to be noted that 3-degree temperature difference impacts the ruby pressure by 0.03 GPa only. The last possibility to explain the difference in the transition pressures relies on the pressure extraction or the pressure application protocol that may differ.

Moreover, the glass transition pressure can also be evaluated by another method: the ruby fluorescence manometer [211]. Unfortunately, this publication does not provide the value for glycerol even if the authors use the fluorescence manometer method for methanol. In 2013 Klotz et al. studied glycerol and water mixtures under pressure using this technique [212] and found a glass transition pressure of pure glycerol around 5.5 GPa at $(22.8 \pm 0.5)^\circ\text{C}$. More recently, Ahart in 2017 found that the glycerol glass transition in the THz measurements by low-frequency Raman spectroscopy is around 5 GPa [131].

	$P_{g_{FS}}$ (GPa)	$P_{g_{FWHM}}$ (GPa)	P_t (GPa)	P_p (GPa)	$P_{g_{WLF}}$ (GPa)
Benzyl benzoate	0.82 - 1.06	0.62 - 0.80	-	-	0.80
Squalane	0.71 - 1.17	0.7	0.45	1.59	1.446
Glycerol	2.32	1.49	1.03	3.47	3.8

Table 5.1: Summary of the glass transition pressures, transition and plateau pressures and values predicted by the modified WLF model at 20°C .

The values obtained from BLS experiments seem far from the WLF predictions at 20°C for squalane and glycerol. One of the main differences between benzyl benzoate and the other fluids (squalane and glycerol) is the less sharp changes of slope.

The values of P_p from BLS measurements in Figures 5.8 for squalane and 5.10 for glycerol are very close to the glass transition pressures derived from viscosity models fitted on low shear measurements (see Section 3.1), considered as low-frequency data. It corresponds to a change of slope of the frequency shift and to the very beginning of the linewidth plateau, as shown in Figure 5.3.

In the following, the glass transition pressure prediction from the modified WLF model is chosen to normalize the characteristic pressures obtained from the frequency shift and FWHM variations versus pressure of these three fluids.

To conclude, the methods to determine the glass transition, as well as to conduct high-pressure experiments, still need to be studied.

5.2.2. Evolution of Brillouin parameter in function of the glass transition pressure

In this part the evolution of the response of each liquid versus pressure, normalized by the glass transition pressure, is presented.

Figure 5.14 represents the frequency shift of benzyl benzoate, squalane, and glycerol results obtained from the TFP-1. All results are in function of the pressure normalized by the glass transition pressure given by the WLF model.

It is clear that the behavior changes for $\frac{P}{P_g} = 1$.

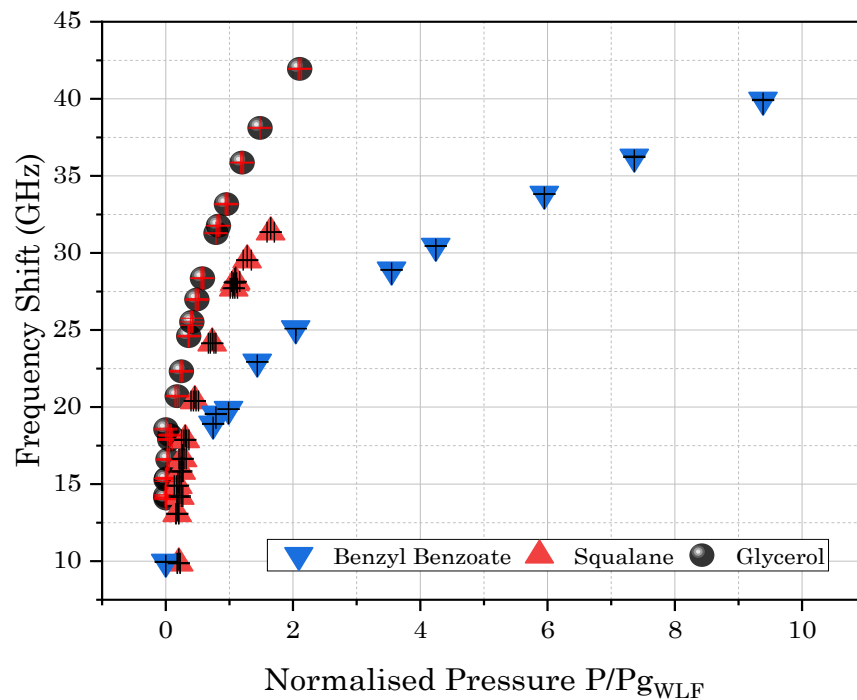


Figure 5.14: Frequency shift of benzyl benzoate, squalane and glycerol vs. pressure normalized by $P_{g,WLF}$, at room temperature. All results were obtained with the high-pressure DAC and the TFP-1 interferometer.

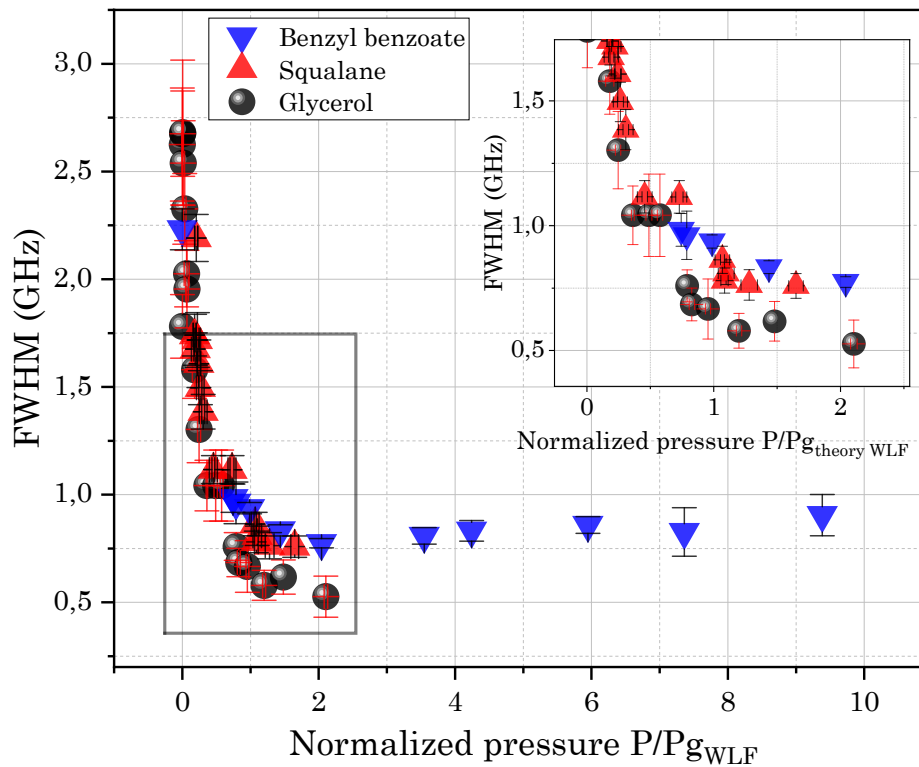


Figure 5.15 : FWHM of benzyl benzoate, squalane and glycerol vs. pressure normalized by the glass transition pressure predicted by the WLF model, at room temperature. All results were obtained with the high-pressure DAC and the TFP-1 interferometer.

When the sample experiences a pressure above the glass transition pressure, this regime is therefore reminiscent of a purely propagative regime, characteristic of solid-like materials [148]. It can be explained by the existence of a very compact sample at high pressure involving high proximity of molecules (see Section 1.3.2), which favors sound wave propagation.

The pressure scaling in of Figures 5.14 and 5.15 highlights that the transition between liquid to glassy state is very similar for the 3 fluids.

The first regime is diffusive due to the maximum linewidth, the frequency shift of the 3 samples evolves very similarly. Low pressure associated to the first regime could be attributed to a very low elastic modulus of the samples in viscoelastic materials. The second regime, between P_t and P_p , is the transition between viscoelastic and glassy states. Finally, for pressure higher than P_p , the third regime is associated with solid-like materials, the frequency shift depends on the nature of the materials. This is consistent with a solid-like material driven by its elastic property.

This is also in line with the literature, as reported in Chapter 1, even if the glass transition determination seems to be challenging when the change of slope is not sharp or occurs over a non-negligible range of pressure.

Another classical parameter derived from the ratio between the linewidth and the frequency shift is the loss tangent which is called the damping factor $\tan(\delta)$ in the literature.

Damping factor:

A simple parameter can be derived from the spectra measurements called by different names: the quality factor, the damping factor or the $\tan(\delta)$. It is defined as the ratio of the FWHM (sound damping) by the frequency shift (sound propagation), which is the same as for the ratio of the viscous to the elastic response of a viscoelastic material [15,34,213]. The ratio taken from Brillouin measurements is not dependant on the density. From this definition, it represents the energy dissipation potential of the material.

The damping factor is plotted versus pressure in Figure 5.16 for the benzyl benzoate samples tested in Brillouin light scattering. Data from the present work are superimposed with the ones recorded by Ndiaye [38,41] at three temperatures: 20°C, 40°C 60°C with TFP-1. To perform these temperature measurements, the ring was connected to a heating system ensuring thermal regulation with a precision of ± 0.1 °C. A thermocouple was used to measure the temperature close to the sample. It can first be noted from Figure 5.16 that the damping factor derived from the spectra are superimposed. It has an L-shape corresponding to the transition between a viscous state at low pressure and a glassy state at high pressure but the maximum peak shape is not reached.

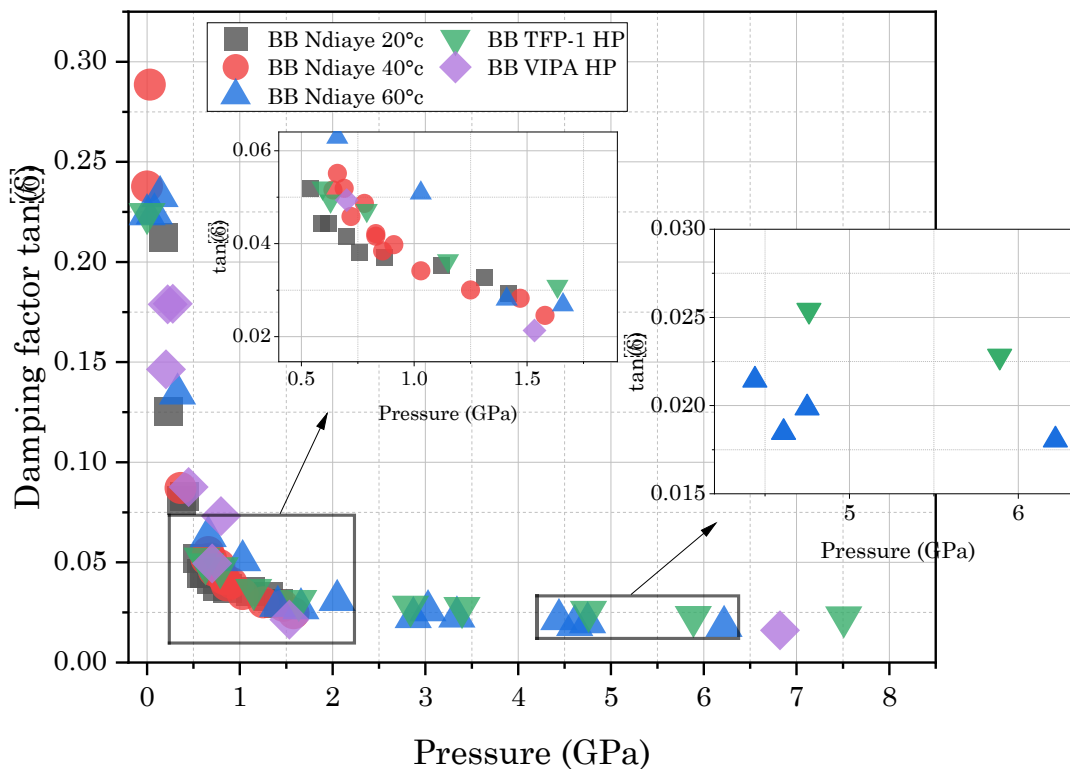


Figure 5.16 : Damping factor $\tan \delta = FWHM/FS$ of of benzyl benzoate at three temperatures, 20°C, 40°C and 60°C versus pressure from reference [38], with results obtained from the low and high-pressure DAC. Brillouin measurements were taken from TFP-1 interferometer and VIPA spectrometers.

The quality factor is sharper than the FWHM presented in Figure 5.15, which highlights the glass transition and the glassy state. The very low value of the quality factor at high pressures means that the sample is driven by elasticity (through the Brillouin peak frequency shift) and that viscous dissipation (through the Brillouin FWHM) is negligible.

The three transition pressures P_g , one for each temperature, are derived as the intersection of the two limiting regimes. Values of the order of 0.6 GPa, 0.7 GPa and 0.8 GPa are respectively found for 20°C, 40°C and 60°C. On the other side, plateau pressures P_p are estimated from the (measurable) beginning of the quality factor plateau. They are of 0.80 GPa at 20°C, in the range of [1 – 1.2] GPa at 40°C, and in the range of [1.2 – 1.4] GPa at 60°C. Moreover, the pressure of the transition increases with the temperature. Values predicted by the WLF-Yasutomi model of Equation 3.2 have been used. They are of 0.8 GPa, 1 GPa and 1.2 GPa at respectively 20°C, 40°C and 60°C. Again, the values derived are very close to the glass transition pressures P_g predicted by the WLF-Yasutomi model. Figure 5.16 does not show a significant difference between the damping factors at different temperature. Perhaps, the temperature variation was not large enough to show the complete transition between liquid to solid-like states.

A phase diagram is shown in Figure 5.17 to compare rheological and BLS characteristic pressures. The glass transition pressure versus temperature $P_g(T)$ plotted is derived from the WLF-Yasutomi rheological model (equation 3.2). The three values of both P_t and P_p at 20°C, 40°C and 60°C from BLS measurements are superposed. Error bars are estimated from the graphical determination of each value.

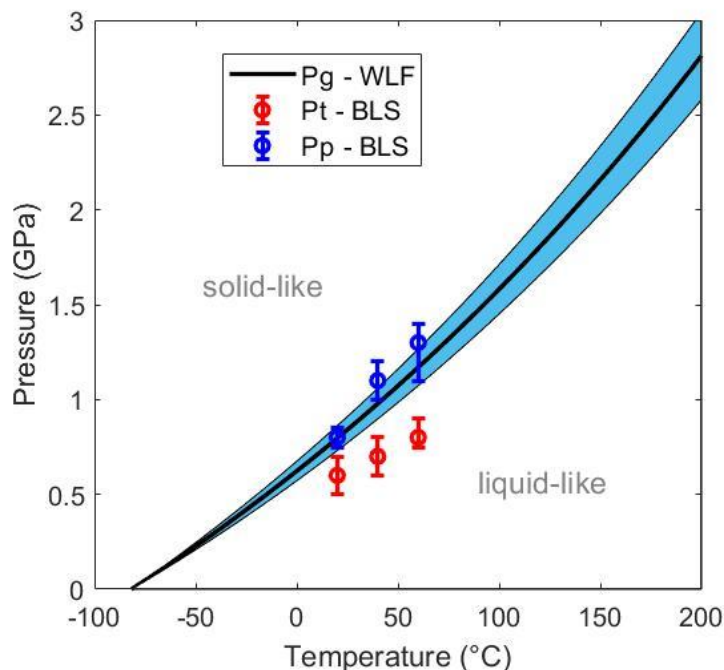


Figure 5.17 : Phase diagram of the benzyl benzoate from the modified WLF-Yasutomi rheological law $P_g(T)$ and the experimental characteristic pressures P_t and P_p derived from BLS measurements. The 8.24% uncertainty of the $P_g(T)$ law [94] is represented by the blue area around the black line.

It comes that temperature and pressure enable to define the macroscopic behavior of a fluid, between a « liquid-like » behavior and a « solid-like » one for which molecular motion significantly slows down. Increasing the temperature leads to an increase in the thermal energy of molecules thus their velocity. To freeze any motion, it is therefore necessary to reach higher pressures. Conversely, the pressure is linked to the molecular jamming. Increasing pressure tends to reduce the free volume in the volume of fluid, and therefore to decrease the degrees of freedom of the molecules. A higher pressure is thus sufficient to freeze any motion. This was already noticed in the literature, in particular by Alsaad and coworkers [31] as shown in Figures 1.16 and 1.17.

It can also be recalled that glass transition is known to take place over a wide range of pressures. From Figure 5.8, the P_g predicted by the modified WLF Yasutomi model closely matches the plateau pressure P_p estimated from BLS measurements. As P_p marks the beginning of the “solid-like” regime, it seems that P_g corresponds to the pressure from which the glassy behavior of the fluid is established.

This study performed a supplementary dataset of benzyl benzoate using the TFP-1 and the VIPA spectrometers as shown in Figure 5.18. The damping factor is expressed as a function of the normalized pressure.

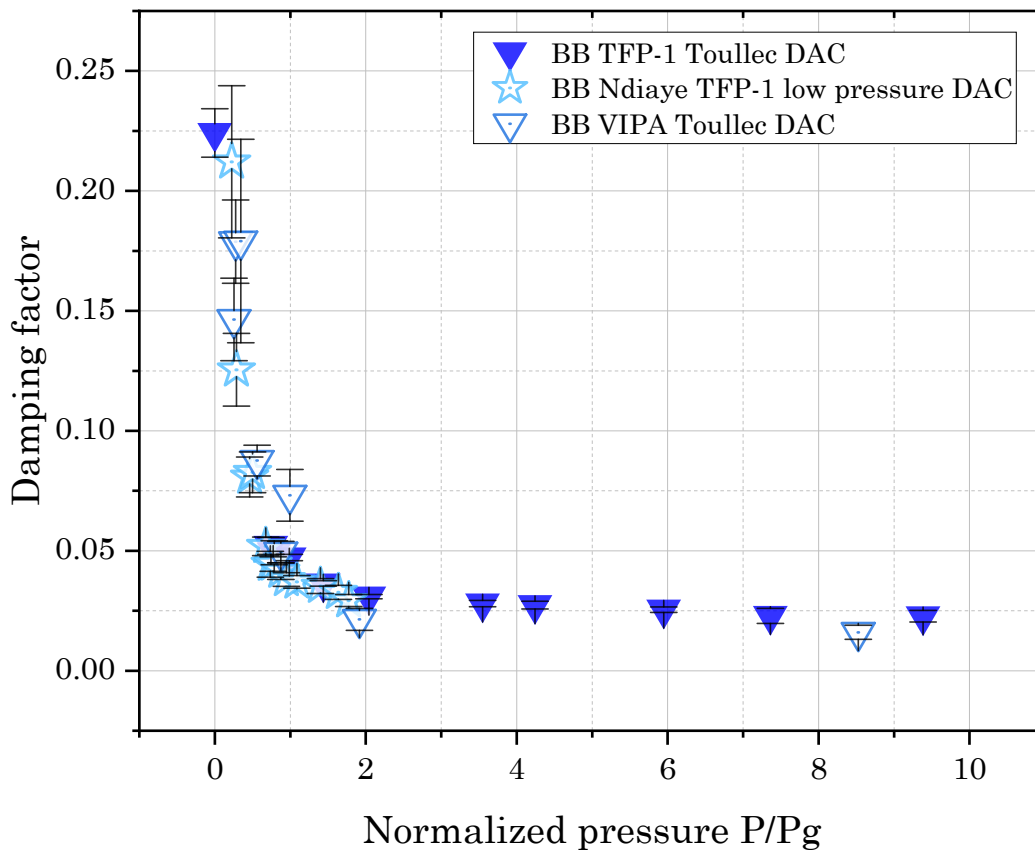


Figure 5.18 : Damping factor $\tan \delta = FWHM/FS$ of benzyl benzoate versus pressure, with results obtained from the low (open blue stars) and high-pressure DAC (full and open blue upside-down triangles). Brillouin measurements were taken from TFP-1 interferometer and VIPA spectrometers.

Figure 5.18 shows a superposition of all experimental data.

The same analysis is done on squalane and glycerol in Figure 5.19. It is clear from this Figure that the three liquid curves of the damping factor evolve similarly, with a L-shape, in function of pressure even if the of the three samples behave differently.

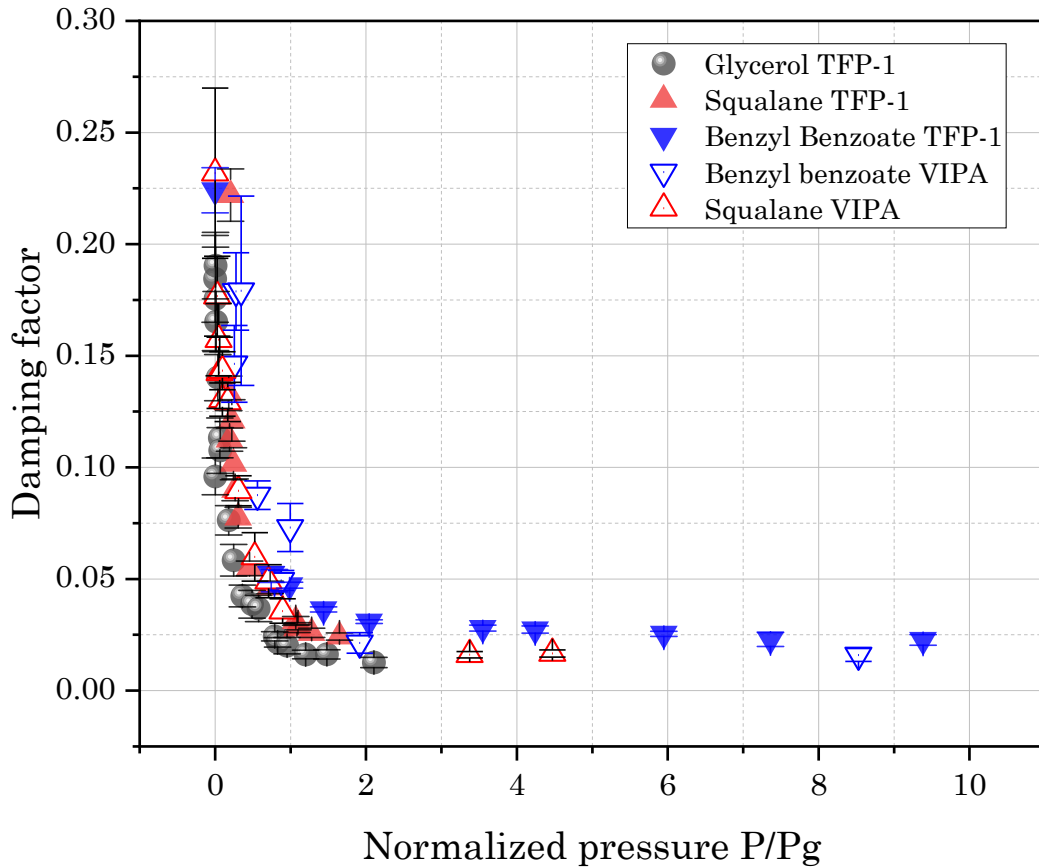


Figure 5.19 : Damping (quality factor) $\tan \delta = FWHM/FS$ of three fluids, benzyl benzoate squalane and glycerol, in the function of the Normalized pressure. Both setups are represented, TFP-1 (full symbols) and VIPA (open symbols).

From Figure 5.19, the characteristic pressures are derived for the three fluids probed and are summarized in Table 5.2 together with the glass transition pressure P_g extrapolated from the rheological WLF-Yasutomi model described in section 3.1.

	P_g (GPa)	P_t (GPa)	P_p (GPa)
BB	0.8	0.6	0.8
SQ	1.45	0.5	1.75
GLY	4.15 [90]	1	3.48

Table 5.2: Synthesis of the characteristic pressures at 20°C for the three fluids: P_g derived from the WLF-Yasutomi model (cf section 3.1), P_t and P_p derived from the damping factor of Figure 5.16.

To make a summary of this section, the glass transition pressure extraction method, by computing linear fit on the edge and extrapolating to make those lines cross. In Figures 5.4 to 5.7, the linear fits represented as dashed or solid lines, are computed on. On one hand, the glass transition pressure for benzyl benzoate is identified close to the predicted P_g value by the modified WLF model. On the other hand, squalane and glycerol show large transition regions between the viscoelastic state and the solid-like state. Two other characteristic pressures P_t and P_p from the BLS linewidth to identify the regions: the liquid, transition and solid like regions. For these 2 fluids, P_p seems closer to the glass transition pressure predicted by the modified WLF model. By comparing the glass transition pressure to the literature, there is a disagreement about the glycerol glass transition pressures. This is due to the variety of methods available to measure the glass transition and variation in the experimental protocol. Another method found for the detection of the glass transition is the study of the inhomogeneity of the pressure across the DAC after passing the glass transition pressure.

Moreover, by studying the evolution of Brillouin parameters in function of the glass pressure, the scaling highlights that the transition between viscoelastic to glass state is very similar for the 3 fluids. The damping factor derived from the spectra parameters is superimposed for all results at all temperatures studied. The very low value of the quality factor at high pressures means that the sample is driven by elasticity (through the Brillouin peak frequency shift) and that viscous dissipation (through the Brillouin FWHM) is negligible. A further parameter study has to be explored in the following section.

5.3. Evaluation of mechanical parameters

The mechanical parameters of the sample, the speed of sound V and the D of the sample, (equation 2.42), or the real parts M' and imaginary part M'' of the longitudinal modulus, from equations 2.33, 2.40 and 2.41, can be calculated. Their calculation requires the knowledge of the fluid density and refractive index in function of temperature and pressure, provided for each fluid in section 3.1.

The wave vector q is calculated from Equation 2.14 which the refractive index n , the laser wavelength in vacuum λ_0 , and the incident angle θ_i (with $\theta_i = \pi$ in backscattering geometry). The refractive index has to be calculated in a function of pressure. The extraction of its value comes from equation 2.35. Then the pressure-dependent refractive index is calculated using equation 5.1:

$$n(P) = \sqrt{\frac{2X+1}{1-X}} \text{ with } X = \left(\frac{4\pi}{3}\right) * \left(\frac{\rho(P)}{M_w}\right) N_a \alpha \quad (5.1)$$

The sound velocity in equation 2.19 the frequency shift f_b and the wave vector q . Finally, the longitudinal kinematic viscosity is the Brillouin linewidth Γ_b divided by the wave vector q squared (equation 2.42).

	Benzyl benzoate	Squalane	Glycerol
$q (P_{\text{atm}}, T_{\text{atm}}) [m^{-1}]$	$5.900 \cdot 10^6$	$5.459 \cdot 10^6$	$5.548 \cdot 10^6$
$f_b [GHz] (P_{\text{atm}}, T_{\text{atm}})$ from chap 4	10,05653	8,95998	15,9624
$\Gamma_b [GHz] (P_{\text{atm}}, T_{\text{atm}})$ from chap 4	2.28716	1.31362	2.01515
$V (P_{\text{atm}}, T_{\text{atm}}) [m \cdot s^{-1}]$	1704.32	1641.32	2877.08
$D (P_{\text{atm}}, T_{\text{atm}}) [cm^2 \cdot s^{-1}]$	0.6570	0.4408	0.6547

Table 5.3 : f_b , q , V , and D parameters using the frequency shift, the FWHM, and refractive index from Table 3.3. All parameters are calculated at atmospheric pressure and temperature.

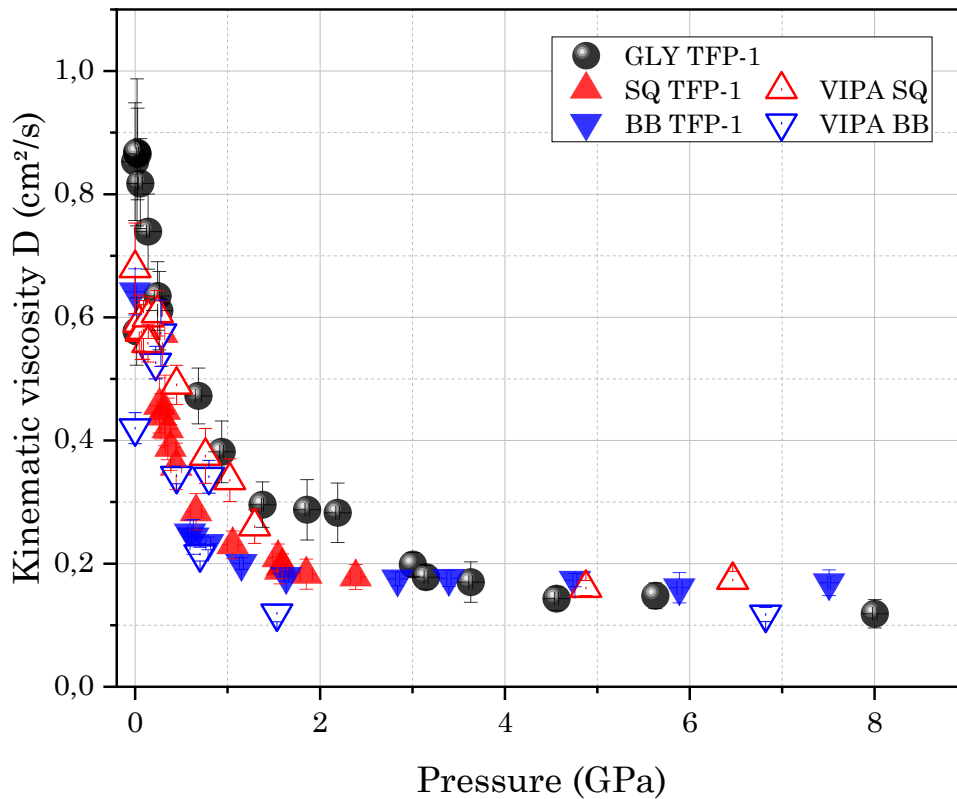


Figure 5.20: Longitudinal kinematic viscosity of benzyl benzoate, squalane, and glycerol in function of pressure in the Toullec DAC, at 22°C.

Figure 5.20 represents the longitudinal kinematic viscosity of all fluids, showing an L-shape decreasing to values below $0.2 \text{ cm}^2 \cdot \text{s}^{-1}$

The comparison of D measured from BLS and inelastic X-ray scattering (IXS) which typically measures the unrelaxed values of D on glycerol has shown a good match below the glass transition temperature [8]. This indicated the absence of excess damping in Brillouin light scattering data over the IXS unrelaxed ones at the transition. It led to the assumption that

only the α relaxation was significant in this case. This was noted as a peculiar behavior of glycerol, not to generalize to other molecular liquids

Yet positioning the transition does not agree with an important note of [8] which indicates that the structural relaxation process is accompanied by a maximum of the absorption (or attenuation) D , as shown in Figure 1.11(right) and also a maximum in the damping factor $\tan \delta = \text{FWHM}/\text{FS}$. In this study, it was expected to find this maximum of D or damping. Instead, Figures 5.16, 5.18, 5.19 and 5.20 show a behavior already on the glass transition.

The sound propagation velocity is computed from the frequency shifts for all fluids in Figure 5.2. The evolution of the sound velocity follows that of the frequency shift (see Figure 5.2). It is the same for the kinematic viscosity D and the linewidth (cf Figure 5.3).

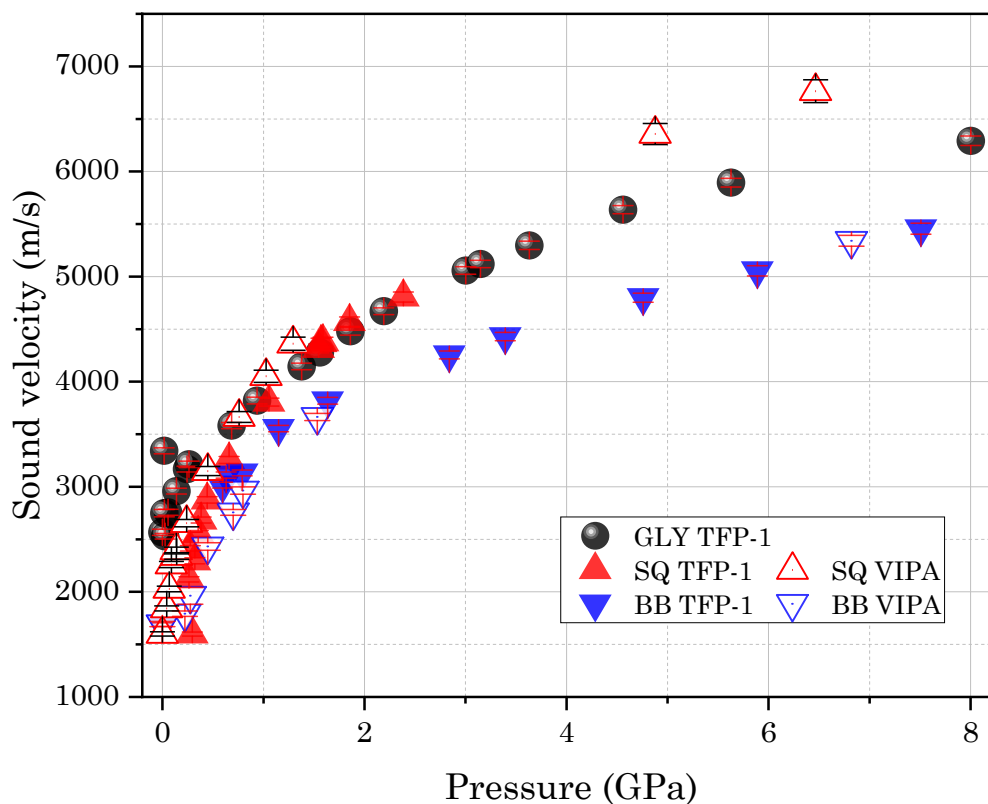


Figure 5.21 : Sound propagation velocity V of benzyl benzoate, squalane and glycerol in function of pressure in the Toullec DAC, at 22°C.

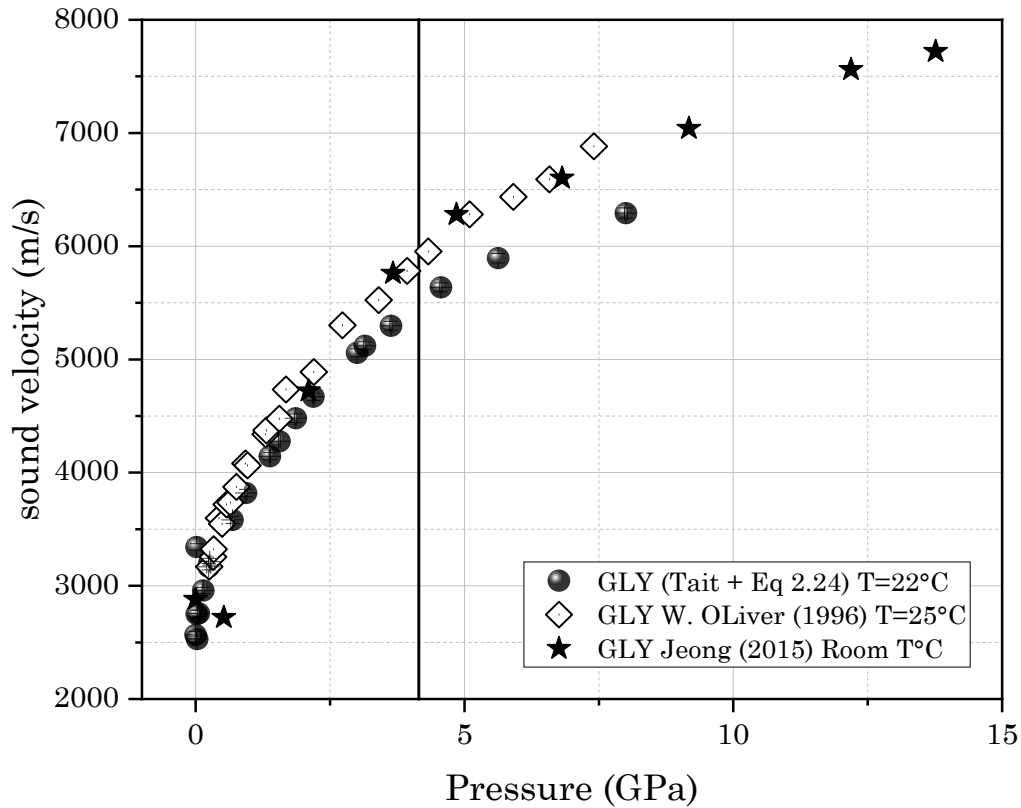


Figure 5.22 : Sound velocity extracted from Oliver (open diamond) [205], Jeong (stars) [19] and from this study calculated with the frequency shift, density extrapolated from the Tait model, and the Clausius-Mossotti equation. The vertical line represents the glass pressure transition.

Figure 5.22 focuses on glycerol studied by several authors. In this figure, our data are compared to data from the literature. The sound velocity is calculated from our spectra using density from the Tait model, which is defined from 0 to 800 MPa and extrapolated on the range of pressure used. The Jeong and Oliver studies used the platelet geometry in combination with the backscattering geometry to extract the density. Their density methods take into account the transition which could explain the difference. The density extrapolated from the Tait model seems to diverge from the sound velocity extracted from Brillouin measurements after the glass transition pressure. It seems to under estimate the density when the fluid is in the glassy state.

The value of viscosity measured in a rheometer can be compared to the longitudinal viscosity η_L . Care must be taken in the meaning of this viscosity, which must be distinguished from the shear viscosity of fluids. η_L conditions the damping of the longitudinal waves, *i.e.* the diffusion of the waves. Therefore, as shown in Figure 5.23, it decreases with pressure since the increase in pressure brings molecules in the sample closer to each other and favors the propagation of the acoustic waves. Moreover, at atmospheric pressure, one order of magnitude of the longitudinal viscosity η_L and the zero-shear viscosity conventionally measured with a were observed. Indeed, the shear viscosities of benzyl benzoate and squalane from the WLF models presented in chapter 3 (section 3.1) are respectively 10.1 mPa.s and 33.4 mPa.s (See Appendix E.2 Figure E.6 at 10). This may be attributed to the frequency of observation, and

in addition, to the difficulty of Brillouin spectroscopy in relating to other measurement techniques in a quantitative manner.

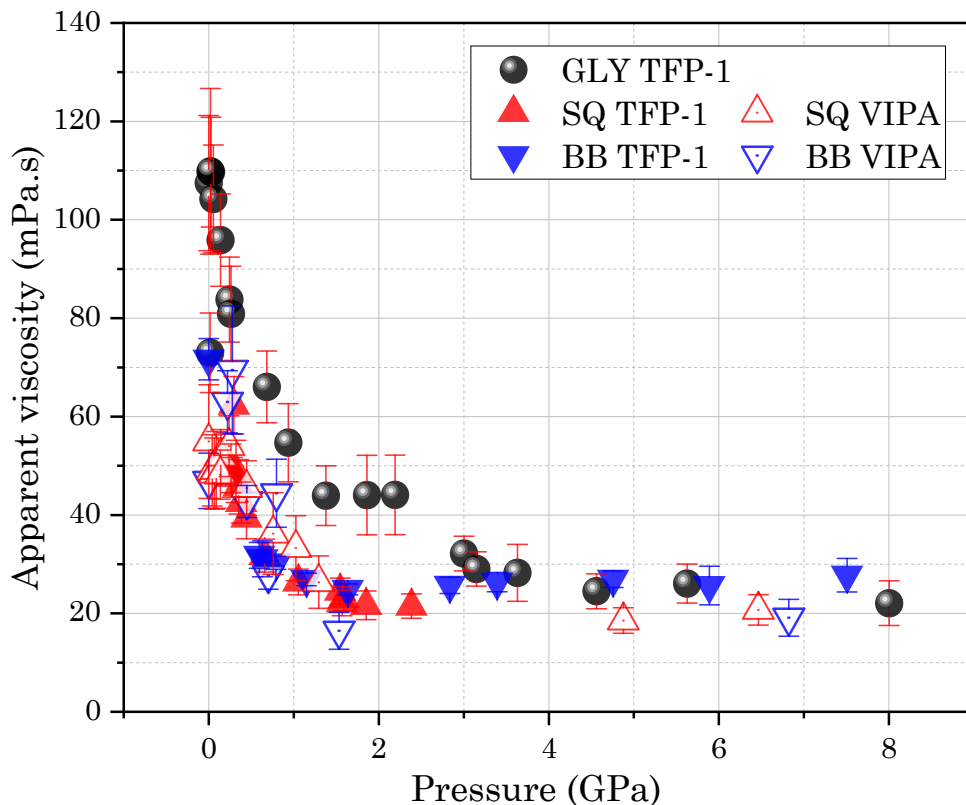


Figure 5.23: Longitudinal viscosity of benzyl benzoate and squalane in function pressure. Data are from the TFP-1 at 22°C.

To get more insight into mechanical parameters, the real and imaginary part of the longitudinal modulus can be plotted versus pressure, as it was already done versus temperature in [18,34,213]. The evolution of M' and M'' are presented in Figures 5.24, 5.25 and 5.26 for the 3 fluids from equation 2.40 and 2.41. This should provide a quantitative estimation for both contribution in liquid-like and solid-like states. It must however be noted that, as stated in sections 2.3.2 to 2.4.4, close to the glass transition, relaxation processes are strongly coupled with the acoustic waves

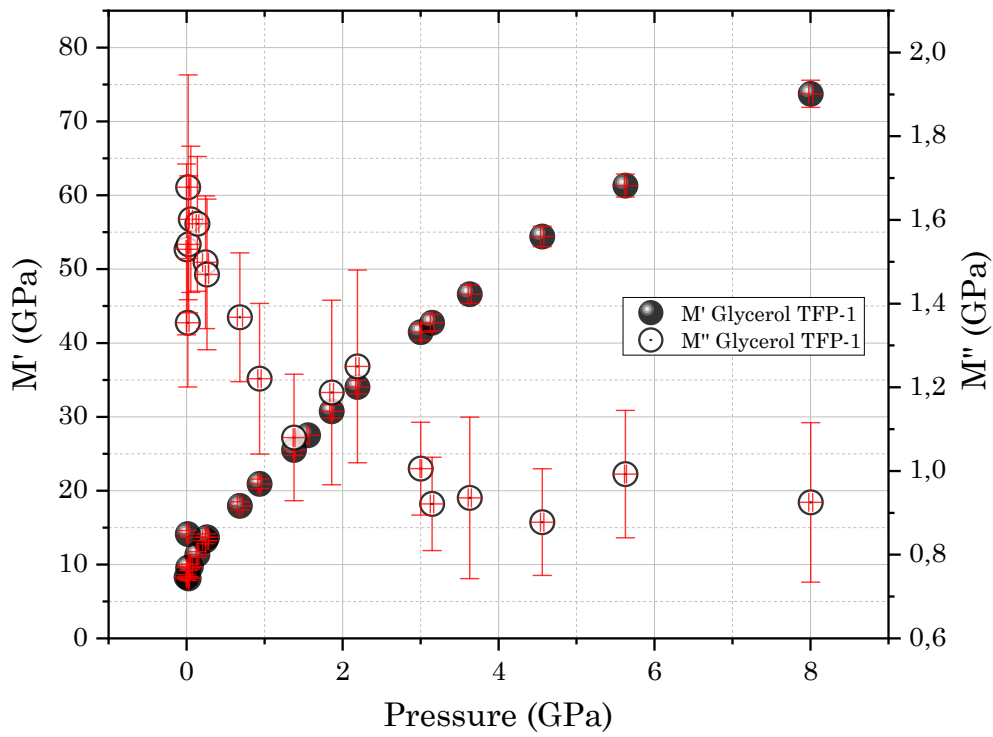


Figure 5.24: Storage (left) and loss (right) longitudinal modulus of glycerol using the DHO model of in function of pressure, in the Toullec DAC, at 22°C.

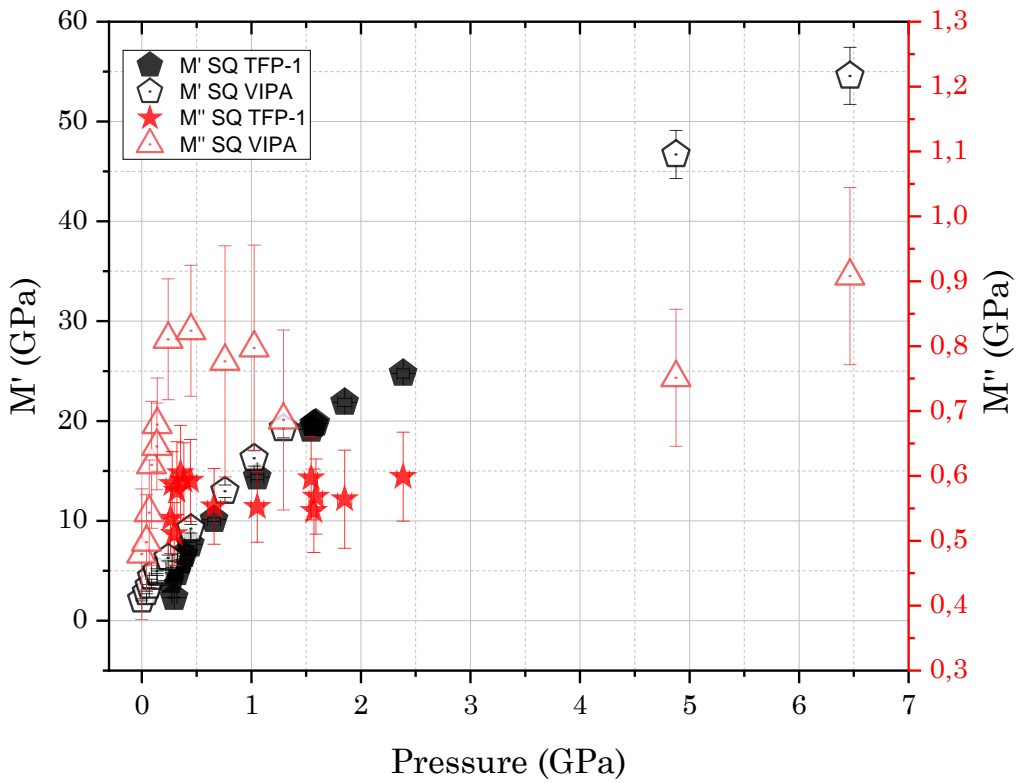


Figure 5.25 : Storage (left) and loss (right) longitudinal modulus using the DHO model on squalane under pressure in the Toullec DAC, at 22°C.

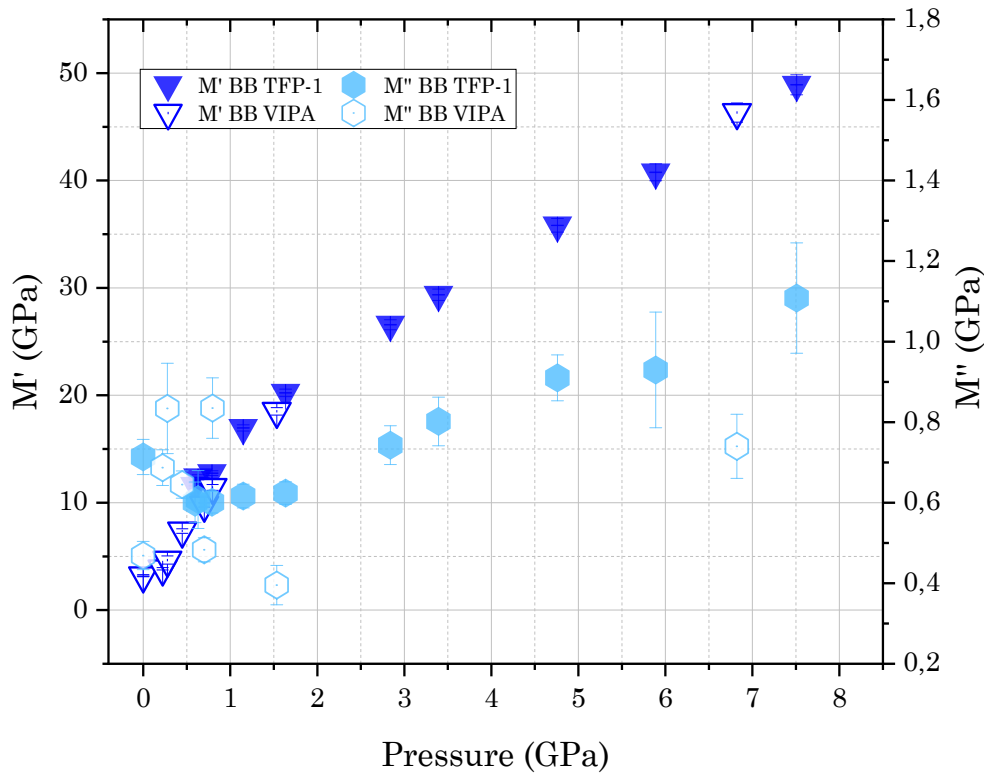


Figure 5.26 : Storage (left) and loss (right) longitudinal modulus using the DHO model on benzyl benzoate under pressure in the Toullec DAC, at 22°C.

In Figures 5.24, 5.25, and 5.26 the storage modulus of glycerol, squalane, and benzyl benzoate shows a similar behavior, increasing gradually in function of pressure, following the frequency shift. Nevertheless, the loss modulus has a completely different behavior. Indeed, squalane reports at low pressure a peak below 1 GPa and then increases to high values. The same can be noted for benzyl benzoate at low pressure showing a beginning of peak below 1 GPa and a similar increase of the loss modulus at high-pressure. Finally, glycerol has the same behavior of the loss modulus as the linewidth.

As seen in Figure 2.13 in section 2.3.2, the peak could represents an α relaxation but further exploration has to be done to fully conclude. The increasing loss modulus for squalane and benzyl benzoate is very similar to the scenario proposed in Figure 2.13, is identified as “solid-like” behavior. Nevertheless, the storage modulus does not show an asymptotic behavior.

According to Comez and coworkers [8], at temperatures higher than T_g (so a liquid sample), the strong dependence of the FWHM with temperature is indicative of a regime dominated by the structural relaxation (α) process. On the other side, they report in [213] (also reported by [8]) that if the modulus M'' is greater than 0 in the glassy regime, the residual absorption can be attributed to a secondary relaxation process. It is associated with a more localized motion of the molecules than the structural relaxation process, which remains activated even in the glassy state. As mentioned in 1.3.2, it is associated to intermolecular motion which can have different origins.

If the asymptotic low value of the linewidth is constant, the secondary processes can be considered negligible. For instance, for the case of glycerol, no dependence on temperature

was noted on the linewidth for temperatures lower than T_g [8]. This meant that no evidence of intramolecular relaxations was observed, and it led to the conclusion of an α relaxation-only scenario for the dynamics of glycerol.

Our results presented in Figure 5.24 exhibit for the glycerol a low level of M'' , which does not depend on pressure, for pressure higher than P_g . Like the study of glycerol versus temperature reported by Comez and coworkers [8], we can assume that there is no excess absorption of acoustic waves in this regime, meaning that the influence of β relaxation is insignificant on the density fluctuations. However, it is more surprising for benzyl benzoate with phenyl rings, compared to the o-terphenyl which exhibits significant β relaxation processes [8].

Anyway, in a contact, the β relaxation processes are probably not predominant in fluids experiencing shear rates between 10^4 s^{-1} et 10^7 s^{-1} . As stated by Comez and coworkers [13] for the glycerol, the structural relaxation is the leading contribution to the relaxational dynamics in the GHz frequency window.

To summarize complex modulus calculation, see in Appendix D.3 Figures D.4 and D.5 all modulus calculations put together.

Several remarques on calculation have to be addressed. The calculation of q was simplified within the calculation of the sound propagation velocity. Indeed, the laser wavelength was taken as a static value. Concerning the VIPA setup, It was impossible to use a pinhole to define a single q vector and to use a low numerical aperture, which broadens the spectra, as suggested in [202,204]. All parameters using the density or the refractive index in function of pressure and temperature (M_0' , M_0'' , V) are computed are extrapolated through a transition. This element could explain the lower density found for the glycerol sample when the sound propagation velocity is calculated.

5.4 Correlation with friction measurements

A correlation between the macroscopic behavior of the fluid due to pressure and temperature conditions and the friction regime had already been established in [41] for benzyl benzoate, (see Figure 1.18). The present work intends to show whether such a correlation is also found for a lubricating fluid, such as squalane. For this, the same approach as that described in [10] for the benzyl benzoate is applied to the squalane. Friction tests are performed with the tribometer Jerotrib described in chapter 3.5. The test conditions with the squalane are given in Table 5.4.

Tested temp.	20°C			40°C			60°C
Specimen materials	steel-steel	steel - sapphire	WC-WC	steel-steel	steel - sapphire	WC-WC	steel - sapphire
P_H (GPa)	0.9 - 1.6	1.21 - 2	1.35 - 2.58	0.8 - 1.59	1.2 - 1.99	1.37 - 2.28	1.2 - 1.6
\bar{P} (GPa)	0.6 - 1.06	0.8 - 1.33	0.9 - 1.7	0.53 - 1.06	0.8 - 1.33	0.91 - 1.52	0.8 - 1.07
U_e ($m.s^{-1}$)	0.3			0.8			1.7
h_c (nm)	96-108.6	92 - 102.7	88 - 101.3	99.1 - 115.1	95 - 106.1	94.4 - 104.4	100.5 - 107
SRR	-50% - 0 -+ 50%						

Table 5.4 : Operating conditions for friction measurements with squalane WC stands for tungsten carbide.

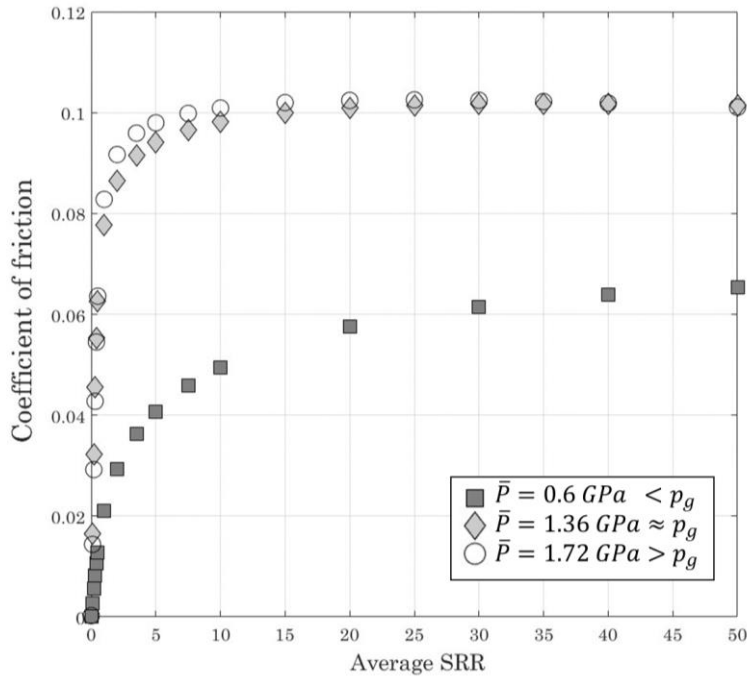


Figure 5.27 : Friction measurements on squalane performed at $T = 20^\circ\text{C}$ and $U_e = 0.3 \text{ m.s}^{-1}$, for Hertzian contact pressures from 0.9 to 2.58 GPa the error is about 1,1%. $P_{gWLF}(T = 20^\circ\text{C}) = 1.44 \text{ GPa}$.

Figure 5.27 represents three friction curves corresponding to 3 mean pressures matching three conditions $\bar{P} < P_g$, $\bar{P} \sim P_g$, and $\bar{P} > P_g$. The friction curves of Figure 5.27 exhibit the friction regimes already widely described in the literature (see Figure 1.5).

Looking more closely at the friction curves of squalane in Figure 5.27, it appears that the onset of the friction plateau depends on the pressure average in the contact on the maximum SRR of the test. It is noticed that at high SRRs thermal effects dominate friction by inducing a decrease in the coefficient of friction. This makes a pure friction plateau very difficult to reach experimentally. Indeed, some friction curves of squalane exhibit a decline after a brief friction maximum and do not reach a plateau.

In Figure 5.28, the parameter of apparent viscosity at low shear rates is derived from friction measurements. It is defined as the ratio between the mean contact shear stress τ_m in the first linear friction regime (thus at very low SRR) and the shear rate at the center of the contact $\dot{\gamma}_c$. For that, the coefficient of friction is converted into shear stress by assuming that $C_f = F_x/F_z = \bar{\tau}/\bar{P}$. The shear rate at the center of the contact is defined as the ratio between the sliding velocity between the two solid surfaces and the film thickness at the center h_c . It is estimated from the Chittenden prediction model [201] and is valid for isothermal conditions and a Newtonian fluid. This viscosity, more than being representative of a physical quantity, is used as a parameter qualitatively representative of the macroscopic behavior of the lubricant when it is weakly impacted by shear. It is plotted in Figure 5.28 for the squalane, scaled by the value of the apparent viscosity in the plateau regime, as a function of the normalized pressures \bar{P}/P_g .

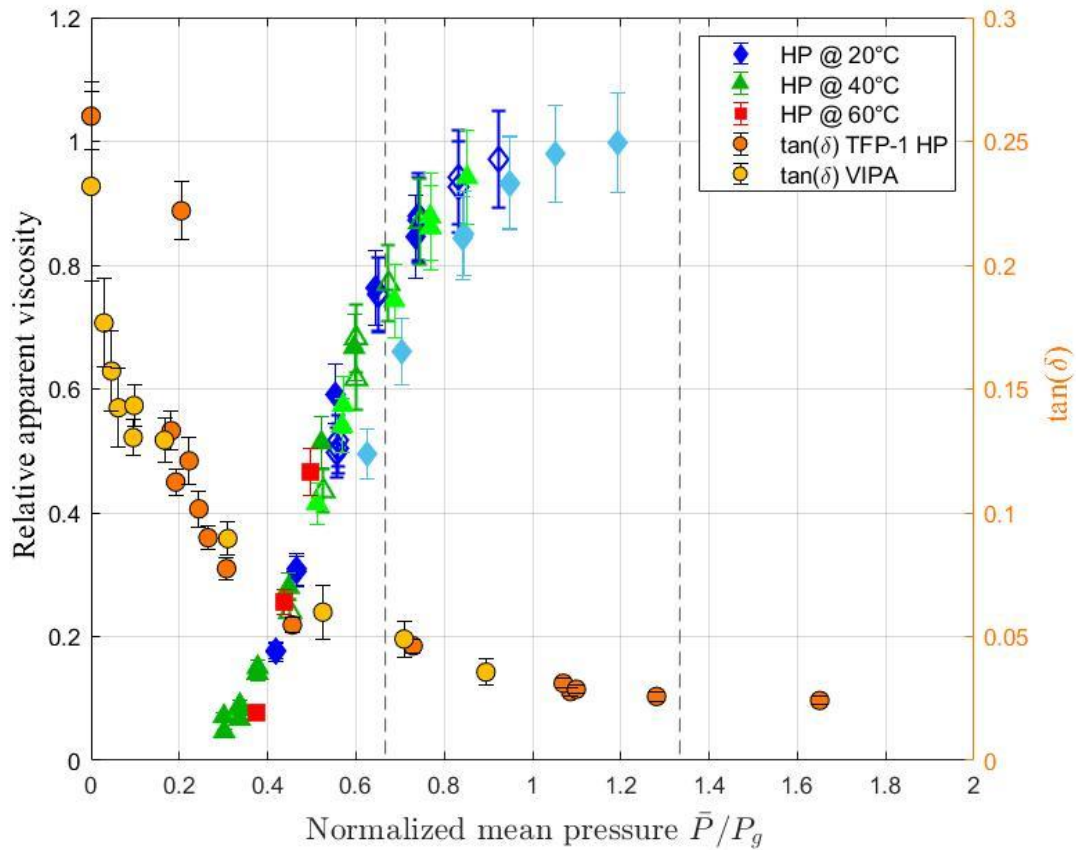


Figure 5.28 : Relative apparent viscosity (left axis) and the damping factor (right axis) of the squalane at 3 temperature in function of the normalized mean pressure of the contact ($\bar{P} = 2/3 P_H$) by the glass transition pressure $P_g(T)$. The relative apparent viscosities are deriving from friction measurements at low shear rates. plain symbols with dark colors stand for steel–steel surfaces, open symbols stand for steel–sapphire surfaces, and plain symbols with light colors stand for WC–WC surfaces. The damping factor is derived from Brillouin spectra. The vertical dashed line corresponds to $P_H = P_g$ and $P_H = 2 * P_g$.

The squalane seems to follow the same behavior as that already describe in [41] for the benzyl benzoate. However, it should be noted that only the very beginning of the apparent viscosity plateau is reached in Figure 5.28. This can be explained because the glass transition pressures measured for squalane are higher than for benzyl benzoate, at the same temperatures. Unfortunately, the highest pressures that can be applied in our tribometer do not allow to measure friction for $\bar{P} \gg P_g$ for the squalane. Moreover, this is in line with the conclusions given by [94] who noticed a similar friction behavior of benzyl benzoate and squalane, which was driven by their thermodynamic state in the contact, despite their very different nature.

To directly compare the behavior of the two fluids, friction results are superimposed on Figure 5.29.

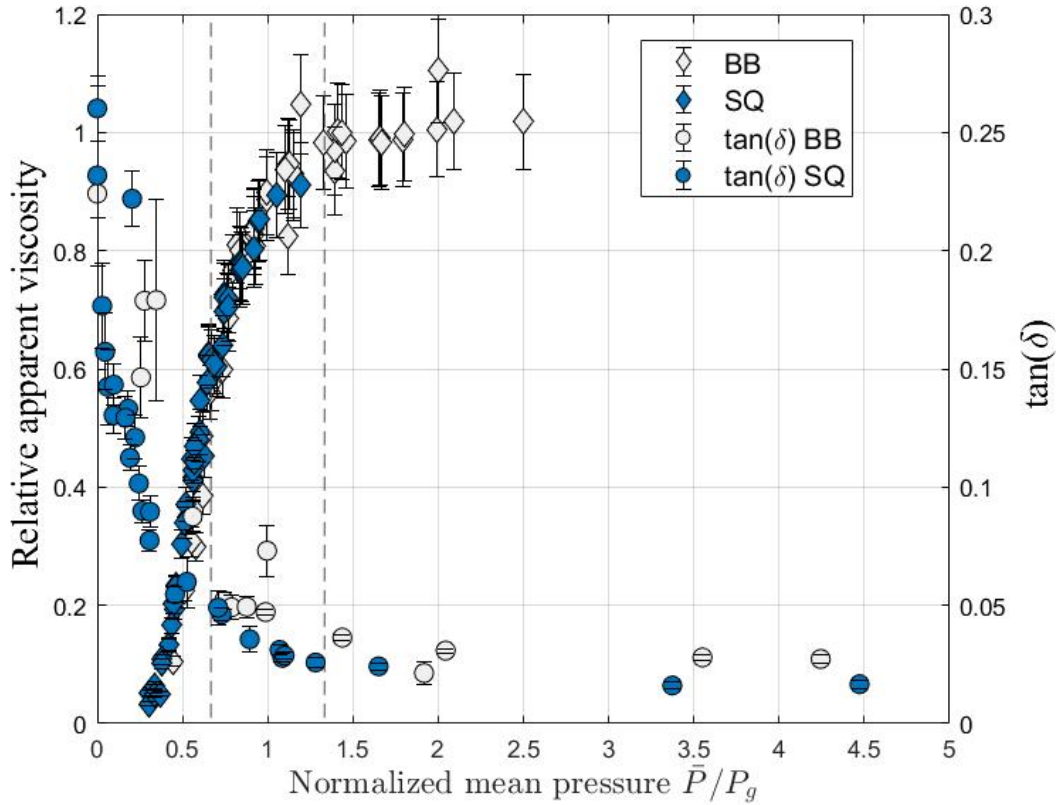


Figure 5.29 : Relative mean viscosity derived from friction measurements at low shear rates (left axis) and dissipation factor from BLS spectra (right axis) in function of the normalized pressure $\bar{P}/P_{g,WLF}$ for benzyl benzoate and squalane. Data come from various temperatures (20°C, 40°C and 60°C) and various solid materials (steel-steel, steel-sapphire and WC-WC). The vertical dashed line corresponds to $P_H = P_g$ and $P_H = 2 * P_g$.

This figure illustrates that there is a transition behavior in the normalized apparent viscosity relative to the mean of the lubricating fluid concerning the mean contact pressure, for the two fluids studied: a lubricant and a model fluid.

It was shown in Appendix E.2 that the shear rate, at low range probed ($\dot{\gamma} < 10^4 s^{-1}$), led to reduced linewidth of the Brillouin spectra. This means that the contribution of the lubricant response is also reduced. This suggests the contribution of the shear rate tends to accelerate the drop of the damping factor measured in Figure 5.19 at rest. This could result to a slight shift toward lower pressures of the damping factor $\tan(\delta)$.

5.6. Results conclusion

The chapter investigates the influence of two parameters (pressure, temperature) on the behavior of lubricants. The aim is to decouple these parameters and to understand their individual effects on the lubricant's properties. Three fluids were chosen: one traction-like fluid the benzyl benzoate, one lubricants squalane and glycerol serving as a reference fluid for Brillouin spectroscopy.

The first set of experiments focuses on Brillouin Light Scattering (BLS) measurements by investigating the pressure and temperature dependencies. Properties of the lubricants are extracted. For instance, in section 1.4.1, the glass transition, defined as the change of slope in Brillouin spectra with temperature or pressure, was identified for all fluids based on the Full Width at Half Maximum (FWHM) and the frequency shift (FS) values. For that, the pressure dependency of three fluids was studied using Toullec diamond anvil cells. The high-pressure data obtained in this study were compared to the low-pressure data extracted from previous studies conducted in 2017 by Ndiaye [38], and an updated fitting methodology using the triple Lorentz fit was applied. Additionally, the setup equipped with the VIPA spectrometer presented in Chapter 3 was used to perform another set of high-pressure measurements, and these data were included in the analysis. These datasets were found to be consistent in the behavior with those obtained using TFP-1 but some differences have to be highlighted. The initial pressure values for the frequency shift seems shifted between all set-ups in function of the pressure that could be explained by the pressure calculation method that differs from the Ndiaye study. Moreover, a substantial gap on the glycerol FWHM at high-pressure for the glycerol sample could come from the interferometer used, the deconvolution method, a lack of similarity for the pressurization of the sample.

The comparison of the three fluids behavior under pressure revealed similar trends in terms of linewidth and frequency shift, even when the lubricant type was different. The linewidth exhibited a more distinct change of slope compared to the frequency shift. For benzyl benzoate, the glass transition pressure $P_{g:FWHM}$ at 20°C was found to be around 0.8 GPa, which matches with the predictions of the Williams-Landel-Ferry (WLF) model. The glass transition pressure extraction method was then applied to squalane and glycerol for which the transition laid over a wide range of pressures. The glass transition pressure extracted from Brillouin measurements for squalane covers the following range: $P_{g:FWHM} \approx [0.7 - 1.17]$ GPa, and $P_{g:FWHM} \approx [1.5 - 2.32]$ GPa for glycerol. These values appear to deviate from the predictions of the glass transition pressure values from the modified WLF model at 20°C, which predicted glass transition pressures $P_{gSQ-WLF} = 1.446$ GPa, and $P_{gGLY-WLF} = 3.8$ GPa. In the low-pressure regime, the spectra showed a strong dependence on pressure, with an increase in frequency shift and a significant decrease in linewidth as the pressure increased. In the high-pressure regime, the dependence of spectra on pressure became weaker. To clarify these transition regimes, two parameters, namely P_t and P_p , were introduced. The plateau pressures (P_p), estimated from the quality factor plateau at high-pressure for squalane and glycerol, are close to the predicted glass transition pressures (P_g) by the WLF-Yasutomi model.

For the mechanical properties extracted from Brillouin measurements, the estimation of the density of the fluids using the Tait density of states allows for the derivation of the refractive

index (n) using the Lorentz-Lorenz equation. The phonon scattering wavenumber (q) is calculated based on the refractive index, laser wavelength, and incident angle. The sound velocity and longitudinal kinematic viscosity are determined using the frequency shift (ω_b), wave number (q), and Brillouin linewidth (Γ_b). The evolution of sound velocity and kinematic viscosity follows that of the frequency shift and linewidth, respectively.

The evolution of the damping factor, which represents the energy dissipation potential of the sample, is sharper than the full-width half-maximum (FWHM) for the observed spectra. It was calculated for all samples and all temperatures tested. At high pressures, the sample is driven by elasticity, indicated by a very low damping factor, while viscous dissipation becomes negligible. Furthermore, it was shown that the damping factor curves of the three liquid samples evolve similarly, despite their different nature. The pressure of glass transition for these fluids differs, suggesting that if they transition from a liquid to a solid-like state, the damping factor should exhibit a peak value. It is clear that L-shape shows that all samples already progressed toward the glassy state, which suggests that the lubricants are already in the transition range at low pressure.

The storage and loss parts of the longitudinal modulus calculated using the DHO model are plotted against pressure. In the liquid and glassy regimes, the real part (M') of the modulus increases with pressure, while the imaginary part (M'') has a more complex behavior. The squalane sample shows an α relaxation signature at low pressure, but further investigation has to be done to validate. Those results on the squalane sample are compared to the local pressure derived from the spectra of several rubies in Chapter 4 which revealed that above the glass transition pressure, the standard deviation of the ruby pressure starts to increase significantly and show a non-hydrostatic condition. However, this spatial heterogeneity does not induce special dispersion of the characteristics of the measured Brillouin spectra. This may be due to the little changes happening at high-pressure.

For benzyl benzoate, it appears that the low pressure corresponds to the conclusion of the glass transition and subsequently transitions to a glassy state quite rapidly. The glycerol shows a plateau regime on the loss modulus at high pressure. The linewidth behavior indicates the dominance of structural relaxation processes in the liquid regime. For the studied fluids, M'' does not depend on pressure above a certain transition pressure (P_t), suggesting the insignificance of β relaxation processes on relaxation density fluctuation. Structural relaxation is considered to be the primary contribution to the relaxational dynamics in the studied frequency window.

Considering the dynamic nature of a contact, where lubricants experience rapid variations in pressure, temperature, confinement, and shear rates, the equilibrium concept of the glass transition needs to be reconsidered. The highly dynamic nature of contact can strongly impact the lubricant's response, particularly under high contact pressure.

Finally, the data measured on the sample at rest submitted to hydrostatic pressure were compared to data derived from friction test in a tribometer. The correlation between the two sets of data already presented in [41] for the benzyl benzoate was extended to the squalane.

6. General conclusion

Table of content

6.1	CONCLUSION	198
6.2	LIMITATION OF THIS WORK	199
6.3	PERSPECTIVES.....	200

6.1 Conclusion

Friction plays a critical role in various industrial applications, ranging from automotive engineering to manufacturing processes. By enhancing the physical mechanisms understanding behind friction in extreme conditions, this research could highly contribute to the maximum potential savings of 8.7 % of the total global energy consumption envisaged by Holmberg and Erdmir [49]. Yet, the complex nature of lubricant behavior under extreme pressures and shear rates, identified as the ElastoHydroDynamic regim, poses significant difficulties in accurately predicting frictional behavior and developing relevant predictive rheological models. Besides, highly loaded contacts, these mechanisms remain poorly understood due to the challenges of imposing extreme experimental conditions.

The present work was conducted as part of a broader project, motivated to improve friction prediction in highly loaded lubricated contacts. The experimental approach utilized Brillouin spectroscopy to locally measure the behavior of the lubricant under conditions similar to those experienced in a contact. Specifically, the concepts of fluid rheology, namely glass transition (static approach), was investigated in relation to the high-pressures and shear rates experienced by lubricants in contact.

The study began by reviewing the existing approaches in the literature for measuring the physical quantities associated with glass transition and relaxation time, focusing primarily on temperature-pressure-related studies. Fundamental concepts of the ElastoHydroDynamic lubrication (or EHD) were presented. One main hypothesis behind the plateau regime, identified as the limiting shear stress (LSS), is explored. The literature highlighted the pivotal role of intrinsic lubricant properties, especially pertaining to the glass transition, as a potential origin of the plateau phenomenon. Subsequently, the glass transition of the lubricant under extreme conditions was explored using Brillouin spectroscopy technique.

Brillouin spectroscopy has been previously employed for the identification of both the glass transition and mechanical characteristics of lubricants. In this work, fundamental understanding of inelastic spectroscopic technique was extensively described followed by a section about spectra analysis in different state of matter and models associated used in the literature.

Subsequently, an important part of the thesis was dedicated to the elaboration and implementation of a modular microscope and of a new interferometer VIPA spectrometer technology designed for Brillouin spectroscopy in the LaMCoS laboratory. The experimental set-up allows the coupling with a rheometer or a tribometer. It was also used with a high-pressure cell. This set-up enabled simultaneous measurement of the thermodynamic state, structural dynamics, and resulting macroscopic friction of the lubricant. The complete set-up allows to obtain relatively reliable and exploitable data in a short period of time. It opens new perspectives for lubricant characterization inside the laboratory.

Extensive validation of the test rig was conducted against experimental data obtained from another Brillouin spectroscopy set-up, the 6 passes tandem Fabry-Pérot interferometer. Two test campaigns were then carried out, one in a high-pressure cell and another in a rheometer. The analysis of these measurements resulted in several advancements over the existing literature.

For high-pressure measurements, glycerol was taken as a reference sample. Its comparison with the literature (Jeong 2015 and Oliver 1996), highlights the mismatch between linewidth values shows the difficulty of producing reproducible data from different set-ups. As seen in the manuscript, the optical set-up, objectives and distortion of the signal influence the final results. The glass transition extracted from this series of experiments also shows a mismatch with the data provided in the literature.

One hypothesis for this mismatch is that high-pressure measurements are not well-documented on the pressure protocol. In fact, the rate of pressure during Brillouin measurements is not explicitly stated in the literature. The pressure rate influence on physical properties during high-pressure experiments is a recent research axis. A second one is the numerical aperture of the lens that broadens the signal.

Finally, the behavior of the benzyl benzoate and squalane in the function of pressure have been compared to friction data measurements from the tribometer. It enables the extension of the correlation between macroscopic state and frictional behavior, previously proposed for a lubricant with distinct properties [41].

The investigation of the influence of shear rate on the local behavior of lubricating fluids through coupled rheometer and Brillouin spectroscopy measurements at atmospheric pressure was introduced in the appendix E. This pre-study shows that the shear rate affects the viscous contribution of the longitudinal modulus, potentially accelerating the macroscopically "solid-like" behavior of the lubricating fluid in the contact.

6.2 Limitation of this work

However, it is important to consider the limitations associated with these results. Several points for criticism and potential improvement were identified, both in the experimental set-up and the analysis of results.

Experimentally, limitations include the inability to directly derive the shear modulus from Brillouin spectroscopy measurements due to the backscattering geometry used and the restricted range of shear rates achievable in a rheometer compared to those experienced in contacts.

Regarding result analysis, considerations include the assumption of a constant polarizability coefficient with pressure.

6.3 Perspectives

To further advance this work, several perspectives are proposed.

In terms of result analysis, further examination of the data obtained from coupled shear and spectroscopy experiments is necessary. Indeed, it is required to establish correlations between shear and longitudinal viscosities (from simple shear tests) and between shear and longitudinal moduli (from oscillation tests). Additionally, the analysis of complete spectra using the fitting procedure described in Chapter 5 should be reevaluated by varying the stretching parameter β to achieve a more accurate description of the structural relaxation process.

From an experimental standpoint, several campaigns are suggested. First, one involving Brillouin spectroscopy measurements using a high-pressure cell in an oblique scattering configuration to derive the refractive index of fluids. This includes experiment can be done on validation of the constant polarizability coefficient hypothesis and the density law of the lubricating fluids. Moreover, a set of experiments can be made on the backscattering configuration using crossed-polarized analysis VV and VH. Finally, the new set-up should be coupled to the tribometer to conduct in situ tests, comparing local lubricant behavior with calibration results, and studying macroscopic friction in relation to the local lubricant characterization are planned.

So far in the pre-study of the high-pressure cells in platelet geometry, several improvements as to be done to the microscope (See Appendix E). First, the angular adjustment has to be changed from macro to micro-displacement to ensure symmetry. Second, the microscope fixation on the arch creates uncertainties in the placement. Another fixation system has to be found.

Brillouin measurements using this configuration are challenging due to the complicated optical path inside the DAC over a large range of pressure. To ensure the alignment of both Units, another laser has to be installed on the reception arm, pointing at the sample. Superposing both lasers ensures the perfect position to receive the inelastic light.

In the second experiment in the backscattering configuration, the crossed-polarized analysis could not be performed due to technical problems. In fact, the analyzer placed before the optical fiber coupler creates a force that bends the cage maintaining the coupler. This has the consequence of losing all signals even in VV configuration. Another fixation system has to be found.

In the third experimental campaign, the Brillouin spectrometer will be coupled to the tribometer to facilitate in situ tests. This will enable the measurement of the local behavior of the lubricant as it flows through the contact. The obtained results will be compared to the calibration results presented in this work to determine the state of the fluid and assess the influence of contact conditions. Furthermore, the simultaneous recording of macroscopic friction will be examined in conjunction with this localized characterization of the lubricant.

In the pre-study performed with Jerotrib (See Appendix F), several technical problems arose. In addition to previous technical problems addressed upper, due to the backscattering configuration on a reflective surface, the VIPA CMOS camera becomes quickly saturated by the reflected light.

Moreover, the micro displacement in the vertical axis has to be changed to another more precise one. A series of experiments in the ball-disc contact using an X10 and X20 Mitutoyo long-distance objectives were not sufficient to get a signal.

Bibliography

- [1] H. P. Jost, *Lubrication: Tribology; Education and Research; Report on the Present Position and Industry's Needs (Submitted to the Department of Education and Science by the Lubrication Engineering and Research) Working Group* (HM Stationery Office, 1966).
- [2] H. P. Jost and J. Schofield, *Energy Saving through Tribology: A Techno-Economic Study*, Proc. Inst. Mech. Eng. **195**, 151 (1981).
- [3] P. Jost, *Economic Impact of Tribology*, Proc Mech. Fail. Prev. Gr. 117 (1976).
- [4] F. W. Smith, *Lubricant Behaviour in Concentrated Contact Systems - the Castor Oil-Steel System*, Wear **2**, 250 (1959).
- [5] Y. Zhang and S. Wen, *An Analysis of Elastohydrodynamic Lubrication with Limiting Shear Stress: Part II—Load Influence*, Tribol. Trans. **45**, 211 (2002).
- [6] L. D. Wedeven, *What Is EHD*, Lubr. Eng. **31**, 291 (1975).
- [7] T. A. Litovitz and C. M. Davis, *Structural and Shear Relaxation in Liquids*, Vol. 2 (ACADEMIC PRESS INC., 1965).
- [8] L. Comez, C. Masciovecchio, G. Monaco, and D. Fioretto, *Progress in Liquid and Glass Physics by Brillouin Scattering Spectroscopy*, Vol. 63 (Elsevier, 2012).
- [9] W. Gotze and L. Sjogren, *Relaxation Processes in Supercooled Liquids*, Reports Prog. Phys. **55**, 241 (1992).
- [10] S.N. Ndiaye, L. Martinie, D. Philippon, N. Devaux, and P. Vergne, *A Quantitative Friction-Based Approach of the Limiting Shear Stress Pressure and Temperature Dependence*, Tribol. Lett. **65**, 1 (2017).
- [11] D. A. Pinnow, S. J. Candau, J. T. LaMacchia, and T. A. Litovitz, *Brillouin Scattering: Viscoelastic Measurements in Liquids*, J. Acoust. Soc. Am. **43**, 131 (1968).
- [12] P. Bezot, G. M. Searby, and P. Sixou, *Low Frequency Light Scattering from Liquid and Supercooled Ethyl Benzoate*, J. Chem. Phys. **62**, 3813 (1975).
- [13] L. Comez, D. Fioretto, F. Scarponi, and G. Monaco, *Density Fluctuations in the Intermediate Glass-Former Glycerol: A Brillouin Light Scattering Study*, J. Chem. Phys. **119**, 6032 (2003).
- [14] P. Voudouris, N. Gomopoulos, A. Le Grand, N. Hadjichristidis, G. Floudas, M. D. Ediger, and G. Fytas, *Does Brillouin Light Scattering Probe the Primary Glass Transition Process at Temperatures Well above Glass Transition?*, J. Chem. Phys. **132**, 74906 (2010).
- [15] G. Floudas, G. Fytas, and I. Alig, *Brillouin Scattering from Bulk Polybutadiene: Distribution of Relaxation Times versus Single Relaxation Time Approach*, Polymer (Guildf). **32**, 2307 (1991).
- [16] S. C. Santucci, L. Comez, F. Scarponi, R. Verbeni, J. Legrand, C. Masciovecchio, A. Gessini, and D. Fioretto, *Onset of the Alpha -Relaxation in the Glass-Forming Solution LiCl – 6H 2 O Revealed by Brillouin Scattering Techniques*, J. Chem. Phys. **1** (2009).
- [17] D. Fioretto and F. Scarponi, *Dynamics of a Glassy Polymer Studied by Brillouin Light Scattering*, Mater. Sci. Eng. A **521–522**, 243 (2009).

- [18] D. Fioretto, C. Masciovecchio, M. Mattarelli, G. Monaco, L. Palmieri, G. Ruocco, and F. Sette, *Brillouin Light and X-Ray Study of Glass-Forming Polybutadiene*, *Philos. Mag. B* **82**, 273 (2002).
- [19] M. S. Jeong, J. H. Ko, Y. H. Ko, and K. J. Kim, *High-Pressure Acoustic Properties of Glycerol Studied by Brillouin Spectroscopy*, *Phys. B Condens. Matter* **478**, 27 (2015).
- [20] M. Li, F. Li, W. Gao, C. Ma, L. Huang, Q. Zhou, and Q. Cui, *Brillouin Scattering Study of Liquid Methane under High Pressures and High Temperatures*, *J. Chem. Phys.* **133**, (2010).
- [21] Y. Fujita and H. Kobayashi, *Dispersion and Attenuation on the Brillouin Sound Waves of a Lubricant: Di(2-Ethylhexyl) Sebacate under High Pressures*, *J. Appl. Phys.* **110**, (2011).
- [22] S. C. Ng, T. J. C. Hosea, and S. H. Goh, *Glass Transition of Polyethylene as Studied by Brillouin Spectroscopy*, *Polym. Bull.* **18**, 155 (1987).
- [23] T.-H. Kim, J.-H. Ko, E.-M. Kwon, and J.-G. Jun, *Micro-Brillouin Spectroscopy Applied to the Glass Transition of Anti-Inflammatory Egonol*, *J. Opt. Soc. Korea* **14**, 403 (2010).
- [24] L. Comez, M. Pietrella, D. Fioretto, G. Monaco, F. Scarponi, R. Verbeni, and L. Palmieri, *Brillouin-Scattering Study of the Fast Dynamics of m-Toluidine*, *Philos. Mag.* **87**, 651 (2007).
- [25] L. Comez, D. Fioretto, G. Monaco, and G. Ruocco, *Brillouin Scattering Investigations of Fast Dynamics in Glass Forming Systems*, *J. Non. Cryst. Solids* **307**, 148 (2002).
- [26] Y. Nakamura, I. Fujishiro, and H. Kawakami, *Estimation of Refractive Index and Density of Lubricants under High Pressure by Brillouin Scattering*, in *AIP Conference Proceedings*, Vol. 309 (American Institute of Physics, 1994), pp. 1519–1522.
- [27] Y. Nakamura, I. Fujishiro, H. Kawakami, Y. Nakamura, I. Fujishiro, and H. Kawakami, *Estimation of Refractive Index and Density of Lubricants under High Pressure by Brillouin Scattering*, **1519**, (1994).
- [28] Y. Nakamura, I. Fujishiro, K. Nishibe, and H. Kawakami, *Measurement of Physical Properties of Lubricants under High Pressure by Brillouin Scattering in a Diamond Anvil Cell*, *J. Tribol.* **117**, 519 (1995).
- [29] P. Bezot, G. M. Searby, and P. Sixou, *Comparison of the Transverse Viscoelastic Properties of Benzyl Benzoate from Ultrasonic and Light-Scattering Measurements*, *Opt. Commun.* **16**, 278 (1976).
- [30] P. Bezot, C. Hesse-Bezot, D. Berthe, G. Dalmaz, and P. Vergne, *Viscoelastic Parameters of 5P4E as a Function of Pressure and Temperature by Light Scattering Technique*, *J. Tribol.* **108**, 579 (1986).
- [31] M. A. Alsaad, W. O. Winer, F. D. Medina, and D. C. O'Shea, *Light-Scattering Study of the Glass Transition in Lubricants*, *J. Lubr. Technol.* **100**, 418 (1978).
- [32] P. Bezot, G. M. Searby, P. Sixou, P. Bezot, G. M. Searby, and P. Sixeu, *Low Frequency Light Scattering from Liquid and Supercooled Ethyl Benzoate*, *J. Chem. Phys.* **62**, 3813 (1975).
- [33] A. Polian, *Brillouin Scattering at High Pressure: An Overview*, *J. Raman Spectrosc.* **34**, 633 (2003).
- [34] D. Fioretto, L. Comez, G. Socino, L. Verdini, S. Corezzi, and P. A. Rolla, *Dynamics of Density*

- Fluctuations of a Glass-Forming Epoxy Resin Revealed by Brillouin Light Scattering*, Phys. Rev. E - Stat. Physics, Plasmas, Fluids, Relat. Interdiscip. Top. **59**, 1899 (1999).
- [35] B. Vincent, C. Rouxel, Didier Martinet, and J. Margueritat, *Spectroscopie Brillouin : Introduction et Exemples*, in *Spectroscopies Vibrationnelles. Théorie, Aspects Pratiques et Applications*, Editions d (France, 2020), pp. 247–272.
- [36] H. P. Zhang, A. Brodin, H. C. Barshilia, G. Q. Shen, H. Z. Cummins, and R. M. Pick, *Brillouin Scattering Study of Salol: Exploring the Effects of Rotation-Translation Coupling*, Phys. Rev. E - Stat. Physics, Plasmas, Fluids, Relat. Interdiscip. Top. **70**, 22 (2004).
- [37] N. J. Tao, G. Li, and H. Z. Cummins, *Brillouin-Scattering Study of the Liquid-Glass Transition in CaKNO₃: Mode-Coupling Analysis*, Phys. Rev. B **45**, 686 (1992).
- [38] S. N. Ndiaye, *Ultimate Behavior of Confined Fluids under Very High Pressure and Shear Stress*, thesis dissertation, Université de Lyon, INSA de Lyon, 2017.
- [39] S. S. Bair, O. Andersson, F. S. Qureshi, M. M. Schirru, S. S. Bair, O. Andersson, F. S. Qureshi, and M. M. Schirru, *New EHL Modeling Data for the Reference Liquids Squalane and Squalane Plus Polyisoprene*, Tribol. Trans. **0**, 1 (2017).
- [40] V. Jadhao and M. O. Robbins, *Probing Large Viscosities in Glass-Formers with Nonequilibrium Simulations*, Proc. Natl. Acad. Sci. **114**, 7952 (2017).
- [41] S. Ndiaye, L. Martinie, D. Philippon, M. Gonon-Caux, J. Margueritat, and P. Vergne, *On the Influence of Phase Change in Highly Loaded Frictional Contacts*, Tribol. Lett. **68**, 54 (2020).
- [42] J. R. Sandercock, *Brillouin Scattering Study of SbSI Using a Double-Passed, Stabilised Scanning Interferometer*, Opt. Commun. **2**, 73 (1970).
- [43] J. R. Sandercock, *Some Recent Developments in Brillouin Scattering*, Rca Rev **36**, 89 (1975).
- [44] H. K. Mao, J. Xu, and P. M. Bell, *Calibration of the Ruby Pressure Gauge to 800 Kbar under Quasi-Hydrostatic Conditions*, J. Geophys. Res. **91**, 4673 (1986).
- [45] D. D. Ragan, R. Gustavsen, and D. Schiferl, *Calibration of the Ruby R1 and R2 Fluorescence Shifts as a Function of Temperature from 0 to 600 K*, J. Appl. Phys. **72**, 5539 (1992).
- [46] Z. Dong and Y. Song, *Novel Pressure-Induced Structural Transformations of Inorganic Nanowires*, in *Nanowires-Fundamental Research* (IntechOpen, 2011).
- [47] P. Vergne, *Super Low Traction under EHD & Mixed Lubrication Regimes*, in *Superlubricity* (Elsevier, 2007), pp. 427–443.
- [48] IEA (2010), *Energy Technology Perspectives 2010*, IEA, Paris
<https://www.iea.org/reports/energy-technology-perspectives-2010>, License: CC BY 4.0
- [49] K. Holmberg and A. Erdemir, *Influence of Tribology on Global Energy Consumption, Costs and Emissions*, Friction **5**, 263 (2017).
- [50] P. M. Lee and R. Carpick, *Tribological Opportunities for Enhancing America's Energy Efficiency*, A Rep. to Adv. Res. Proj. Agency-Energy US Dep. Energy **14**, (2017).
- [51] S. C. Cha and A. Erdemir, *Coating Technology for Vehicle Applications* (Springer, Basel, Switzerland, 2015).

- [52] K. Holmberg, K.-R. Päivi, P. Härkisaari, K. Valtonen, and A. Erdemir, *Global Energy Consumption Due to Friction and Wear in the Mining Industry*, Tribol. Int. **115**, (2017).
- [53] B. Bhushan, *Modern Tribology Handbook, Two Volume Set* (CRC press, 2000).
- [54] A. Dorinson and K. C. Ludema, *Mechanics and Chemistry in Lubrication*, Vol. 9 (Elsevier, 1985).
- [55] M. H. Jones and D. Scott, *Industrial Tribology: The Practical Aspects of Friction, Lubrication and Wear*, Vol. 8 (Elsevier, 1983).
- [56] H. A. Spikes, *Sixty Years of EHL*, Lubr. Sci. **18**, 265 (2006).
- [57] S. Boyde, *Green Lubricants. Environmental Benefits and Impacts of Lubrication*, Green Chem. **4**, 293 (2002).
- [58] A. N. Grubin and I. E. Vinogradova, *Central Scientific Research Institute for Technology and Mechanical Engineering*, Moscow, DSIR Transl. **115**, (1949).
- [59] D. Dowson and G. R. Higginson, *A Numerical Solution to the Elasto-Hydrodynamic Problem*, J. Mech. Eng. Sci. **1**, 6 (1959).
- [60] D. Dowson and G. R. Higginson, *Elasto-Hydrodynamic Lubrication: The Fundamentals of Roller and Gear Lubrication* (Pergamon Press, 1966).
- [61] C. Barus, *Isothermals, Isopiestic and Isometrics Relative to Viscosity*, Am. J. Sci. **3**, 87 (1893).
- [62] J. Wheeler, P. Vergne, N. Fillot, and D. Philippon, *On the Relevance of Analytical Film Thickness EHD Equations for Isothermal Point Contacts: Qualitative or Quantitative Predictions?*, Friction **4**, 369 (2016).
- [63] L. Martinie and P. Vergne, *Lubrication at Extreme Conditions: A Discussion About the Limiting Shear Stress Concept*, Tribol. Lett. **63**, 21 (2016).
- [64] W. Habchi, S. Bair, and P. Vergne, *On Friction Regimes in Quantitative Elastohydrodynamics*, Tribol. Int. **58**, 107 (2013).
- [65] H. Hertz, *Le Mémoire de Hertz Sur Les Contacts Ponctuels* (Ecole nationale supérieure d'arts et métiers, 1987).
- [66] W. Habchi, P. Vergne, N. Fillot, S. Bair, and G. E. Morales-Espejel, *A Numerical Investigation of Local Effects on the Global Behavior of TEHD Highly Loaded Circular Contacts*, Tribol. Int. **44**, 1987 (2011).
- [67] S. Bair, *A Traction (Friction) Curve Is Not a Flow Curve*, Lubricants **10**, 221 (2022).
- [68] A. W. Crook, *The Lubrication of Rollers IV. Measurements of Friction and Effective Viscosity*, Philos. Trans. R. Soc. London. Ser. A, Math. Phys. Sci. **255**, 281 (1963).
- [69] A. Dyson, *Frictional Traction and Lubricant Rheology in Elastohydrodynamic Lubrication*, Philos. Trans. R. Soc. London. Ser. A, Math. Phys. Sci. **266**, 1 (1970).
- [70] W. Hirst and A. J. Moore, *Non-Newtonian Behaviour in Elastohydrodynamic Lubrication*, Proc. R. Soc. London. A. Math. Phys. Sci. **337**, 101 (1974).

- [71] F. W. Smith, *Lubricant Behaviour in Concentrated Contact Systems—the Castor Oil-Steel System*, *Wear* **2**, 250 (1959).
- [72] R. Gohar and A. Cameron, *Optical Measurement of Oil Film Thickness under Elasto-Hydrodynamic Lubrication*, *Nature* **200**, 458 (1963).
- [73] W. O. Winer and S. Bair, *Shear Strength Measurements of Lubricants at High Pressure*, *J. Lubr. Technol* **101**, 251 (1979).
- [74] F. W. Smith, *The Effect of Temperature in Concentrated Contact Lubrication*, *ASLE Trans.* **5**, 142 (1962).
- [75] M. A. Plint, *Third Paper: Traction in Elastohydrodynamic Contacts*, *Proc. Inst. Mech. Eng.* **182**, 300 (1967).
- [76] K. L. Johnson and R. Cameron, *Fourth Paper: Shear Behaviour of Elastohydrodynamic Oil Films at High Rolling Contact Pressures*, *Proc. Inst. Mech. Eng.* **182**, 307 (1967).
- [77] K. L. Johnson and J. L. Tevaarwerk, *Shear Behaviour of Elastohydrodynamic Oil Films*, *Proc R Soc London Ser A* **356**, 215 (1977).
- [78] M. Alsaad, S. Bair, D. M. Sanborn, and W. O. Winer, *Glass Transitions in Lubricants: Its Relation to Elastohydrodynamic Lubrication (EHD)*, *Bull. Japan Pet. Inst.* **19**, 1 (1977).
- [79] C. R. Evans and K. L. Johnson, *The Rheological Properties of Elastohydrodynamic Lubricants*, *Proc. Inst. Mech. Eng. Part C J. Mech. Eng. Sci.* **200**, 303 (1986).
- [80] F. Laplant, E. J. Hutchinson, and D. Ben-Amotz, *Raman Measurements of Localized Pressure Variations in Lubricants above the Glass Transition Pressure*, *J. Tribol.* **119**, 817 (1997).
- [81] A. Ponjavic, L. di Mare, and J. S. S. Wong, *Effect of Pressure on the Flow Behavior of Polybutene*, *J. Polym. Sci. Part B Polym. Phys.* **52**, 708 (2014).
- [82] P. Šperka, I. Křupka, and M. Hartl, *Evidence of Plug Flow in Rolling–Sliding Elastohydrodynamic Contact*, *Tribol. Lett.* **54**, 151 (2014).
- [83] M. Kaneta, H. Nishikawa, and K. Kameishi, *Observation of Wall Slip in Elastohydrodynamic Lubrication*, *J. Tribol.* **112**, 447 (1990).
- [84] F. Guo, X. M. Li, and P. L. Wong, *A Novel Approach to Measure Slip-Length of Thin Lubricant Films under High Pressures*, *Tribol. Int.* **46**, 22 (2012).
- [85] X. M. Li, F. Guo, and P. L. Wong, *Shear Rate and Pressure Effects on Boundary Slippage in Highly Stressed Contacts*, *Tribol. Int.* **59**, 147 (2013).
- [86] L. Chang, *On the Shear Bands and Shear Localizations in Elastohydrodynamic Lubrication Films*, *J. Trib.* **127**, 245 (2005).
- [87] S. Bair and C. McCabe, *A Study of Mechanical Shear Bands in Liquids at High Pressure*, *Tribol. Int.* **37**, 783 (2004).
- [88] S. Bair, F. Qureshi, and W. O. Winer, *Observations of Shear Localization in Liquid Lubricants under Pressure*, (1993).
- [89] S. Bair, F. Qureshi, and M. Khonsari, *Adiabatic Shear Localization in a Liquid Lubricant*

- under Pressure*, J. Tribol. **116**, 705 (1994).
- [90] A. Ponjavic, M. Chennaoui, and J. S. S. Wong, *Through-Thickness Velocity Profile Measurements in an Elastohydrodynamic Contact*, Tribol. Lett. **50**, 261 (2013).
- [91] A. W. Crook, *The Lubrication of Rollers III. A Theoretical Discussion of Friction and the Temperatures in the Oil Film*, Philos. Trans. R. Soc. London. Ser. A, Math. Phys. Sci. **254**, 237 (1961).
- [92] W. Habchi, P. Vergne, S. Bair, O. Andersson, D. Eyheramendy, and G. E. Morales-Espejel, *Influence of Pressure and Temperature Dependence of Thermal Properties of a Lubricant on the Behaviour of Circular TEHD Contacts*, Tribol. Int. **43**, 1842 (2010).
- [93] J. P. Ewen, C. Gattinoni, J. Zhang, D. M. Heyes, H. A. Spikes, and D. Dini, *On the Effect of Confined Fluid Molecular Structure on Nonequilibrium Phase Behaviour and Friction*, Phys. Chem. Chem. Phys. **19**, 17883 (2017).
- [94] A. Porras-Vazquez, L. Martinie, P. Vergne, and N. Fillot, *Independence between Friction and Velocity Distribution in Fluids Subjected to Severe Shearing and Confinement*, Phys. Chem. Chem. Phys. **20**, 27280 (2018).
- [95] R. Xu, L. Martinie, P. Vergne, L. Joly, and N. Fillot, *An Approach for Quantitative EHD Friction Prediction Based on Rheological Experiments and Molecular Dynamics Simulations*, Tribol. Lett. **71**, 69 (2023).
- [96] W. Hirst and A. J. Moore, *Elastohydrodynamic Lubrication at High Pressures*, Proc. R. Soc. A Math. Phys. Eng. Sci. **360**, 403 (1978).
- [97] S. Bair and W. O. Winer, *The High Pressure High Shear Stress Rheology of Liquid Lubricants*, J. Tribol. **114**, 1 (1992).
- [98] C. A. Foord, W. C. Hammann, and A. Cameron, *Evaluation of Lubricants Using Optical Elastohydrodynamics*, ASLE Trans. **11**, 31 (1968).
- [99] S. Bair, C. McCabe, and P. T. Cummings, *Calculation of Viscous EHL Traction for Squalane Using Molecular Simulation and Rheometry*, Tribol. Lett. **13**, 251 (2002).
- [100] M. D. Ediger, C. A. Angell, and S. R. Nagel, *Supercooled Liquids and Glasses*, J. Phys. Chem. **100**, 13200 (1996).
- [101] C. M. Roland, *Characteristic Relaxation Times and Their Invariance to Thermodynamic Conditions*, Soft Matter **4**, 2316 (2008).
- [102] U. Bianchi, A. Turturro, and G. Basile, *Pressure Effects on Glass Transition in Polymers. II. A Study of the Factors Affecting DTg/DP Values*, J. Phys. Chem. **71**, 3555 (1967).
- [103] C. A. Angell, *Formation of Glasses from Liquids and Biopolymers*, Science (80-.). **267**, 1924 (1995).
- [104] S. Granick, *Motions and Relaxations of Confined Liquids*, Science (80-.). **253**, 1374 (1991).
- [105] S. Bair, *The Viscosity at the Glass Transition of a Liquid Lubricant*, Friction **7**, 86 (2018).
- [106] P. Debye, *Polar Molecules. By P. Debye, Ph. D., Pp. 172. New York: Chemical Catalog Co., Inc., 1929. \$3.50*, J. Soc. Chem. Ind. **48**, 1036 (1929).

- [107] S. S. Bair, *High Pressure Rheology for Quantitative Elastohydrodynamics* (Elsevier, 2019).
- [108] H.-W. Hu, G. A. Carson, and S. Granick, *Relaxation Time of Confined Liquids under Shear*, Phys. Rev. Lett. **66**, 2758 (1991).
- [109] G. P. Johari and M. Goldstein, *Viscous Liquids and the Glass Transition. II. Secondary Relaxations in Glasses of Rigid Molecules*, J. Chem. Phys. **53**, 2372 (1970).
- [110] C. A. Angell, K. L. Ngai, G. B. McKenna, P. F. McMillan, and S. W. Martin, *Relaxation in Glassforming Liquids and Amorphous Solids*, J. Appl. Phys. **88**, 3113 (2000).
- [111] C. M. Roland, *Relaxation Phenomena in Vitrifying Polymers and Molecular Liquids*, Macromolecules **43**, 7875 (2010).
- [112] L. Larini, A. Ottochian, C. De Michele, and D. Leporini, *Universal Scaling between Structural Relaxation and Vibrational Dynamics In glass-Forming Liquids and Polymers*, Nat. Phys. **4**, 42 (2008).
- [113] G. N. Greaves and S. Sen, *Inorganic Glasses, Glass-Forming Liquids and Amorphizing Solids*, Adv. Phys. **56**, 1 (2007).
- [114] P. G. Debenedetti and F. H. Stillinger, *Supercooled Liquids and the Glass Transition*, Nature **410**, 259 (2001).
- [115] B. Bhushan, *Nanotribology and Nanomechanics: An Introduction* (Springer, 2008).
- [116] W. Xu, E. I. Cooper, and C. A. Angell, *Ionic Liquids: Ion Mobilities, Glass Temperatures, and Fragilities*, J. Phys. Chem. B **107**, 6170 (2003).
- [117] M. Paluch, Z. Dendzik, and S. J. Rzoska, *Scaling of High-Pressure Viscosity Data in Low-Molecular-Weight Glass-Forming Liquids*, Phys. Rev. B **60**, 2979 (1999).
- [118] H. E. Schweyer, *Glass Transition of Asphalts under Pressure*, J. Test. Eval. **2**, (1974).
- [119] R. G. Budynas and J. K. Nisbett, *Shigley's Mechanical Engineering Design*, Vol. 8 (McGraw-Hill New York, 2008).
- [120] A. A. Pronin, M. V Kondrin, A. G. Lyapin, V. V Brazhkin, A. A. Volkov, P. Lunkenheimer, and A. Loidl, *Glassy Dynamics under Superhigh Pressure*, Phys. Rev. E **81**, 41503 (2010).
- [121] M. Paluch, A. Patkowski, and E. W. Fischer, *Temperature and Pressure Scaling of the α Relaxation Process in Fragile Glass Formers: A Dynamic Light Scattering Study*, Phys. Rev. Lett. **85**, 2140 (2000).
- [122] M. J. Stevens and M. O. Robbins, *Simulations of Shear-Induced Melting and Ordering*, Phys. Rev. E **48**, 3778 (1993).
- [123] G. W. White and S. H. Cakebread, *The Glassy State in Certain Sugar-containing Food Products*, Int. J. Food Sci. Technol. **1**, 73 (1966).
- [124] Y. H. Roos, *The Glassy State*, Food Mater. Sci. Princ. Pract. **67** (2008).
- [125] Y. H. Roos, *CHAPTER 8 - Mapping the Different States of Food Components Using State Diagrams*, in *Modern Biopolymer Science*, edited by S. Kasapis, I. T. Norton, and J. B. Ubbink (Academic Press, San Diego, 2009), pp. 261–276.

- [126] P. J. Haines, M. Reading, and F. W. Wilburn, *Handbook of Thermal Analysis and Calorimetry Vol. 1* (Elsevier, Amsterdam, Netherlands, 1998).
- [127] G. Floudas, *2.32 - Dielectric Spectroscopy*, in edited by K. Matyjaszewski and M. B. T.-P. S. A. C. R. Möller (Elsevier, Amsterdam, 2012), pp. 825–845.
- [128] K. Deshmukh, S. Sankaran, B. Ahamed, K. K. Sadasivuni, K. S. K. Pasha, D. Ponnamma, P. S. Rama Sreekanth, and K. Chidambaram, *Chapter 10 - Dielectric Spectroscopy*, in *Micro and Nano Technologies*, edited by S. Thomas, R. Thomas, A. K. Zachariah, and R. K. B. T.-S. M. for N. C. Mishra (Elsevier, 2017), pp. 237–299.
- [129] R. E. Wetton, R. D. L. Marsh, and J. G. Van-de-Velde, *Theory and Application of Dynamic Mechanical Thermal Analysis*, *Thermochim. Acta* **175**, 1 (1991).
- [130] U. Buchenau, *Amorphous Materials: Low-Frequency Vibrations*, in edited by K. H. J. Buschow, R. W. Cahn, M. C. Flemings, B. Ilshner, E. J. Kramer, S. Mahajan, and P. B. T.-E. of M. S. and T. Veyssi re (Elsevier, Oxford, 2001), pp. 212–215.
- [131] M. Ahart, D. Aihaiti, R. J. Hemley, and S. Kojima, *Pressure Dependence of the Boson Peak of Glassy Glycerol*, *J. Phys. Chem. B* **121**, 6667 (2017).
- [132] S. C. Santucci, L. Comez, F. Scarponi, G. Monaco, R. Verbeni, J.-F. Legrand, C. Masciovecchio, A. Gessini, and D. Fioretto, *Onset of the α -Relaxation in the Glass-Forming Solution LiCl–6 H₂O Revealed by Brillouin Scattering Techniques*, *J. Chem. Phys.* **131**, 154507 (2009).
- [133] A. B. Singaraju, D. Bahl, and L. L. Stevens, *Brillouin Light Scattering: Development of a near Century-Old Technique for Characterizing the Mechanical Properties of Materials*, *AAPS PharmSciTech* **20**, 1 (2019).
- [134] F. Scarponi, L. Comez, D. Fioretto, and L. Palmieri, *Brillouin Light Scattering from Transverse and Longitudinal Acoustic Waves in Glycerol*, *Phys. Rev. B - Condens. Matter Mater. Phys.* **70**, (2004).
- [135] D. Fioretto, M. Mattarelli, C. Masciovecchio, G. Monaco, G. Ruocco, and F. Sette, *Cusp-like Temperature Behavior of the Nonergodicity Factor in Polybutadiene Revealed by a Joint Light and x-Ray Brillouin Scattering Investigation*, *Phys. Rev. B - Condens. Matter Mater. Phys.* **65**, 2242051 (2002).
- [136] L. Palmieri, *Acoustic Phonons in an Epoxy Resin Studied*, *IEEE Ultrason. Symp.* 731 (1997).
- [137] R. J. Poole, *The Deborah and Weissenberg Numbers*, *Rheol. Bull* **53**, 32 (2012).
- [138] A. G. M. Ferreira, A. P. V Egas, I. M. A. Fonseca, A. C. Costa, D. C. Abreu, and L. Q. Lobo, *The Viscosity of Glycerol*, *J. Chem. Thermodyn.* **113**, 162 (2017).
- [139] R. Zondervan, F. Kulzer, G. C. G. Berkhout, and M. Orrit, *Local Viscosity of Supercooled Glycerol near T_g Probed by Rotational Diffusion of Ensembles and Single Dye Molecules*, *Proc. Natl. Acad. Sci.* **104**, 12628 (2007).
- [140] M. Alsaad, S. Bair, D. M. Sanborn, and W. O. Winer, *Glass Transitions in Lubricants: Its Relation to Elastohydrodynamic Lubrication (EHD)*, *J. Lubr. Technol.* **100**, 1 (1977).
- [141] C. Way, P. Wadhwa, and R. Busch, *The Influence of Shear Rate and Temperature on the Viscosity and Fragility of the Zr₄₁. 2Ti₁₃. 8Cu₁₂. 5Ni₁₀. 0Be₂₂. 5 Metallic-Glass-Forming Liquid*, *Acta Mater.* **55**, 2977 (2007).

- [142] C. A. A. Angell, *Relaxation in Liquids, Polymers and Plastic Crystals — Strong/Fragile Patterns and Problems*, J. Non. Cryst. Solids **131**, 13 (1991).
- [143] R. Prevedel, A. Diz-Muñoz, G. Ruocco, and G. Antonacci, *Brillouin Microscopy: An Emerging Tool for Mechanobiology*, Nat. Methods **16**, 969 (2019).
- [144] J. G. Dil, *Brillouin Scattering in Condensed Matter*, Reports Prog. Phys. **45**, 285 (1982).
- [145] J. Sandercock, *Trends in Brillouin Scattering: Studies of Opaque Materials, Supported Films, and Central Modes*, Light Scatt. Solids III 173 (1982).
- [146] K. J. Koski and J. L. Yarger, *Brillouin Imaging*, Appl. Phys. Lett. **87**, 17 (2005).
- [147] G. Scarcelli and S. H. Yun, *Confocal Brillouin Microscopy for Three-Dimensional Mechanical Imaging*, Nat. Photonics **2**, 39 (2008).
- [148] S. Mattana, S. Caponi, F. Tamagnini, D. Fioretto, and F. Palombo, *Viscoelasticity of Amyloid Plaques in Transgenic Mouse Brain Studied by Brillouin Microspectroscopy and Correlative Raman Analysis*, J. Innov. Opt. Health Sci. **10**, (2017).
- [149] J. Margueritat et al., *High-Frequency Mechanical Properties of Tumors Measured by Brillouin Light Scattering*, Phys. Rev. Lett. **122**, (2019).
- [150] E. S. Zouboulis, M. Grimsditch, A. K. Ramdas, and S. Rodriguez, *Temperature Dependence of the Elastic Moduli of Diamond: A Brillouin-Scattering Study*, Phys. Rev. B **57**, 2889 (1998).
- [151] T. C. Ransom, M. Ahart, R. J. Hemley, and C. M. Roland, *Acoustic Properties and Density of Polyurea at Pressure up to 13.5 GPa through Brillouin Scattering Spectroscopy*, J. Appl. Phys. **123**, (2018).
- [152] J. D. Bass, S. V. Sinogeikin, and B. Li, *Elastic Properties of Minerals: A Key for Understanding the Composition and Temperature of Earth's Interior*, Elements **4**, 165 (2008).
- [153] S. Sinogeikin, J. Bass, V. Prakapenka, D. Lakshtanov, G. Shen, C. Sanchez-Valle, and M. Rivers, *Brillouin Spectrometer Interfaced with Synchrotron Radiation for Simultaneous X-Ray Density and Acoustic Velocity Measurements*, in *Review of Scientific Instruments*, Vol. 77 (2006).
- [154] J. Peatross and W. Michael, *Physics of Light and Optics* (2015).
- [155] R. Scheps, *Basic Concepts*, in *Introduction to Laser Diode-Pumped Solid State Lasers* (SPIE PRESS, n.d.).
- [156] P. Pradhan, D. Sengupta, L. Wang, C. Tremblay, S. LaRochelle, and B. Ung, *The Brillouin Gain of Vector Modes in a Few-Mode Fiber*, Sci. Rep. **7**, 1552 (2017).
- [157] C. Kittel, *Introduction to Solid State Physics Eighth Edition*, seven (Wiley, 2021).
- [158] T. Still, *Basics and Brillouin Light Scattering BT - High Frequency Acoustics in Colloid-Based Meso- and Nanostructures by Spontaneous Brillouin Light Scattering*, in edited by T. Still (Springer Berlin Heidelberg, Berlin, Heidelberg, 2010), pp. 9–34.
- [159] G. Simon, *Spectroscopies Vibrationnelles: Théorie, Aspects Pratiques et Applications* (Editions des archives contemporaines, 2020).

- [160] Y. Muanenda, C. J. Oton, and F. Di Pasquale, *Application of Raman and Brillouin Scattering Phenomena in Distributed Optical Fiber Sensing*, *Front. Phys.* **7**, 155 (2019).
- [161] P. A. Fleury and J. P. Boon, *Laser Light Scattering in Fluid Systems*, Vol. 24 (Wiley Online Library, 1973).
- [162] I. Butler, *Rayleigh-Brillouin Spectroscopy of Condensed Systems*, 1984.
- [163] A. San Miguel, *Solid State Physics in a Nutshell* (2014).
- [164] M. Philipp, U. Müller, R. Sanctuary, P. Seck, and J. Krüger, *Scanning Brillouin Microscopy: Acoustic Microscopy at Gigahertz Frequencies*, *Arch. Sci. (Grand-Duché de Luxembourg (Luxembourg))*, 2011).
- [165] A. Smekal, *Zur Quantentheorie Der Streuung Und Dispersion*, *Naturwissenschaften* **16**, 612 (1928).
- [166] T. Still and T. Still, *Basics and Brillouin Light Scattering*, *High Freq. Acoust. Colloid-Based Meso-and Nanostructures by Spontaneous Brillouin Light Scatt.* **9** (2010).
- [167] P. Martine, M. Ulrich, S. Roland, S. Pierre, and K. Jan-Krestian, *Scanning Brillouin Microscopy: Acoustique Microscopy at GigaHertz Frequencies*, *Arch. Des Sci. Nat. Phys. Mathématiques NS* **46**, (2012).
- [168] G. Chartier, *Introduction to Optics* (Springer-Verlag New York, 2005).
- [169] K. J. Koski, P. Akhenblit, K. McKiernan, and J. L. Yarger, *Non-Invasive Determination of the Complete Elastic Moduli of Spider Silks*, *Nat. Mater.* **12**, 262 (2013).
- [170] D. Rouxel, C. Thevenot, V. S. Nguyen, and B. Vincent, *Brillouin Spectroscopy of Polymer Nanocomposites*, in *Spectroscopy of Polymer Nanocomposites* (Elsevier, 2016), pp. 362–392.
- [171] B. A. Auld, *Acoustic Fields and Waves in Solids* (Wiley, 1973).
- [172] D. Heiman, D. S. Hamilton, and R. W. Hellwarth, *Brillouin Scattering Measurements on Optical Glasses*, *Phys. Rev. B* **19**, 6583 (1979).
- [173] M. Jeong, J. Hyun, J. Ko, Y. Ho, and K. Joo, *Pressure Dependence of Acoustic Behaviors and Refractive Index of Amorphous Kel F-800 Copolymer Studied by Brillouin Spectroscopy*, *Curr. Appl. Phys.* **13**, 1774 (2013).
- [174] C. E. Bottani and D. Fioretto, *Brillouin Scattering of Phonons in Complex Materials*, *Adv. Phys. X* **3**, 607 (2018).
- [175] L. Landau and G. Placzek, *Structure of the Undisplaced Scattering Line*, *Phys. Z. Sowiet. Un* **5**, 79 (1965).
- [176] R. D. Mountain, *Spectral Distribution of Scattered Light in a Simple Fluid*, *Rev. Mod. Phys.* **38**, 205 (1966).
- [177] S. Cazzato, M. G. Izzo, T. Bryk, T. Scopigno, and G. Ruocco, *Propagating Density Fluctuations in Hydrodynamics and Beyond*, *Atti Della Accad. Peloritana Dei Pericolanti-Classa Di Sci. Fis. Mat. e Nat.* **98**, 2 (2020).
- [178] J. P. Boon and S. Yip, *Molecular Hydrodynamics*, Dover (Dover Publication, New York, 1991).

- [179] C. J. Montrose, V. A. Solovyev, and T. A. Litovitz, *Brillouin Scattering and Relaxation in Liquids*, J. Acoust. Soc. Am. **43**, 117 (1968).
- [180] R Kubo, *The Fluctuation-Dissipation Theorem*, Reports Prog. Phys. **29**, 255 (1966).
- [181] G. Janecke and O. Weis, *Spatial Correlation of Density Fluctuations and Brillouin Scattering*, Nuovo Cim. B **52**, 578 (1967).
- [182] J.-H. Ko, M.-S. Jeong, B. W. Lee, J. H. Kim, Y. H. Ko, K. J. Kim, T. H. Kim, S. Kojima, and M. Ahart, *Pressure Dependence of Acoustic Properties of Liquid Ethanol by Using High-Pressure Brillouin Spectroscopy*, Korean J. Opt. Photonics **24**, 279 (2013).
- [183] G. Monaco, D. Fioretto, L. Comez, and G. Ruocco, *Glass Transition and Density Fluctuations in the Fragile Glass Former Orthoterphenyl*, Phys. Rev. E **63**, 61502 (2001).
- [184] C. H. Wang and J. Zhang, *Studies of Depolarized and Polarized Rayleigh–Brillouin Spectra of a Supercooled Liquid: Salol*, J. Chem. Phys. **85**, 794 (1986).
- [185] V. Jadhao and M. O. Robbins, *Probing Large Viscosities in Glass-Formers with Nonequilibrium Simulations*, Proc. Natl. Acad. Sci. **114**, 7952 (2017).
- [186] C. Mary, D. Philippon, L. Lafarge, D. Laurent, F. Rondelez, S. Bair, and P. Vergne, *New Insight into the Relationship between Molecular Effects and the Rheological Behavior of Polymer-Thickened Lubricants under High Pressure* (2013).
- [187] S. S. Bair, *Private Conversation*, (2016).
- [188] S. Bair, *Reference Liquids for Quantitative Elastohydrodynamics: Selection and Rheological Characterization*, Tribol. Lett. **22**, 197 (2006).
- [189] S. K. Mylona, M. J. Assael, M. J. P. Comuñas, X. Paredes, F. M. Gaciño, J. Fernández, J. P. Bazile, C. Boned, J. L. Daridon, and G. Galliero, *Reference Correlations for the Density and Viscosity of Squalane from 273 to 473 K at Pressures to 200 MPa*, J. Phys. Chem. Ref. Data **43**, 13104 (2014).
- [190] R. L. Cook, C. A. Herbst, and H. E. King Jr, *High-Pressure Viscosity of Glass-Forming Liquids Measured by the Centrifugal Force Diamond Anvil Cell Viscometer*, J. Phys. Chem. **97**, 2355 (1993).
- [191] P. W. Bridgman, *Statistical Mechanics and the Second Law of Thermodynamics*, Science (80-.). **75**, 419 (1932).
- [192] J. B. Segur and H. E. Oberstar, *Viscosity of Glycerol and Its Aqueous Solutions*, Ind. Eng. Chem. **43**, 2117 (1951).
- [193] S. M. Lindsay, M. W. Anderson, and J. R. Sandercock, *Construction and Alignment of a High Performance Multipass Vernier Tandem Fabry–Perot Interferometer*, Rev. Sci. Instrum. **52**, 1478 (1981).
- [194] J.R. Sandercock, Tandem Fabry–Pérot Interferometer: Operator Manual, n.d.
- [195] Z. Meng and V. V Yakovlev, *Precise Determination of Brillouin Scattering Spectrum Using a Virtually Imaged Phase Array (VIPA) Spectrometer and Charge-Coupled Device (CCD) Camera*, Appl. Spectrosc. **70**, 1356 (2016).

- [196] G. Yan, A. Bazir, J. Margueritat, and T. Dehoux, *Evaluation of Commercial Virtually Imaged Phase Array and Fabry-Pérot Based Brillouin Spectrometers for Applications to Biology*, *Biomed. Opt. Express* **11**, 6933 (2020).
- [197] I. Jubault, *Application de La Microspectrometrie Raman Aux Mesures in Situ Dans Les Contacts Dynamiques. Contribution a l'étude Du Contact Elastohydrodynamique*, l'Université des Antilles et de la Guyane, 2002, Disertation de thèse.
- [198] M. Guerette and L. Huang, *A Simple and Convenient Set-up for High-Temperature Brillouin Light Scattering*, *J. Phys. D. Appl. Phys.* **45**, (2012).
- [199] F. Datchi, A. Dewaele, P. Loubeyre, R. Letoullec, Y. Le Godec, and B. Canny, *Optical Pressure Sensors for High-Pressure-High-Temperature Studies in a Diamond Anvil Cell*, in *High Pressure Research*, Vol. 27 (2007), pp. 447–463.
- [200] H. S. Cheng, *Isothermal Elastohydrodynamic Theory for the Full Range of Pressure-Viscosity Coefficient*, *J. Lubr. Technol.* **94**, 35 (1972).
- [201] R. J. Chittenden, D. Dowson, J. F. Dunn, and C. M. Taylor, *A Theoretical Analysis of the Isothermal Elastohydrodynamic Lubrication of Concentrated Contacts. I. Direction of Lubricant Entrainment Coincident with the Major Axis of the Hertzian Contact Ellipse*, *Proc. R. Soc. London. A. Math. Phys. Sci.* **397**, 245 (1985).
- [202] G. Antonacci, M. R. Foreman, C. Paterson, and P. Török, *Spectral Broadening in Brillouin Imaging*, *Appl. Phys. Lett.* **103**, 5 (2013).
- [203] M. El Mekki-Azouzi, C. S. P. Tripathi, G. Pallares, V. Gardien, and F. Caupin, *Brillouin Spectroscopy of Fluid Inclusions Proposed as a Paleothermometer for Subsurface Rocks*, *Sci. Rep.* **5**, (2015).
- [204] W. F. Oliver, C. A. Herbst, S. M. Lindsay, and G. H. Wolf, *A General Method for Determination of Brillouin Linewidths by Correction for Instrumental Effects and Aperture Broadening : Application to Highpressure Diamond Anvil Cell Experiments A General Method for Determination of Brillouin Linewidths by Correction*, **1884**, (2013).
- [205] W. F. Oliver, *Relaxation Phenomena and Thermodynamics of Liquids at Very High Pressures*, *MRS Online Proc. Libr.* **464**, 21 (1996).
- [206] T. Seoudi, *Non-Intrusive CdSe-Based Quantum Dots for Sensing Pressure and Temperature in Lubricated Contacts*, (2020).
- [207] J.R. Sandercock, GHOST 6.75 Multichannel Analyser, n.d.
- [208] S. V Adichtchev, Y. A. Karpegina, K. A. Okotrub, M. A. Surovtseva, V. A. Zykhova, and N. V Surovtsev, *Brillouin Spectroscopy of Biorelevant Fluids in Relation to Viscosity and Solute Concentration*, *Phys. Rev. E* **99**, 62410 (2019).
- [209] J.-H. Ko, *Private Communication*, (2023).
- [210] C. Yuan, J. Wang, X. Zhang, Y. Xu, S. Feng, and H. Li, *Influence of Dynamic Compression on the Phase Transition of Cyclohexane*, *J. Mol. Liq.* **363**, 119836 (2022).
- [211] J. M. Drake, J. Klafter, and R. Kopelman, *Dynamics in Small Confining Systems III: Volume 464* (Materials Research Society, 1996).

- [212] S. Klotz, K. Takemura, T. Strässle, and T. Hansen, *Freezing of Glycerol–Water Mixtures under Pressure*, *J. Phys. Condens. Matter* **24**, 325103 (2012).
- [213] L. Comez, D. Fioretto, L. Verdini, and P. A. Rolla, *Brillouin Light Scattering from Shear Waves in an Epoxy Resin through the Glass Transition*, *J. Phys. Condens. Matter* **9**, 3973 (1997).
- [214] C. Kittel, *Introduction to Solid State Physics*, seven (Wiley, 1996).
- [215] R. D. Mountain, *Thermal Relaxation and Brillouin Scattering in Liquids*, *J. Res. Natl. Bur. Stand. Sect. A, Phys. Chem.* **70**, 207 (1966).
- [216] A. I. Vakis et al., *Modeling and Simulation in Tribology across Scales: An Overview*, *Tribol. Int.* **125**, 169 (2018).
- [217] C. M. Lehr, O. Astasheva, and J. Baller, *Brillouin Light Scattering during Shearing of Complex Fluids*, *Opt. Express* **29**, 16019 (2021).

Appendix

Table of content

<u>A. APPENDIX: THEORETICAL BACKGROUND.....</u>	218
A.1: ACOUSTIC WAVE IN A TWO ATOMS CRYSTALLINE STRUCTURE	218
A.2 RELATIONSHIP BETWEEN THE DIELECTRIC FLUCTUATION PROVOKED BY THE DENSITY FLUCTUATION AND INTENSITY OF THE SCATTERED LIGHT.....	219
A.3 TWO RELAXATION PROCESSES: EXAMPLE OF POLYBUTADIENE	221
<u>B. APPENDIX: DETERMINATION OF THE LASER SPOT SIZE USING CLEAVED SILICON SAMPLE AND BRILLOUIN SPECTROSCOPY.....</u>	223
<u>C. APPENDIX: MICROSCOPE DESIGN</u>	226
C.1: DESCRIPTION OF B AND C UNITS	226
C.2. ANGLE CALCULATION	228
C.3 POLARIZATION EFFECT ON INTERFACES	230
<u>D. APPENDIX: BRILLOUIN SPECTRA ANALYSIS.....</u>	231
D.1 : SPECTRA ASYMMETRY.....	231
D.2 ZOOM ON FIGURES FROM CHAPTER 5	232
D.3 COMPLEX MODULUS CALCULATION	234
<u>E. APPENDIX: RHEOLOGY AND BRILLOUIN SPECTROSCOPY.....</u>	236
E.1 RHEOMETER	236
E.2 INFLUENCE OF SHEAR RATE ON THE BLS SPECTRA	239
<u>F. APPENDIX: PERSPECTIVES ON THE WORK.....</u>	244

A. Appendix: Theoretical background

A.1: Acoustic wave in a two atoms crystalline structure

This appendix goes deeper using equations below to describe acoustic and optical phonons in a diatomic linear molecule. The displacement of the longitudinal acoustic wave moves atoms' planes, referred as S as shown in Figure A.1, by a quantity u_x for atoms with mass M_1 and v_x for atoms with mass M_2 .

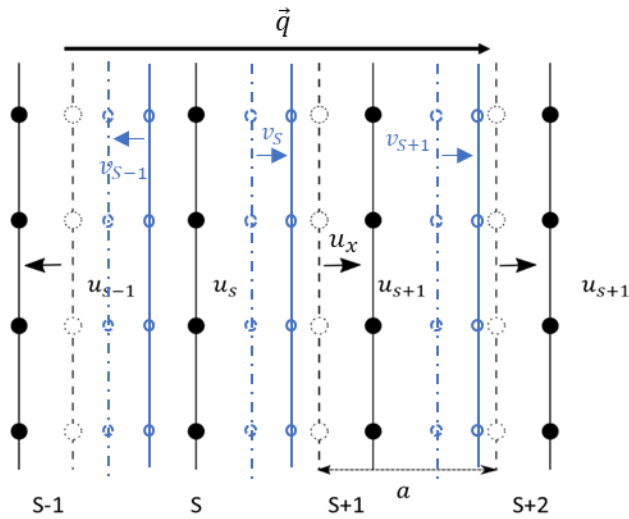


Figure A.1 : Representation of the atoms' plane at equilibrium in dashed lines (black and blue). The longitudinal acoustic wave going from left to right, in the \vec{q} direction, creates a displacement u_x for atoms with mass M_1 and a displacement v_x for atoms with mass M_2 , represented by small arrows. a is the distance between atomic layers. The figure is inspired by the reference [214].

The Hook law allows to express the force-displacement between of one atom contained in the S plane. We consider a spring with a spring constant C between the nearest-planes. :

$$F_{atom} = C(u_{s+1} - u_s) + C(u_{s-1} - u_s) \quad (A.1)$$

Taking the previous example of a two-atoms-per-unit cell, with mass M_1 and M_2 , the equation of motion for each atom of the S plane is expressed in equations A.2 and A.3.

$$M_1 \frac{d^2 u_s}{dt^2} = C(v_s + v_{s-1} - 2u_s) \quad (A.2)$$

$$M_2 \frac{d^2 v_s}{dt^2} = C(u_s + u_{s+1} - 2v_s) \quad (A.3)$$

Where $u_s = u \exp i(sqa - \omega t)$ and $v_s = v \exp i(sqa - \omega t)$ that depends on time. From those equations, the substitution leads to a system of equation:

$$\begin{cases} M_1 \omega u = C v (1 + \exp(-iqa)) - 2Cu & \text{(A.4)} \\ M_2 \omega v = C u (1 + \exp(-iqa)) - 2Cv & \text{(A.5)} \end{cases}$$

The final dispersion relations for $qa \ll 1$ close to the Brillouin zone center are then derived::

$$\omega^2 = \frac{1}{2} \frac{C}{M_1 + M_2} q^2 a^2 \quad \text{(Acoustic)} \quad \text{(A.6)}$$

$$\omega^2 = 2C \left(\frac{1}{M_1} + \frac{1}{M_2} \right) \quad \text{(optic)} \quad \text{(A.7)}$$

In equation A.6 it is clear that the frequency is proportional to the wave vector \vec{q} .

A.2 Relationship between the dielectric fluctuation provoked by the density fluctuation and intensity of the scattered light

Taking into consideration a transparent material with a crystalline structure, atoms that constitute this material are in permanent movement, their position oscillates around the equilibrium position due to thermal agitation.

The spatial displacement of atoms creates an oscillation of the electronic cloud that affects the dielectric susceptibility and the dielectric constant ε [215]. The dielectric constant fluctuation tensor $\delta\varepsilon$ in equation A.8, varies from the original position by a displacement \vec{r} and time t [166].

$$\varepsilon(\vec{r}, t) = \varepsilon_0 I + \delta\varepsilon(\vec{r}, t) \quad \text{(A.8)}$$

where I is a second rank-tensor unit that represents the spectrum power, ε_0 the average dielectric constant.

Therefore, when an incoming monochromatic electromagnetic light passes through the transparent material with heterogeneities, it scatters the monochromatic light in all directions [167]. The following development is detailed in reference [216].

From equation A.8, the total electrical field at a large distance \vec{R} from the scattered volume is the sum of the incident and scattered electromagnetic field: $E = E_i + E_s$. The scattered field E_s is affected by the density and dielectric constant fluctuation, the incident and scattered light polarization, $\overrightarrow{dir_i}$ and $\overrightarrow{dir_s}$ respectively. Then the scattered light can be written:

$$E_s(R, t) = \frac{E_0}{4\pi R \varepsilon_0} \exp(ik_s R \int_V d^3r \times \exp i(\vec{q} \cdot \vec{r} - \omega_i t [\overrightarrow{dir_s} \cdot \vec{k}_s \times (\delta\varepsilon_{is}(\vec{r}, t) \cdot \overrightarrow{dir_i})]) \quad \text{(A.9)}$$

The scattering wave vector \vec{q} is the difference between \vec{k}_s the scattered wave vector and \vec{k}_i the incident light wave vector, represented in Figure 2.9.

$$\vec{q} = \vec{k}_i - \vec{k}_s \quad \text{(A.10)}$$

The dielectric fluctuation is expressed as the function of the scattering wave vector using the spatial Fourier transform:

$$\delta\varepsilon(\vec{q}, t) = \int_V d^3r \exp i\vec{q} \cdot \vec{r} \delta\varepsilon(\vec{r}, t) \quad (\text{A.11})$$

The scattered field E_s introduced in equation A.9 is simplified in the following equation:

$$E_s(R, t) = \frac{-k_s^2 E_0}{4\pi R \varepsilon_0} \exp(i(k_s R - \omega_i t) \delta\varepsilon_{is}(\vec{q}, t)) \quad (\text{A.12})$$

with $\delta\varepsilon_{is}(\vec{q}, t) \equiv \overrightarrow{dir_s} \cdot \delta\varepsilon(\vec{q}, t) \cdot \overrightarrow{dir_i}$, these represent the light incoming and scattered polarization, that influence the dielectric function fluctuation tensor.

To describe the time-dependent dynamics of the system, the time correlation function of the scattered field is written:

$$\langle E_s^*(R, 0) E_s(R, t) \rangle = \frac{k_s^4 |E_0|^2}{16\pi^2 R^2 \varepsilon_0^2} \langle \delta\varepsilon(\vec{q}, t) \rangle \exp(-i\omega_i t) \quad (\text{A.13})$$

By applying the Fourier transform to the time-dependent equation, we obtain the frequency-dependent spectral density I_{is} :

$$I_{is}(\vec{q}, \omega_s, R) = \left(\frac{I_0 k_s^4}{16\pi^2 R^2 \varepsilon_0^2} \right) \frac{1}{2\pi} \int_{-\infty}^{+\infty} dt \langle \delta\varepsilon_{is}(\vec{q}, 0) \delta\varepsilon_{is}(\vec{q}, t) \rangle \exp(i(\omega)t) \quad (\text{A.14})$$

Where $I_0 \equiv |E_0|^2$

Finally, the spectral density is proportional to the Fourier transform of the fluctuation of the dielectric constant:

$$I_{is}(q, \omega) \propto \int_{-\infty}^{+\infty} dt \langle \delta\varepsilon_{is}^*(\vec{q}, 0) \delta\varepsilon_{is}(\vec{q}, t) \rangle \quad (\text{A.15})$$

A.3 Two relaxation processes: example of polybutadiene

As presented in Sections 2.3 and 2.5, the spectra can be analyzed by fitting the complete spectra using the appropriated model. The Debye model is used for sample experiencing an α relaxation. This section present an example of a two relaxation in polybutadiene. Polybutadiene at 270 K has been investigated in 2002 by D. Fioretto and al. [135] by the combination of ultrasonic measurements, Brillouin light scattering and inelastic Xray scattering that enlarges the frequency window from 10^{-5} to 10^3 GHz. In this range of frequency, this polymer experiences a supercooled and glassy state.

The sample was studied between 30 and 328 K using polarized and depolarized spectra in backscattering geometry with Brillouin spectroscopy. The resulting isotropic spectra are related to the dynamic structure factor $S(q, \omega)$ as presented previously in Section 2.3.3. Thus, the generalized hydrodynamic formalism (Sections 2.3.3 and 2.3.4) to extract the main parameters can be applied to BLS and XLS spectra.

As the temperature increases, the frequency shift goes down, whereas the FWHM seems to increase. An important feature is pointed out by the authors for low-temperature measurements. The combination of a non-negligible quasi-elastic mountain peak situated at the center of the spectra and an instrumental function smaller than the inelastic peak indicates the presence of relaxation of the system.

Two relaxations have been identified in the publication. A structural alpha and a beta relaxation. Nine parameters are needed to describe its behavior by the generalized hydrodynamic formalism that takes into account those two relaxations using the Debye model:

$$M^*(\omega) = M'_\infty - \frac{\rho\Delta_1}{(1 + i\omega t_{rel1})^{\beta_1}} - \frac{\rho\Delta_2}{(1 + i\omega t_{rel2})^{\beta_2}} + i\omega\eta_\infty \quad (\text{A.16})$$

where $t_{rel1,2}$, $\beta_{1,2}$ are the relaxation times and stretching parameters of the structural and secondary relaxations, respectively. $\Delta_{1,2}$ are the difference between modulus depending on the low- intermediate and high longitudinal modulus as the following: $\Delta_1 = M_{\infty\alpha} - M_\infty$ and $\Delta_2 = M_0 - M_{\infty\alpha}$. Each modulus is written in a function of the corresponding longitudinal acoustic velocities.

Other characterization techniques, ultrasonic and IXS, are used to reduce the number of undefined parameters.

The low-frequency longitudinal velocity V_o (c_0 in the publication) is estimated by ultrasonic measurements in the function of temperature: $V_o = [1525 - 3,09T (^{\circ}c)] \text{ m/s}$ [135]. It is close

to the values obtained from Brillouin light scattering. Similar observations for glycerol samples using ultrasonic measurements and BLS have been published [13].

The unrelaxed modulus is generally investigated by the IXS experiments.

At one temperature the evolution of the storage and loss modulus across frequencies displays these two relaxation processes in Figure 2.15.

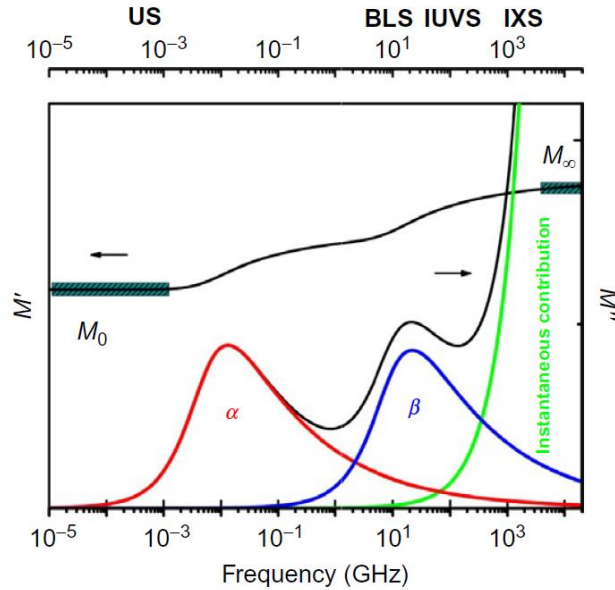


Figure A.2: Schematic from Comez and al. 2012 showing the storage and loss modulus for polybutadiene at 270 K [8] in function of the frequency.

Most of the experiments characterizing glass transition are conducted in function of temperature. In our studies, the dependency are the temperature and the pressure dependence of the physical properties.

B. Appendix: Determination of the laser spot size using cleaved silicon sample and Brillouin spectroscopy

To calculate the spot size through 1 cm glass (BK-7), the same method as the one presented in the reference [206] is followed. This method requires a transparent disc, a laser, in this study the Torus laser of $\lambda = 532,1 \text{ nm}$, and a long-distance objective Mitutoyo (MY10X-803 and MY20X-804).

To measure the spot size through a disc that mimics conditions inside the tribometer contact, a system of glass disc, silicon slice, and squalane was used. The microscope was in normal incidence, backscattering geometry. The displacement is done by a 40 mm linear stage with a resolution of $10 \mu\text{m}$. For each position as seen in Figure B.1, the Brillouin spectrum of the squalane is taken and fitted by the Lorentzian function to extract the intensity of each inelastic peak as presented in Section 4.3.1. Then, each intensity is averaged for each distance.

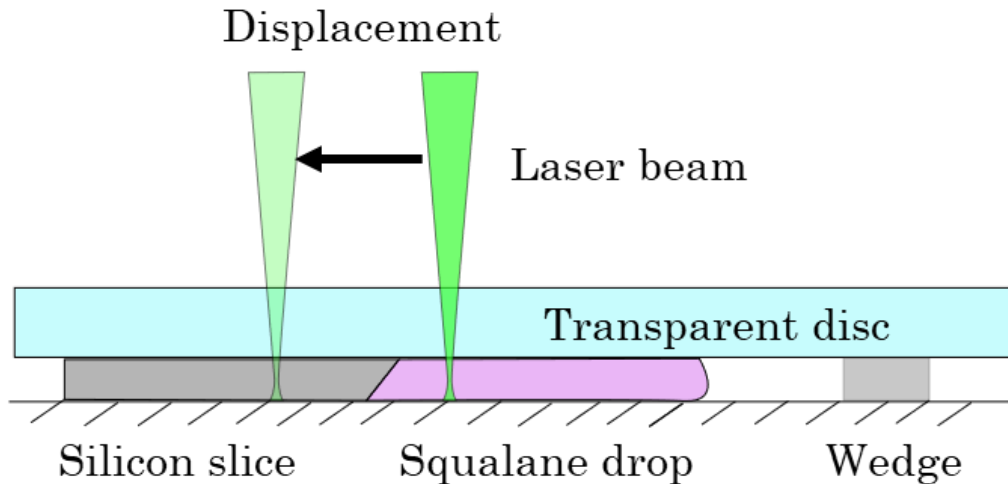


Figure B.1 :Side view of the disc, silicon, and squalane system for spot size determination.

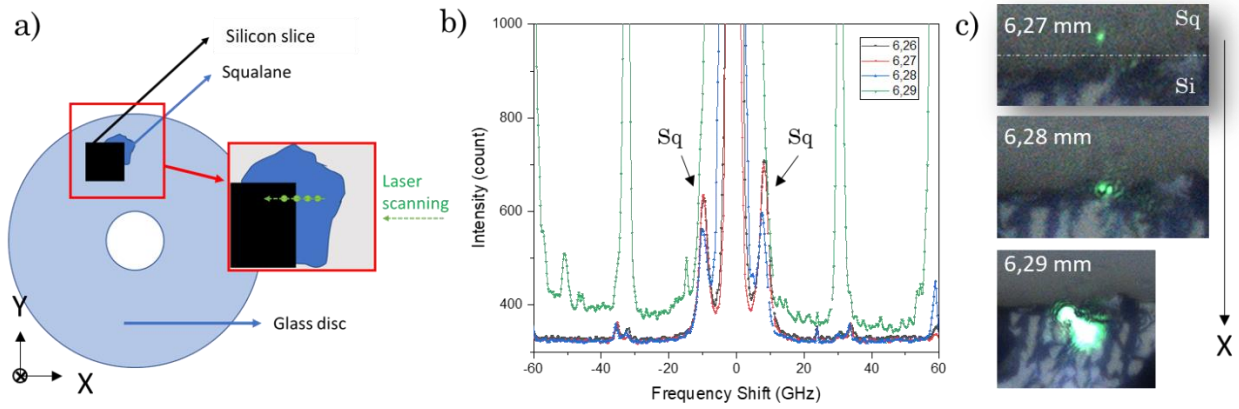


Figure B.2 : a) Methodology for spot size determination through a disc of 1 cm. b) Brillouin spectra taken at 3 positions from the squalane to the silicon slice along the X-direction. The squalane signal is situated around 10GHz. c) These 3 images on the right side were taken in the experiments at 3 positions cited in b). In the first top image the delimitation between squalane (SQ) and silicon (Si) is indicated by the dash line.

In the first line of the table B.1, Y_0 is the baseline of the fitting function, the intensity in the second line is the height of the two inelastic peaks fitted, the third line is the average between them and finally real intensity is the subtraction of the baseline and the average intensity.

X10	6,26 mm		6,27 mm		6,28 mm		6,29 mm
Y0 (count)	L:320,65	R:320,65	L:316,00	R:316,00	L:315,23	R:315,23	
Intensity (count)	L:635,97	R:722,04	L:644,48	R:711,84	L:566,65	R:596,95	
Average (count)	679,005		678,16		581,8		0
Real Intensity (count)	358,355		362,16		266,57		

Table B.1: Data of spectra measured on squalane versus the position (ref 6.26mm) of the laser spot from the lubricant to the silicon slice in the X direction for a long-distance Mitutoyo X10. The intensity is related to the inelastic scattering of squalane using Brillouin spectroscopy.

From this table B.1, the real intensity is plotted in function of the distance in Figure B2.1 for the X10.

The same process for the X20 is done with the same method. The distance intensity in the function of the distance is summarized in Table B.2.

X20	6,20	6,22	6,24	6,26	6,28	6,29	6,3						
Y0 (count)	315,31	315,31	317,16	317,16	315,97	315,97	316,54	316,27	309,75				
Intensity (count)	469,99	497,74	472,65	511,02	470,69	495,07	493,35	520,77	486,26	517,36	453,05	479,50	
Average (count)	483,865		491,88		482,88		507,06		501,81		466,275		0
Real intensity (count)	168,55		176,72		166,91		190,5		185,54		156,52		

Table B.2 Position of the laser spot from the lubricant to the silicon slice in the X direction for the X20 long-distance Mitutoyo. The intensity is related to the inelastic scattering of squalane using Brillouin spectroscopy.

From these two experiments, the spot size is calculated using the curve in Figure B.3 and B4 between 100% to 0% of intensity. Data have been fitted by the normal calculative distribution function:

$$y = y_0 + A \int_0^x \frac{1}{\sqrt{2\pi}\sigma} e^{-\frac{(x-x_c)^2}{2\sigma^2}} dt \quad (\text{B.1})$$

where y_0 is the offset, A is the amplitude, x the distance and x_c is the center of the decay and σ the standard deviation.

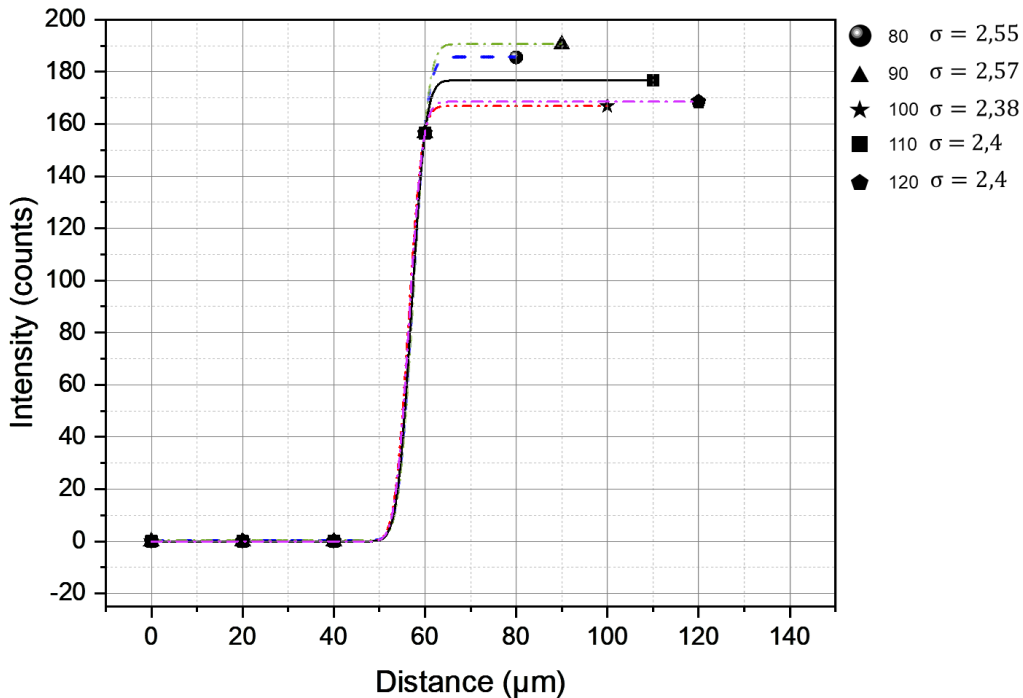


Figure B.3 : The real intensity (count) in the function distance of the laser spot calculated in Table B.2 for a long-distance Mitutoyo X20. Each symbol represents the intensity taken at a distance from the reference. σ represents the standard deviation.

Finally, the spot size is about 10 μm . Unfortunately, the precision of the stage used is not enough.

C. Appendix: Microscope design

C.1: Description of B and C units

This appendix is dedicated to an additional presentation of the angular microscope presented in Figure C.1.

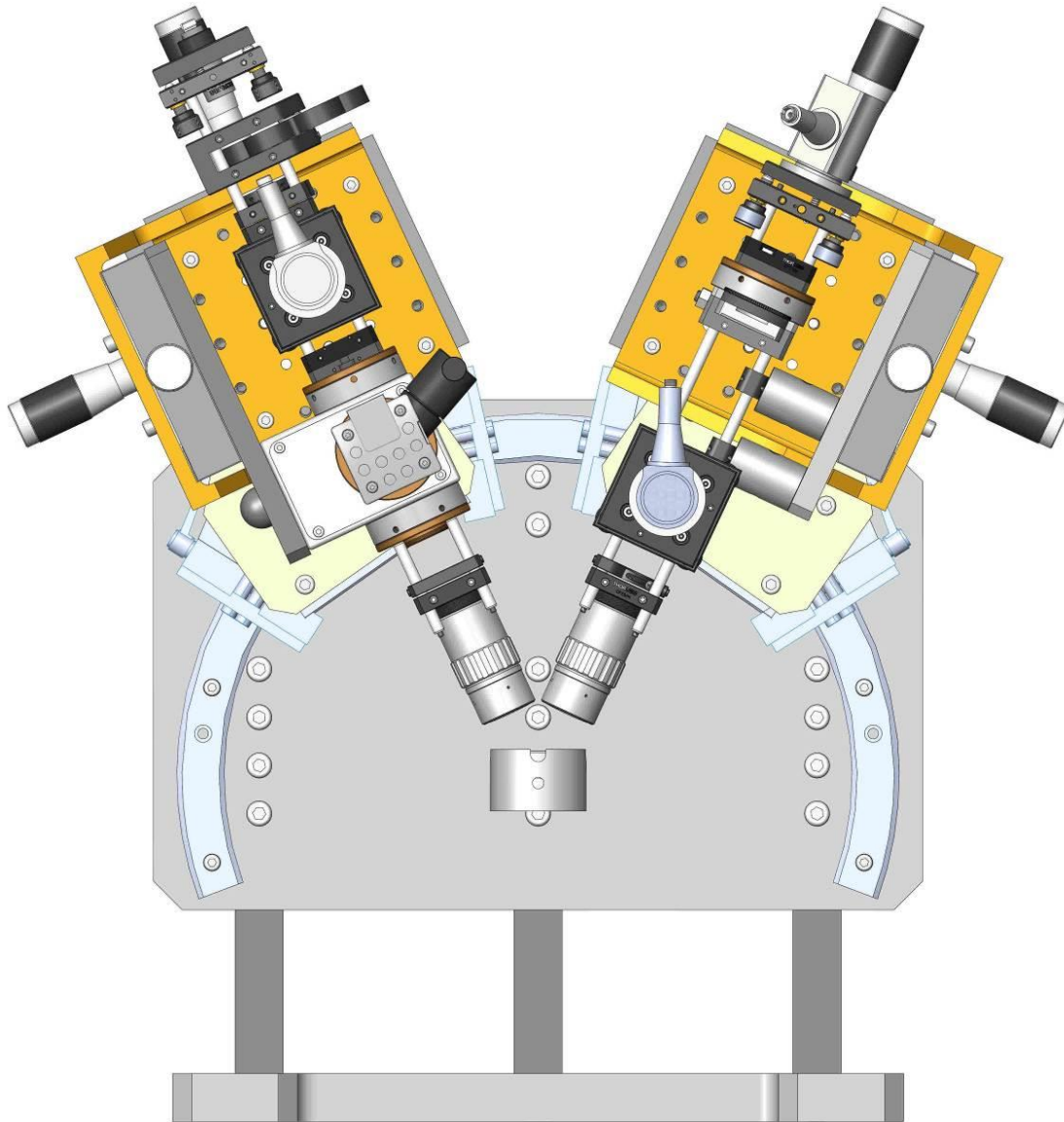


Figure C.1 : Schematic of the oblique set-up. The left block (C module) is designed to inject incident light, to visualize the sample and to record ruby spectra in a high pressure cell. The B module on the right is created to record the inelastic scattering.

Both parts are described in Figures C.2 for the B unit and C.3 for the C unit. The module C is dedicated to light injection and ruby luminescence detection, and the module B is built to

record the inelastic light scattering. The inclination is monitored by two dual-axis inclinometers $\pm 45^\circ$ precise at $0,001^\circ$ and installed behind each platform.

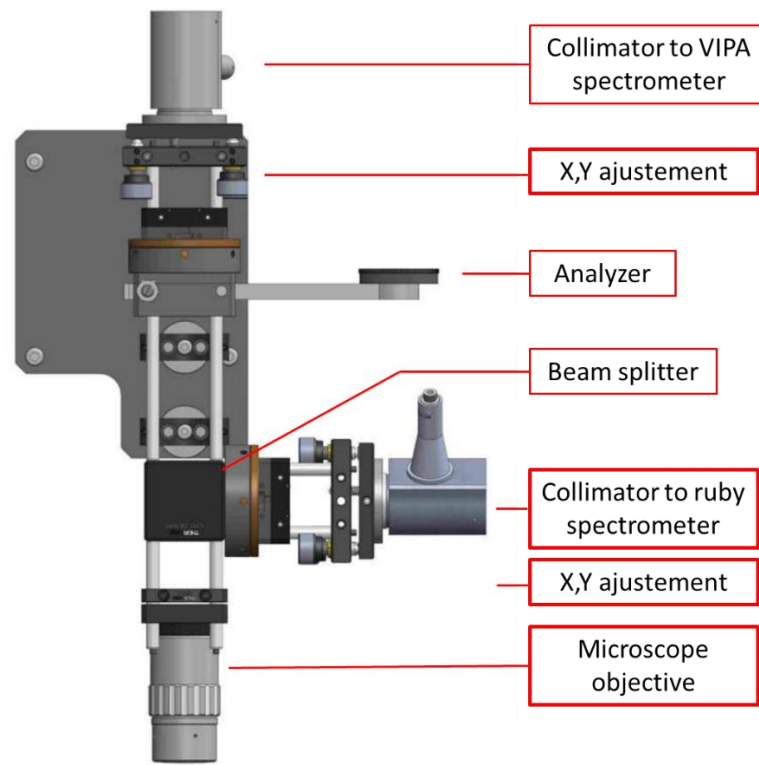


Figure C.2 : B unit with all compounds.

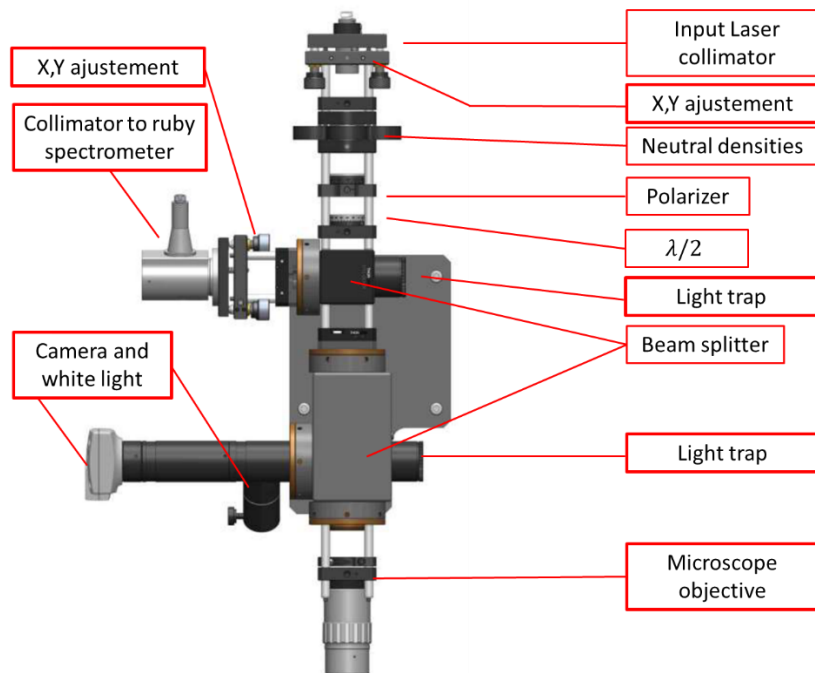


Figure C.3 : C unit with all compounds.

C.2. Angle calculation

Since the microscope is fixed on a circular arch, both objectives are easily focused on the same point, as shown in Figure C.4. However, the optical path changes when it passes through a material such as glass, diamonds, or Sapphire.

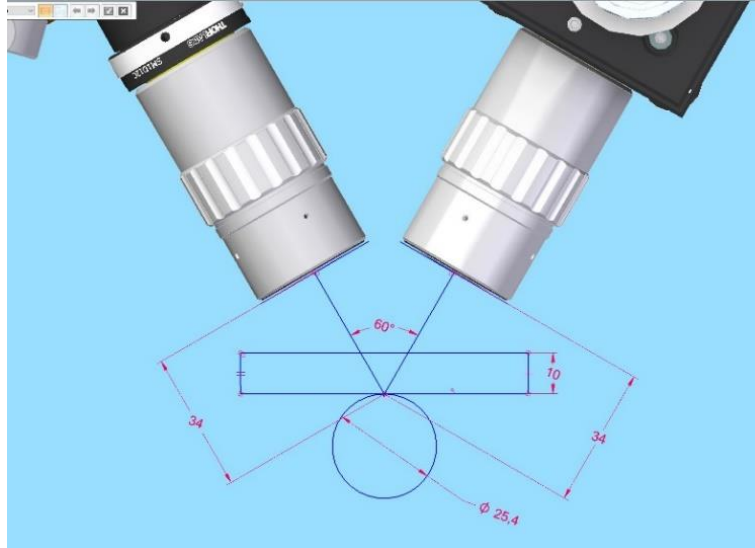


Figure C.4 : Example of an optical path on a ball system in the oblique configuration without considering the disc optical properties.

Using the Snell-Descartes law, the optical path angle at the interface between air and the material changes as represented in Figure C.5. The distance difference between these two-path is represented by Δx .

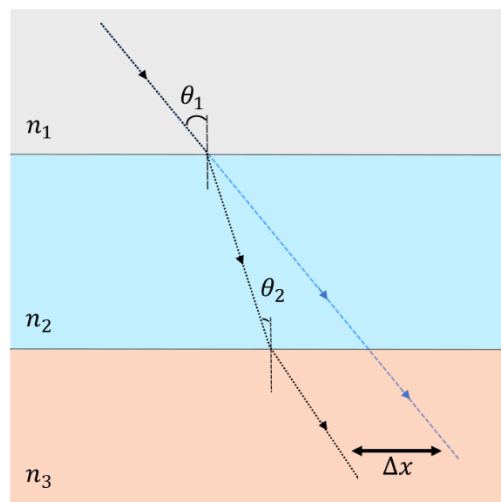


Figure C.5 : Optical path in black through 3 mediums represented in grey ($n_1 = \text{air}$), blue ($n_2 = \text{disc}$), and orange ($n_3 = \text{lubricant}$) with $n_2 > n_3 > n_1$. The blue line represents the optical path without the medium. Δx is the distance that separates the two optical paths.

The laser beam path is designed to pass through either a diamond window of 2 mm in a high pressure cell) or a sapphire or glass disc with a thickness of 1cm in a tribometer. Taking the disc example, the refractive index of sapphire and glass are respectively 1.77 and 1.51.

In Figure C.6 below, the laser beam goes through an interface (disc) with an angle θ_1 to the surface perpendicular, from the air to the glass medium. Snell-Descartes law shows that the optical path changes the angle to a smaller angle θ_2 . It makes a final difference Δf .

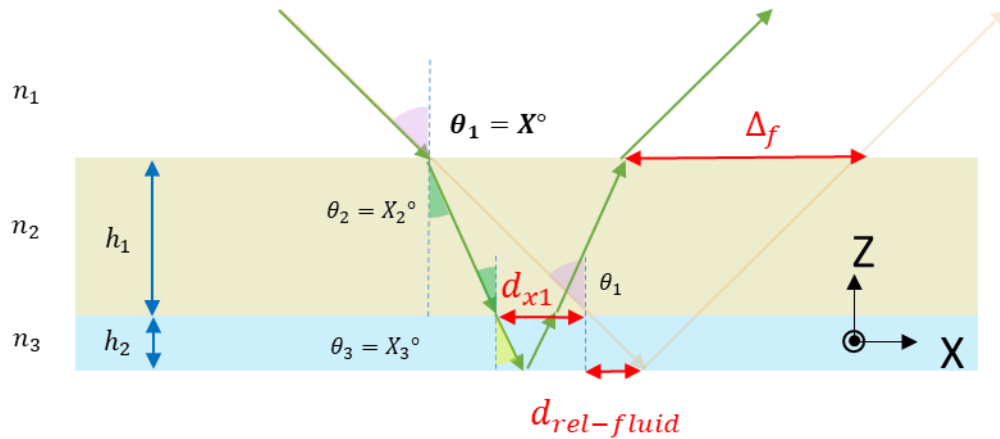


Figure C.6 : Representation of the optical path through 1cm disc in the XZ plane. White ($n_1 = \text{air}$), green ($n_2 = \text{disc}$), and blue ($n_3 = \text{lubricant}$)

The final shift Δf is calculated in table C.1 below.

ANGLE °	BENZYL BENZOATE Δf (MM)	SQUALANE Δf (MM)	GLYCEROL Δf (MM)
35	7.153381918	7.15338821	7.15340238
45	11.284384	11.284393	11.284414
65	30.96790	30.96792	30.96796

Table C.1 : Δf in the X direction calculated for a film of lubricant of 100 nm of each lubricant for 3 incident angles θ_1 .

C.3 Polarization effect on interfaces

This part is dedicated to the characterization of the transmittance and reflectivity at the interfaces of the glass disc used in friction measurements and the laser beam for Brillouin spectroscopy. The angle is taken as the surface normal. Figures C.7 and C.8 show a maximum transmission for the TM (transversal magnetic) mode between 50° and 60° for the air/glass in a larger band than the air/sapphire interface which shows a maximum transmission at 60° .

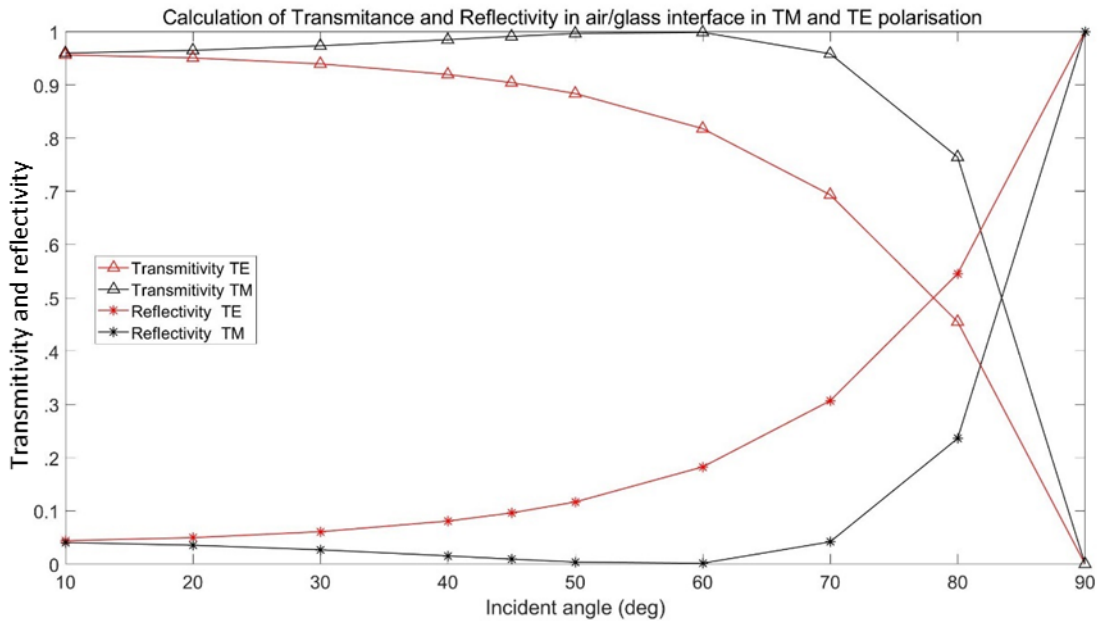


Figure C.7 : Calculation the the transmittance and reflectivity at the air/glass interface.

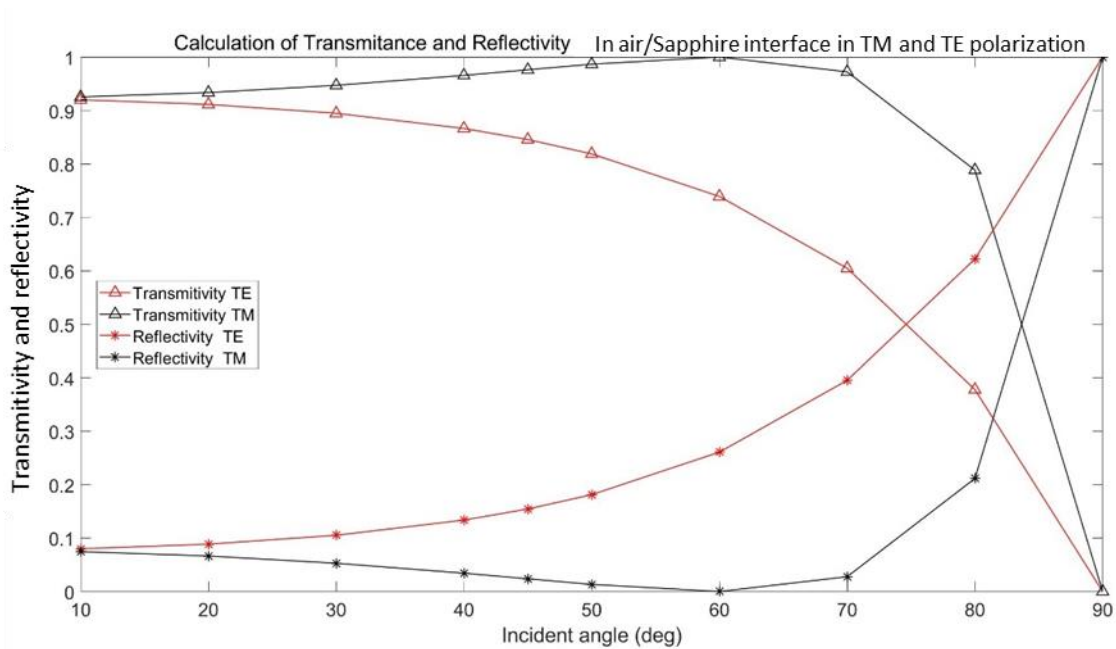


Figure C.8 : Calculation the the transmittance and reflectivity at the air/sapphire interface.

D. Appendix: Brillouin spectra analysis

D.1 : Spectra asymmetry

As presented in Section 4.4, the VIPA spectrometer used in this study shows an asymmetry in the Brillouin spectra due to misalignment of the optics in the spectrometer. In Figure D.3 are some examples of asymmetry found in the post-process for data presented in the thesis.

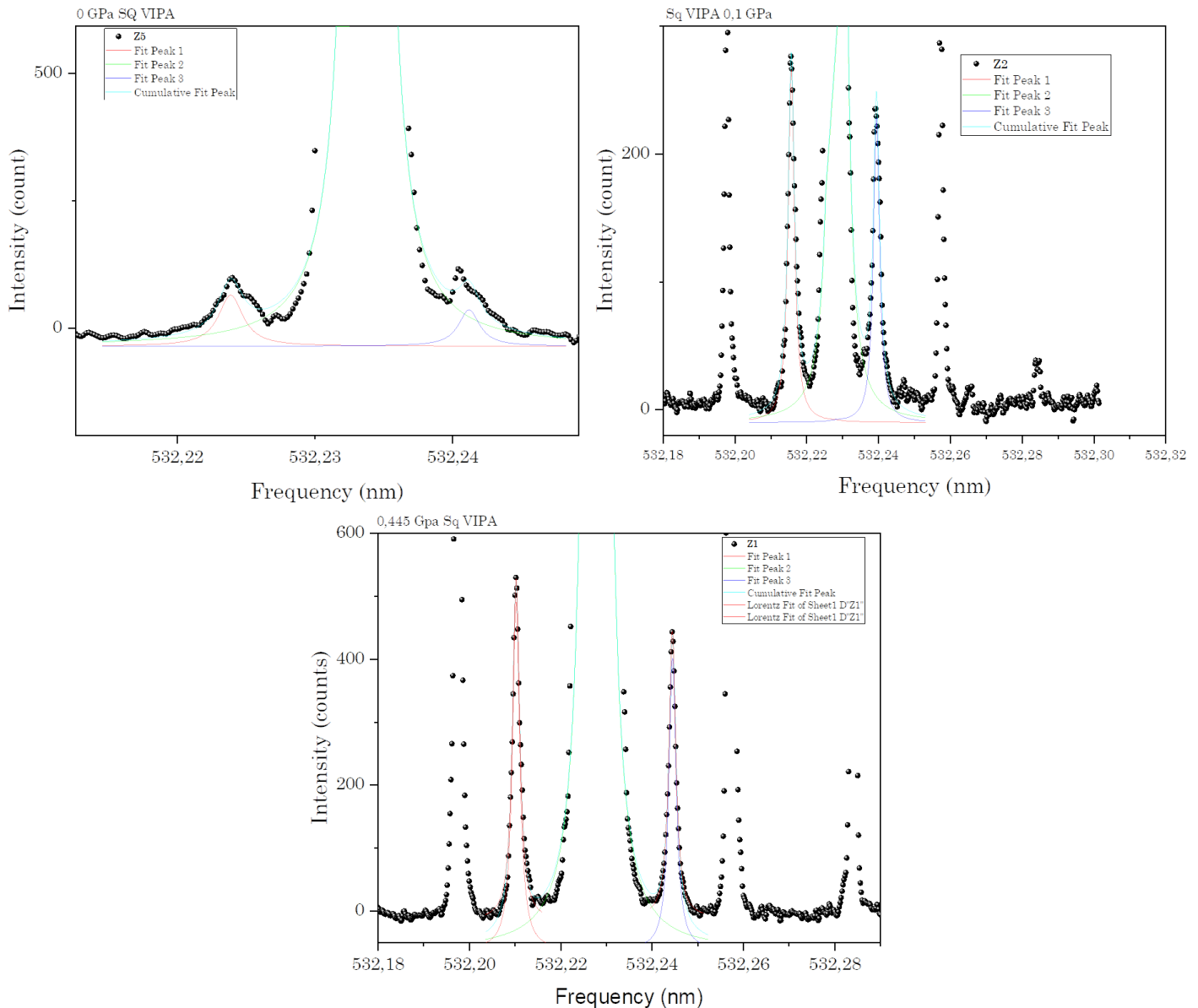


Figure D.1 : VIPA spectra of squalane at three pressures. The top left shows a shift during the acquisition. Both the top right and bottom display an asymmetry onto the doublet.

D.2 Zoom on Figures from Chapter 5

This part provides supplementary figures from the results Chapter 5. Figure D.2 is related to Figure 5.4, which shows the frequency shift in function of the pressure, the superposition of all data of benzyl benzoate taken from TFP-1 and VIPA evidences a shift of results towards higher pressures for data measured by VIPA compared to data measured by TFP, as mentioned in section 5.2.1. In the zoom in the bottom right of Figure D.2 below, it is clear that this shift impacted the determination of the glass transition pressure.

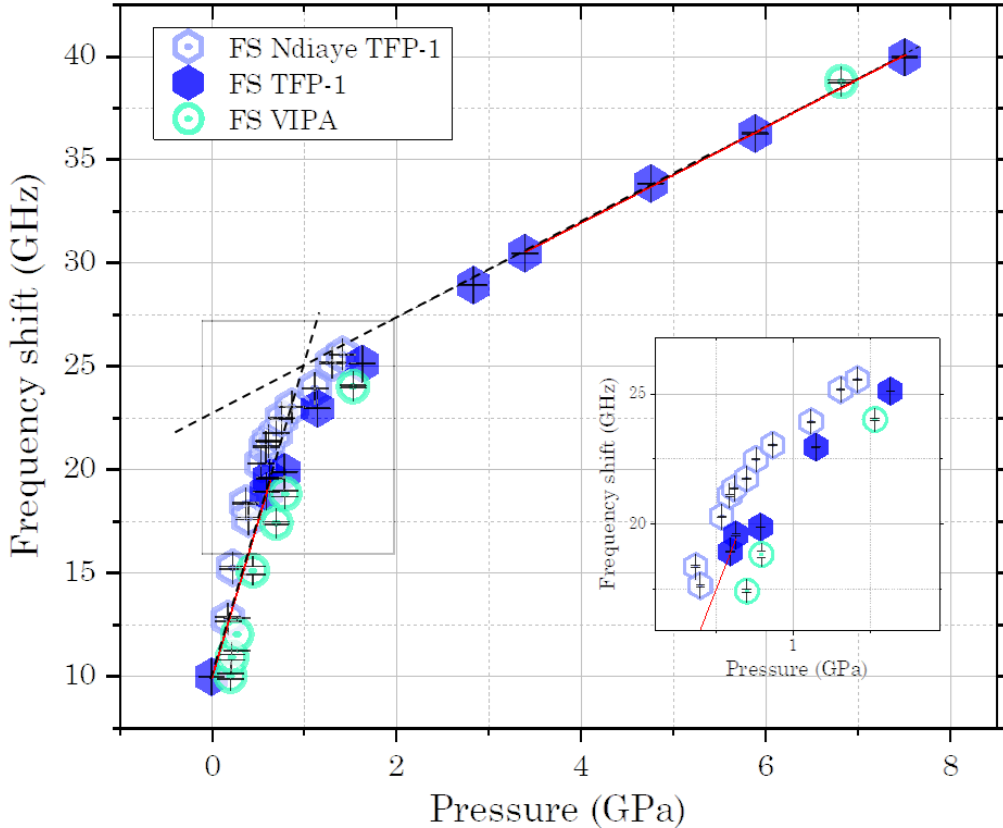


Figure D.2 : Frequency shift of benzyl benzoate for 3 datasets: one at low pressure (from Ndiaye [38]) with the TFP-1 and two at high-pressure with the TFP-1 and VIPA interferometers from this work).

Figure D.3 is a zoom made on FWHM of the same dataset of benzyl benzoate as plotted in Figure D.2. Linear fits are performed at the edges of each dataset in order to find the pressure of glass transition. 3 glass transition pressure are found $P_{g_{Ndiaye}} = 0.62 \text{ GPa}$, $P_{g_{TFP-1}} = 0.69 \text{ GPa}$, $P_{g_{VIPA}} = 0.72 \text{ GPa}$.

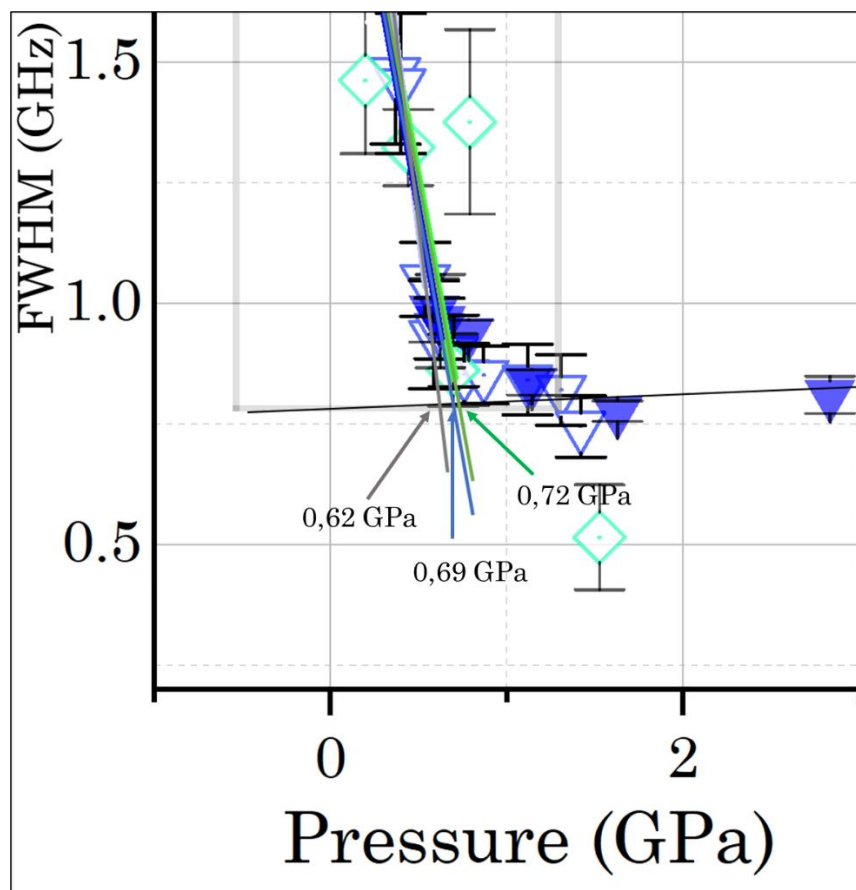


Figure D.3 : Light blue upside down open triangles with a central dot stand for data recorded in the low-pressure cell by Ndiaye using a X10 microscope objective [38] and fitted by the triple Lorentz. High-pressure experiments on benzyl benzoate from this work recorded with a X20 objective are superimposed: the dark blue upside-down open triangles with a central dot stand for TFP-1 data and the green open diamonds with a central dot stand for the VIPA data. 3 linear fits were performed on the edges of the dataset to be able to find P_g .

D.3 Complex modulus calculation

This part provides supplementary figures on the complex modulus calculation provided in Section 5.3 in Figures 5.24 for glycerol, 5.25 for squalane, and 5.26 for benzyl benzoate.

In Figure D.4, all the storage moduli are superposed in function of pressure to compare their values. The glycerol storage modulus possesses higher values compared to the squalane and benzyl benzoate.

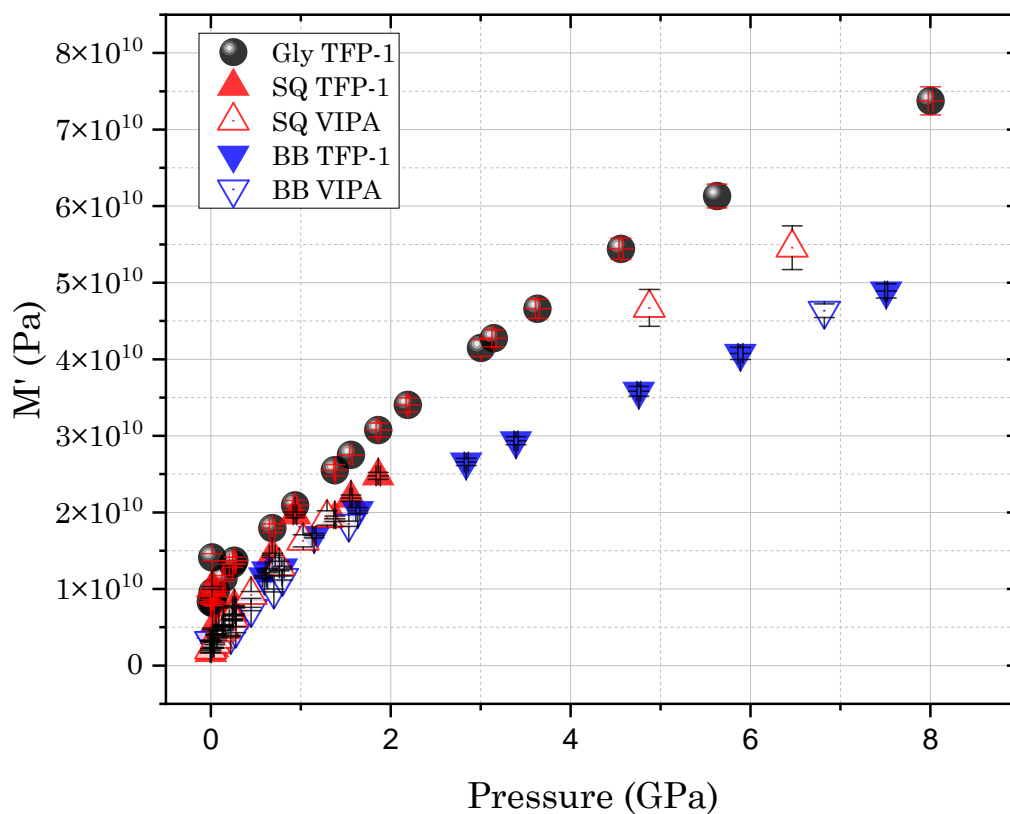


Figure D.4 : Storage modulus over pressure calculated for all fluids of the study at 22°C using the TFP-1 and VIPA interferometers.

Figure D.5 shows that the loss modulus of glycerol below 4 GPa is much higher than squalane and benzyl benzoate. After 4 GPa, their values become similar.

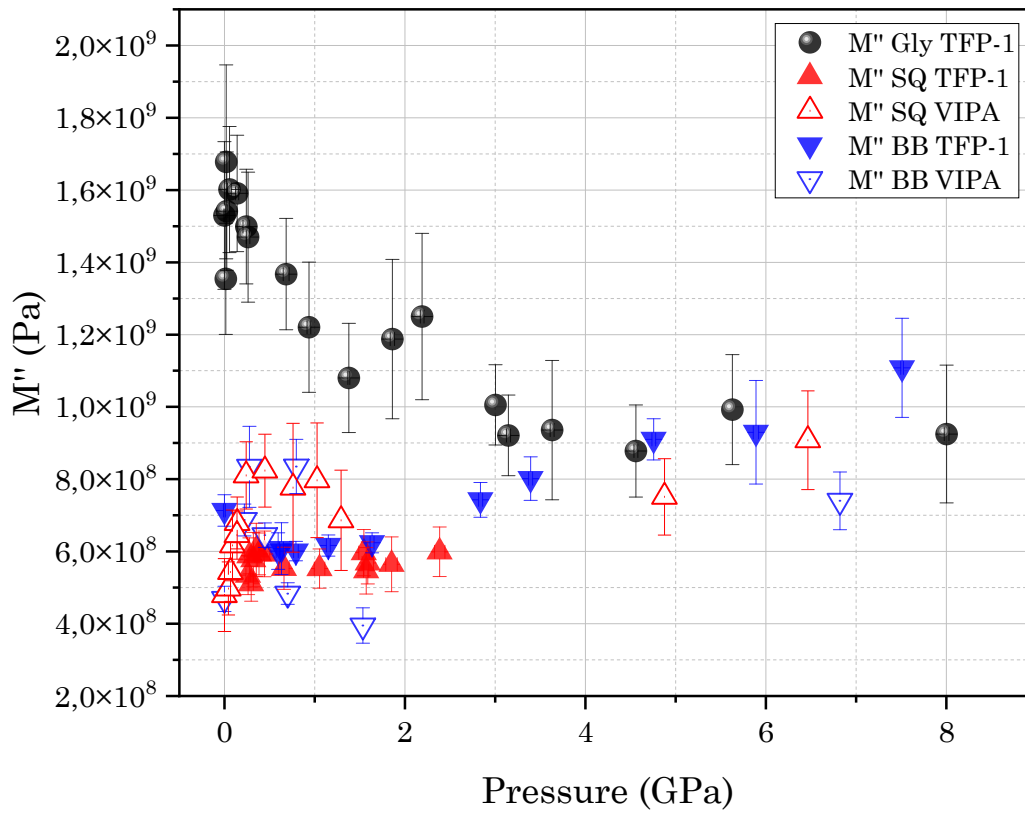


Figure D.5: Loss modulus over pressure calculated for all fluids of the study at 22°C using the TFP-1 and VIPA interferometers.

E. Appendix: Rheology and Brillouin spectroscopy

E.1 Rheometer

An optical rheometer (Physica MCR301, Anton Paar) was coupled to the Brillouin set-up to simultaneously characterize the physical and rheological properties of fluids at atmospheric pressure, fixed temperature under imposed shear rates. Measurements were performed using backscattering microscope identify as unit A as described in Section 3.3.2. Two rotational geometries were available: parallel-plates of $r = 20\text{mm}$ radius and cone-plate of $r=20\text{mm}$ radius, 1.008° cone angle and $76\ \mu\text{m}$ truncation. Both geometries consists in the upper rotating steel plate or cone and the fixed lower glass plate (3 mm thick) which allows performing spectroscopic measurements, as illustrated in Figure E.1. The shear rate is imposed by the rotation of the upper plates or cone driven by the servo motor and the resulting torque is measured to calculate the corresponding shear stress and viscosity.

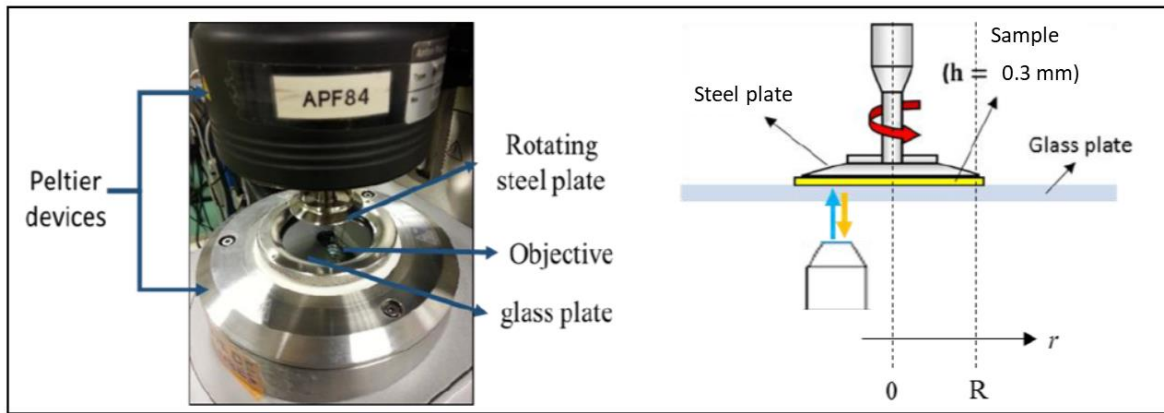


Figure E.1: (left) Picture of the top view of the rheometer used. (Right) Side view of the rheometer coupled with a microscope objective

Thanks to the increasing gap from the center, the cone-plates geometry allows maintaining a constant shear across the sample. However, at very high shear rates, due to the gap ($\sim 0.5\text{ mm}$) at the outer radius of the geometry, the fluid may flow out of the geometry. Therefore, this geometry is rather used with high viscosity fluids. This is the case of glycerol.

In the parallel-plates geometry, the sample is confined between two plates by capillarity forces and can hardly escape at high shear rate. The thickness of the sample introduced into the gap between the two plates is constant and chosen here $H_0=300\mu\text{m}$. This results in a shear rate $\dot{\gamma}$ varying linearly with r , the radius from the rotation axis (i.e from the plate center at $r = 0$) to the considered measurement point. The shear rate varies as follow:

$$\dot{\gamma}(r) = r \frac{\Omega_{\text{Rheo}}}{H_0} \quad (\text{E.1})$$

where Ω_{Rheo} is the angular velocity of the rotating steel plates (in rotation per second). This geometry is adapted for lower viscosity fluids such as benzyl benzoate and the squalane. With the parallel plates geometry, a preliminary shear stress share rates ramp was systematically performed for each fluid at 20°C with a 100 μm and 200 μm gap to verify that the curves were superimposed and that no slip at the wall influenced the measurements. It was found that for some cases, the 100 μm gap tests lead to lowers stresses than tests perform a higher gap at 200 or 300 μm . However, the 200 and 300 μm tests were always superimposed, as shown in Figure E.2. Thus, the 300 μm gap was selected as a relevant gap.

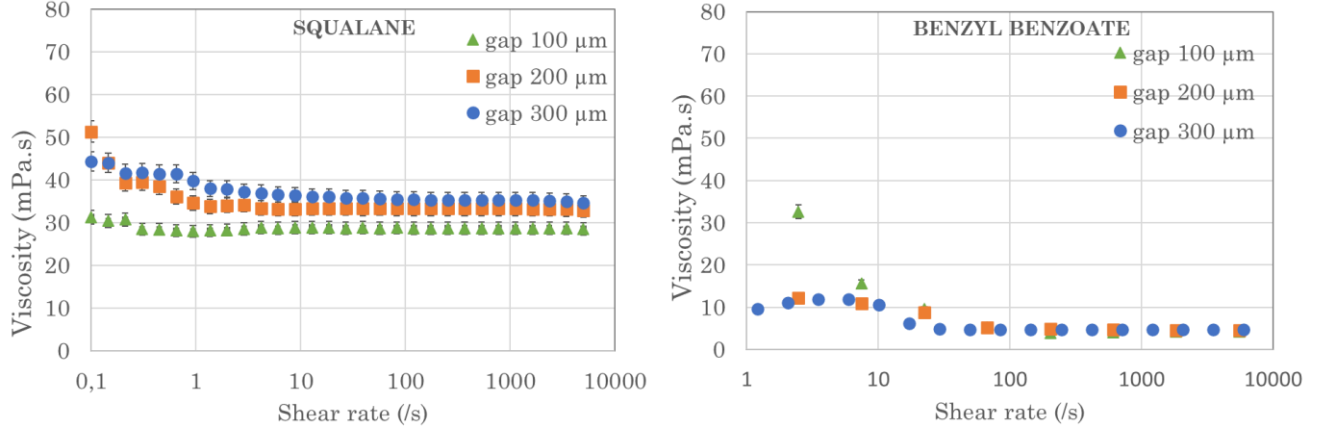


Figure E.2: Viscosity in function of shear rate for 3 gaps (100 μm , 200 μm and 300 μm) for squalane (left) and benzyl benzoate (right)

Spectroscopic measurements were performed at $r = \frac{2}{3} * R$ for the local shear rates to match the macroscopic one provided by the rheometer in the case of parallel plates.

$$\overline{(\dot{\gamma})} = \frac{1}{A_{\text{rea}}} \int_{A_{\text{rea}}} \dot{\gamma}(r) dA_{\text{rea}} = \dot{\gamma} \left(r = \frac{2}{3} R \right) \quad (\text{E.2})$$

Were $\overline{(\dot{\gamma})}$ is the average shear rate found in the parallel plate geometry, A_{rea} is the surface plane, R is the plate radius. A small gap of about 0.1 mm is imposed. For that, the shear rate in the fluid sample at $r=2/3R$ is varied up to 50,000 s^{-1} .

The backscattering microscope unit A was set on a motorized micro-positioning system on an existing XY stage in order to accurately adjust the position of the laser beam relatively to the sample (resolution of 2 μm). The Z direction (beam focus) is adjusted manually to get the highest signal intensity.

The temperature is regulated by Peltier system, fixed at 20°C. It is measured by a Pt100 sensor, which has a precision of $\pm 0.03 \text{ K}$, located near the sample and under the measuring gap. The whole set-up was couple, as shown in Figure E.3.

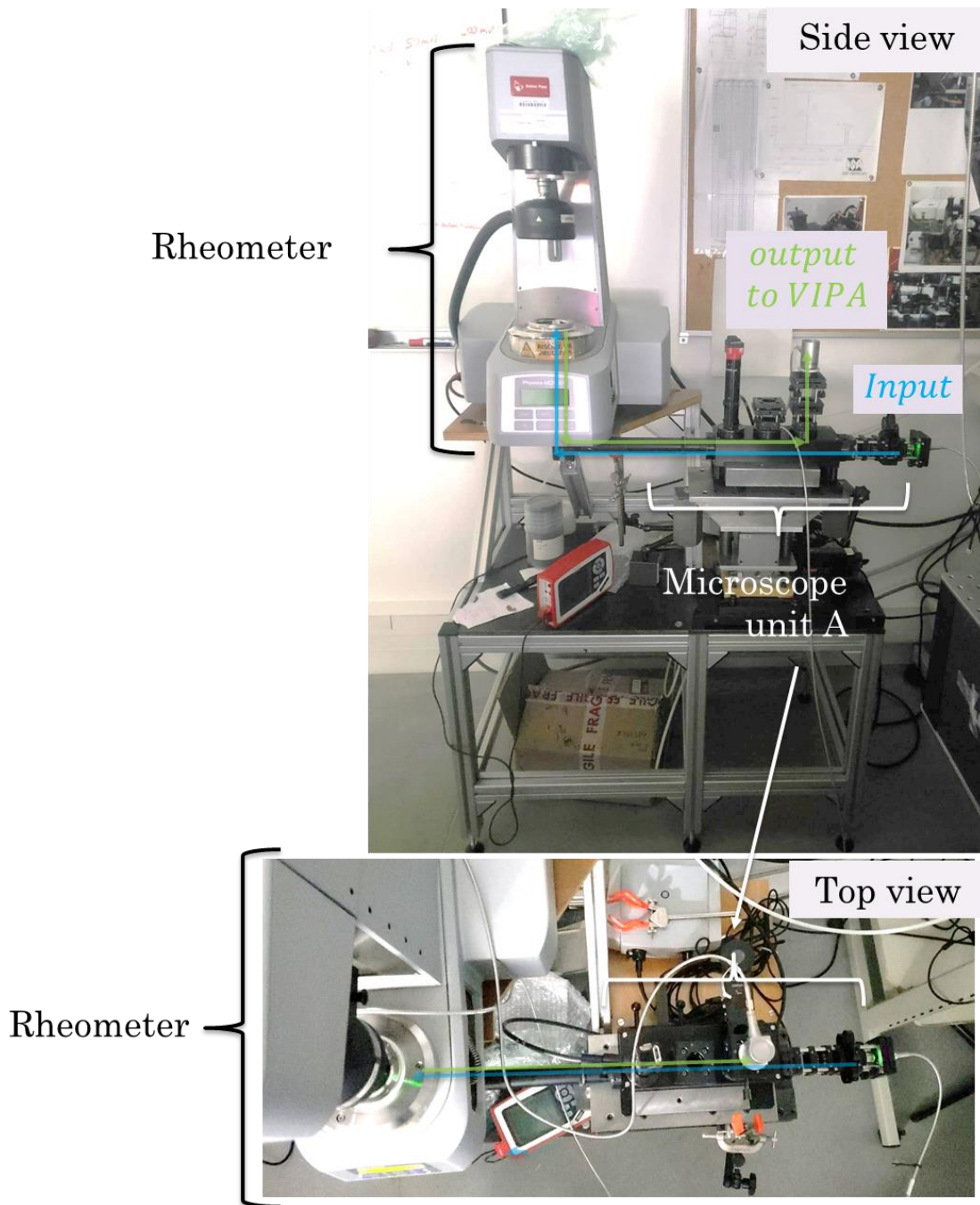


Figure E.3: side and top view of the rheometer-Brillouin coupling using the unit A microscope. Blue arrows shows the laser incident path and in green the scattered light path.

The three fluids glycerol, benzyl benzoate, and squalane were rheologically probed with simple shear tests at 20 °C. The shear rates was varied in the range $[10^{-1}, 10^4]s^{-1}$ and spectroscopic measurements were simultaneously performed. Each spectroscopic measurement was carried out while imposing a constant share rate to the sample. The same protocol was always applied. For each fluid, the temperature was set at 20°C. Then, a 30 minute waiting time was observed for the temperature to be homogeneous into sample.

After this time, plateaus of constant rotational shear rates were applied during two minutes, from the lower shear rates to the higher one. For each shear rate value, the shear stress was recorded in time. When no evolution of shear stress was noted in time, the spectroscopic measurement was performed, with various acquisition time from 500 ms with 300 averaging to 10 s straight depending on the setting of the pump killer. Acquisition time was adjusted so that the signal-to-noise-ratio (SNR) laid to the range of (40-89) for benzyl benzoate, (20-40) for squalane, (130-240) for glycerol. The shear stress corresponding to each constant shear rate was finally calculated as the average value over the recording time. This way, for each shear rate, both the shear viscosity and the Brillouin spectrum were recorded simultaneously. They are plotted in Section E.2.

E.2 Influence of shear rate on the BLS spectra

In addition to the characterization of the three fluids versus pressure, BLS measurements have been performed in a rheometer where the lubricant is submitted to severe shear .

The Brillouin spectroscopy set-up was coupled to a rheometer described in the previous Section E.1. It was then possible to simultaneously measure the macroscopic rheological properties of the fluids and the Brillouin spectra at atmospheric pressure and fixed at 20°C. The idea is to vary the shear rate applied to the sample and to simultaneously measure the rheology curves and the spectra of the fluid. The question is whether a macroscopic and homogeneous shear applied in a rheometer model can modify the behavior of the fluid simultaneously characterized by the Brillouin spectra.

Two remarks should be made on the limits of using a commercial rheometer.

The first one is that the pressure is necessarily the atmospheric pressure. It does not allow to probe the samples in a nominal (i.e at rest or at low frequency) glassy state, according to the $(T_g; P_g)$ conditions predicted by the modified WLF-Yasutomi model. Indeed, we remind here that, as stated previously in Section 3.1, at atmospheric pressure the glass transition temperatures of benzyl benzoate and squalane measured in DSC are respectively -76.3 °C and -101.9°C. The one of glycerol from the literature is of the order of -90°C [120]. But this range of temperatures is not accessible in the rheometer used.

The second remark is that the range of shear rates reached in a rheometer is lower than the maximum shear rates experienced by a lubricant in a ball-disc contact. As stated in 1.2.2, the shear rates experienced by lubricants in a non-conforming contact in the EHD regime are in the range of $[10^5-10^7]$ s⁻¹ due to the low film thicknesses. This range is not recovered by the maximum (homogeneous) shear rate achievable in a rheometer (of the order of 10⁴ s⁻¹).

In any case, despite these limits, tests performed in a rheometer enable to know whether the influence of a macroscopic shear rate on the rheological characteristics of fluids can be measured.

Two types of tests are carried out with the rheometer. First, a simple shear flow, i.e. a permanent shear rate imposed to the sample is used to measure the effect of shear. Second, an oscillatory shear flow, applied by imposing a rotational frequency at a fixed maximum

strain, is used to measure the rheological properties of the samples. Brillouin spectra are recorded directly in the rheometer cell simultaneously with rheological data. Spectra are then fitted with a triple Lorentzian following the procedure detailed in Chapter 4.

For the case of simple shear flow, spectra have been recorded at 20°C and analyzed for mean shear rates in the gap ranging from 0.1 s^{-1} to 10^5 s^{-1} . Frequency shifts and linewidths have been derived and are plotted versus shear rate in Figures E.4 and E.5. It has to be kept in mind that for benzyl benzoate and squalane, the shear is not homogeneous across the plate-plate configuration. The shear rate is dependent on the position in the gap as mentioned in equation E.2 in Section E.1. Moreover, the shear is also averaged across the beam spot of the Brillouin measurements. So, in Figures E.4 to E.6, the corresponding shear rate is the mean.

First, it can be noted that the values of both frequency shift and linewidth measured in the rheometer cell at zero shear rate are similar to the ones measured in the high-pressure cell at atmospheric pressure (Figures 5.4, 5.9 and 5.11).

Then, from Figure E.4, no significant influence of the shear rate is noted on the frequency shift in the range of shear rates tested. As stated in equation 2.40 which links the storage modulus and the frequency shift, it means that the shear does not influence the elastic contribution M'_0 of the longitudinal modulus. A significant drop in the frequency shift of the glycerol at the highest shear rate, which may be attributed to some fluid leaking the gap.

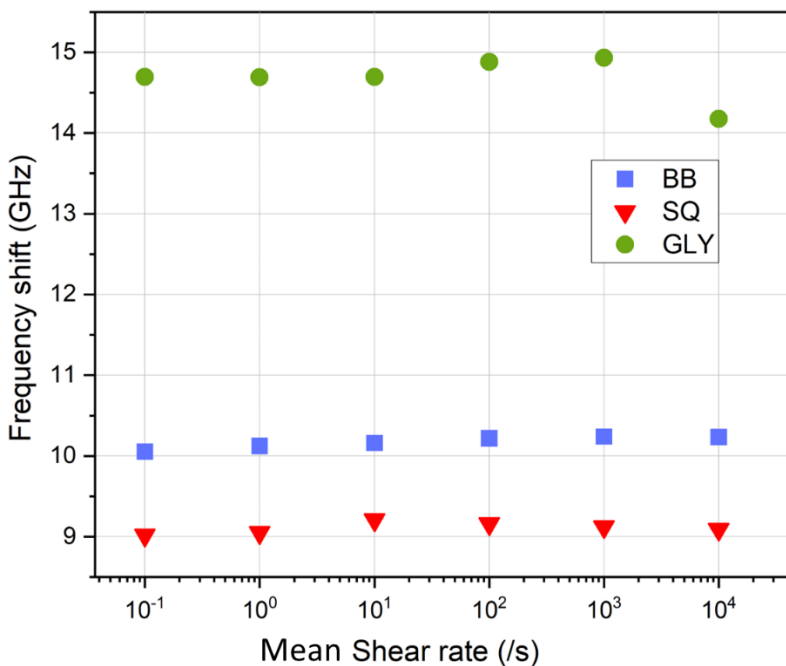


Figure E.4 : Frequency shift of the Brillouin light scattering spectra in function the imposed mean shear rate in the rheometer for the benzyl benzoate, the squalane and the glycerol (simple shear), at 20°C. Error bars are within the size of the markers.

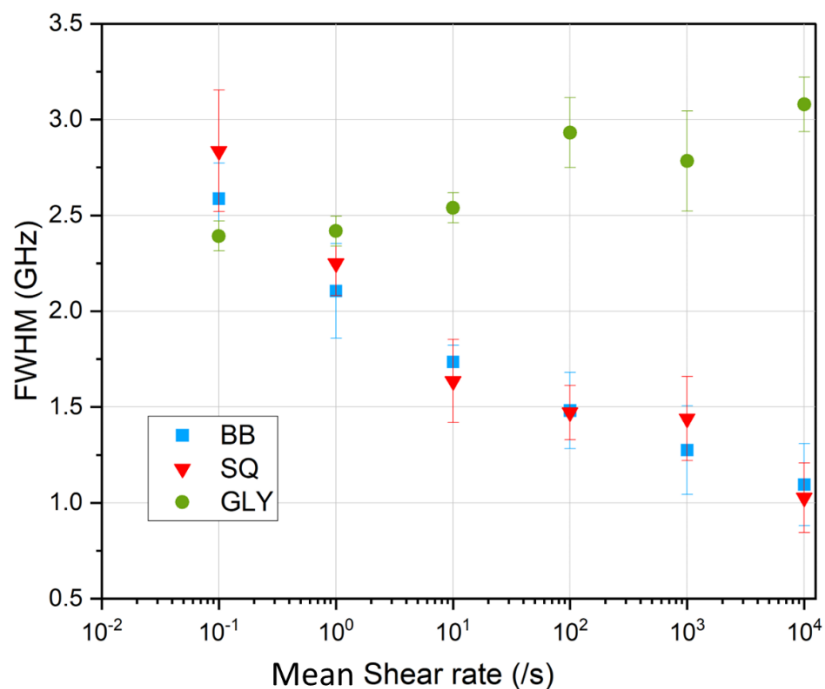


Figure E.5: Linewidth of the Brillouin light spectroscopy spectra in function of the imposed mean shear rate in the rheometer for the benzyl benzoate, the squalane and the glycerol at 20°C.

Interestingly, a clear trend is shown on the linewidth displayed in Figures 5.6 and 5.8 for both benzyl benzoate and squalane. The FWHM significantly decreases with the shear rate, which tends to show that shear reduces the viscous modulus of fluids M_0'' in equation 2.41. On the other hand, looking at the macroscopic shear data simultaneously recorded by the rheometer, and plotted on Figure E.3, the shear viscosity appears to be approximately constant across the shear rate range probed, even though it decreases slightly at low shear rates. It means that the decrease of FWHM does not correspond to a shear thinning behavior of the fluid over the entire range of shear rates. Care must be taken when directly comparing the rheological (so macroscopic) viscosity and the viscous contribution of the fluid from Brillouin spectroscopy.

It can be also noted in Figure E.5 that the linewidth value measured at atmospheric pressure in the rheometer cell tends to reach, at high shear stress, the low linewidth limit value of 0.75 GHz measured at high pressures in the Toullec DAC. If this limit value is representative of a “solid-like” behavior, then it may be stated that for $\dot{\gamma} = 10^4 \text{s}^{-1}$, the convergence of experimental and relaxation timescale initiates the glass transition according to Ediger [100] (see Section 1.3.2) is not reached.

On the other hand, for the glycerol, the FWHM slightly increases with the shear rate, however with large error bars which makes difficult any conclusion

In addition de spectroscopic data, as already mentioned the simple shear viscosity recorded by the rheometer simultaneously with the BLS spectra in Figures E.4 and E.5 is plotted in Figure E.6. For both benzyl benzoate and squalane, a decrease in viscosity is observed on the lowest shear rates, followed by a plateau over 3 orders of magnitude of shear rate

(from 10 s^{-1} to 10^5 s^{-1}). A slight drop of viscosity on the last point (at 10^4 s^{-1}) is observed, which is probably due either to the heating of the fluid, stronger for a more viscous fluid, or to some fluid leaking the gap.

From E.6, the behavior of macroscopic viscosity measured with the rheometer surprisingly appears to follow to the frequency shift. This is detailed in Figure E.7 which superimposes, for each fluid, the viscosity measured by a rheometer and the frequency shift of the spectra measured simultaneously.

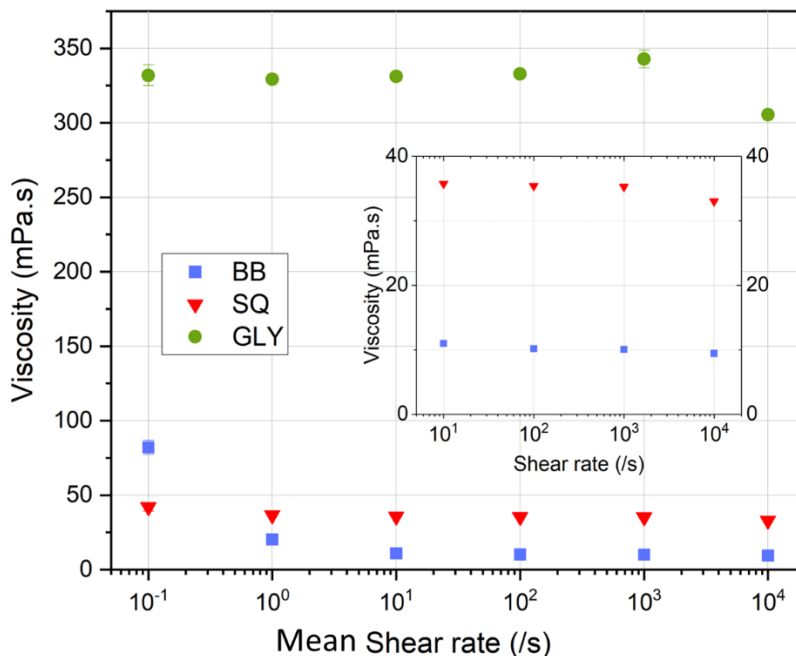


Figure E.6: Viscosity of benzyl benzoate, squalane and glycerol at 20°C versus shear rate measured in a rheometer, following the experimental protocol given in Appendix E.1. Error bars are within the size of the markers. The inset is a zoom on the benzyl benzoate and squalane dataset at high shear rates.

For glycerol, as well as for benzyl benzoate and squalane at shear rates higher than 1 s^{-1} , frequency shifts and rheological viscosities perfectly fit over the range of shear rates tested. It means that the macroscopic behavior of the fluid is governed by the elastic contribution of the fluid modulus M' . This was already noticed in [217] on a diluted polymer (PVP1300000), whose molecule size was much larger than that of the fluids tested here.

For the lower shear rates (0.1 and 1 s^{-1}), a significant discrepancy appears between the Brillouin light scattering frequency shift and the rheological viscosity of benzyl benzoate and squalane. This could imply that at such low shear rates, the viscous contribution of the fluid modulus (M'' correlated with FWHM) plays a significant role in the macroscopic fluid behavior. It is indeed for these low shear rates that the linewidth is the highest (see Figure E.6).

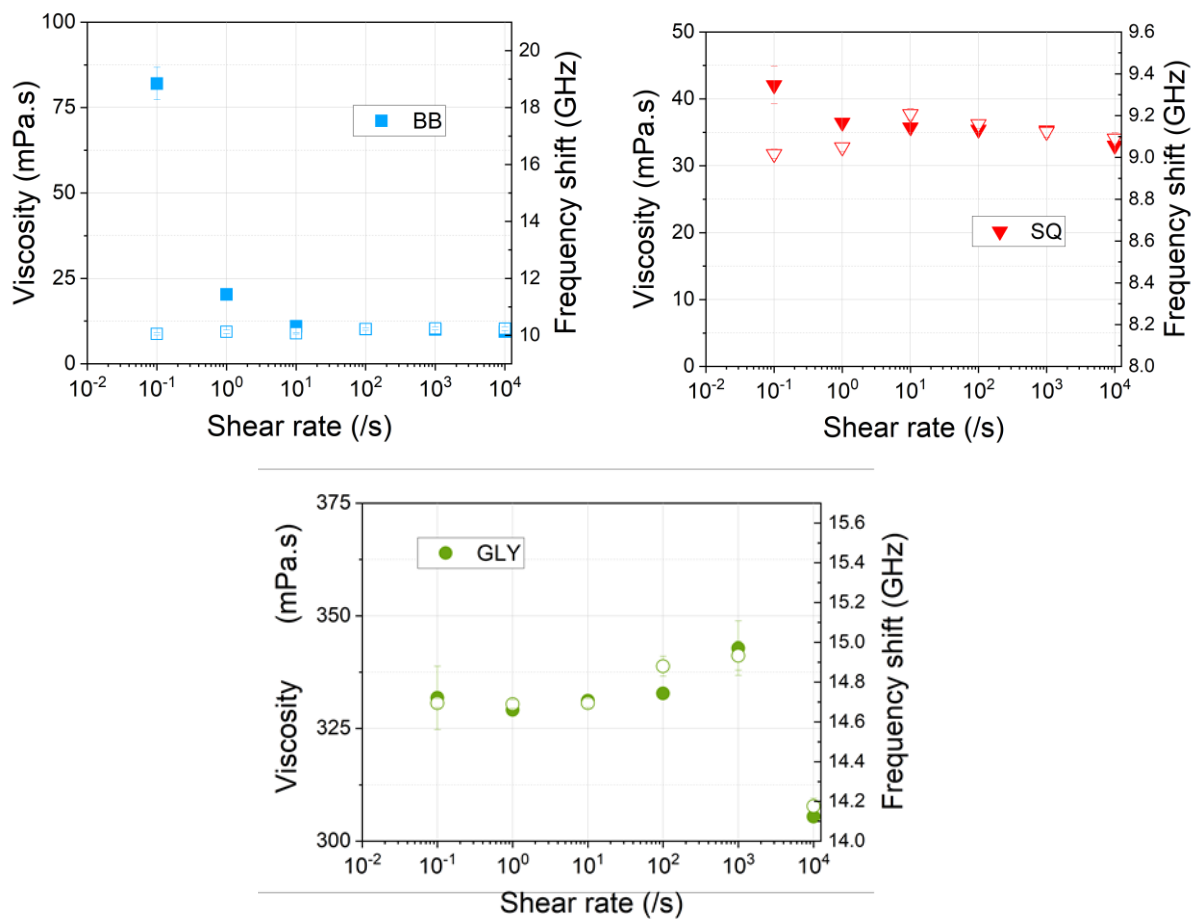


Figure E.7 : Comparison of the shear macroscopic viscosity measured by the rheometer (plain symbols, data from Figure E.6) and the frequency shift measured by Brillouin spectroscopy (open symbols, data from Figure E.5). for each fluid. Scales are adjusted for the data to be comparable.

To go further, one can anticipate that in a contact, the effect of shearing is added to that of the pressure. For the two lubricants probed, benzyl benzoate and squalane, the shear rate experienced by the lubricant in contact should not play a significant role on the elastic part of the fluid modulus (see Figure E.4). However, both shear and pressure decrease the linewidth (see Figures 5.3 and E.5), and thus make the viscous contribution M'' of the fluid modulus (longitudinal or shear) insignificant.

To conclude, the rheometer plays a crucial role in understanding the influence of shear flow on the behavior of lubricant samples. It is utilized to study the rheological properties of the samples under controlled shear rates and temperatures at atmospheric pressure. The rheometer applies simple shear flow at atmospheric pressure, by subjecting the lubricant to different shear rates, ranging from low to high. The combination of Brillouin light spectroscopy with rheological measurements in the rheometer provides valuable data on how shear flow affects the lubricant's properties, shedding light on its viscoelastic behavior and helping to establish correlations between macroscopic behavior and temperature conditions.

F. Appendix: perspectives on the work

This appendix shows pre-work done during this PhD. Figure F.1 shows a high-pressure experiment on squalane performed in the platelet geometry using the C and B unit on the Toullec 11.

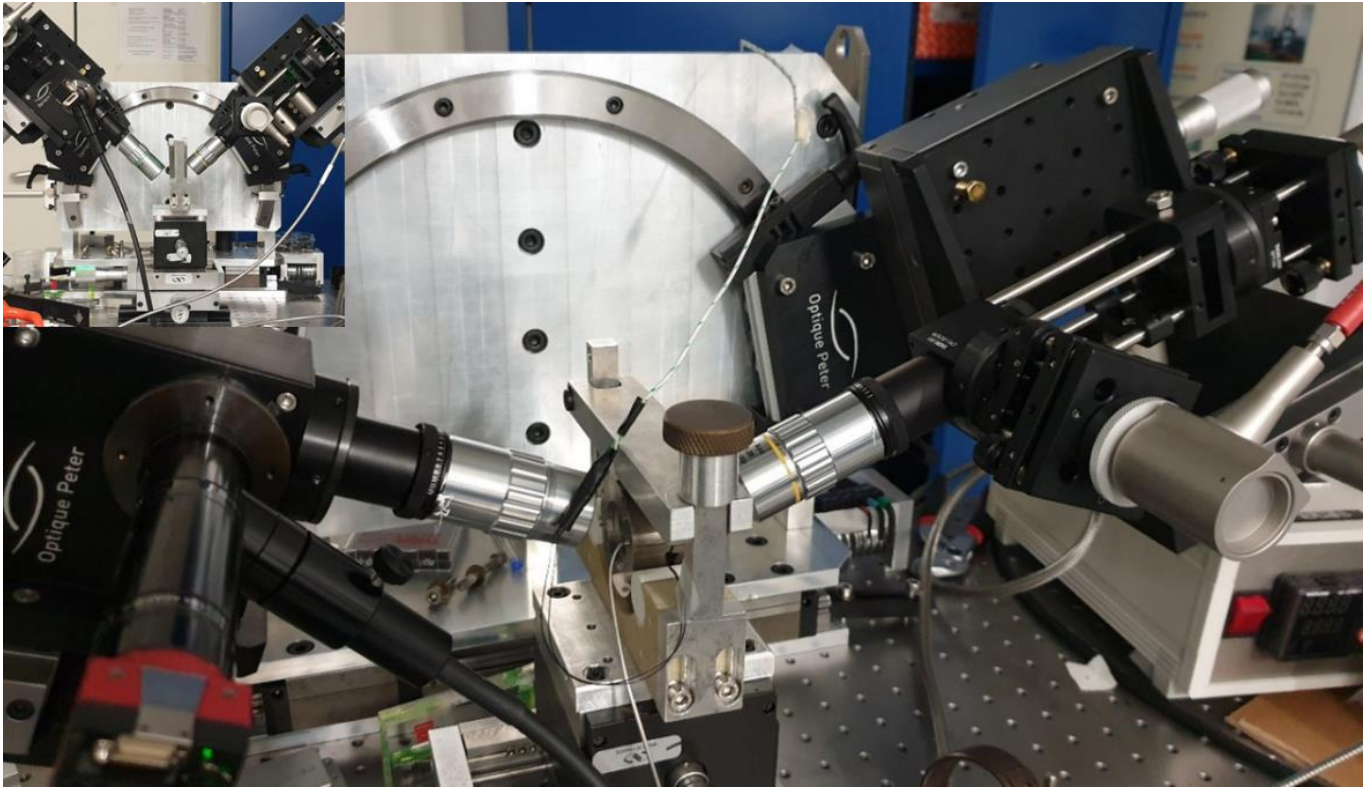


Figure F.1 : Side picture of the pre-study performed on squalane under pressure using Toullec 11 and the angular configuration. Another point of view is situated in the top left corner. B and C units are articulated around the DAC.

Figure F.2 shows the pre-study tribo-Brillouin performed inside the contact using the A unit during a friction test.

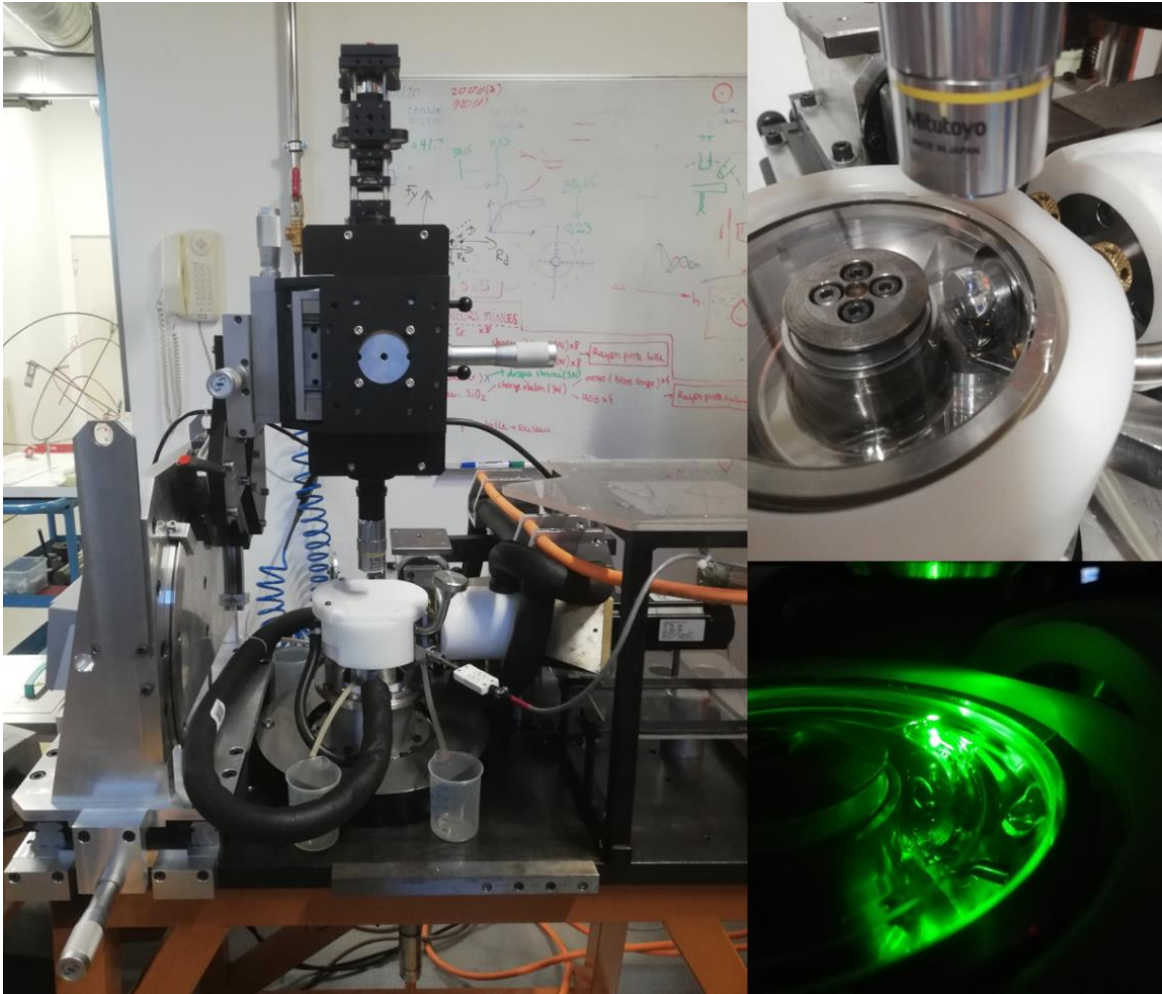


Figure F.2: Pre-study performed on the coupling between the optical microscope and Jerotrib.



FOLIO ADMINISTRATIF

THESE DE L'INSA LYON, MEMBRE DE L'UNIVERSITE DE LYON

NOM : GONON-CAUX (née CAUX)

DATE de SOUTENANCE :

Prénoms : Marjolaine

TITRE : Doctorante

NATURE : Doctorat

Numéro d'ordre : AAAAINSALXXXX

Ecole doctorale : MEGA (Mécanique, Énergétique, Génie Civil, Acoustique)

Spécialité : Mécanique

RESUME: This doctoral research focuses on lubricants behavior in highly loaded lubricated contacts (pressure > 1 GPa), or EHD (elastohydrodynamic) contacts, a vital aspect of engineering and industry. Under such high load, the friction coefficient (= tangential force/normal load) measured in these contacts may display a plateau regime at medium to high sliding velocities of the solid surfaces. It means that the macroscopic average shear stress becomes shear rate independent, associated in the literature to the lubricant Limiting Shear Stress (LSS)]. Previous work provided on molecular dynamic simulations revealed homogeneous and linear lubricant velocity profiles across the lubricant film thickness, even in the friction plateau regime, with no sliding at the walls. This implies that the friction plateau should result from an intrinsic property of the lubricant, reminiscent of the lubricant glass transition scenario. The present study investigates three model fluids: squalane, benzyl benzoate, and glycerol. Those fluids have been characterized in a high-pressure diamond anvil cell and a rheometer, both combined to two Brillouin light scattering spectroscopy set-ups. The results obtained from the new VIPA rig have been compared to those from TFP-1 and the literature. The results from high-pressure experiments have been compared to friction measurements previously conducted on squalane and benzyl benzoate. The study shows a correlation between the glass transition of these fluids and the onset of the friction plateau in EHD contacts. This research advances our understanding on friction in highly loaded lubricated contacts and highlights the importance of considering local dynamics when studying complex fluids under extreme conditions. These insights have the potential to improve lubricant development and to address friction-related challenges in engineering and industry.

MOTS-CLÉS : Contrainte limite de cisaillement, contacts lubrifiés fortement chargés, cellule à enclume de diamants, transition vitreuse, mesure in situ.

Laboratoire (s) de recherche : LaMCoS

Directeur de thèse : Professeur émérite Philippe Vergne

Président de jury :

Composition du jury :